

**STUDIES ON PLASMONIC RESPONSES OF METAL
NANOPARTICLES OF VARIED MORPHOLOGIES AND
THEIR INTERACTION WITH SEMICONDUCTOR
NANOSTRUCTURES**

By
SHWETA VERMA

Enrolment No: PHYS03201504012

Raja Ramanna Centre for Advanced Technology, Indore

*A thesis submitted to the
Board of Studies in Physical Sciences*

*In partial fulfillment of requirements
for the Degree of*

DOCTOR OF PHILOSOPHY

of

HOMI BHABHA NATIONAL INSTITUTE



November, 2019

Homi Bhabha National Institute¹

Recommendations of the Viva Voce Committee

As members of the Viva Voce Committee, we certify that we have read the dissertation prepared by Shweta Verma entitled "Studies on plasmonic responses of metal nanoparticles of varied morphologies and their interaction with semiconductor nanostructures" and recommend that it may be accepted as fulfilling the thesis requirement for the award of Degree of Doctor of Philosophy.

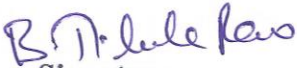
Chairman	Dr. Aparna Chakrabarti	
Guide / Convener	Dr. J. Jayabalan	
Examiner -	Dr. Soma Venugopal Rao	
Member 1-	Dr. T. K. Sharma	
Member 2-	Dr. A. K. Sinha	
Member 3-	Dr. M. K. Chattopadhyay	
External Member -	Dr. G. Ravi Kumar	
Technical Advisor -	Dr. B. Tirumala Rao	

Final approval and acceptance of this thesis is contingent upon the candidate's submission of the final copies of the thesis to HBNI.

We hereby certify that we have read this thesis prepared under our direction and recommend that it may be accepted as fulfilling the thesis requirement.

Date: 15-07-2020

Place: RRCAT, Indore


Signature

Technical advisor



Signature

Guide

¹ This page is to be included only for final submission after successful completion of viva voce.

STATEMENT BY AUTHOR

This dissertation has been submitted in partial fulfillment of requirements for an advanced degree at Homi Bhabha National Institute (HBNI) and is deposited in the Library to be made available to borrowers under rules of the HBNI.

Brief quotations from this dissertation are allowable without special permission, provided that accurate acknowledgement of source is made. Requests for permission for extended quotation from or reproduction of this manuscript in whole or in part may be granted by the Competent Authority of HBNI when in his or her judgment the proposed use of the material is in the interests of scholarship. In all other instances, however, permission must be obtained from the author.



Shweta Verma

DECLARATION

I, hereby declare that the investigation presented in the thesis has been carried out by me. The work is original and has not been submitted earlier as a whole or in part for a degree / diploma at this or any other Institution / University.



Shweta Verma

List of publications arising from the thesis

Journal

1. "Growth temperature dependent surface plasmon resonances of densely packed gold nanoparticles' films and their role in surface enhanced Raman scattering of Rhodamine6G" Shweta Verma, B. Tirumala Rao, S. Bhartiya, V. Sathe, L. M. Kukreja, *Applied Surface Science*, **2015**, 346, 379-387.

2. "Surface plasmon resonances of Ag-Au alloy nanoparticle films grown by sequential pulsed laser deposition at different compositions and temperatures", Shweta Verma, B. Tirumala Rao, A. P. Detty, V. Ganesan, D. M. Phase, S. K. Rai, A. Bose, S. C. Joshi, L. M. Kukreja, *Journal of Applied Physics*, **2015**, 117 133105:1-11.

3. "A facile synthesis of broad plasmon wavelength tunable silver nanoparticles in citrate aqueous solutions by laser ablation and light irradiation", Shweta Verma, B. T. Rao, A.P. Srivastava, D. Srivastava, R. Kaul, B. Singh, *Colloids and Surfaces A*, **2017**, 527, 23-33.

4. "Optical and surface enhanced Raman scattering responses of densely packed Ag-Au alloy nanoparticle films of varied composition and thickness, Shweta Verma, B. Tirumala Rao, V. Sathe, S. Bhartiya, H.S. Patel, R. Kaul, B. Singh, *Journal of Alloys and Compounds*, **2018**, 753, 395-406.

5. "Studies on growth of Au cube-ZnO core-shell nanoparticles for photocatalytic degradation of methylene blue and methyl orange dyes in aqueous media and in presence of different scavengers", Shweta Verma, B. Tirumala Rao, J. Jayabalan, S.K. Rai, D.M. Phase, A.K. Srivastava, R. Kaul, *Journal of Environmental Chemical Engineering*, **2019**, 7, 13209:1-13.

Conferences

1. "Studies on optical properties of Au-ZnO nanocomposite structures" B. Tirumala Rao, Shweta Verma, Tithi Thakur, S. Satapathy, M.K. Singh, S.K. Rai, D. M. Phase, R. Kaul, B. Singh, *Proc. DAE-BRNS National Laser Symposium-NLS 24 RRCAT, Indore*, **2015**.

2. "Optical and photo-catalytic properties of ZnO and Au-ZnO nano-composites grown by pulsed laser ablation", Shweta Verma, B. Tirumala Rao, Sonal Batham, H.

Anamika, S. Satapathy, S.K. Rai, R. Kaul, B. Singh, *Proc. DAE-BRNS National Laser Symposium-NLS 24 RRCAT, Indore, 2015.*

3. "Formation of silver triangular nanoplates using liquid phase pulsed laser ablation and light irradiation", Shweta Verma, B. Tirumala Rao, Sonal Batham, Rakesh Kaul, Bijendra Singh, *Proc. DAE-BRNS National Laser Symposium-NLS 25, Orrisha, 2016.*

4. "Spectroscopic ellipsometry and SERS of ZnO-Au/Ag nanoparticle composite films grown by pulsed laser deposition", Shweta Verma, Binoy Krishna De, B. Tirumala Rao, R. Singh, V. G. Sathe, R. Kaul, *Proc. DAE-BRNS National Laser Symposium-NLS 27, RRCAT, Indore, 2018.*

5. "Dielectric response of ultrathin Au films of different morphologies prepared by Pulsed Laser Deposition", Shweta Verma, B. Tirumala Rao, R. Singh, R. Kaul, *submitted to National Laser Symposium-NLS 28, 2019.*



Shweta Verma

DEDICATED TO,

“My Parents”

ACKNOWLEDGEMENTS

I take this opportunity to sincerely thank my Ph.D. supervisor Dr. J. Jayabalan for his valuable guidance and constant support throughout this work. His prompt response, technical excellence and support in numerical simulations helped me to complete this work in time. I also thank my technical advisor Dr. B. Tirumala Rao for technical discussions, support in experiments and timely suggestions. Without their reverent scientific attitude and selfless support, this research work would not have been completed timely. I thank all the members of doctoral committee, for their fruitful suggestions and constructive comments during yearly evaluation meetings.

I extend my sincere thanks to Shri. Rakesh Kaul, Head of Division (HOD) and former HODs Shri. B. Singh, Dr. L.M. Kukreja for their constant support, encouragement and providing amicable environment for carrying out this research. I also thank Dr. Rama Chari and Dr. T. Sharma for sparing their valuable time in evaluating the progress of the research work yearly at divisional level. I would like to thank Dr. P.D. Gupta, Chairman, Standing Academic Committee, RRCAT for providing permission to pursue Ph.D. programme through HBNI. I also thank Dr. A. Banerjee for his lectures on research methodology.

I further extend my gratitude to Dr. S.K. Rai and Shri. R. Dhawan for XRD and XRR measurements, Dr. V. Ganesan, Shri. Mohan and Smt. S. Bhartiya for AFM measurements, Dr. V. Sathe, Dr. H.S. Patel and Shri. Ajay for Raman measurements, Dr. M.K. Singh and Smt. Rashmi Singh for SEM measurements, Dr. A. Srivastava, Dr. A. P. Srivastava, Dr. D. Srivastava and Shri P. Mondal for TEM measurements, Dr. D.M. Phase and Shri A. Wadikar for XPS measurements, Dr. S. Satapathy and Shri. P. Deshmukh for zeta potential measurements. Thanks are also due to Shri. M.O. Ittoop,

Shri. B.S. Rawat and Shri. Tamboli for providing electrical related support, Shri. Ram Nihal, Shri. C.H. Prem Singh and Shri. Prabhakar for mechanical related support. I also thank Ms. Anamika, Ms. Sonal and Ms. Harshita for assisting in different measurements and Smt. Asha Singh for time resolved measurements. I also thank Dr. P. Ganesh, Dr. Manoj Kumar, Dr. C.P. Paul, Shri. R.K. Gupta, Shri. P. Bhargava and Shri. Ashish Singh for fruitful discussions and their encouragement during the research work.

I express deep sense of gratitude to my parents, sisters, brother, and family friends for their unconditional affection, which has always been a constant source of motivation. I also thank my friends, who always made me smile and comfortable, irrespective of the situations.



Shweta Verma

CONTENTS

	Page No.
SUMMARY	i
LIST OF FIGURES	iii
LIST OF TABLES	xi
LIST OF ABBREVIATIONS	xii
CHAPTER 1 INTRODUCTION	1-26
1.1 Localized surface plasmon resonance in metal nanoparticles	2
1.1.1 Optical absorption and scattering by plasmonic nanoparticles	4
1.1.2 Near-field enhancement by plasmonic nanoparticles	6
1.2 Application of plasmonic nanoparticles	7
1.2.1 Application of plasmonic nanoparticles for surface enhanced Raman scattering (SERS)	11
1.3 Plasmonic metal-semiconductor nano- composites	12
1.3.1 Photocatalytic degradation of dye	13
1.4 Motivation and problem formulization	14
1.5 Objectives	22
1.6 Organization of thesis	24
CHAPTER 2 GROWTH TEMPERATURE CONTROLLED PLASMONIC RESPONSE OF Au NANOPARTICLE FILMS FOR SERS APPLICATION	27-64
2.1 Effective dielectric response of metal thin films	29
2.1.1 Contribution from geometry of nanoparticles	30
2.1.2 Contribution of substrate	30
2.1.3 Contribution from interaction between the nanoparticles	31
2.1.4 Overall contribution of substrate and other nanoparticles at high coverage	32
2.2 Optical transmission of Au thin films	34
2.3 LSPR wavelength tunability with morphological parameters	35
2.4 Spectroscopic ellipsometry based determination of effective dielectric response (ϵ_{eff})	36

2.4.1	Dispersion models for determination of optical properties from ellipsometry	38
2.5	Dielectric response of Au thin films of different thicknesses	43
2.6	Growth temperature induced LSPR characteristics and their correlation with morphological parameters	48
2.7	Effect of alumina layer capping and LSPR characteristics of Au nanoparticle films	56
2.8	Comparison of SERS response of films of varied morphologies	59
2.9	Summary	63
CHAPTER 3 PLASMONIC RESPONSE TUNABLE Ag-Au ALLOY NANOPARTICLE FILMS FOR SERS AT DIFFERENT WAVELENGTHS		65-99
3.1	Dielectric function of alloys	66
3.2	Growth of Ag-Au alloy nanoparticle films of varied compositions	70
3.3	Optical response and LSPR characteristics of Ag-Au alloy nanoparticle films	75
3.4	Analytical calculation of LSPR response of Ag-Au alloy nanoparticle films	84
3.5	Experimental determination of dielectric response of alloy nanoparticle films using spectroscopic ellipsometry	87
3.6	SERS response of Ag-Au nanoparticle films	91
3.7	Summary	98
CHAPTER 4 LASER ABLATION AND LIGHT IRRADIATION BASED SYNTHESIS OF SPHERICAL AND TRIANGULAR Ag NANOPARTICLES FOR SERS APPLICATION		100-127
4.1	Growth of colloidal Ag nanoparticles by laser ablation	102
4.2	Effect of citrate concentration on laser ablation based growth of colloidal Ag nanoparticles	103
4.3	Calculation of number concentration of Ag nanoparticles	106
4.4	Effect of pH on growth of Ag nanoparticles by laser ablation	110
4.5	Light irradiation of LPPLA grown Ag nanoparticles	112
4.6	Effect of citrate concentration on photo-mediated shape transformation	117
4.7	Effect of Ag ions on photo-mediated shape transformation	118

4.8	Effect of solution pH on shape transformation of Ag nanoparticles	122
4.9	SERS response of spherical and triangular shape Ag nanoparticles	124
4.10	Summary	126
CHAPTER 5 STUDIES ON OPTICAL AND PHOTO-CATALYTIC DYE DEGRADATION RESPONSE OF Au CUBE - ZnO CORE-SHELL NANOPARTICLES		128-159
5.1	Discrete dipole approximation for arbitrary shape nanoparticles	129
5.2	Growth of Au-ZnO core-shell nanoparticle	132
5.3	Optical absorption of Au-ZnO nanoparticles during growth of shell layer	135
5.4	Effect of annealing on optical response and structural characteristics of core-shell nanoparticles	136
5.5	Photocatalytic dye degradation kinetics	140
5.6	Photo-degradation of MB dye	141
	5.6.1 Effect of presence of various scavengers	148
	5.6.2 Effect of pH	151
5.7	Photo-degradation of MO dye	154
5.8	Summary	157
CHAPTER 6 PHOTO-CATALYTIC DEGRADATION OF DIFFERENT DYES AND THEIR MIXTURES USING Au DECORATED ZnO NANORODS		160-187
6.1	Synthesis of Au nanoparticle decorated ZnO nanorods	161
6.2	Structural and compositional properties	163
6.3	Photocatalytic response of Au decorated ZnO nanorods	167
	6.3.1 Effect of scavengers	173
	6.3.2 Effect of pH	177
6.4	Degradation of mixed dyes at different pH conditions	178
6.5	Transient Response of Ag-ZnO nanoparticle films	182
6.6	Summary	187
CHAPTER 7 CONCLUSION AND FUTURE SCOPE		188-194
REFERENCES		195-213

LIST OF FIGURES

S. No.	Figure caption	Page No.
1.1	Schematic of LSPR excitation in metal nanoparticles.	2
1.2	Different attributes of plasmon resonance in metal nanoparticles and related applications.	8
1.3	Different applications of plasmon-semiconductor nanocomposites.	13
2.1	SEM image of Au films of ~ 3.5 nm thickness, grown (a) at RT and (b) substrate temperature of 300°C .	28
2.2	Schematic of nanoparticle and continuous films of dielectric response ϵ_{eff} and bulk ϵ_{Au} respectively.	30
2.3	Schematic showing interaction between particle dipole and image dipole.	31
2.4	Schematic showing particle-particle and particle-image dipole interactions.	32
2.5	Schematic showing particle and its mirror image in a substrate at different aspect ratios.	33
2.6	Schematic of thin film supported on a substrate of finite thickness.	34
2.7	Tunable range of LSPR wavelength of Au nanoparticles films with morphological parameters.	35
2.8	Schematic of spectroscopic ellipsometry measurement principle.	37
2.9	Schematic of the PLD experimental setup.	43
2.10	Transmission of Au films produced at (a) RT and (b) substrate temperature of 300°C .	44
2.11	Measured (symbols) and fitted (lines) ellipsometry data (Ψ , Δ) of Au films deposited at (a,b) RT and (c,d) 300°C substrate temperature with 4000 ablation pulses.	46
2.12	Variation of dielectric response of RT grown Au films grown with	

	varied ablation pulses, dashed line represents the same for bulk Au.	47
2.13	Variation of dielectric response of Au films grown at 300 °C with different number of ablation pulses.	48
2.14	Transmission of Au nanoparticle films of (a) 3.5 nm and (b) 5.5 nm thickness, inset presents the LSPR characteristics of the film.	49
2.15	Effect of growth temperature on film morphology (AFM images scan area 1 μ m x 1 μ m and line profile) of 5.5 nm thickness Au films.	51
2.16	Transmission of Au films of (a) 8 nm and (b) 17 nm thickness.	52
2.17	Effect of growth temperature on film morphology (AFM images scan area 1 μ m x 1 μ m and line profile) of 8 nm thickness Au films.	53
2.18	Effect of growth temperature on film morphology (AFM images scan area 1 μ m x 1 μ m and line profile) of 17 nm thickness Au films.	54
2.19	Schematic of effect of growth temperature on film morphology.	55
2.20	Comparison of transmission of Au films deposited at different combination of laser pulses and growth temperature.	56
2.21	Transmission of Au films of (a) 5.5 nm and (b) 8 nm thickness after capping with alumina layer.	57
2.22	SERS intensity spectra of Rh6G dye in absence and presence of Au nanoparticle films of (a) 5.5 nm and (b) 8 nm film thickness.	61
2.23	SERS spectra of Rh6G dye in presence of Au nanoparticle films of (a) 8 nm and (b) 17 nm film thickness.	62
3.1	Comparison of model-I, II and III predicted real(ϵ) and imaginary (ϵ) of (a) Ag, (b) 1:1 alloy, (c) Au and combinedly in (d).	69
3.2	XRD intensity of a thick Ag-Au alloy film grown with 1:1 pulses ratio of Ag and Au with total 30000 pulses; inset: GIXRD intensity pattern of alloy films of different compositions deposited with total 6000 pulses.	72
3.3	Variation of XPS BE spectra (a) Ag 3d and (b) Au 4f core level with alloy composition.	73

3.4	EDS spectrum of Ag-Au alloy film.	75
3.5	Transmission of Ag-Au alloy films deposited with total (a) 2000 (b) 4000 and (c) 6000 pulses and varied ratio of laser pulses of Ag and Au.	76
3.6	AFM images along with distributions of diameter of Ag-Au nanoparticles grown with total 2000 pulses at 300°C temperature.	79
3.7	AFM images along with line scan and distribution of diameter of Ag-Au nanoparticles grown with total 4000 pulses at 300°C temperature.	80
3.8	UV-Vis. transmission spectra of Ag-Au alloy films deposited at RT for (a) 2000 and (b) 4000 total pulses.	82
3.9	AFM images along with line scan and distributions of diameter of Ag-Au nanoparticles grown with total 4000 pulses at RT.	83
3.10	Calculated transmission of Ag-Au alloy films of varied compositions deposited with total 4000 ablation pulses at 300°C, using the three analytical models.	85
3.11	LSPR wavelength of Ag-Au films versus volume filling fraction and percentage of Ag in the films.	87
3.12	Variation of LSPR strength (ΔT) and wavelength with Ag:Au laser pulses ratio.	88
3.13	Experimentally observed (symbols) ellipsometry parameters (Ψ : solid, Δ : open) at four AOI along with model fitted data (lines) obtained for Ag-Au alloy nanoparticle films deposited with total 2000 laser pulses.	89
3.14	Variation of (a) real ϵ_{eff} and (b) imag ϵ_{eff} of Ag-Au alloy films deposited with total 2000 laser pulses for varied ratio of Ag and Au laser pulses.	90
3.15	Comparison of calculated (open symbol) and experimental (solid line) transmission of Ag-Au alloy films deposited with total 2000	

	laser pulses.	90
3.16	Imag (ϵ_{eff}) of Ag-Au films deposited with different total pulses and (a) 1:0 and (b) 2:1 ratio of Ag and Au laser pulses.	91
3.17	Typical AFM image of closely spaced noble metal nanoparticle film grown by PLD.	92
3.18	SERS intensity of Rh6G Dye molecules obtained with 488 nm excitation wavelength, in presence of Ag-Au alloy films deposited with varied total number of laser pulses.	94
3.19	SERS intensity of Rh6G Dye molecules obtained with 633 nm excitation wavelength, in presence of Ag-Au alloy films.	95
3.20	SERS intensity of Rh6G dye molecules in presence of Ag-Au alloy films measured with 50 s (5X) integration time.	96
3.21	Comparison of LSPR tuning by varying alloy composition and film thickness for application of efficient SESRS substrate.	97
4.1	Variation of (a) absorbance of Ag nanoparticles with ablation time during growth and (b) its TEM image after 30 min. ablation.	103
4.2	Variation of absorbance of Ag nanoparticles with ablation time during growth in citrate solution of (a) 0.5 mM, (b) 10 mM; inset: particle size distribution (c) 100 mM and (d) TEM image of Ag nanoparticles obtained in 10 mM citrate solution.	105
4.3	Schematic of laser ablation of Ag coin producing Ag nanoparticle solutions, and the obtained variation of peak absorbance versus (a) laser ablation time and (b) citrate concentration	106
4.4	Experimental and calculated absorbance of Ag nanoparticles	109
4.5	(a) Absorbance spectra of Ag nanoparticles produced in varied pH conditions and (b) variation of LSPR absorbance with pH value of the solution.	111
4.6	XRD spectra of Ag nanoparticles produced at different pH conditions.	112
4.7	Fig. 4.7 (a) Intensity spectrum of the irradiation lamp, (b)	

	photographic image of Ag nanoparticles and (c) absorption spectra after different irradiation time.	113
4.8	TEM images of Ag nanoparticles obtained after (a) 6 hrs and (b) 24 hrs of light irradiation.	114
4.9	Variation in peak absorbance of Ag nanoparticles at ~ 400 and ~690 nm with irradiation time.	115
4.10	Fig. 4.10 Absorption spectra of Ag nanoparticles formed in varying concentrations of citrate after (a) 6 hrs. and (b) 24 hrs. of irradiation.	118
4.11	Fig. 4.11 UV-Vis. absorption of Ag nanoparticles formed in 10 mM citrate solution and irradiated in presence of silver salt of (a) 0.1 mM and (b) 0.2 mM and TEM images obtained after (c) 06 hrs. and (d) 24 hrs. of irradiation.	120
4.12	UV-Vis. absorption of Ag nanoparticles formed in varied concentrations of citrate and irradiated in presence of 0.1 mM silver salt for (a) 6 hrs (b) 24 hrs, and TEM images of Ag nanoparticles formed in 25 mM citrate after irradiation of (c) 06 hrs and (d) 24 hrs.	121
4.13	UV-Vis. absorption of Ag nanoparticles formed in 10 mM citrate of pH 10 (a) before and after addition of AgNO ₃ solution of (b) 0.1 mM and (c) 0.2 mM, at different irradiation time and its (d) TEM image after 24 Hrs of light irradiation time.	123
4.14	SERS spectra of Rh6G molecules of (a) 1μM and (b) 500 nM concentration in presence of spherical and triangular Ag nanoparticles.	125
4.15	SERS spectra of MB molecules of 1μM concentration in presence of spherical and triangular Ag nanoparticles.	125
5.1	Extinction efficiency of Au nanocubes of (a) varied edges lengths, and (b) with smoothed edges.	132
5.2	(a) SEM image of Au nanocubes, and TEM images of Au-ZnO core shell nanoparticles (b,c) before and (d) after annealing.	134
5.3	Optical absorption spectra of core-shell nanoparticles during growth.	136

5.4	(a) Optical absorption spectra and (b) FTIR spectra of annealed Au-ZnO core-shell nanoparticles.	137
5.5	XRD intensity of as-grown and annealed Au-ZnO core-shell nanoparticles.	139
5.6	XPS BE spectrum of (a) Zn-2p, (b) O-1s and (c) Au-4f, Zn-3p of Au-ZnO core-shell and ZnO nanoparticle.	140
5.7	Absorbance spectra of MB dye versus irradiation time in presence of (a) as-grown, 600°C annealed (b) Au-ZnO and (c) ZnO nanoparticles, (d) corresponding normalized dye concentration.	142
5.8	Comparison of (a) dye degradation process under irradiation of UV-A and UV-C light and (b) their intensity pattern.	145
5.9	(a) Normalized dye concentration versus irradiation time (b) inverse of apparent rate constant for different initial dye concentrations.	146
5.10	Normalized dye concentration versus irradiation time for MB dye of initial concentration (a) 25 and (b) 50 μM , in presence of different loading of photocatalyst.	147
5.11	Normalized dye concentration versus irradiation time for MB dye [50 μM] mixed with 1g/L of CS600 and scavengers (a) EDTA- Na_2 , (b) NaN_3 and (c) IPA of varied concentrations.	149
5.12	Normalized dye concentration versus xenon lamp irradiation for MB dye (50 μM) mixed with 1g/L of CS600 without and with scavengers.	151
5.13	Normalized dye concentration versus irradiation time for MB dye [50 μM] mixed with 1 g/L of CS600 (a) under varied pH condition (b) and different scavengers.	153
5.14	Photographic image of core-shell nanoparticles and effect of UV irradiation time, pH and scavenger on degradation of MB solution when mixed with these nanoparticles.	154
5.15	Variation of (a) absorbance of MO dye and (b) normalized dye concentration versus irradiation time for varied concentrations of MO	

	dye mixed with 1g/L of CS600.	155
5.16	Normalized dye concentration versus irradiation time for MO dye [50 μ M] mixed with 1g/L of CS600 and (a) NaN ₃ , (b) EDTA-Na ₂ , (c) IPA scavengers and (d) at different pH conditions.	157
6.1	Photographic images of the ZnO nanopowder (a) before and after UV irradiation in presence of (b) 3 and (c) 5 mL of 25 mM HAuCl ₄ solution.	162
6.2	SEM images of the ZnO nanopowder (a) before and after UV irradiation in presence of (b) 3 and (c) 5 mL of 25 mM HAuCl ₄ solution.	163
6.3	XRD spectra of the ZnO nanorods annealed at different temperatures.	164
6.4	XRD spectrum of ZnO nanorods annealed at different temperatures.	165
6.5	XPS intensity spectra of (a) O 1s, (b) Zn-2p and (c) Au-4f binding energy peaks of Au nanoparticle decorated ZnO nanorods.	166
6.6	Chemical structure of the dyes used for photocatalytic degradation	168
6.7	Variation of normalized concentration of MB dye with irradiation time in presence of ZnO nanorods without and with Au nanoparticles.	169
6.8	Variation of normalized concentration of (a) MB, (b) MO, (c) Rh6G, and (d) RhB dyes and corresponding $(k_{app})^{-1}$ with irradiation time in presence of Au-ZnO nanorods.	172
6.9	Variation of normalized concentration of 50 μ M MB dye with irradiation time, in presence of (a) EDTA-Na ₂ , (b)NaN ₃ and (c) IPA of varied concentrations.	173
6.10	Variation of normalized concentration of 50 μ M MO dye with irradiation time, in presence of (a) EDTA-Na ₂ , (b)NaN ₃ and (c) IPA of varied concentrations.	175
6.11	Variation of normalized concentration of 30 μ M Rh6G dye with irradiation time, in presence of (a) EDTA-Na ₂ , (b)NaN ₃ and (c) IPA of varied concentrations.	176

6.12	Variation of normalized concentration of 30 μM RhB dye with irradiation time, in presence of (a) EDTA- Na_2 , (b) NaN_3 and (c) IPA of varied concentrations.	176
6.13	Variation of normalized concentration of (a) MB, (b) MO, (c) Rh6G, and (d) RhB dyes with irradiation time at different pH conditions of the solution, in presence of Au-ZnO nanorods.	178
6.14	Variation of absorbance of mixed dyes of 30 mM concentration each, (a) MB+Rh6G, (b) MB+RhB, (c) MB+MO and (d) RhB+Rh6G, with irradiation time in presence of Au-ZnO nanorods.	179
6.15	Variation of absorbance of mixed dyes of 30 mM concentration each, (a) MB+Rh6G, (b) MB+RhB, (c) MB+MO and (d) RhB+Rh6G, with irradiation time at pH 12, in presence of Au-ZnO nanorods.	180
6.16	Variation of absorbance of mixed dyes of 30 mM concentration each, (a) MB+Rh6G, (b) MB+RhB, (c) MB+MO and (d) RhB+Rh6G, with irradiation time at pH 3, in presence of Au decorated ZnO nanorods.	181
6.17	The absorbance spectra of Ag nanoparticle and Ag-ZnO nanoparticle films.	182
6.18	Representative AFM images and corresponding height profiles of (a) and (b) Ag nanoparticle film and (c) and (d) Ag nanoparticle film coated with 3000 pulses of ZnO. (e) shows the AFM scan on a region of pure Ag to Ag coated with ZnO in 3D.	183
6.19	The schematic of the transient absorption measurement setup.	184
6.20	The transient transmittance of the Ag and Ag-ZnO nanoparticle films. The solid line shows the best fit to the decay part with single exponential function.	185

LIST OF TABLES

S. No.	Table	Page No.
2.1	LSPR characteristics of Au films without and with alumina over layer deposited at varied substrate temperatures.	59
3.1	Mass thickness and C corrected Binding energy (BE) peak positions of Ag-3d _{5/2} and Au-4f _{7/2} of Ag-Au films.	74
3.2	Average diameter (nm) and number density (cm ⁻²) of nanoparticles in Ag-Au films deposited with different ratio of Ag and Au ablation pulses.	81
5.1	Zeta potential (ζ) of 600°C annealed Au-ZnO core-shell nanoparticles (CS600)	152

LIST OF ABBREVIATIONS

AFM:	Atomic Force microscopy
ASF:	Atomic Sensitivity Factor
BE:	Binding Energy
DDSCAT:	Discrete Dipole Scattering
EF:	Enhancement Factor
IB:	Inter-Band
LPPLA:	Liquid Phase Pulsed Laser Ablation
LSPR:	Localized Surface Plasmon Response
MB:	Methylene Blue
MO:	Methyl Orange
PLD:	Pulsed Laser Deposition
Rh6G:	Rhodamine6G
RhB:	RhodamineB
SEM:	Scanning Electron Microscopy
SERS:	Surface Enhanced Raman Scattering
TEM:	Transmission Electron Microscopy
XPS:	X-ray Photoelectron Spectroscopy
XRD:	X-ray Diffraction

Chapter 7

Conclusion and future scope

In the first part of the thesis, growth of i) controlled morphologies of Au and Ag-Au alloy nanoparticle films and ii) high concentration Ag nanoparticles dispersed in aqueous solution, has been demonstrated using pulsed laser ablation technique. These nanoparticle films exhibited tunable LSPR response in visible to near IR region suitable for SERS application. The second part of the thesis is focused on optimization of synthesis of Au-ZnO nano-composites of two morphologies (core-shell and Au decorated ZnO nanorod) useful for photocatalytic dye degradation of different dyes for water treatment application, using hydrothermal method.

In order to obtain LSPR response in as-grown films (i.e. in single step) of Au or Ag, high substrate temperature during film deposition was found to be important. Other than realizing LSPR response, variation of substrate temperature was found to be helpful in controlling nucleation density or film morphology for fine tuning of the LSPR of a given thickness of these metal films. The films produced at optimum substrate temperature of about 300°C have shown blue shifted and narrow band LSPR. In all the cases, the films were formed with densely packed nanoparticles and increasing film thickness resulted large size nanoparticles and red shifted LSPR response. At optimum substrate temperature (about 300°C) the grown Au films of thickness about 5-15 nm resulted strong and narrow LSPR band tunable in range of about 600-800 nm. Alumina layer capping on these metal nanoparticle films has resulted redshifted LSPR response. Au films grown at low substrate temperature (< 300 °C) resulted formation of interconnected nanoparticles due to high nucleation density and those grown at 500 °C

produced high aspect ratio nanoparticles of irregular shapes. Substrate temperature of about 300 °C resulted relatively uniform size nanoparticles of average size in the range of 20-35 nm.

Pulsed nature of film deposition in PLD was explored for growth of composition control Ag-Au alloy nanoparticle films for tuning of LSPR wavelength without much change in its broadening. Alloy composition was varied by changing ratio of ablation pulses of two targets (i.e. Ag and Au) in sequential laser ablation process. The composition of the alloy films has been determined from XPS and EDS, and were found to be in consistent with amount of Ag and Au deposited by their respective number of ablation pulses. By varying alloy composition and film thickness, the LSPR wavelength tuning was achieved in the range of 450-900 nm. At RT growth, Ag has shown more tendency to form nanoparticle films compared to Au, as a result, only Ag and Ag rich films showed LSPR response. However, at optimum substrate temperature of 300-400 °C, all films of different alloy compositions showed formation of densely packed nanoparticles with particle densities in the range of $\sim 10^{10}$ to 10^{11} cm⁻² with tunable LSPR response.

Effective dielectric function of these films of known thickness and nanoparticle sizes were determined from effective medium theory, which accounts particle-particle and particle-substrate interactions pertinent to the formed densely packed nanoparticles. For these calculations, the required input dielectric function of Au and Ag was taken from the literature and for Ag-Au alloy nanoparticle films of different compositions it is obtained from different theoretical models. Optical response determined from this effective dielectric function revealed that same LSPR wavelength can be realized with different combinations of particle aspect ratio and metal volume filling fraction nanoparticles in these films. These theoretical

predictions helped in determining the possible range of LSPR tunability in Au or Ag or their alloy films. This confirms Ag-Au alloy nanoparticles formation and further revealed the reasons for the experimental observation of same LSPR wavelength in different thickness films grown at different substrate temperatures.

Further, effective dielectric function of films of different morphologies (i.e. either continuous or percolated or nanoparticles without knowing their morphological parameters) is also determined experimentally from spectroscopic ellipsometry. Fitting of the ellipsometry data was carried out with combination of Drude and Gaussian oscillators based analytical model that revealed the variation of free electron response with film thickness and growth temperature. In RT grown Au films of high thickness of about 38 nm, the free electrons have shown Drude model type response. However, for the films grown at 300 °C, the free electrons have shown oscillator type behavior, which reveals LSPR response in these films. The oscillator energy was found to be red-shifted with increasing film thickness or Au percentage in alloy films, which is in consistent with the optical transmission. The imaginary part of dielectric response has shown LSPR excitation peak which red shifted with film thickness or Au percentage and also inter-band absorption edge, which red-shifted only with Au percentage. Calculated transmission from the obtained dielectric response of these films also matched with the experimentally measured transmission spectra.

These densely packed nanoparticle films have been used as SERS substrates for trace detection of Rh6G molecules. Wide wavelength range LSPR tuning in these films allowed Raman measurement at different excitation wavelengths. For a given film thickness, those grown at 300 °C with strong LSPR band near the excitation wavelength have shown largest

SERS EF of the order of about 2.5×10^6 . In case of Ag-Au alloy films grown at optimum temperature, the SERS EF varied with film composition and thickness. Films of very low thickness (< 3 nm) with weak LSPR strength did not result significant increase in SERS intensity. For 488 nm excitation wavelength, Ag and Ag rich films of 3-10 nm thickness produced the highest SERS enhancement factor in the range of $5 \times 10^5 - 1.6 \times 10^6$, compared to Au and Au rich films. For 633 nm excitation wavelength, alloy films produced larger enhancement factor in the range of $5 \times 10^4 - 1.5 \times 10^5$, compared to pure Ag and Au films. The observed variation in SERS enhancement factor was attributed to overlap of LSPR wavelength and its strength at the excitation wavelength of Raman measurement.

With intrinsic high LSPR strength offered by Ag or Ag rich alloy nanoparticle films resulted maximum SERS signal but due to atmospheric tarnishing, these films are not stable for more than a month in normal ambience. In this regard, high concentrations of Ag nanoparticles of spherical and triangular shapes in aqueous solution of single reagent has been produced using a novel method based on laser ablation and light irradiation. These nanoparticles are stable for more than one year of observation and exhibit LSPR response in wide wavelength range. In this method, laser ablation of Ag coin in citrate solution at optimum concentration of about 10 mM produced spherical and uniform shape Ag nanoparticles of average size of about 13 nm. Mie theory-based calculation revealed that for 30 min. of laser ablation resulted into about 1.1×10^{12} Ag nanoparticles /mL and this concentration can be increased further with ablation time. At low citrate concentration or in pure DI water formation of inter-connected irregular shape nanoparticles was obtained. With irradiation under sodium lamp these Ag nanoparticles transformed into triangular shape nanoplates with broad LSPR band. In this

photo-mediated shape transformation process, addition of external Ag^+ ions during irradiation helped in increasing the yield of Ag nanoplates. The shape transformation process was found to be efficient at citrate concentration of about 10 mM and smaller triangular nanoplates were formed at pH \sim 10 and above 25 mM of citrate. With the help of the grown Ag triangular nanoplates, detection of Rh6G of low concentration (1 μM) through SERS is also demonstrated. In this case, the nanoparticles colloids are mixed with aqueous dye solution, it is drop casted and dried on glass substrate, maximum SERS enhancement was observed in regions formed with large aggregates of the nanoparticles.

Au-ZnO nanocomposites of two morphologies, (i) core-shell and (ii) Au nanoparticle decorated ZnO nanorods have been prepared and their photocatalytic response was studied. To form core-shell nanoparticle, Au nanocubes were synthesized in CTAC solution and ZnO shell layer was grown on these Au nanoparticles using ascorbic acid assisted growth method. Optical absorption variation during this growth and DDSCAT based analytical calculation of optical response of nanocubes revealed smoothening of Au nanocube edges during the shell growth. Crystallinity and photocatalytic response of these core-shell nanoparticles is significantly improved with annealing at temperatures more than 400°C. On the other hand, as-grown ZnO nanorods through hydrothermal method (without CTAC/CTAB and AA) have shown good crystallinity. By photo-mediated reduction of Au salt, Au nanoparticles were deposited on ZnO nanorods. With 1 g/L loading of these nanoparticles, photocatalytic degradation of four different dyes namely MB, MO, RhB and Rh6G has been demonstrated. Compared to other dyes, MB dye has shown relatively faster degradation. As per LH model, for very low initial concentrations of MB (below 5 μM), the degradation is first order limiting

case and it approached to zeroth order at higher concentration ($> 75 \mu\text{M}$). Presence of different scavengers: EDTA (for photo-generated holes), NaN_3 (for hydroxyl and singlet oxygen) and IPA (for hydroxyl radicals) have shown inhibition of dye degradation process. About 2.5 mM concentration of either EDTA or NaN_3 have almost ceased the dye degradation, whereas for IPA, it occurred at 25 mM. Surface charge characteristics of both type of nanoparticles (i.e. core-shell and nanorods) significantly varied with changing pH of the solution. At low pH, they have shown positive zeta potential but at very high pH, they exhibited negative zeta potential. MB was found to degrade faster at higher pH ~ 12 . However, MO, RhB and Rh6G dyes showed very little change in degradation within 3-10 pH range and at pH ~ 12 the degradation efficiency was found to decrease. The study showed that the produced nanoparticles could degrade both cationic and anionic dyes as well as their mixtures. In these dye mixtures also, MB has shown relatively faster degradation in comparison to other three dyes. The synthesized nanoparticles are environmentally friendly and the process is cost effective, which shows their use in treatment of dye water effluents.

This research work has shown pulsed laser ablation is versatile for producing different morphological Au and Au-Ag alloy plasmonic nanoparticle films and Ag nanoparticle collides of tunable LSPR response. This work can be further extended for production of other different cost-effective alloy or composite nanoparticles of Ag-Cu, Al-Cu etc, with protective dielectric capping for tunable and long term sustainable plasmon response, and growth of plasmonic nanoparticles of different metals in presence of varied capping agents. The effective dielectric response determined from theoretical analysis is useful in precise estimation of optical absorption, scattering and reflection of these films. This knowledge is highly useful for

preparing desired LSPR characteristic plasmonic nanoparticles films, which are required to explore research in many other upcoming application areas. It includes dynamic color changing display technology, nano-structuring of silicon of different morphologies of via metal assisted chemical etching (MACE) process, broadband optical absorption coating for solar light harvesting, optical filters and plasmon enhanced photovoltaic and optoelectronic devices; apart from SERS at different excitation wavelengths, as demonstrated. We noticed that with same thickness of Au film deposited at different substrate temperatures, it is easier to form silicon nanowires (with RT grown film) and nano-porous substrates (with 300°C growth) through MACE, exhibiting significantly enhanced light absorption. Further, the knowledge gained in photocatalytic process is useful in developing photo-reactor for dye effluent treatment at large scale. Detailed studies on transient absorption in metal-semiconductor composite nanostructures will help in better understanding of charge transfer characteristics for realizing many more applications. The grown nanocomposites are useful for studying the photocatalysis related other applications like water splitting and CO₂ to fuel conversion etc.

SUMMARY

The present research work comprises of comprehensive study of plasmonic response of Au, Ag and their alloy nanoparticles films of varied morphologies, composition and mass thicknesses. The role of substrate temperature during the growth of these films for obtaining and tuning of localized surface plasmon resonance (LSPR) response has been addressed. Optical response and LSPR wavelength of the films is calculated as a function of volume filling fraction and aspect ratio of the nanoparticles, using modified Yamaguchi effective medium theory involving particle-substrate and particle-particle interactions. Morphology dependent effective dielectric response of Ag-Au alloy films is determined using spectroscopic ellipsometry, considering multiple oscillators based analytical model fitting of the experimental data. A correlation between LSPR response of the films and Raman excitation wavelength is obtained for trace level detection of Rhodamine 6G dye up to 500 nM concentration. Further, a novel method based on laser ablation in liquid followed by light irradiation is demonstrated for producing spherical and triangular Ag nanoparticles in a single reagent for SERS application.

Au-ZnO nanocomposites in core-shell and decorated geometries are synthesized and photocatalytic response was studied through degradation of different organic cationic and anionic dyes. Effect of dye concentration, amount of nanoparticles, pH of the solution on degradation efficiency is addressed. Role of reactive oxygen species underlying the degradation process is studied in presence of different

scavengers at varied concentrations. The results reveal that hydroxyl radical plays vital role in this photocatalytic dye degradation process. These nanoparticles are environmental friendly and the process was optimized with low power UV light for cost effectiveness in treatment of industrial wastewater containing different dyes.

Chapter 01

Introduction

Currently studies on plasmonic metal nanoparticles has emerged as a prominent research area, finding applications in many fields like surface enhanced Raman spectroscopy [1-3], colorimetric sensors [4,5], photocatalysis [6-8], photovoltaics [8-10], optoelectronic devices etc. [10, 11]. Collective oscillations of free electrons present in a metal nanoparticle is termed as plasmon. When light is incident on a nanoparticle, oscillating electric field of light drives oscillations of free electrons in the metal, which are confined by boundary of nanoparticle [11,12]. The immobile positive ions in nanoparticle exerts restoring force on the electrons, resulting in a resonance of collective oscillations of the electrons, as shown schematically in Fig. 1.1, which is termed as localized surface plasmon resonance (LSPR). When the incident light frequency matches with LSPR frequency, the nanoparticle act as a nano-antenna, resulting strong absorption and scattering of the incident light [3,4,12]. Further at LSPR excitation, the metal nanoparticles also show enhanced local electric field around them [9, 12]. The LSPR wavelength can be tuned by changing size, shape, metal composition, surrounding medium and spatial separation between the nanoparticles [4,12]. Au and Ag metals are chemically inert and their LSPR response is tunable in visible and near infrared regions, due to which, these nanoparticles are better choice in various applications as compared to other metals like Al, Cu etc. [13-16]. For effective use of these nanoparticles for different applications, synthesis and understanding of morphology dependent plasmonic response of metal nanoparticles

and their composites is essential.

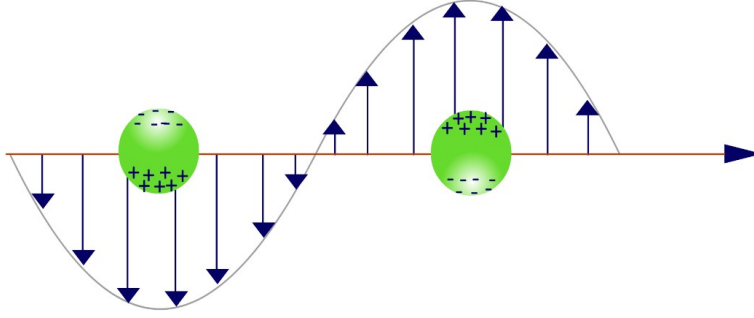


Fig. 1.1 Schematic of LSPR excitation in metal nanoparticles.

1.1 Localized surface plasmon resonance in metal nanoparticles:

As shown in Fig. 1.1, for spherical metal nanoparticle of size (a), much smaller than the incident light wavelength (λ) i.e. in quasi-static approximation, optical response of nanoparticle can be described in terms of its polarizability (α), as [11,12]

$$\alpha = 4\pi\epsilon_d a^3 \frac{\epsilon(\omega) - \epsilon_d}{\epsilon(\omega) + 2\epsilon_d}, \quad \dots (1.1)$$

where, $\epsilon(\omega)$ is dielectric function of nanoparticle, which is complex ($\epsilon_1 + i\epsilon_2$) and depends on frequency (ω), and ϵ_d is dielectric constant of surrounding medium. The polarizability of nanoparticle becomes maximum when the denominator term: $\epsilon(\omega) + 2\epsilon_d$ is minimum i.e. $\epsilon_1(\omega) = -2\epsilon_d$; this is known as Frohlich or LSPR condition [11-12]. The frequency meeting this condition is termed as plasmon resonance frequency (ω_{LSPR}). This resonance condition is satisfied only when the material of the nanoparticle possess negative dielectric response, which is fulfilled in case of metals (below their plasma frequency) [11]. The quality factor of LSPR depends on real and imaginary parts of the dielectric response at ω_{LSPR} and it is quantified as; $-\epsilon_1/\epsilon_2$ [12,17,18]. In metals, ϵ_2 depends on electron scattering frequency (Γ) which has

different contributions i.e. electron-electron, electron-phonon, electron-surface and electron-defects [12,18]. Further, the dielectric response of the metals has contributions from free electrons (intra-band transitions) as well as bound electrons (inter-band transitions). For Ag, inter-band transitions occur near UV-region, above the plasma frequency, resulting high resonance quality factor [17]. In case of Au, inter-band transitions occur in visible region overlapping with the plasmon or collective excitations of free electrons, resulting lower quality factor as compared to Ag nanoparticles [12,17,18]. For other transition metals with partially filled d or f levels, quality factor is very low due to IB transitions [18]. Therefore, distinct LSPR response is observed in metal nanoparticles that possess significantly high plasma frequency with respect to damping frequency, along with low probability of IB transitions [18]. These factors play major role for variation of quality factor of different metals, belonging to same group of periodic table. For example, Cu, Ag and Au which lie in I(B) group, the resonance quality factor near their LSPR frequency is about 10, 97 and 34 respectively [18]. The highest quality factor of Ag is attributed to minimum overlap of inter-band transitions with the plasmon band.

With change in shape of nanoparticles, the polarizability (Eq. 1.1) gets modified as a result the LSPR frequency also changes. For example, in case of ellipsoidal shape nanoparticles, the polarizability along one of the principle axis, modifies as [12]:

$$\alpha_j = 4\pi a_1 a_2 a_3 \frac{1}{3} \frac{\varepsilon(\omega) - \varepsilon_d}{\varepsilon_d + L_j (\varepsilon(\omega) - \varepsilon_d)}; \quad \dots (1.2)$$

where, $j = 1-3$ denotes the principal axes and L_j is known as depolarization or shape factor along the j^{th} axis, satisfying the relation $\Sigma L_j = 1$. For spherical particles,

$a_1 = a_2 = a_3$, hence the depolarization factor becomes 1/3, and as the particle become more elongated about the $j=3$ axis, the depolarization factor in the direction (L_3) decreases [12,19]. According to this, the Frolich condition is:

$$\varepsilon(\omega) = -\left(\frac{1}{L_j} + 1\right)\varepsilon_d, \quad \dots (1.3)$$

For metals, frequency (ω) dependent dielectric function predicted by Drude model with negligible scattering losses (Γ) is [19]:

$$\varepsilon(\omega) = 1 - \frac{\omega_p^2}{\omega^2}, \quad \dots (1.4)$$

where, ω_p is the bulk plasma frequency. For ellipsoidal nanoparticles with smaller L_j , the LSPR condition is satisfied at larger magnitude of $\varepsilon(\omega)$, i.e. resonance wavelength is red-shifted from that of spherical nanoparticle. Therefore, particle shape affects the LSPR response because of modified particle polarizability. For spherical, ellipsoidal and rod shape of nanoparticles, optical response can be calculated using Mie and Mie-Gans theories based on analytical approach [20,21]. However, for other shapes, which possess sharp edges or corners, analytical solution cannot be obtained and in this case the polarizability can be obtained from numerical techniques [22-24].

1.1.1 Optical absorption and scattering by plasmonic nanoparticles

The plasmon excitation driven charge oscillations makes the nanoparticle act as a dipole antenna that strongly absorbs the incident electromagnetic radiation and reradiate (scatter) it in different directions. Due to absorption, some part of incident electromagnetic energy converts into heat. For nanoparticles of diameter much less than the wavelength of light, the electromagnetic interaction is almost instantaneous

throughout the nanoparticle. In this electrostatic approximation, the absorption and scattering cross-sections are given by [20]:

$$\sigma_{abs} = \frac{2\pi}{\lambda} \text{Im}[\alpha], \quad \text{and} \quad \dots (1.5)$$

$$\sigma_{sc} = \frac{1}{6\pi} \left(\frac{2\pi}{\lambda} \right)^4 |\alpha|^2, \quad \dots (1.6)$$

Respectively. Here, λ is wavelength of incident light. These relations show that σ_{abs} scales with a^3 whereas σ_{sca} scales with a^6 . At resonance i.e. the frequency at which $\epsilon_1 = -2\epsilon_d$, which occurs in visible or near infrared regions for Ag and Au, both σ_{abs} and σ_{sca} becomes significantly high. This resonance does not occur for either dielectric or semiconductor nanoparticles because these materials possess positive ϵ_1 particularly in the above-mentioned frequency range. For very small nanoparticles, σ_{sca} is much smaller than σ_{abs} and hence the extinction (sum of absorption and scattering) is dominated by absorption. However, for large nanoparticles with perimeter comparable to or larger than λ , the scattering process becomes significant. For spherical Au nanoparticles of sizes below 50 nm, typically $\sigma_{sca}/\sigma_{abs}$ is < 0.1 which shows very low scattering [25]. For nanoparticles of size about 80 nm, this ratio becomes about 0.6, i.e. scattering becomes comparable to the absorption [25].

The strong absorption and scattering of metal nanoparticles renders them very high extinction coefficient, of the orders of $10^9 \text{ M}^{-1}\text{cm}^{-1}$, which is about two to three order higher than that of colorful dyes and pigments [26,27]. In metal nanoparticle films, preferential scattering into supporting substrate has been shown to increase the light coupling and enhanced photocurrent for photovoltaic applications [28,29]. The light coupling efficiency is found to depend on the size and shape of plasmonic

nanoparticles and is maximum at the LSPR wavelength [29].

1.1.2 Near-field enhancement by plasmonic nanoparticles

Another remarkable attribute of plasmon excitation in metal nanoparticles is electric field enhancement in their close vicinity, termed as near-field enhancement [17]. As mentioned above, in smaller nanoparticles, plasmon excitation results oscillating dipole field, which possess near-field as well as far-field. The near-field consists of transverse and longitudinal fields whereas the far-field is transverse [30]. The near-field localized to the dipole i.e. the nanoparticle, exists within a few tens of nanometers about it. Due to plasmon excitation, the observed near-field at the nanoparticle is more than that of interacting light. In electrostatic approximation, the maximum electric field amplitude on the surface of the nanoparticle of radius ‘ a ’ interacting with light of electric field $E_o(r,t) = Re(E_o(r)e^{-i\omega t})$ is [17],

$$E_{\max} = (1 + 2\zeta)E_o, \text{ where } \zeta = \frac{\varepsilon(\omega) - \varepsilon_d}{\varepsilon(\omega) + 2\varepsilon_d}. \quad \dots (1.7)$$

Based on this, the local electric field intensity enhancement (FE) factor is,

$$FE = \left| \frac{E_{\max}}{E_o} \right|^2 = |1 + 2\zeta|^2 = 9 \left| \frac{\varepsilon(\omega)}{\varepsilon(\omega) + 2\varepsilon_d} \right|^2. \quad \dots (1.8)$$

It shows that, the field intensity enhancement factor depends on dielectric function of metal (ε) and dielectric constant of surrounding medium (ε_d). Considering the reported optical constants of Au and Ag by Palik [31], the field intensity enhancement factor of these metals is about 20 and 118 at 528 nm and 355 nm wavelengths respectively. For ellipsoid nanoparticles, the field enhancement factor becomes,

$$FE = |1 + 3(1 - L_j)\zeta_j|^2 = \left| \frac{\varepsilon(\omega)}{\varepsilon_d + L_j(\varepsilon(\omega) - \varepsilon_d)} \right|^2. \quad \dots (1.9)$$

For Au nanoparticle, by increasing the aspect ratio up to 5, the field intensity enhancement can increase by about 3 orders of magnitude at LSPR [17]. If the aspect ratio is increased further (>6), the resonance wavelength significantly red-shifts, whereas the FE remains almost same [17]. The variation of FE with particle aspect ratio is due to red-shift of plasmon wavelength and frequency dependent variation in dielectric response. For other shape nanoparticles having sharp corners e.g. ellipsoid, nanorods, triangular nanoplates etc, local electric field enhancement is significantly more than that produced with spherical shape nanoparticles of same volume [22,32]. This is due to accumulation of more charges at the sharp regions attributed to lightning rod effect [12,33]. In case of nanoparticle films, inter-particle interaction also occurs through near-field and far-field coupling that depends on their separation. If inter-particle separation is larger than wavelength of light, far-field coupling dominates with inverse of particle's separation [34]. This far-field coupling affects (red-shifts) the plasmon resonance of corresponding individual nanoparticle [35]. However, for closely spaced (lesser than wavelength) nanoparticles, near-field interaction also occur along with generation of 'hot-spot' (regions with significantly high FE) between the nanoparticles [35]. These hot-spots have been found to be very useful for ultrasensitive detection of molecules through surface enhanced spectroscopic methods e.g. SERS, modified fluorescence etc [34, 36].

1.2 Application of plasmonic nanoparticles

LSPR excitation of metal nanoparticles has led many important applications in

different fields like SERS [1-3,33,34,36], dynamic color tuning [37-42], plasmonic solar cells [6,8-10,43], colorimetric sensors [5,44-52], thermo-plasmonics [53-55] etc, as schematically shown in Fig. 1.2.

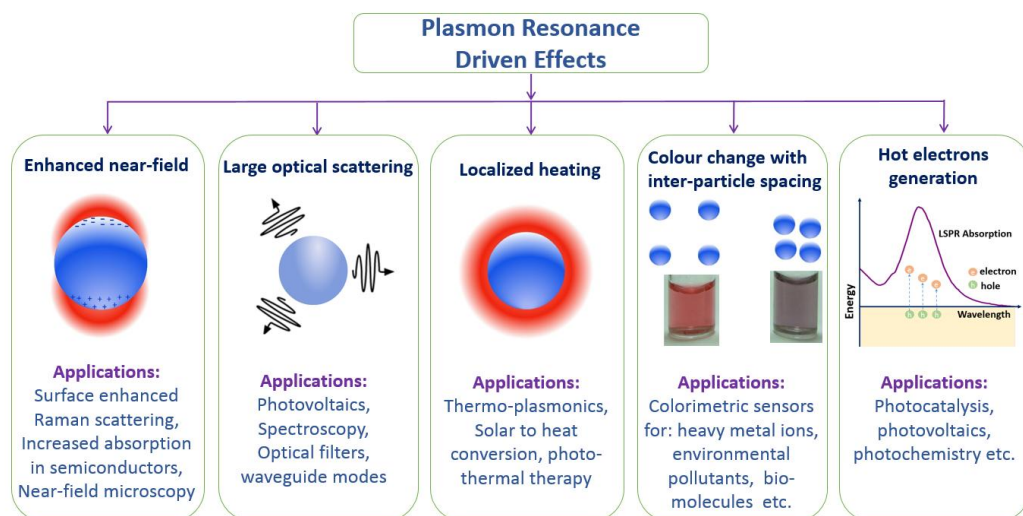


Fig. 1.2 Different attributes of plasmon resonance in metal nanoparticles and related applications.

Plasmonic nanostructures exhibit intense bright colors and variation of these colors arise from interaction of incident light with nanoparticles of different morphologies i.e. size, shape and inter-particle spacing. Recently use of plasmonic nanostructures for active coloring and emerging electronic displays e.g. plasmonic electronic paper technology has generated lot of interest in last couple of years [37,38]. These plasmonic nanoparticles are much more stable than colored organic molecules. Other than Au, more economic metals such as Ag, Cu and Al are also explored with suitable protective layer [38]. These plasmonic nanostructures can be used for high resolution large area display. Recently, different methods for active color tuning of plasmonic colors have been demonstrated. These include: i) modulation of LSPR

wavelength of metal nanoparticles through electrochemical processes [39], ii) using conducting polymer matrices [40], iii) use of electro-mechanical forces on plasmonic nanoparticles [41], iv) by mechanical control on plasmonic nanostructures using stretchable substrates, flexible embedding mediums [42] etc. Use of dynamic color changing plasmonic nanoparticles as smart materials have also been demonstrated for low cost colorimetric strain and temperature sensors.

Improved efficiency of different types (organic, thin film and hybrid) of solar cells, has been demonstrated, using plasmonic metal nanoparticles [8,9]. This occurs due to improved light trapping by scattering of metal nanoparticles [28,29], near-field enhancement and hot carrier generation due to plasmon excitation [43]. Individual weightage of these processes depends on the size, shape and geometrical arrangement of plasmonic metal nanoparticles with respect to the photo active layer [9]. For example, when the size of the nanoparticles is large (>50 nm), far-field scattering dominates, increasing the effective optical path length. Smaller size nanoparticles induce near-field effects, mostly useful for near-field enhanced absorption processes [9]. On the other hand, confined shape nanoparticles are shown to be efficient for hot electron induced processes [43].

Use of plasmonic nanoparticles, particularly Au and Ag exhibiting visible range LSPR, as colorimetric sensors has also been demonstrated for fast and field-ready economic detection (even with naked eye) of heavy metal contaminants (e.g. Hg, Pb, As, Cd) in water [44-46], various bio-molecules [5], ions (fluoride, iodide, cyanide, nitrite, etc) [47,48], other molecules like glucose [49], organophosphates [50], natural

and synthetic toxins etc [51]. The colorimetric detection is based on either aggregation induced color change of nanoparticles in presence of analytes or anti-aggregation based reverse color change using specific capping agents. Various molecules have been used for variation of inter-particle spacing of nanoparticles [5]. Further, variation of fluorescence (both quenching and enhancement) in presence of plasmonic nanoparticles is also demonstrated for detection of different molecules or ions [5, 52].

Plasmonic metal nanoparticles have also shown potential application for generating localized heating regions around them [53-55]. A metal nanoparticle with strong light absorption can act as nanoscale source of heat, which has ability to be controlled remotely by light. Using 3D assembly of plasmonic nanoparticles, solar light driven water desalination is demonstrated [54], where LSPR excitation by metal nanoparticles results in efficient absorption of broad solar band and heating of the underlying water surface. Further based on localized heating, use of Au nanoparticles has been also widely explored for photo-dynamic therapy, targeted drug delivery, heat induced chemical process controlled at nanoscale etc [53,55]. Other than these, production of large-scale one-dimensional Si nanostructures has also been demonstrated based on metal assisted chemical etching process using Ag and Au nanoparticle films, which are useful for optoelectronics and efficient hybrid inorganic-organic solar cells [56].

The present research work mainly focuses on two applications i.e. i) SERS based trace level analyte (dye) detection using Au nanoparticle films of varied morphologies, Ag-Au alloy nanoparticle films of different compositions for different

Raman excitation wavelengths and Ag nanoparticle colloids of spherical and triangular shape and ii) photocatalytic dye degradation using Au-ZnO nanocomposites for effluent water treatment. Therefore, the following sections briefly present SERS and photocatalysis of plasmonic metal-semiconductor nanocomposites.

1.2.1 Application of plasmonic nanoparticles for surface enhanced Raman scattering (SERS)

Raman scattering is inelastic scattering of photons with molecular vibrations or phonons caused by change in molecular polarizability in presence of electric field of light [57]. When photons gain energy from the phonons, it is called anti-stokes Raman scattering and when they lose some part of energy to molecular vibrations, it is known as Stokes Raman scattering. The energy of vibrational modes depends on molecular structure i.e. mass, bond length, molecular arrangement and their surroundings [57]. Consequently, Raman scattering spectrum can be treated as molecular fingerprint, useful for identification or detection of molecules. However, Raman scattering is very weak, typically few out of million photons get inelastic scattered due to very small change in polarizability during vibration. Since Raman scattering is two photon process, being inelastic scattering of photons with vibrational modes of the molecule, it is almost million times weaker than elastic scattering and fluorescence [1,57]. In this regard, SERS is very sensitive spectroscopic technique for detection of trace level analyte molecules adsorbed on metal nanoparticles or rough metallic surfaces with roughness order less than wavelength of light [58]. SERS becomes very important for enhancing the Raman signal, sometimes even by 10^{10}

times can be achieved [59]. This large enhancement is mainly attributed to electromagnetic field intensity enhancement near the metal nanoparticles. A weaker contribution from chemical enhancement has also been attributed to the overall SERS enhancement [57]. Various research studies are in progress for obtaining reproducible, cost effective and stable SERS substrates. Use of colloidal metal nanoparticle aggregates [59], roughened metal films [58], different metal nanoparticle films as SERS substrates [60,61] have been reported. This is in parallel with many theoretical studies attempting to optimize different metal nanoparticles, geometrical parameters such as size, shape and inter-particle distance between the particles and metal volume filling fraction [62]. The maximum enhancement has been reported for either aggregated colloidal nanoparticles or closely packed nanoparticles of different shapes, because of very high local field enhancements in the gaps between the nanoparticles due to large number of hot-spots [62,63]. The SERS intensity has been shown to be proportional to E^4 , in this, power of two is from excitation process and another power two is from the emission process [64].

1.3 Plasmonic metal-semiconductor nano-composites

Recently, composite materials of Ag/Au metal nanoparticles with semiconductor nanostructures have evolved as technologically important materials for different photocatalysis process as schematically shown in Fig. 1.3 [6-8, 65]. In these composite nanoparticles, light can couple with either plasmonic metal nanoparticles or semiconductor nanostructure, or simultaneously in both the materials depending on the wavelength of light and morphology of composites [65]. Photo-generated charge

carrier transfer between the two materials at their interface is helpful in effective utilization of photo-generated electron-hole pairs for chemical reactions.

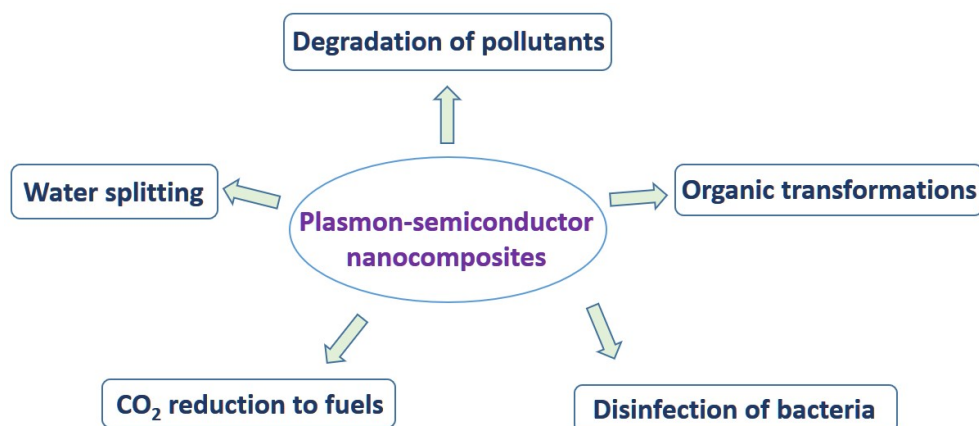


Fig. 1.3 Different applications of plasmon-semiconductor nanocomposites.

Photocatalytic dye degradation for treatment of industrial effluents is one of the important applications apart from other photocatalytic applications like water splitting and fuel generation from CO_2 using these composites. Various semiconductor materials have been explored for these photocatalytic applications [8], though ZnO is promising when stability, growth of various morphologies and nano-toxicity are of concern [66,67]. Various morphologies of Au/Ag-ZnO nanocomposites like decorated structures, hetero-junction structures with and without insulating layers, Janus and core-shell structures have been studied for different photocatalysis processes [66-70].

1.3.1 Photocatalytic degradation of dye

The photocatalysis process involves photo-induced chemical reactions, initiated by electron-hole pairs generated by absorption of light in semiconductor photocatalyst. The basic steps of photocatalysis process are i) light absorption or charge carrier generation, ii) charge separation and iii) transfer/migration of charge for utilization for

specific reactions. Incorporation of metal (Au, Ag) nanoparticles in semiconductor (e.g. ZnO, TiO₂) photocatalytic systems helps in charge separation process [65]. Plasmonic nanoparticles are shown to contribute in steps (ii) and (iii) by charge carrier trapping, increased contact area, enhanced creation and separation of electron-hole pairs through Schottky junction and localized heating [65]. When plasmonic metal nanoparticles are coupled to semiconductor active layers, three additional processes, i) light trapping by scattering of plasmonic metal nanoparticles, ii) near-field enhancement and iii) hot electron transfer, either one or multiple of these are responsible for enhancing charge carrier generation in composite structures [8]. Individual contributions of these processes depend on the size, shape and geometrical arrangement of metal nanoparticles with respect to the semiconductor photocatalyst. These charge carriers produce highly reactive radicals (e.g. hydroxyl, superoxide etc.), which trigger various reactions [8,65,68].

1.4 Motivation and problem formulization

Nanoparticle films with wide LSPR wavelength tunable substrates are important for various applications like SERS, plasmon based optical filters, dynamic color tuning, photovoltaics etc. To realize these applications, growth of plasmonic nanoparticles with tunable optical response in the form of uniform film supported on a substrate or dispersed in solution with minimum chemicals is inevitable requirement. The optical response of the plasmonic nanoparticles given by eq. (1), shows that LSPR wavelength depends on four parameters which are, i) size, ii) shape factor (L_j), iii) nanoparticle dielectric function ($\epsilon(\omega)$) which changes with alloy composition and

iv) surrounding medium dielectric constant (ϵ_d). For producing plasmonic nanoparticle films on a substrate, physical vapor deposition (PVD) methods are attractive because the growth occurs in high vacuum, hence provides minimum contamination [71-73]. Au and Ag metals, whose melting point is about 1000 °C are deposited with thermal evaporation method. The deposited metal thin films of few nanometers thickness grows into continuous or percolated form, devoid of plasmonic response. Therefore, to obtain the plasmonic response, the deposited thin metal films are subsequently annealed to change the film morphology into island or nanoparticle films [74-75]. Annealing process causes de-wetting of metal on the supporting substrate, and results into formation of nanoparticles. However, for 5 nm or higher thickness films, de-wetting temperature and annealing time are more and also produces less uniform nanoparticles [75]. Further, at low film thickness, the room temperature grown films (without annealing) also change their morphology with aging [76].

In PVD growth, formation of nanoparticles or continuous metal films depends on initial nucleation density and this can be controlled by varying the substrate temperature during the film growth [77]. Using high substrate temperature, depositing nanoparticle films in a single step process, avoids nanoparticles contamination during second step of annealing and also morphology of these films does not change with time. Pulsed laser deposition (PLD) is one of the important PVD method, widely known for growing multi-elemental compound films because of its congruent evaporation [78-80]. In literature, PLD technique has been mostly used for dielectric and semiconductor films [79,80]. However, PLD is advantageous for the growth plasmonic nanoparticle

films, because, combination of pulsed nature of deposition and high substrate temperature allows diffusion of ad-atoms in between laser ablation pulses, thus maintains low nucleation density as required to form nanoparticles rather continuous films [77]. Further in PLD technique, the amount of Au required to form each nanoparticles film is significantly smaller than that required for other PVD techniques. This enables to study large number of process parameters with low consumption of Au metal. Controlling the morphology of Au films at different substrate temperatures and film thicknesses for tuning of plasmonic characteristics (i.e. LSPR wavelength and broadening) using PLD technique and their application for SERS has not been reported in literature.

It may be noted that by controlling substrate temperature and film thickness, LSPR can be tuned, however it significantly affects the broadening of the plasmon band [77]. On the other hand, tuning of LSPR response without much change in broadening can be realized by producing alloy nanoparticles of varied compositions. In literature, growth of bimetallic films and subsequent annealing at high temperature for mixing of the metals has been mentioned [81,82]. In another case, single composite target of Ag and Cu metals was used for growth of Ag-Cu alloy films [83]. However, varied alloy compositions of plasmonic nanoparticles growth from individual metal targets through sequential laser ablation has not been reported. PLD is suitable for growth of alloy nanoparticles from sequential deposition because of pulsed nature of deposition and each pulse deposits only fraction of one atomic monolayer. By depositing two metals individually in a sequence of few pulses, at high substrate temperature it can form

monolayer of alloy nanoparticle films.

Understanding the variation of dielectric function (both real and imaginary parts) of the films of different thickness and alloy compositions is important in optimizing the process parameters for strengthening LSPR response. Spectroscopic ellipsometry is a non-destructive method for experimental determination of dielectric response of plasmonic metal nanoparticle films [84,85]. Ellipsometry data fitting with multiple oscillator based analytical modeling helps in determination of the wavelength dependent contributions of both bound and free electrons in the optical response of films. Moreover, for metal nanoparticle films, the plasmon resonance frequency, width and amplitude, which depend on the particle density, shape and surrounding medium, can be determined from ellipsometry without detailed knowledge on their morphological parameters. Though ellipsometry can provide effective dielectric response of the films, it does not provide the details of role of different effects like particle size, shape, particle-particle and particle-substrate interactions pertinent to densely packed nanoparticles films. The polarization in the substrate creates image dipole, which interacts with particle plasmon excitation [86,87]. Further, if inter-particle distance is few tens of nanometers or less, particle-particle and particle-image dipole of other surrounding particles affect the overall LSPR response of films. The role of these factors individually on LSPR response can be determined from analytical models that predict the effective dielectric function.

Nanoparticles embedded in a homogeneous matrix can be described as an effective medium, where the effective dielectric response ($\epsilon_{eff}(\omega)$) depends on

nanoparticle volume filling fraction and dielectric function of the constituent materials [88,89]. Maxwell-Garnett and other effective medium theories have been used, which works well only for homogeneous and dilute dispersions of metal nanoparticles [89,90]. However, for monolayer 2D nanoparticle films at high metal filling fractions, modified Yamaguchi model has been developed, taking account of optical interactions from the underlying substrate [88]. From this model, it is possible to determine variation in LSPR by different effects like particle shape, particle-particle and particle-substrate interactions. Application of such analytical model for predicting plasmon response of either Au or Ag-Au alloy nanoparticle films of varied morphologies and compositions has not been studied yet. A comparative study on analytical model predicted LSPR tuning and its validation using experimental results would be helpful for optimizing experimental conditions for utilization of these films for SERS application at different excitation wavelengths. This will also help in understanding the effect of individual interactions as mentioned above on the optical response. However, it is applicable only for nanoparticle films and the morphological parameters i.e. size and aspect ratio of the particles are required to obtain the effective dielectric response.

It is observed that densely packed Ag nanoparticle films without any protective layer show strong SERS, however in normal atmospheric ambience these films are not stable for more than a month [91,92]. This arises due to reaction of Ag with sulphur and oxygen present in air, as a result LSPR response decrease and it is termed as atmospheric tarnishing. In case of colloidal Ag nanoparticles, such atmospheric

tarnishing problem does not occur, but to obtain longer shelf life of nanoparticles without aggregation, they need to be protected with some surface capping agent. It is desirable to have mild reducing as well as capping agent like tri-sodium citrate (TSC), which is widely used for chemical reduction synthesis and protection of Au nanoparticles [93,94]. It may be noted that variation in optimum concentrations of TSC or Au metal salt can lead to formation of irregular size and shapes of nanoparticles [95]. However, it is difficult to produce smaller and uniform size Ag nanoparticles using TSC [96]. In this respect, liquid phase pulsed laser ablation (LPPLA) can be an alternative method for growth of stable Ag nanoparticles at relatively larger range of TSC concentration. Synthesis of Ag nanoparticles in TSC is also attractive for photo-mediated shape transformation of the produced nanoparticles into triangular shape nanoplates without further addition of other chemicals. In case of chemical route-based synthesis of Ag triangular nanoplates different chemical reagents are required, which also include strong reducing agents like sodium borohydride [97,98]. In literature, optimum TSC concentration range and solution pH for synthesis of high concentration Ag nanoparticles thorough LPPLA method and subsequent shape transformation into triangular shape nanoparticles has not been studied. These stable triangular nanoparticles produced in single reagent are attractive for SERS due to enhanced local field by the sharp corners of these triangular nanoparticles.

Apart from SERS application of plasmonic nanoparticles, their composite nanoparticles formed with semiconductor nanostructures are technologically

important towards photocatalysis based dye degradation for water treatment application [7,8]. Au being chemically more inert than Ag, and ZnO is non-toxic semiconductor that can be grown in various morphological nanostructures, Au-ZnO nano-composites are attractive for photocatalysis application in terms of longer or multiple uses [68-70,99]. Several synthesis approaches like chemical reduction, sol-gel, hydrothermal, co-precipitation, photo-reduction etc. have been reported for producing the composite nanostructures [68-70,100-103]. Control over the dimensions and morphological structure of the components have been the key issues to be addressed to maximize their efficiency and commercial use. It has been demonstrated that Au-ZnO nano-composites show efficient dye degradation under UV lamp irradiation [68,104]. In photocatalytic dye degradation process, first adsorption of the dye molecules on the nanoparticles surface occurs and then chemical reactions with different reactive oxygen species (produced from photo-generated electrons and holes) result degradation of dye. The amount of dye adsorbed on the photocatalyst surface depends on the morphology of the nanoparticles [104]. When the nanoparticles are large (~500 nm), they can settle at the bottom of the solution very quickly and it limits effective interaction of light with the nanoparticles. To avoid this, in general, continuous stirring of the dye solution with nanoparticles is carried out during the photocatalysis process.

Depending on the morphological arrangement, these composites, either in form of metal decorated or core-shell type nanoparticles, can show dye degradation [8,65]. In case of metal nanoparticle decorated nano-composites, size of semiconductor

nanostructures is significantly larger than the metal nanoparticles [65,105]. On the other hand, core-shell nanoparticles have maximum interface between the two components and outer oxide semiconductors protect photo or chemical corrosion of metal nanoparticles and its aggregation. In core-shell morphology, comparable size (~50 nm) of both metal and semiconductor with maximum interface in the composite nanoparticles can be synthesised in aqueous medium by hydrothermal method [106]. By using relatively smaller size nanoparticles, it is possible to minimize the stirring of the dye solution during photocatalysis. Further, industrial dye effluents can contain certain compounds, which may scavenge the radicals, leading to inhibition of photocatalytic dye degradation. Though many studies were carried out on photocatalysis, but detailed studies based on Au-ZnO nano-composites in core-shell and decorated type nanoparticles for degradation of different dyes (i.e. cationic or anionic), under low power UV lamp irradiation, in presence of different scavengers of varied concentrations, and effect of pH and different dye mixtures has not been reported in literature.

From the above presented brief review on literature related to plasmonic nanoparticles, it is clear that realization of plasmonic nanoparticle films of controlled optical response is one of the key step for their best possible utilization towards different applications. PLD being versatile method for single step growth of nanoparticles with tunable plasmon response along with fabrication of their composites with other materials, will further simplify in realizing many upcoming application areas. Therefore, the first part of this thesis, puts emphasis on PLD

method based synthesis of LSPR wavelength tuneable plasmonic nanoparticle films by varying growth temperature, film thickness and alloy compositions, and LPPLA based synthesis of Ag nanoparticles of spherical and triangular shape nanoparticles in a single reagent. This research problem provides important knowledge on understanding and optimization of the process for producing LSPR controllable plasmonic nanoparticles useful for SERS based detection of very low concentration of analyte molecules. Therefore, SERS response at different laser wavelengths of these nanoparticle films and colloidal nanoparticles were studied and correlated with their LSPR response. In the second part of the thesis, emphasis has been given to understand the photocatalytic dye degradation process of different dyes using two different morphologies i.e. core-shell and decorated type of Au-ZnO nanocomposites. To do these studies, synthesis of the nanocomposites is optimized using cost effective hydrothermal method in aqueous phase. The role of different process parameters on the dye degradation mainly dye concentration, nanoparticles loading, different scavengers at varied concentration and pH of the solution have been addressed. This work will be helpful in optimizing the photocatalysis process for various types of dyes in more economical manner to explore the feasibility of implementation of this technique at industrial level.

1.5 Objectives

Pulsed laser ablation process (PLD and LPPLA) with many inherent advantages is explored for producing LSPR wavelength tunable noble metal nanoparticle films in this research work. Emphasis is also given on understanding of their optical response

through effective dielectric response, determined experimentally and through analytical model. Further stable and high concentrations of spherical and triangular Ag nanoparticles are grown in single mild reagent through LPPLA followed by light irradiation. Application of these nanoparticles for trace molecular detection using SERS has been addressed for different thicknesses of Au nanoparticle films, Ag-Au alloy films and colloidal Ag nanoparticles. In addition, Au-ZnO nanocomposites of two morphologies (core-shell and decorated forms) have been synthesized and their photocatalytic properties are studied comprehensively for different dyes and their combinations. These studies were carried out with the following objectives:

1. To determine optimum process parameters of PLD for producing wide range LSPR wavelength tunable Au and Ag-Au alloy nanoparticle films in single step by controlling substrate temperature, film thickness, alloy composition and protective dielectric layer. Further attaining desired LSPR characteristics to achieve maximum SERS response for trace level detection of about 200 ppb of Rhodamine6G at different excitation wavelengths.
2. Theoretical understanding of plasmonic response of densely packed nanoparticle films using effective dielectric function: (i) determined from analytical model including particle-particle and particle-substrate interactions based on morphological parameters and alloy compositions of films and (ii) experimental determination through spectroscopic ellipsometry for both nanoparticle and continuous films based on multi-oscillator model, without involving morphological parameters of the films.

3. To produce high concentration and stable Ag spherical nanoparticles using LPPLA and determine optimum pH and Ag^+ ion concentration for efficient photo-induced transformation of these spherical nanoparticles into triangular nanoplates, exhibiting wide wavelength plasmonic response in presence of single mild reagent, suitable for SERS detection.
4. Optimization of growth conditions for Au nanocube core-ZnO shell nanoparticles, experimental and theoretical understanding of their optical response during the growth and subsequent annealing. Understanding the photocatalytic response of these nanoparticles in dye degradation process with respect to dye concentration, loading of nanoparticles, pH of the solution and different scavengers of varied concentrations.
5. Synthesis of Au nanoparticle decorated ZnO nanorods and optimization of process conditions for efficient photocatalytic degradation of four different (cationic and anionic) dyes in presence of different scavengers of varied concentrations, pH conditions and dye mixtures to understand the degradation kinetics and realization of few liter quantity of dye degradation using low power UV lamps.

1.6 Organization of thesis

To meet the above objectives, comprehensive studies were carried out for understanding the plasmon response of noble metal nanoparticle films and their semiconductor (ZnO) composites, along with their applications in SERS and photocatalytic dye degradation respectively. The results of this research work has been arranged in the following chapters.

Chapter 2 presents the LSPR characteristics of Au nanoparticle films grown at different substrate temperatures, film thickness and with alumina over-layer. Correlation of morphological features and the LSPR characteristics with calculated optical response and SERS response of the films has been presented.

In **Chapter 3**, the procedure for tuning the LSPR wavelength in Ag-Au alloy nanoparticle films with alloy composition and film thickness (morphology), optical response calculated using three different analytical models for Ag-Au alloy dielectric functions are presented. Further, variation of effective dielectric response at different alloy compositions determined from spectroscopic ellipsometry and SERS response of these films at different excitation wavelengths are also presented.

Chapter 4 presents a novel method for synthesis of spherical and triangular shape Ag nanoparticles in a single reagent by liquid phase pulsed laser ablation followed by light irradiation respectively. Role of tri-sodium citrate concentration, solution pH, presence of additional Ag ions and ablation/irradiation time for high yield Ag nanoparticles and their SERS response for trace detection of molecules is presented.

Chapter 5 addresses the optical and photocatalytic response of Au-ZnO core-shell nanocomposite. Effect of annealing on optical, crystalline quality and morphology of nanoparticles and photocatalytic degradation of cationic methylene blue and anionic methyl orange dyes at different dye concentrations, amount of nanoparticles, different scavengers at varied concentrations and pH conditions are also presented.

Chapter 6 presents the photocatalytic response of Au nanoparticles decorated ZnO nanorods. Photocatalytic degradation of four different dyes of varied concentrations,

kinetics of the process, effect of different scavengers of varied concentrations, pH conditions and degradation of dye mixtures has also been presented in this chapter.

Chapter 7 summarizes the conclusions of the thesis drawn from the above studies and future scope.

Chapter 2

Growth temperature controlled plasmonic response of Au nanoparticle films for SERS application

Plasmonic response of metal nanoparticles is collective resonance oscillations of free electrons, which is a consequence of dielectric confinement of metal possessing negative bulk dielectric response surrounded by positive dielectric environment. The resonance wavelength depends on morphological parameters i.e. size and shape of nanoparticle due to variation in induced polarization by these parameters [12]. In case of nanoparticle films supported on a substrate, plasmonic response also changes with inter-particle spacing and dielectric constant of the substrate. In PVD process, the morphology of grown film depends on initial nucleation density, which varies with incoming atomic flux and diffusion coefficient of adatoms on the substrate [107]. In comparison to other PVD processes, PLD technique offers pulsed form of material deposition in which laser produced plasma containing atoms of target material, expands in high vacuum and impinge on the substrate. With nanosecond pulsed laser of typical 10 Hz repetition rate, sufficient long time is available for diffusion of deposited adatoms on the substrate in between successive laser ablation pulses [108]. It is possible to control atomic flux impinging on substrate by laser fluence and target to substrate distance, whereas adatoms diffusion distance on the substrate can be controlled by substrate temperature. Due to this, we observed significant variation in morphology and LSPR response of Au films grown at different temperatures [77]. For example, Fig. 2.1 compares morphology

from SEM images of Au films of about 3.5 nm thickness grown at room temperature (RT) and substrate temperature of 300 °C. The film mass thickness was estimated from X-ray reflectivity method. For this, thick continuous films were deposited at room temperature (RT) and the thickness was found to be proportional to number of pulses used for the deposition. Using this, mass thickness of the films deposited at other number of pulses was estimated. It may be noted that the amount of Au deposited i.e. mass thickness for both the films, in this case is same. However, morphology of RT grown film showed percolated to near continuous film formation, in contrast to the film grown at 300 °C, showing formation of densely packed nanoparticles. This is because of variation in initial nucleation density during the film growth that depends on ratio of incident atomic flux diffusion distance of adatoms [107,109]. The typical diffusion distance of Au adatoms on oxide substrates is about 3.5Å and 3400 Å at RT and 300 °C respectively [109]. Therefore, for the film grown at 300 °C, the nucleation density is expected to be about 1000 times lesser than that grown at RT.

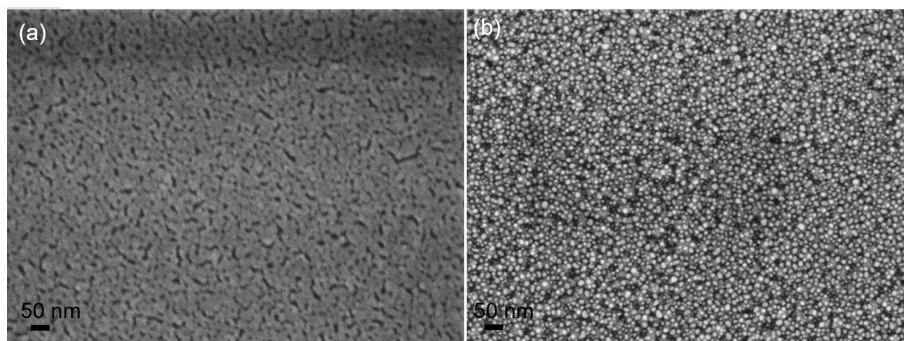


Fig. 2.1 SEM image of Au films of ~ 3.5 nm thickness, grown (a) at RT and (b) substrate temperature of 300 °C.

With initial high nucleation density in RT growth, further Au deposition (for

growth of the film) would lead to formation of inter-connected islands that results into percolated or continuous films [109]. Controlling the morphology of Au films by substrate temperature, and depositing atomic flux by target to substrate distance (TSD), and film mass thickness by number of laser pulses, enable growth of LSPR response tunable films in a single step avoiding annealing. Therefore, the effect of these process parameters, correlation of the observed LSPR with morphological characteristics of films and theoretical understanding of effective dielectric response of the films along with their SERS response are discussed in this chapter.

2.1 Effective dielectric response of metal thin films

The plasmon resonance frequency of isolated and smaller nanoparticles can be determined from Frolich condition $\epsilon_d + L_j[\epsilon_{Au}(\omega) - \epsilon_d] \approx 0$, as mentioned in Eq. 1.2 of Chapter 1. For exactly spherical nanoparticles, $L_{j=1,2,3} = 1/3$, and it becomes lesser than $1/3$ for oblate shape particles of high aspect ratio (γ , i.e. diameter/height is >1), along the major axis. In PVD growth, the formed nanoparticles on a substrate are not exactly spherical (generally of more lateral size than height) and has distribution in size and shape [77,110]. The optical response of these metal nanoparticle films can be predicted from an effective dielectric response (ϵ_{eff}), which is different from dielectric response of the bulk metal [86-88,111]. Fig. 2.2 (a) schematically represents the nanoparticle film of height h and metal volume filling fraction q , whose optical response is obtained from ϵ_{eff} . Fig. 2.2 (b) shows that the same mass thickness film in continuous form for which optical response can be determined from ϵ_{bulk} i.e. bulk dielectric response of the metal. Maxwell-Garnet effective medium theory, an

extension of Clausius-Mossotti relation, is the simplest theory to obtain effective dielectric function, however, it is applicable for nanoparticles dispersed homogeneously in another medium [12,111,112].

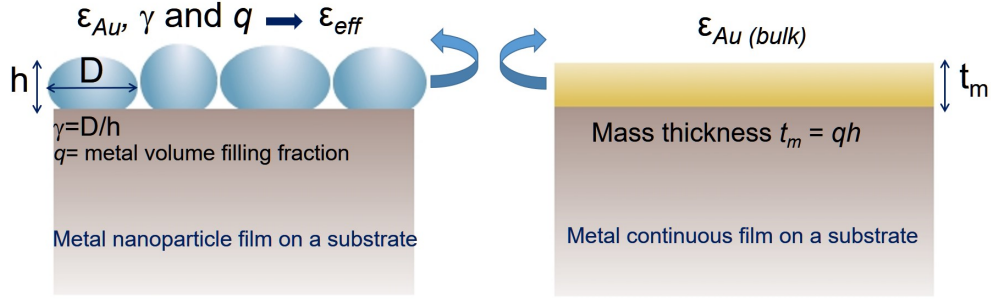


Fig. 2.2 Schematic of nanoparticle and continuous films of dielectric response ϵ_{eff} and bulk ϵ_{Au} respectively.

For nanoparticles supported on a substrate, Yamaguchi *et al* provided effective medium theory considering the effect of underlying substrate, [86]. According to it, the effective dielectric response of the nanoparticle film is given by

$$\epsilon_{eff} = \epsilon_d \left(q \frac{\epsilon(\omega) - \epsilon_d}{\epsilon_d + L_{eff} (\epsilon(\omega) - \epsilon_d)} + 1 \right) \quad \dots (2.1)$$

where, q is volume filling fraction of metal, $L_{eff} (= L_{shape} + L_{substrate} + L_{PI})$ is the constant which depends on shape and other contributions from substrate and particle-particle interactions [86,88].

2.1.1 Contribution from geometry of nanoparticles: The parameter, γ i.e. aspect ratio (diameter/height) of the nanoparticle quantifies the variation in geometry of nanoparticle either spherical (~ 1) or oblate spheroidal shape (> 1). The role of particle shape on effective dielectric response of nanoparticle films is represented by a constant term L_{shape} that depends on γ with the following relation [86]

$$L_{Shape} = \frac{\gamma^2}{2\sqrt{(\gamma^2 - 1)^3}} \left[\frac{\pi}{2} - \frac{\sqrt{(\gamma^2 - 1)}}{\gamma^2} - \arctan\left(\frac{1}{\sqrt{(\gamma^2 - 1)}}\right) \right] \quad \dots \quad (2.2)$$

2.1.2 Contribution of substrate: For nanoparticles films supported on a substrate, optical response is influenced by induced polarization in the substrate [87]. With excitation of plasmon in the nanoparticle, corresponding an image dipole is induced in the substrate, as schematically shown in Fig. 2.3. It alters the particle polarizability (α_{eff}) parallel to the substrate surface, and causes anisotropic response. In presence of incident electric field (E) of light, particle polarizability, parallel to the substrate, is given by [86]:

$$\alpha_{eff,\Pi} = \frac{V[\varepsilon(\omega) - \varepsilon_d]}{\varepsilon_d + L_{\Pi}(\varepsilon(\omega) - \varepsilon_d)}, \text{ where } L_{\Pi} = \frac{1}{3} \left[1 - \frac{1}{8} \left(\frac{d_i}{R} \right)^3 \left(\frac{\varepsilon_{sub} - \varepsilon_d}{\varepsilon_{sub} + \varepsilon_d} \right) \right], \dots \quad (2.3)$$

where, L_{Π} is the contribution to effective shape factor from induced polarization in the substrate, which is a function of d_i : distance between the particle dipole considered to be at the center of the particle and its image dipole. For spherical nanoparticles, d_i becomes equal to the particle diameter ($2R$). ε_{sub} and ε_d are the dielectric constant of underlying substrate and surrounding medium respectively.

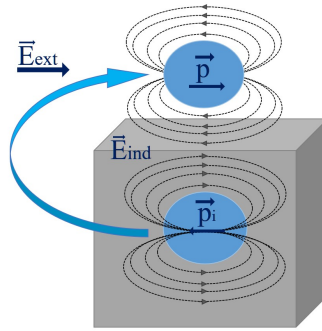


Fig.2.3 Schematic showing interaction between particle dipole and image dipole.

2.1.3 Contribution from interaction between the nanoparticles

In nanoparticle films, when the particles are closely spaced with each other, as

shown schematically in Fig. 2.2, the dipolar field of one particle interacts with that of the surrounding ones. The polarizability of each nanoparticle induced from incident electric field of light, is modified by the field from other surrounding nanoparticles and their image dipoles also, as schematically shown in Fig. 2.4.

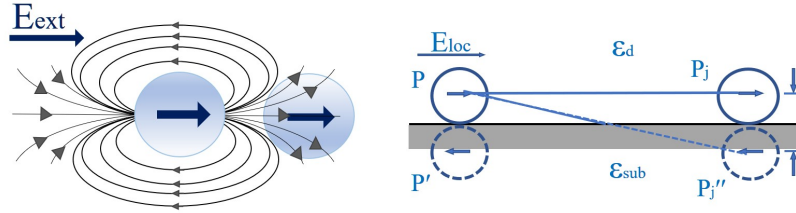


Fig.2.4 Schematic showing particle-particle and particle-image dipole interactions.

Taking into account of these interactions, their contribution factor as determined in reference [86,88], is given as,

$$L_{eff} = L_{shape} - \frac{\gamma^2}{24} \left(\frac{\epsilon_{sub} - \epsilon_d}{\epsilon_{sub} + \epsilon_d} \right) - 0.719 \left(\frac{6}{\pi} \right)^{1/2} \frac{1}{\gamma} \left(\frac{\epsilon_d}{\epsilon_{sub} + \epsilon_d} \right) q^{3/2}. \dots (2.4)$$

From the above expression, it can be noticed that the factor L_{eff} has been decreased with different contributions from the substrate and other surrounding nanoparticles. With this decreased shape factor, the Frolich condition presented for isolated spherical nanoparticle would shift to get satisfied at lower frequency side, leading to considerable red-shifted plasmon resonance excitation in nanoparticle films.

2.1.4 Overall contribution of substrate and other nanoparticles at high coverage

In the above expression of L_{eff} , Fedotov *et al* identified few limitations at high coverage of nanoparticles [88]. When the coverage of nanoparticles i.e. metal volume filling fraction $q > 0.5$ and for oblate shape particles of $\gamma > 3$, Eq. 2.4 results into negative value. This would imply that for metal nanoparticle possessing negative bulk

dielectric function, the Frohlic condition (Eq. 1.4) is not satisfied, i.e. absence of resonance, at large value of q and γ . This is because of the considered point dipole approximation for interactions between different nanoparticles and their mirror images [88]. For spherical nanoparticles of smaller sizes only, which are placed at distances larger than size of these nanoparticles, this approximation of point dipole at the centre of nanoparticle is applicable. However, for oblate spheroidal shape nanoparticles this approximation does not work. At higher metal volume filling fraction where inter-particle separation is very less, this approximation fails to produce correct results. Further, for oblate shape nanoparticles, separation between particle dipole and its image dipole decreases, as schematically shown in Fig. 2.5.

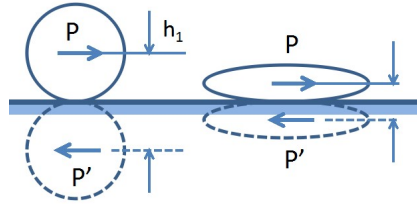


Fig. 2.5 Schematic showing particle and its mirror image on a substrate at different aspect ratios.

In the model developed by Yamaguchi *et al*, increasing aspect ratio, results rapid increase in field generated by image dipoles ($E_{imag} \propto h^{-3}$). To remove this inconsistency, Fedotov *et al* considered exact expression of electric field of oblate spheroids, and with this, the factor L_{eff} is given as [88],

$$L_{eff} = L_{Shape} - \sum_{i=-2}^2 \sum_{j=-2}^2 A \left(i \sqrt{\frac{2\pi}{3q}}, i \sqrt{\frac{2\pi}{3q}}, 0 \right) - \left(\frac{\epsilon_d - \epsilon_{sub}}{\epsilon_d + \epsilon_{sub}} \right) \sum_{i=-2}^2 \sum_{j=-2}^2 A \left(i \sqrt{\frac{2\pi}{3q}}, i \sqrt{\frac{2\pi}{3q}}, \frac{2}{\gamma} \right) - \frac{2\epsilon_d}{\epsilon_d + \epsilon_{sub}} \frac{0.177}{\gamma} \sqrt{\frac{3q^3}{2\pi}} \quad (2.5)$$

where the parameter $A(x,y,z)$ is calculated up to two arrays of nearest neighbourhood particles, accounting for particle-particle and their mirror image dipoles interactions and the last term accounts the interaction with the rest of the particles. This model is more appropriate for determination of ϵ_{eff} of densely packed monolayer nanoparticle films and even nearly continuous films with q value approaching to one.

2.2 Optical transmission of Au thin films

From theoretically calculated ϵ_{eff} of Au nanoparticle films, optical transmission was determined for a thin film supported on thick substrate [113], as schematically shown in Fig. 2.6.

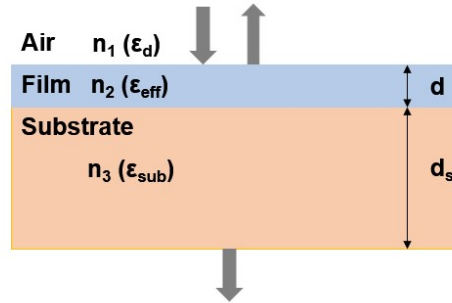


Fig.2.6 Schematic of thin film supported on a substrate of finite thickness.

Transmission of the film is given as [113]

$$T = \frac{|t_{123}|^2 |t_{31}|^2 e^{-2\text{Im}\delta}}{1 - |r_{321}|^2 |r_{31}|^2 e^{-4\text{Im}\delta}}, \quad \dots (2.6)$$

where t_{123} presents the transmitted field strength in medium 3 from medium 1, and r_{321} is the ratio of the electric field strength of the reflected light in medium 1 from medium 3 and of incident wave. These are given by [113],

$$t_{123} = \frac{t_{12}t_{23}e^{i\delta}}{1 + r_{12}r_{23}e^{2i\delta}} \text{ and } r_{321} = \frac{r_{32} + r_{21}e^{2i\delta}}{1 + r_{32}r_{21}e^{2i\delta}}, \quad \dots (2.7)$$

where, t_{ij} and r_{ij} are the Fresnel transmission and reflection coefficients for two mediums of index i and j respectively. δ is the phase change experienced in i^{th} medium of thickness d at normal incidence, which is given by $2\pi n_i d/\lambda$.

2.3 LSPR wavelength tunability with morphological parameters

To determine the LSPR wavelength tunability range with morphological parameters, i.e. q and γ of the particles, transmission spectra were calculated using Eq. 2.6. In these calculations, effective dielectric response of the films was determined by Eq. 2.1. The q values were varied in the range from 0.1 to 0.65. At the lower limit of 0.1, the nanoparticles are far away with each other and on the other hand, the higher limit of 0.65 corresponds to almost touching nanoparticles arranged hexagonally in monolayer film [87, 88]. The aspect ratio of one corresponds to spherical shape and higher values represent oblate spheroid shape particles with fixed diameter of 30 nm. The aspect ratio in the range of 1 - 4 is typical in the nanoparticles films grown from PVD methods.

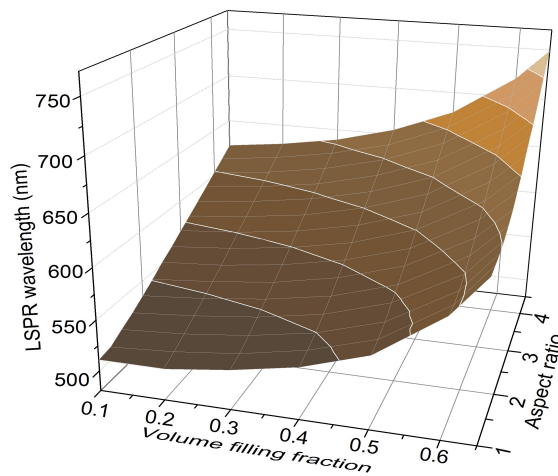


Fig.2.7 Tuneable range of LSPR wavelength of Au nanoparticles films with morphological parameters.

In calculation of ϵ_{eff} , the required dielectric response of Au (ϵ_{Au}) was obtained from analytical model [114] with IB absorption at about 470 and 330 nm. This model fits with the experimental data provided by ‘Johnson and Christy’ (JC) [115]. With these input parameters, the obtained ϵ_{eff} was used in calculating the transmission spectra and LSPR wavelength. Fig. 2.7 presents LSPR wavelength (obtained from optical transmission) versus the morphological parameters (q and γ) of nanoparticles. The figure shows that for aspect ratio close to one and $q \sim 0.1$, the LSPR wavelength is about 520 nm, which is close to that of isolated Au nanoparticles obtained from Mie theory [12]. For a given aspect ratio of nanoparticles, increase of q value resulted red-shift in LSPR wavelength. This red-shift is attributed to increased inter-particle interactions at high metal volume filling fraction. Further, for a fixed q value, as particle aspect ratio is increased, the LSPR wavelength also red-shifted. This is due to increased image dipole interactions with increase of aspect ratio, at reduced particle-image dipole separation.

2.4 Spectroscopic ellipsometry based determination of effective dielectric response (ϵ_{eff})

The above analytical model for determining ϵ_{eff} of metal nanoparticle films has few limitations. These are: i) in the presented analytical model, interaction of incident light electric field with the particles is based on dipole approximation only. Higher order multi-pole interactions, which become important for large size and high aspect ratio nanoparticles, has not been considered; ii) This model is applicable for nanoparticles arranged in monolayer; iii) it requires morphological parameters of the

nanoparticles i.e. aspect ratio and volume filling fraction to determine the ϵ_{eff} . However, in PVD growth, where growth of particles proceeds by formation of small nucleation sites and coalescence, the particles do not evolve into perfect shapes. Further, in case of nearly percolated films or coalesced nanoparticles, determination of morphological parameters becomes difficult. In such cases, direct experimental determination of ϵ_{eff} can be performed with spectroscopic ellipsometry. This section briefly describes the spectroscopic ellipsometry setup and modeling of the ellipsometry data.

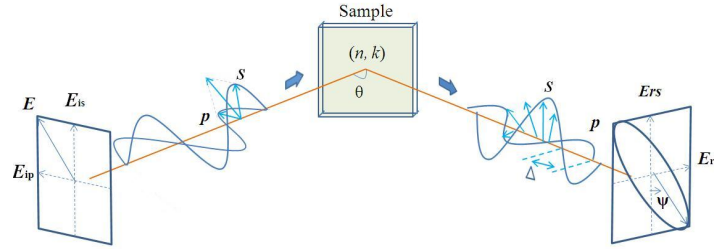


Fig. 2.8 Schematic of spectroscopic ellipsometry measurement principle.

Using ellipsometer, dielectric response of the material or its thin film is measured in terms of two parameters, i) Ψ , which is the ratio of amplitude and ii) Δ , which is the phase difference, between the reflected p and s polarized light [85]. Thus, its relation with the Fresnel coefficients R_p and R_s is given as,

$$\rho = \frac{R_p}{R_s} = \tan(\Psi)e^{i\Delta} \quad \dots (2.8)$$

Measurement of Ψ being ratio and Δ be the difference of two quantities, allows it to be less sensitive to fluctuations of light intensity, making this technique robust and accurate. Also, it does not require standard sample or reference beam. The accuracy of film parameters and optical constants determined from these

measurements depend on optical model used to fit the ellipsometry data (i.e. Ψ and Δ) [84,85]. Therefore, in ellipsometry measurement it is inevitable to use an appropriate physical model for extracting the optical properties. In the simplest case, phase difference (Δ) observed is due to interference and it is related as, $\Delta = 4\pi dn \cdot \cos(\theta_r)/\lambda$ where d is film thickness, λ is incident light wavelength and θ_r is angle of refraction in the film of refractive index n . The precision in thickness is,

$$\delta d = \frac{\lambda}{4\pi n \cos \theta_r} \delta \Delta \quad \dots (2.9)$$

This corresponds to δd of 0.1 Å, for typical values of $\delta \Delta \sim 0.02^\circ$ (typical limit of resolution) $n = 1.5$, $\theta_r = 40^\circ$ ($\theta_i = 70^\circ$) at $\lambda \sim 400$ nm [85]. The precision in thickness is very small, almost comparable to about monolayer.

2.4.1 Dispersion models for determination of optical properties from ellipsometry

From the measured ellipsometry data, Ψ and Δ are fitted with a physical model to determine the optical response of the films. This procedure involves selection of proper fitting parameters, error estimation and statistical measure of the quality of the fit. The fit quality is represented as “maximum likelihood estimator, also known as mean squared error (MSE) and is defined as [116],

$$MSE = \sqrt{\frac{1}{2\eta - m} \sum_{i=1}^{\eta} \left[(\Psi_{\text{exp}} - \Psi_{\text{cal}})^2 + (\Delta_{\text{exp}} - \Delta_{\text{cal}})^2 \right]}, \quad \dots (2.10)$$

where, η is the number of wavelengths for which measurement has been carried out and m is the number of fit parameters. The obtained MSE is a positive value and should approach to the minimum when the calculated data exactly matches with the experimental data. MSE represents the sum of the squares of the differences between

the measured and calculated data, each weighted by the standard deviation (SD) of that particular measured data point. Therefore, if some data point is noisy due to any electrical or mechanical fluctuation, its SD will be large and that measurement point will be less significantly weighted in the fit. The model parameters should yield minimum MSE with least correlation. The error bars on i^{th} fit parameter is given by its figure of merit (FOM) obtained using the standard 90% confidence limit (SCL) and the MSE as, $FOM_i = SCL_i \times (MSE)^{1/2}$ [116]. For a good fit with no systematic errors, the MSE tends towards one and so FOM_i gives the standard 90% confidence limit indicating sharpness of the fit parameters.

For reflecting or continuous metal films, particularly at low energies where free-carrier response is dominant, Drude model best fits the data [117]. For nanoparticle films, Lorentz or Gaussian oscillator models describe either bound electron response or collective resonance oscillation (due to geometrical confinement) of free electrons [118-120]. A brief discussion of these models used in the fitting is presented below.

i) Lorentz oscillator

This model is used to incorporate the bound electron response in overall optical properties of materials, considering oscillations of the electrons oscillate around fixed atomic nucleus [85]. Oscillating electric field $\mathbf{E} = \mathbf{E}_0 \exp(-i\omega t)$ of the incident light acts as external force on the bound electrons in the medium. It has restoring force from nucleus and damping with the lattice. Dielectric polarization induced in the material can be calculated from the resultant displacement of the electron. The

equation of motion of electron is written as:

$$m_e \frac{d^2 x}{dt^2} = -m_e \Gamma \frac{dx}{dt} - m_e \omega_0^2 x - eE_0 \exp(-i\omega t), \quad \dots (2.11)$$

where m_e and e are the mass and charge of electron respectively and Γ is the damping frequency. The first term on the right hand is damping force, which is proportional to velocity of electrons. The second term represents the restoring force on the oscillating electron by the nucleus. The electrons oscillate with the same frequency of incident field, and the solution of the above equation can be written as $x(t) = x_0 \exp(-i\omega t)$ with amplitude x_0 given by,

$$x_0 = -\frac{eE_0}{m_e} \frac{1}{(\omega_0^2 - \omega^2) - i\Gamma\omega}. \quad \dots (2.12)$$

For electron density, N_e , dielectric polarization $P = -e N_e x(t)$. The dielectric function, $\varepsilon = 1 + (P/\varepsilon_0 E)$, results in:

$$\varepsilon = 1 + \frac{e^2 N_e}{\varepsilon_0 m_e} \frac{1}{(\omega_0^2 - \omega^2) - i\Gamma\omega}, \quad \dots (2.13)$$

The real and imaginary parts of ε are:

$$\varepsilon_1 = 1 + \frac{e^2 N_e}{\varepsilon_0 m_e} \frac{(\omega_0^2 - \omega^2)}{(\omega_0^2 - \omega^2)^2 + \Gamma^2 \omega^2} \quad \text{and} \quad \varepsilon_2 = \frac{e^2 N_e}{\varepsilon_0 m_e} \frac{\Gamma \omega}{(\omega_0^2 - \omega^2)^2 + \Gamma^2 \omega^2} \dots (2.14)$$

At resonance frequency (ω_0), ε_2 shows a peak response. This corresponds to absorption with full width half maxima (FWHM) equal to Γ . Higher the Γ , larger the width with reduced amplitude. The limits of the dielectric function at very low and high frequencies are:

$$\varepsilon_s = \tilde{\varepsilon}(\omega \rightarrow 0) = 1 + \frac{\omega_p^2}{\omega_0^2} \quad \text{and} \quad \varepsilon_\infty = \tilde{\varepsilon}(\omega \rightarrow \infty) = 1. \dots (2.15)$$

To account multiple resonances at different energies ($E_{n0,j}$), Lorentz model

can be given, as a function of photon energy E_n as:

$$\varepsilon = 1 + \sum_j \frac{A_j}{E_{n0j}^2 - E_n^2 - i\Gamma_j E_n}, \quad \dots (2.16)$$

where, the subscript j denotes number of oscillators contributing to the ε . This is similar to the quantum mechanically derived expression for inter-band transitions [121]. A more general expression of the Lorentz oscillator is also given as [116]:

$$\varepsilon_{Lorentz} = \frac{A_n B r_n E_n}{E_n^2 - E^2 - i B r_n E}, \quad \dots (2.17)$$

where, A_n and $B r_n$ are approximate value of amplitude and FWHM respectively.

Increasing the number of oscillators shifts the absorption towards UV region.

Lorentz oscillator has been used for transparent or weakly absorbent insulator and semiconductor materials.

ii) Drude model: This is the most widely used model for dielectric response of metals accounting free electron response at low frequencies [85,116,117]. Response of free electrons to the light can be obtained from the Lorentz oscillator model by assigning $\omega_0 = 0$. Thus, the dielectric response of metals with free electron density N_f , and bulk plasma frequency ω_p , can be written as

$$\varepsilon = \varepsilon_\infty \left(1 - \frac{\omega_p^2}{\omega^2 + i\omega\gamma} \right), \quad \dots (2.18)$$

where ε_∞ is high frequency dielectric constant. Here,

$$\omega_p = \left(\frac{e^2 N_f}{\varepsilon_0 \varepsilon_\infty m^*} \right)^{1/2}. \quad \dots (2.19)$$

In metals, ω_p lies in UV/Vis region whereas for semiconductors it lies in IR region.

Reflectance becomes quite high for $\omega < \omega_p$, where free electrons oscillate

synchronously with electric field of light and thus the field gets screened by the presence of free electrons at surface, causing incident light to get reflected [85].

iii) Gaussian oscillator:

In order to account the Gaussian line shape of ε_2 , Gaussian oscillator has been proposed [116,122]. This is expressed in terms of above defined parameters as,

$$\varepsilon_{Gaussian} = A_n \left\{ \left[\Gamma\left(\frac{E-E_n}{\sigma_n}\right) + \Gamma\left(\frac{E+E_n}{\sigma_n}\right) \right] + i \left[\exp\left[-\left(\frac{E-E_n}{\sigma_n}\right)^2\right] + \exp\left[-\left(\frac{E+E_n}{\sigma_n}\right)^2\right] \right] \right\}, \quad \dots (2.20)$$

where $\sigma_n = \frac{Br_n}{2\sqrt{\ln 2}}$. The function Γ is a conversion series used to produce

Kramers-Kronig consistent ε_l function, as described in detail in ref. [122].

iv) Cauchy model:

These models are used for materials which are transparent over a broad spectral range [85,116]. This corresponds to special case of Lorentz model where $\varepsilon_2 \sim 0$. With assumption of $\Gamma \sim 0$ at $\omega \ll \omega_b$, the Eq. 2.13 can be written as (in terms of wavelength, using $\omega/c = 2\pi/\lambda$):

$$\varepsilon = \varepsilon_1 = 1 + \frac{e^2 N_e}{\varepsilon_0 m_e (2\pi c)^2} \frac{\lambda_0^2 \lambda^2}{\lambda^2 - \lambda_0^2} \quad \text{and} \quad \varepsilon_2 = \kappa = 0. \quad \dots (2.21)$$

Expression of Sellmeier model can be obtained from the above equation as [116]

$$\varepsilon_1 = n^2 = A + \sum_j \frac{B_j \lambda^2}{\lambda^2 - \lambda_{0j}^2} \quad \varepsilon_2 = 0, \quad \dots (2.22)$$

where A and B_j are analytical dimensionless parameters. A gives value of refractive index in long wavelength limit. Sellmeier model exhibits normal dispersion i.e. refractive index decreases with wavelength. The more general Cauchy model for dispersive medium, for monotonously decreasing refractive index can be represented from series expansion as follows:

$$n = A + \frac{B}{\lambda^2} + \frac{C}{\lambda^4} + \dots, \quad \kappa = 0, \quad \dots (2.23)$$

The new third parameter C affects the curvature and amplitude at smaller wavelengths. In general, the three parameters follow, $A > 1 > |B| > |C| > 0$. It may be noted that the Kramers-Kronig relation is used to determine the refractive index from the extinction coefficient; however, these two models (Sellmeier and Cauchy) are not suitable to provide the interdependent n and k values [116].

2.5 Dielectric response of Au thin films of different thicknesses

When the film thickness is smaller (< 10 nm) than nearly twice of the mean free path ($2v_f\tau_B$, v_f : electron Fermi velocity and τ_B : bulk collision time) of free electrons in bulk metal, surface scattering of free electrons dominates over bulk scattering, resulting decreased collision time [123]. These films also show variable colors indicating change in reflection and transmission. Using PLD method, Au films of different thickness were grown on transparent and one side roughened glass substrates.

Fig. 2.9 shows the schematic of experimental setup.

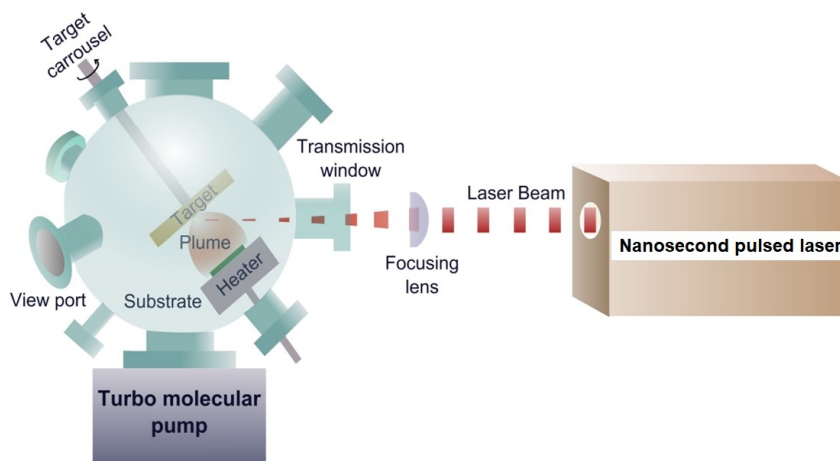


Fig. 2.9 Schematic of the PLD experimental setup.

Ablation of Au target (purity $\sim 99.99\%$) was carried out using a nanosecond

pulsed laser (2nd harmonic Nd:YAG, repetition frequency: 10 Hz, pulse duration: 9 ns) at base pressure of $\sim 8 \times 10^{-6}$ mbar. During growth of all the films, laser fluence was fixed at about 4 J/cm². Growth of different thickness Au films was carried out by varying the total number of ablation laser pulses at room temperature (RT) and 300°C substrate temperature.

Fig. 2.10 (a, b) shows transmission of Au films produced with different number of pulses at RT and 300°C respectively. The RT grown films showed decreased transmission at longer wavelength side, and with increase of number of laser pulses, the overall transmittance decreased. The decreased transmission below 500 nm is due to inter-band (IB) absorption and higher wavelength side is due to increased reflection of the metal film [77,124]. In contrast to this, the films grown at 300°C for the same number of ablation pulses, exhibited characteristic dip in transmission spectra, attributed to plasmon excitation.

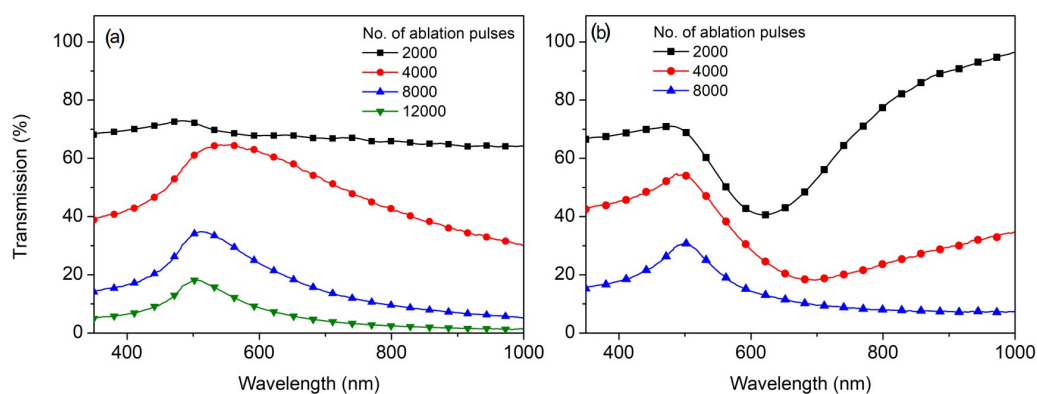


Fig. 2.10 Transmission of Au films produced at (a) RT and (b) substrate temperature of 300°C.

Significant variation in optical transmission in these films shows that the dielectric response changed considerably with substrate temperature and also film

thickness. Variation of characteristics of plasmon excitation with film thickness and substrate temperature has been discussed in detail in the next section.

To determine dielectric response of these films spectroscopic ellipsometry characterization was carried out at four different incident angles. Fig. 2.11 presents the ellipsometry data (Ψ , Δ) for Au films deposited at RT and 300 °C with 4000 ablation pulses. Ellipsometry data is shown only for the films grown with 4000 ablation pulses because for this condition at RT growth optical response of the film is like continuous films and that grown at 300°C has LSPR response. The measured Ψ , Δ were fitted with a physical model consisting of Drude model for free electrons and Gaussian oscillator model for bound electrons (IB excitations) as well as LSPR [117-120]. The glass substrate was roughened backside to avoid back-side reflections.

The sample structure was modeled as metal film on a glass substrate. Dielectric response of glass substrate was modeled using Cauchy dispersion relation. The dielectric response of metal film was modeled as combination of different oscillators [119,120] as expressed by the following equation,

$$\epsilon_{\text{exp}}(E) = \epsilon_1 + i\epsilon_2 = \epsilon_{\infty} + \epsilon_{\text{Drude}} + \epsilon_{\text{IB}}(E) + \epsilon_{\text{LSPR}}(E) = \epsilon_{\infty} + \epsilon_{\text{Drude}} + \sum_{n=1}^{N_{\text{osc}}} \epsilon_{G,n}(E) \quad \dots(2.24)$$

where, ϵ_{∞} is constant which accounts high frequency contribution to the dielectric function, ϵ_{Drude} for free electron response, ϵ_{IB} considers IB transitions and ϵ_{LSPR} for the collective oscillations or LSPR of free electrons.

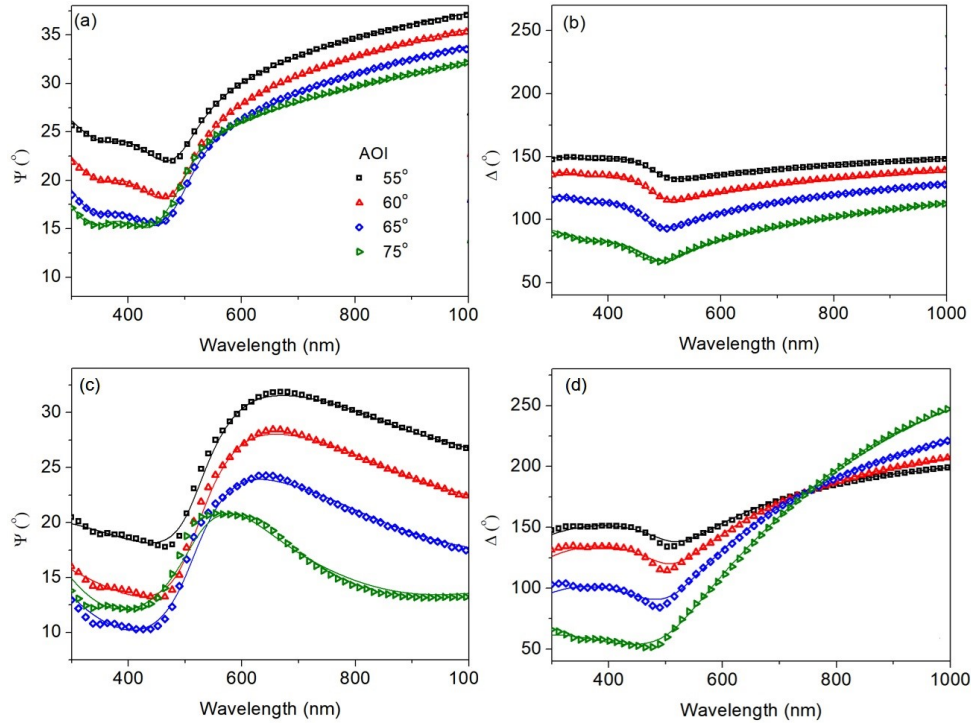


Fig. 2.11 Measured (symbols) and fitted (lines) ellipsometry data (Ψ , Δ) of Au films deposited at (a,b) RT and (c,d) 300 °C substrate temperature with 4000 ablation pulses.

The last two terms accounts oscillator behavior of electrons, which were modeled using Gaussian oscillators. For nanoparticle films which exhibiting LSPR response, two of these oscillator was used for IB transitions of Au (at about 3.1 and 4 eV) [11,12], and two more oscillators for LSPR response (in plane and out of plane). The choice of Gaussian oscillator is because it is convolution of Lorentz oscillators, and is more suitable for accounting inhomogeneous broadening in the optical response of the nanoparticle films arising from particle size distribution [119,120]. Good fitting with low MSE values was observed with Gaussian oscillators as compared to Lorentz oscillators. It was found that the films grown at RT above 4000 pulses, where LSPR is not observed, the ellipsometry data was fitted with one Drude

and two Gaussian oscillators. From the above fitting, thickness of the films grown at RT with 12000, 8000, 4000 and 2000 pulses, were found to be about 38.4, 24.6, 13.9 and 8.1 nm respectively. Fig. 2.12 (a) and (b) show variation of real and imaginary part of ϵ of RT grown Au films respectively. It can be observed that both ϵ_1 and ϵ_2 of the film produced with 12000 ablation pulses is almost close to that corresponding to bulk Au [116], as shown with dashed lines in the graph.

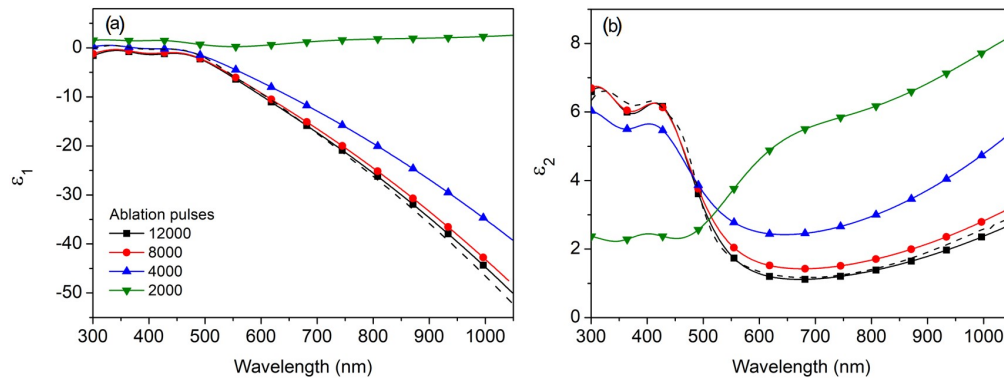


Fig. 2.12 Variation of dielectric response of RT grown Au films grown with varied ablation pulses, dashed line represents the same for bulk Au.

With decreasing film thickness, by ablation pulses, ϵ_1 and ϵ_2 of the film progressively increased at longer wavelengths. Fig. 2.13 (a) and (b) show the variation of ϵ_1 and ϵ_2 of the films grown at 300°C substrate temperature. In this case, both ϵ_1 and ϵ_2 shows significant variation from that observed for RT grown films. The observed variation in ϵ clearly shows oscillator response, which is due to LSPR excitation pertinent to metal nanoparticle films. Corresponding to the resonance behavior as observed in transmission spectra of the films in Fig. 2.10(b), ϵ_2 showed peaks, which red-shifted with increasing film thickness.

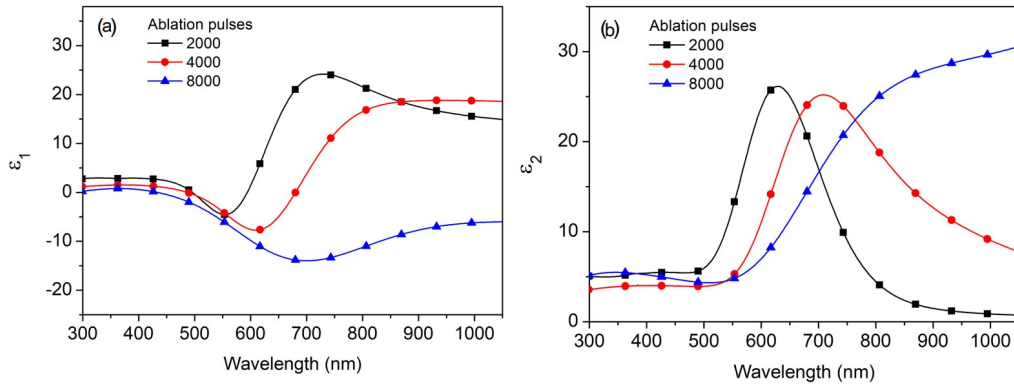


Fig. 2.13 Variation of dielectric response of Au films grown at 300 °C with different number of ablation pulses.

2.6 Growth temperature induced LSPR characteristics and their correlation with morphological parameters

The above results show growth temperature has strong influence on film morphology (Fig. 2.1) and optical response (section 2.5). In order to determine optimum substrate temperature for producing strong LSPR response at different Au films thicknesses using PLD, Au films were grown at different substrate temperature. In PLD growth, the film thickness also varies with TSD (target to substrate distance). Therefore, the film thickness and optical responses can be controlled by TSD also. Different mass thicknesses of Au films were deposited on epi-polished sapphire substrates. The films were deposited with 2500 and 5000 laser pulses at 4.5 and 8 cm TSD and different substrate temperatures of room temperature (RT), 150°C, 300°C and 500°C. The LSPR characteristics of the films were determined from their transmission spectra, measured using a UV-Vis spectrophotometer. Atomic force microscope (AFM) imaging was used to obtain morphology of the nanoparticles, and AFM images were analyzed with Picoquant and Image J software to obtain size and

density of nanoparticles. Mass thickness of the films was obtained using X-ray reflectivity.

Fig. 2.14 (a) and (b) show UV-Vis. transmission of Au films of about 2.8 and 5.5 nm thickness respectively, deposited with 2500 and 5000 pulses at 8 cm TSD and different substrate temperatures. In both these cases, the transmission has varied at longer wavelength region above 500 nm. Below 500 nm, same transmittance value was observed for Au films deposited at different substrate temperature, indicating nearly same mass thickness of these films. At longer wavelength region, the optical response is governed by free electrons [11,12]. In this region, nearly constant or decreased transmittance was observed for the RT grown films, attributed to increased film reflectance. However, films grown at high temperatures exhibited LSPR excitation which confines electrons' response to narrow wavelength region, where the transmission becomes low and again it became high at longer wavelengths. This is characteristics optical response of nanoparticles films [12].

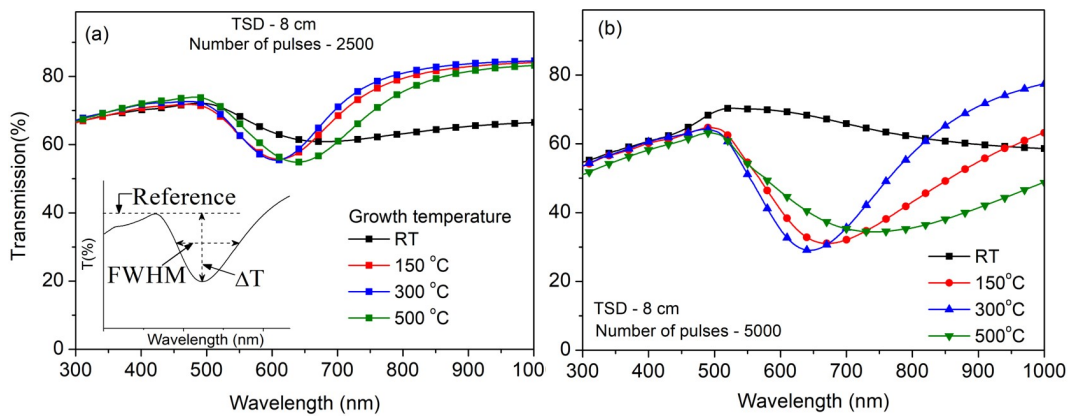


Fig. 2.14 Transmission of Au nanoparticle films of (a) 2.8 nm and (b) 5.5 nm thickness, inset presents the LSPR characteristics of the film.

The LSPR characteristics i.e. resonance wavelength (at which transmission is minimum) and bandwidth (as shown schematically in inset of Fig. 2.13), are determined. The bandwidth is obtained from full width at half maxima (FWHM) of dip in transmission with reference to transmittance at IB edge near 510 nm [77]. For films of 5.5 nm thickness, significant variation in LSPR characteristics with substrate temperature is observed, in comparison to 2.8 nm thickness films. The details of the LSPR characteristics of the films are provided in table 2.1. Increasing growth temperature from 150°C to 300°C, both LSPR wavelength and bandwidth decreased. However, further increase of temperature to 500 °C, the LSPR wavelength red-shifted along with more asymmetric broadening. The above results show that for same film mass thickness, substrate temperature induced morphological changes resulted varied LSPR responses.

Fig. 2.15 shows AFM images with corresponding line profile analyses and particle size distribution of 5.5 nm thick Au films, grown at different substrate temperatures. Formation of small size nanoparticles of average height of about 1.5-2 nm can be observed for Au film grown at RT, which is almost continuous. However, Au films grown at 150°C, 300°C and 500°C showed formation of nanoparticles whose average size was about 22, 28, and 31 nm respectively. The average height of the nanoparticles also increased to ~ 6 nm at high temperature growth. Increase of average size of nanoparticles with growth temperature, also resulted decreased particle number density from 1.1×10^{11} to 5.5×10^{10} /cm².

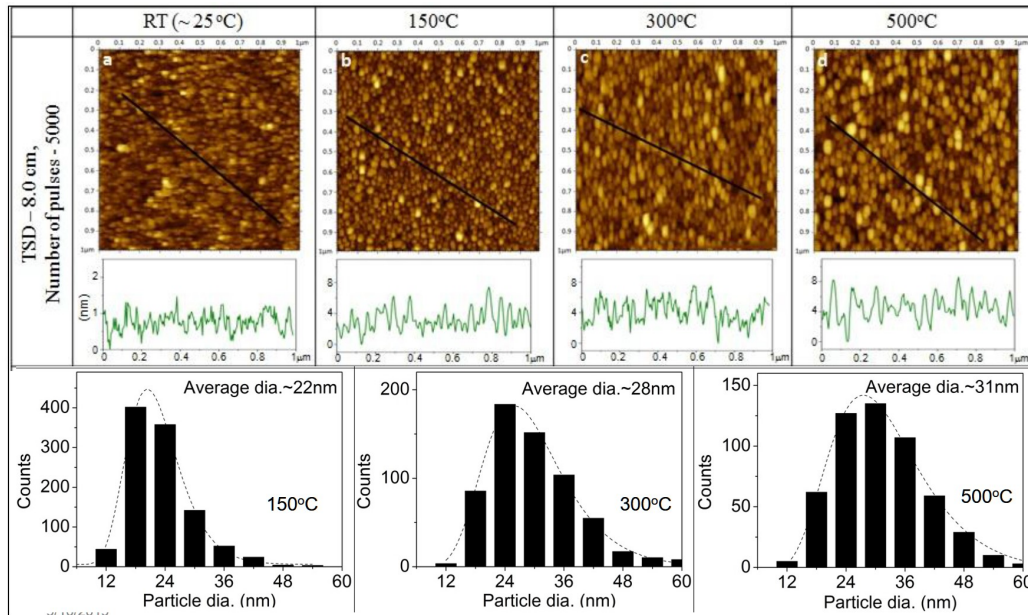


Fig. 2.15 Effect of growth temperature on film morphology (AFM images sacn area $1\mu\text{m} \times 1\mu\text{m}$) and line profile of 5.5 nm thickness Au films.

Au films of about 8 and 17 nm thickness were grown with 2500 and 5000 pulses respectively at 4.5 cm TSD. Fig. 2.16 (a, b) show transmission of these films deposited at different substrate temperatures. It can be observed that only high temperature grown films showed the LSPR response. Similar to the previous case, the LSPR wavelength of Au films deposited at 150 °C and 500 °C was red-shifted to that of the film obtained at 300 °C. For thicker film of 17 nm mass thickness, LSPR response was obtained only for the film at 300°C. The other two films grown at 150 °C and 500 °C showed continuously decreased transmission similar to that obtained for the RT film. From these results, it can be inferred that for films of thickness in the range of 5-15 nm, LSPR characteristics can be tuned by varying substrate temperature. Increasing film thickness by ablation pulses or decreasing TSD, reduced the overall transmission and resulted into broader and red-shifted LSPR band.

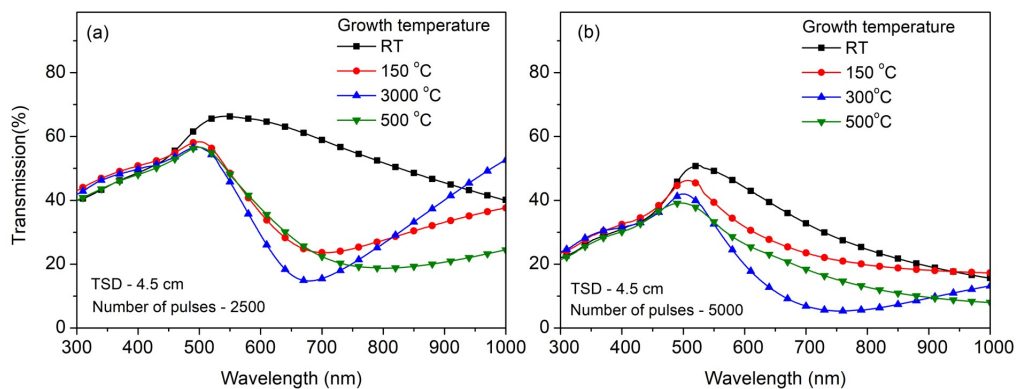


Fig. 2.16 Transmission of Au films of (a) 8 nm and (b) 17 nm thickness.

Fig. 2.17 (a-d) shows AFM images along with the line profile analyses of Au films of ~ 8 nm thickness, grown at different substrate temperatures. Similar to Au films of 5.5 nm thickness, film deposited at RT produced smaller interconnected particles. The average height of nanoparticles was about 2 nm, whereas the films deposited at higher temperatures resulted formation of distinct nanoparticles. Increasing the growth temperature from 150°C to 500°C, the average size of the particles increased from 41 to 46 nm and the average height of the particles was found to be about 6.5-8.5 nm. The particle number density varied as $5.3 \times 10^{10} / \text{cm}^2$, $3.3 \times 10^{10} / \text{cm}^2$ and $3.1 \times 10^{10} / \text{cm}^2$ for the films deposited at 150°C, 300°C and 500°C respectively. It can be observed that for 300°C grown film, the formed nanoparticles are more uniform compared to the films obtained at other substrate temperatures. As a result, narrow LSPR response was observed for this film.

Fig. 2.18 shows AFM images and corresponding line profiles of 17 nm thick Au films deposited at different substrate temperatures. It can be observed that the RT grown film was nearly continuous, whereas high temperature grown films showed inter-connected particles. With increasing growth temperature from 150, 300

to 500 °C, the average diameter of nanoparticles increased from about 75, 90 to 120 nm respectively with number density of about $3.5 \times 10^{10} / \text{cm}^2$ $3.2 \times 10^{10} / \text{cm}^2$ to $2.8 \times 10^{10} / \text{cm}^2$.

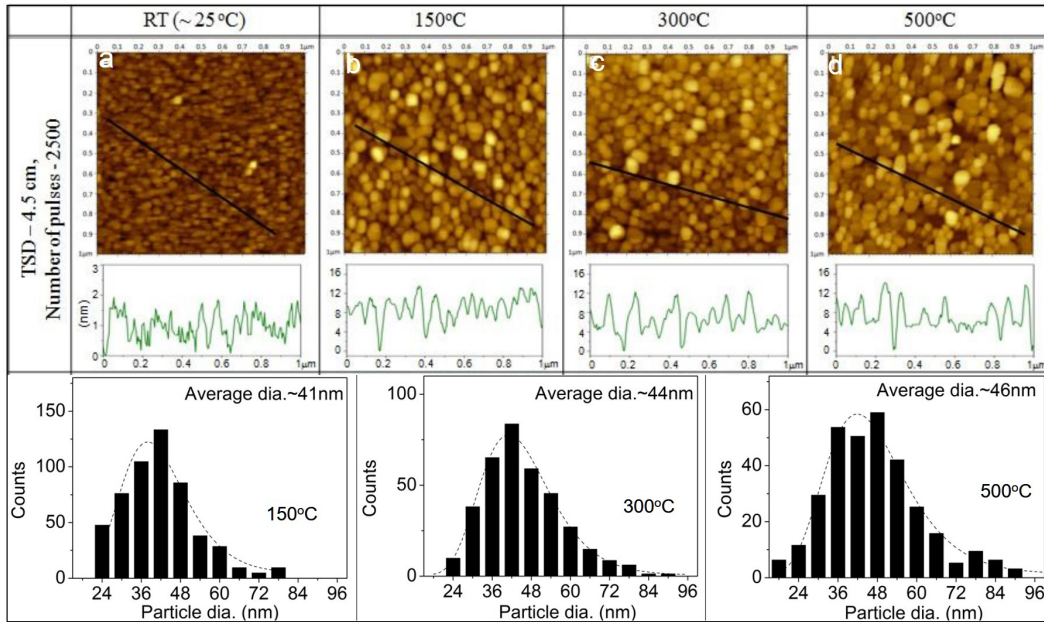


Fig. 2.17 Effect of growth temperature on film morphology (AFM images scan area $1 \mu\text{m} \times 1 \mu\text{m}$ and line profile) of 8 nm thickness Au films.

Thus, for films with high thickness (>15 nm), the average size of grown nanoparticles and shape distribution is large enough to suppress their distinct LSPR response, as observed in Fig. 2.16 (b). From these results of growth temperature induced morphological variation of films of different thicknesses (in the range of 5-17 nm), it can be observed that average size increased with decreased number density from growth temperature and film thickness. These results support the initial nucleation density (proportional to incident atomic flux/diffusion coefficient of adatoms) driven morphological change during the film growth. An empirical relation for diffusion of FCC metals like Ag, Au, Cu, Pt etc. on oxide substrates has been

provided as [108],

$$D_s = 0.014 \exp(13T_{melt} / 2T_{sub}), \quad \dots (2.24)$$

where D_s is the diffusion coefficient, T_{melt} and T_{sub} are melting temperature of the metal and growth temperatures respectively. From this, Au diffusion coefficient comes out to be about 3.6×10^{-15} , 1.6×10^{-11} , 3.6×10^{-19} and 1.8×10^{-7} cm^2/s respectively at RT, 150°C, 300°C and 500°C.

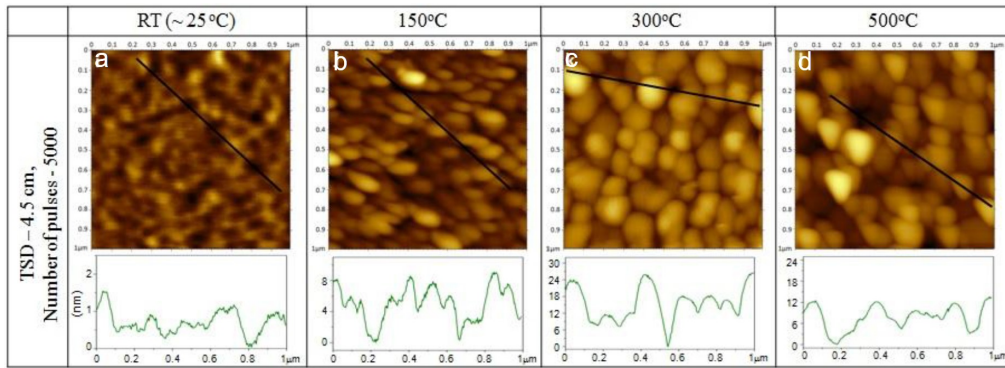


Fig. 2.18 Effect of growth temperature on film morphology (AFM images scan area $1 \mu\text{m} \times 1 \mu\text{m}$ and line profile) of 17 nm thickness Au films.

The effect of substrate temperature on nucleation density (at the initial stage of growth) and subsequent morphology observed from AFM line profile analysis has been shown schematically in Fig. 2.19. RT growth results formation of high nucleation centers, which with further growth leads to interconnected or percolated films, even at very low film thickness. Increasing substrate temperature to 150°C, at low film thickness, nanoparticles growth was noticed and for higher thickness films of above 8 nm, at this temperature, the formed nanoparticles start to coalesce. However, higher substrate temperature of 300°C, resulted nanoparticles growth due to lower nucleation density. Further increased cluster mobility at higher substrate temperature

of 500°C, favored more lateral growth, resulting irregular shape nanoparticles. The intermediate substrate temperature of 300°C is observed to be optimum for growth of relatively uniform size nanoparticles with less size distribution, as a result narrow band strong LSPR response is observed.

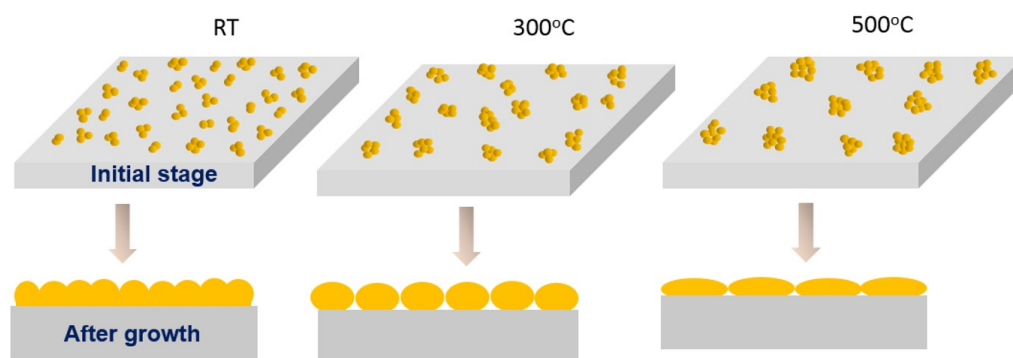


Fig. 2.19 Schematic of effect of growth temperature on film morphology.

On the other hand, in annealing driven nanoparticle formation process also, about 400°C has been reported to be optimum temperature for ~ 5 nm thick Au thin films [125]. In this case, worm-like irregular nano-structures was observed at lower annealing temperature and coalesced larger nanoparticles were observed at higher temperatures. The process involved in temperature induced change in morphology in these cases are quite different, i.e. the present case of high temperature growth involves variation in nucleation density, and post-annealing at high temperature involves thermal de-wetting of thin films. However, in both processes, for obtaining uniform shape nanoparticles with narrow size distribution, optimum temperature was found to be in the same range. The above results show that strong LSPR response Au nanoparticle films can be realized by combination of optimum film thickness (5-10 nm) and optimum growth temperature of about 300°C. Fig. 2.20 compares the LSPR

response of Au films deposited with 2500 pulses at 500°C and 5000 pulses at 300°C. This figure shows that by fine tuning of morphology through substrate temperature, it is possible to obtain almost same LSPR wavelength with different LSPR strength, in films of different thicknesses. This is due to dependence of LSPR wavelength on morphological parameters mainly aspect ratio of nanoparticles and their volume filling fraction in the film. It is in consistence with that observed from theoretical calculation (refer Fig. 2.7) which shows that a particular LSPR wavelength can be realized by different combinations of aspect ratio and volume filling fraction of nanoparticles. These films possessing same LSPR wavelength with different nanoparticle size are important for understanding the role of plasmonic effects in many emerging applications like SERS, as presented in later section.

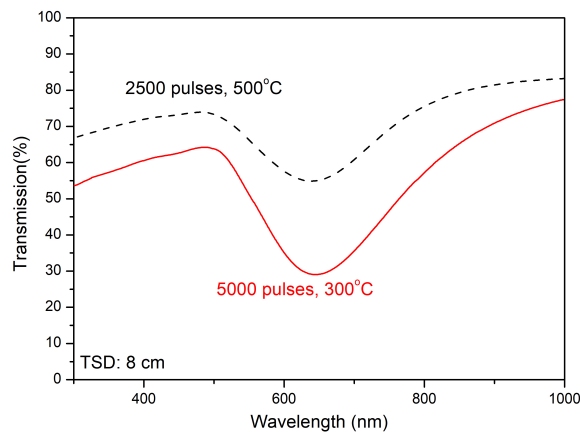


Fig. 2.20 Comparison of transmission of Au films deposited at different combination of laser pulses and growth temperature.

2.7 Effect of alumina layer capping and LSPR characteristics of Au nanoparticle films

PLD method is versatile to grow composite multilayer films [78,126]. With alumina layer coating on Au films, the effect of change in surrounding medium on the

LSPR characteristics was determined. Under the same experimental conditions, Au films were also grown with Al₂O₃ (alumina) over-layer of about 30 nm thickness, by ablating sintered alumina target (purity: 99.999%) with about 2 J/cm² laser fluence. Fig. 2.21 (a, b) present transmission of alumina layer capped Au nanoparticle films of 5.5 and 8 nm thickness films. It can be observed that the film grown at 300°C showed blue-shifted LSPR and narrow band when compared to that obtained at 150°C and 500°C, even after alumina layer capping. Similar variation in LSPR characteristics with growth temperature in absence and presence of alumina layer shows that morphological variation during growth of Au nanoparticles determine the LSPR characteristics. However, after alumina capping, transmission decreased at longer wavelengths above 500 nm and LSPR band broadened. In IB absorption region i.e. < 500 nm, marginally increased transmittance could be due to small amount of re-sputtering of the Au films during capping with alumina layer.

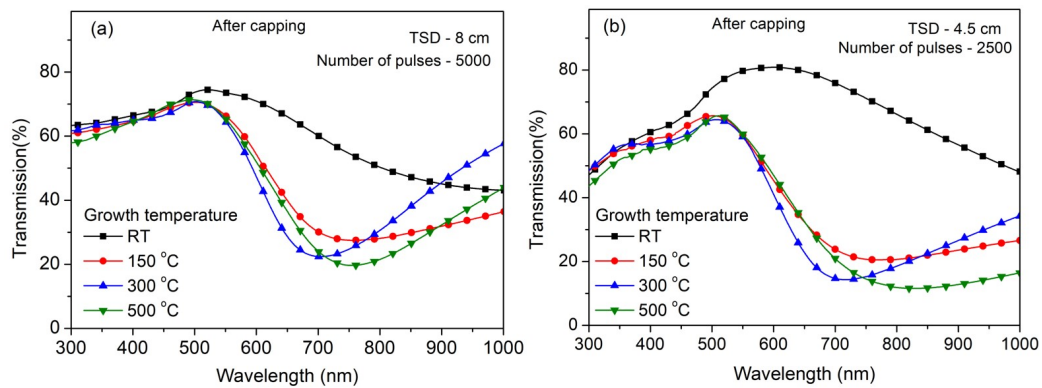


Fig. 2.21 Transmission of Au films of (a) 5.5 nm and (b) 8 nm thickness after capping with alumina layer.

Since in PLD process, the ablated species possess high kinetic energy in the range about 200 eV, which can re-sputter the Au nanoparticle film during the coating

of alumina [127,128]. Re-sputtering of Au nanoparticles has also been reported earlier by during over-layer deposition with alumina [128]. In present case, change in LSPR wavelength by dielectric over-layer on Au films can be explained with two effects, as following. In presence of high dielectric constant material, LSPR wavelength of Au nanoparticles red-shifts. This can be observed from the Frohlich condition and Drude dielectric function as mentioned in Eq. 1.3. The other factor that affect the LSPR wavelength is re-sputtering induced decrease in average size of nanoparticles or increased inter-particle separation [128]. This would cause blue-shifted LSPR response. From comparison of Fig. 2.14 and 2.21, red-shifted and broadened LSPR response with alumina over-layer suggest that first factor is more dominant and capping induced morphological changes is not significant.

Table 2.1 presents the LSPR wavelength and its bandwidth of Au nanoparticle films of varied thicknesses. Further to quantify LSPR strength (ΔT), difference in transmittance value at LSPR wavelength and IB edge was measured, as schematically shown in Fig. 2.14. LSPR wavelength tuning was observed in between 600 - 800 nm wavelength. LSPR wavelength red-shift achieved from increasing mass thickness is found to be relatively more than that produced by capping of Au films with alumina layer. The LSPR strength was found to increase with alumina capping. This is due to red-shift of LSPR band with respect to IB-transition region, resulting lesser damping of collective excitations [12].

Table 2.1 LSPR characteristics of Au films without and with alumina over layer deposited at varied substrate temperatures.

Film thickness (nm)	Growth parameters	Growth Temp. (°C)	LSPR characteristics				
			LSPR wavelength (nm)		LSPR strength (ΔT %)		LSPR bandwidth (nm) (Before)
			Before	After alumina capping	Before	After alumina capping	
2.8	TSD:80 mm, 2500 pulses	150	612	655	16	28	134
		300	606	611	17	24	121
		500	642	655	19	30	164
5.5	TSD:80 mm, 5000 pulses	150	674	756	34	43	264
		300	644	703	36	48	186
		500	746	754	31	51	432
8	TSD:45mm, 2500 pulses	150	703	770	35	46	488
		300	678	716	42	50	288
		500	800	826	38	53	702
17	TSD:45 mm, 5000 pulses	150	970	-	-	-	-
		300	756	~950	37	-	668
		500	-	-	-	-	-

2.8 Comparison of SERS response of films of varied morphologies

As observed from AFM analysis, the films deposited at high temperatures consist of nanoparticles which are closely spaced exhibiting ‘hot spot’ regions in between these nanoparticles. With LSPR excitation of these nanoparticles, near-field becomes very high at these hot spots, which is useful for SERS application. Therefore, SERS response of Au films deposited at varied temperatures were measured with rhodamine6G (Rh6G) dye of 500 nM concentration.

For SERS measurement, the grown Au films were dipped in aqueous solution

of Rh6G of 500 nM concentration for 10 minutes. After that, the films were removed slowly from the solution without formation of any droplet. SERS data was collected using a Raman spectrometer (LabRam HR 800, Horiba) at two different excitation wavelengths of 633 nm and 488 nm with laser power of 9 mW and 10 mW respectively. In all the measurements, the objective lens was 50X and integration time was fixed at 200 s and background correction was performed as reported in literature [129]. The samples did not show any damage during the SERS measurements. The Raman spectrum of Rh6G in absence of Au film was also recorded for reference. Fig. 2.22 (a,b) present SERS intensity of R6G dye measured at 633 nm in presence of Au nanoparticle films of 5.5 nm and 8 nm thickness respectively. In absence of Au film, no distinct Raman spectra of the dye was observed. Also RT grown films did not show measurable Raman signal. In contrast to this, high temperature grown films showed Raman spectra with distinct peaks at about 613, 774, 1180, 1362, 1576, 1598 and 1648 cm^{-1} corresponding to different vibration modes of Rh6G dye, as mentioned in literature [60,130]. Enhancement factor (EF) for specific peak in the spectra was calculated from the expression [60]:

$$EF_{SERS} = \frac{I_{SERS} / C_{SERS}}{I_{RS} / C_{RS}} \quad \dots (2.25)$$

where, I_{SERS} and I_{RS} are intensity of Raman scattering peaks in presence and absence of Au nanoparticle films and C_{SERS} and C_{RS} are concentrations of dye used for obtaining Raman signal in presence and absence of nanoparticle films respectively. The value of C_{RS} is 5 mM in EF calculations. The SERS EF of 1362 cm^{-1} peak is found to be about 4.3×10^5 , 2.1×10^6 , and 2.8×10^5 for nanoparticles films of 5.5 nm

thickness grown at 150, 300 and 500 °C respectively. Similarly, for 8 nm thick Au nanoparticle films, the SERS EF is found to be about 1.4×10^5 , 2.7×10^6 , and 1.1×10^6 grown at 150, 300 and 500 °C respectively. For same mass thickness film, SERS EF was found to vary with the film growth temperature. It is because, SERS EF depends on size and shape of plasmonic nanoparticles and their arrangement, density of hot spots and excitation wavelength used for Raman measurement [130]. For both Au film thicknesses, 300°C grown films showed the highest EF. AFM analysis showed that the films grown at 300°C were formed with relatively uniform nanoparticles. Also, the LSPR band is close to the excitation wavelength.

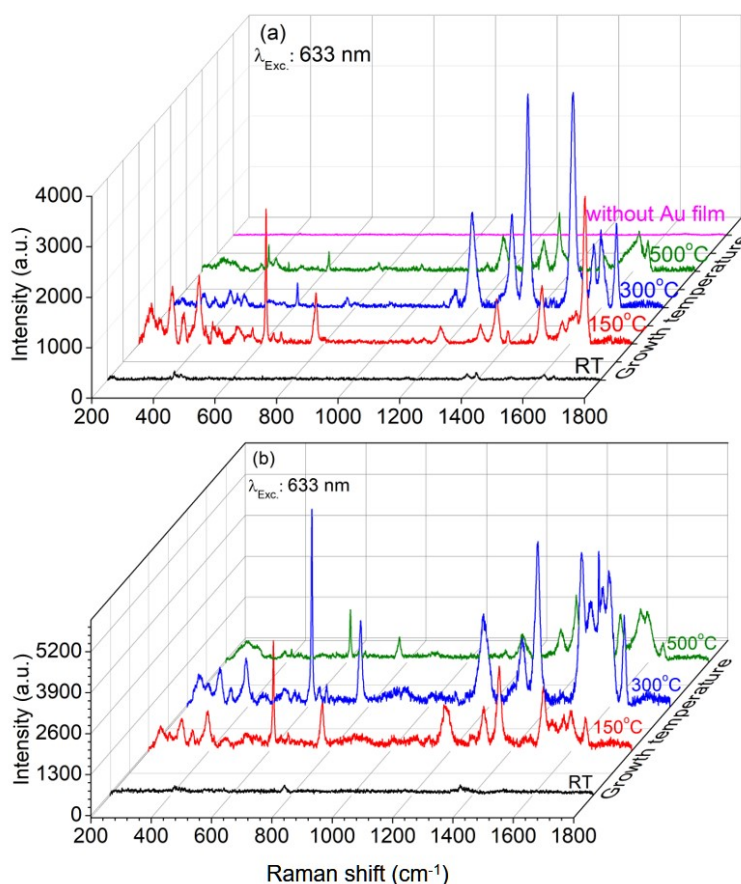


Fig.2.22 SERS intensity spectra of Rh6G dye in absence and presence of Au nanoparticle films of (a) 5.5 nm and (b) 8 nm film thickness.

When the Raman excitation wavelength is close to LSPR wavelength, highest near-field enhancement can be achieved [12,60]. Further, SERS signal was also measured at two more regions of the sample and SERS intensity was found to vary within $\pm 8\%$. Relatively lesser EF observed at 500°C could be due to red-shifted LSPR band with respect to Raman excitation wavelength and also decreased number density of hot spots. To address the role of LSPR wavelength with respect to Raman excitation wavelength, SERS measurements were also performed at 488 nm excitation wavelength. Fig. 2.23 (a) shows SERS intensity of Rh6G dye obtained in presence of 8 nm thick Au nanoparticle films. For all films, peak intensity was significantly decreased (intensity scale is about three times lesser compared to Fig. 2.22 (b)). Au film of about 17 nm thickness also showed similar results, as shown in Fig. 2.23 (b). This figure compares SERS response of RT and 300°C grown Au films at two Raman excitation wavelengths. Though 300°C grown Au film showed high SERS intensity for both the excitation wavelengths of 633 and 488 nm, it is significantly high when excited with 633 nm wavelength. This shows that for the same film, more SERS EF can be obtained, by selecting excitation wavelength close to LSPR wavelength. The above results confirm that the observed SERS enhancement is due to LSPR driven electromagnetic field enhancement in-between the gap of nanoparticles. Au films capped with alumina layer (~30 nm thickness), showed significantly decreased SERS intensity and only few peaks were observed which were prominent in the SERS spectra with Au films without capping, It could be due to increased spacing between analyte molecules and Au nanoparticles. The purpose of alumina capping is to retain

the LSPR response for longer period. The grown Au films were found to be stable and did not show atmospheric tarnishing for more than six months to one year. The alumina capped Au films were found to be stable for more than four years. However, for SERS application, Au nanoparticle films without capping are better to obtain the highest SERS signal.

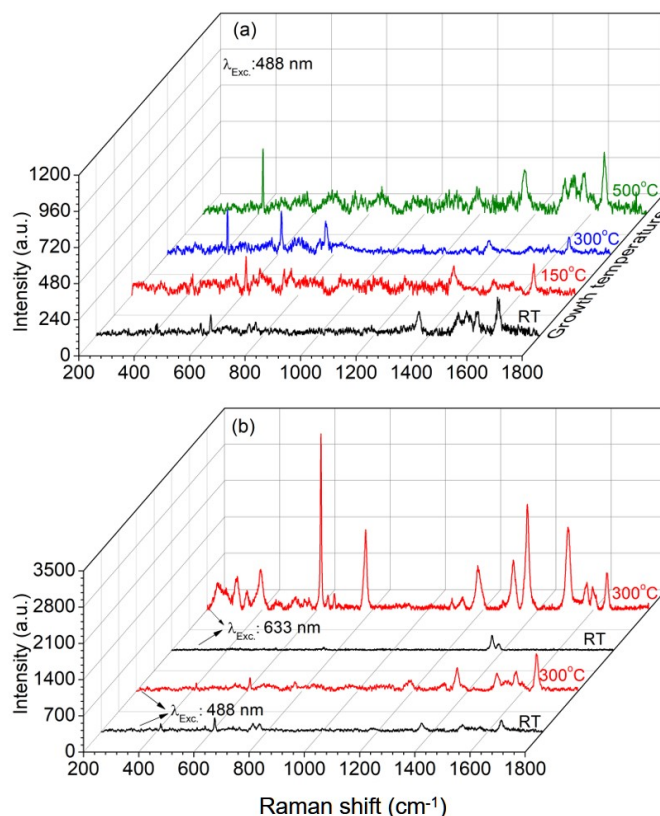


Fig. 2.23 SERS spectra of Rh6G dye in presence of Au nanoparticle films of (a) 8 nm and (b) 17 nm film thickness.

2.9 Summary

Nanoparticle films grown at high temperature showed LSPR response whereas, RT growth resulted in formation of percolated films at low thickness (< 5 nm) and continuous films at higher thickness. Variation in dielectric function and optical response of Au films of different thickness up to 38 nm, grown by PLD at RT and

300°C has been compared. Effective dielectric response of films of varied morphologies (without use of morphological parameters) has been determined from fitting of ellipsometry data using multiple Gaussian oscillators and Drude model. For RT grown Au film of thickness of about 38 nm, Drude model type free electron response well fitted the ellipsometry data and the obtained dielectric response closely matched with that of bulk Au metal. However, due to LSPR excitation in high temperature grown films up to 18 nm thickness or RT grown film up to 4 nm, free electrons have shown oscillator type response. Narrow band LSPR response was observed for the films grown at 300°C due to formation of relatively uniform nanoparticles. By controlling growth temperature, same LSPR wavelength response in different thickness films has been demonstrated. Capping with alumina layer produced stronger and red-shifted LSPR response. The high temperature grown films showed formation of closely spaced nanoparticle films, indicating its potential use as SERS substrates. SERS response was measured at two excitation wavelengths using 500 nm Rh6G as probe. For Au films of same thickness, high temperature grown films showed stronger SERS response compared to RT grown films. Au films grown at 300°C exhibiting narrow LSPR band with uniform size and shape nanoparticles resulted in maximum SERS EF. The films with LSPR wavelength close to Raman excitation wavelength, resulted maximum SERS intensity. These results show that densely packed Au nanoparticle films grown with optimized combination of growth temperature and film thickness can be efficient SERS substrates for SERS sensing application.

Chapter 3

Plasmonic response tunable Ag-Au alloy nanoparticle films for SERS at different wavelengths

Plasmon wavelength tuneable metal nanoparticle films with strong resonance near excitation wavelength are highly suitable for SERS application at multiple wavelengths. LSPR wavelength tunability can be obtained by variation of either extrinsic parameter like size and shape or intrinsic parameter i.e. dielectric response of metal [12,18]. In the film form, the extrinsic parameters also include structural arrangement of nanoparticles and their surrounding dielectric medium. For smaller nanoparticles, the dipolar mode plasmon dominates the overall extinction, whereas in large nanoparticles, higher order multi-pole excitation and scattering become important [9,12,23]. On the other hand, LSPR wavelength tuning in smaller nanoparticles is possible by intrinsic parameter (dielectric function of metal), refer Eq. 1.1. This approach becomes more promising for applications which require LSPR tuning control without compromising hot spot density eg. SERS substrates. The dielectric response of the metal can be changed by alloying of two metals of different dielectric response. In this regard, alloy nanoparticles of noble metal have emerged as promising plasmonic material [13,18,131]. As mentioned earlier, Ag and Au compared to other metals, possess strong LSPR in visible region, making them popular for most of the applications [13-16]. These two metals possess similar atomic lattice constants (Ag:4.086 Å, Au: 4.078 Å), same crystalline structure (FCC) and close atomic size (Ag:172 pm, Au:166 pm). Therefore, according to the Hume

Rothery rules of alloy formation, Ag and Au form completely miscible solid for all compositions [13, 82]. Further, since the two metals belong to same group in periodic table and have similar free electron density, same optical and LSPR response would be expected. However, the variation in the frequency dependent dielectric response arising from bound electrons [11,12] makes them appear as Ag in white and Au in yellow color and also render different LSPR excitation wavelengths. Due to this, alloy of these two metals, will result LSPR tuning between that exhibited by the individual metals. This chapter presents exploring the sequential PLD method for formation of Ag-Au alloy nanoparticle films of varied compositions and effect of different process parameters of LSPR tuning. Effect of substrate temperature, mass thickness and alloy composition on LSPR wavelength tuning and morphological characteristics is discussed. The LSPR response was explained using effective medium theory, mentioned in previous chapter considering three analytical models of alloy dielectric function. UV-Vis. transmission of alloy nanoparticle films was compared for the three models and alloy formation was confirmed. Apart from theoretical calculation of dielectric and optical response of the alloy nanoparticles, their ϵ_{eff} is also determined experimentally using spectroscopic ellipsometry. This becomes imperative because in literature, determination of dielectric response using ellipsometry has been reported for pure metallic nanoparticle films.

3.1 Dielectric function of alloys

The variation in effective dielectric response (ϵ_{eff}) with different compositions is useful in determining the overall optical response and alloy formation. The real part

of it determines LSPR wavelength and bandwidth, whereas damping in the resonance can be seen from large values of its imaginary part [12,18]. Dielectric response of the bulk alloy is required for determining ϵ_{eff} of alloy nanoparticle films. In case of pure Ag and Au, the bulk dielectric function is determined experimentally [31,115] and to predict the same, different analytical models have been also developed [114,132]. However, for Ag-Au alloy, bulk dielectric response is determined experimentally only for limited compositions [82]. In order to obtain bulk alloy dielectric response for any alloy composition, different analytical models have been proposed in literature [133-136]. The simplest model, henceforth called as Model I, is based on composition weighted linear sum of the dielectric function of the two metals [133,134]. According to this, the bulk dielectric function of alloy is,

$$\epsilon_{alloy} = (1 - x)\epsilon_{Ag} + x\epsilon_{Au} \quad \dots (3.1)$$

where, ϵ_{Ag} and ϵ_{Au} are dielectric response of bulk Ag and Au respectively. x represents percentage of Au in the alloy, and varies from 0 (Pure Ag) to 1 (Pure Au). Data of dielectric function of these individual metals was obtained experimentally by Johnson-Christy (JC) [115] and also Palik [31] separately. Analytically, frequency (ω) dependent dielectric function of Ag and Au metal with contribution from both free and bound electrons [12,137], is represented in simplest form as

$$\epsilon_{metal}(\omega) = 1 - \frac{\omega_p^2}{1 + i\tau\omega} + \epsilon_{IB}(\omega) \quad \dots (3.2)$$

where, ϵ_{IB} represents the contribution from bound electrons, τ and ω_p are relaxation time and bulk plasma frequency. The IB transition threshold of Ag and Au occur at about 3.9 and 2.4 eV respectively, due to variation in separation between

d-band and conduction sp-band [12,82,135]. For smaller spherical nanoparticles, the LSPR excitation of Au occurs at ~ 1.9 eV, i.e. close to its IB transition edge. In Ag, the LSPR excitation (at 2.9 eV), is relatively farther from IB transition edge [12]. In alloy film, the two metals when mixed at atomic level uniformly, IB transition edge is expected to be in between that of individual metals and the same has been also confirmed experimentally [138,139]. However, the above model-I would result both the IB edges for all alloy compositions, except pure metal. In order to avoid this inconsistency, Gaudry et al provided another model (Model II) [135], based on shift of IB transition edge, depending on Au percentage. According to this model, for frequency $\omega > 0$ [135],

$$\omega_{IB-alloy}(x) = (1-x)\omega_{IB-Ag} + x\omega_{IB-Au} \quad \dots (3.3a)$$

$$\text{Im}[\varepsilon_{IB-alloy}(x, \omega_{IB-alloy}(x) + \omega')] = (1-x)\text{Im}[\varepsilon_{IB-Ag}(\omega_{IB-Ag} + \omega')] + x\text{Im}[\varepsilon_{IB-Au}(\omega_{IB-Au} + \omega')] \quad \dots (3.3b)$$

Addition of imaginary part of Drude dielectric response in the above Eq. 3.3(b), provides the imaginary part of ε_{Alloy} . Further, using Kramers-Kronig relation which relates the real and imaginary part of the dielectric response, real part of ε_{Alloy} is obtained as per the procedure mentioned in ref 135. In this model, IB transition edge in dielectric response of alloy varies smoothly with percentage of Au in alloy composition. Rioux et al provided another model using critical point analysis of alloy band structure (model III) [136]. This model was found to predict variable IB absorption edge with alloy composition. However free electron response of alloys with varying composition has not been taken into account [136]. Using these three

models, the dielectric function of Ag-Au alloy is calculated and compared. Fig. 3.1(a-c) presents $Re(\epsilon_{\text{Alloy}})$ and $Imag(\epsilon_{\text{Alloy}})$ for pure Ag, Ag-Au alloy of 1:1 composition and pure Au respectively. It can be observed that the $Re(\epsilon_{\text{Alloy}})$ predicted by the three models is almost same at longer wavelength region > 500 nm, and it lies in between that of the two metals (Fig. 3.1(d)). For pure Au, model-II and III predicted $Re(\epsilon_{\text{Au}})$ showed deviation from that predicted by model-I i.e. experimental JC data. This is because the $Re(\epsilon_{\text{Au}})$ is predicted by: K-K relation in model-II, and in model-III by analytic expressions, which showed marginal variation. The $Imag(\epsilon)$ accounts for the band structure and energy gap at X symmetry point that occurs at ~ 495 nm (2.5 eV) for Au and ~ 310 nm (4 eV) for Ag [136].

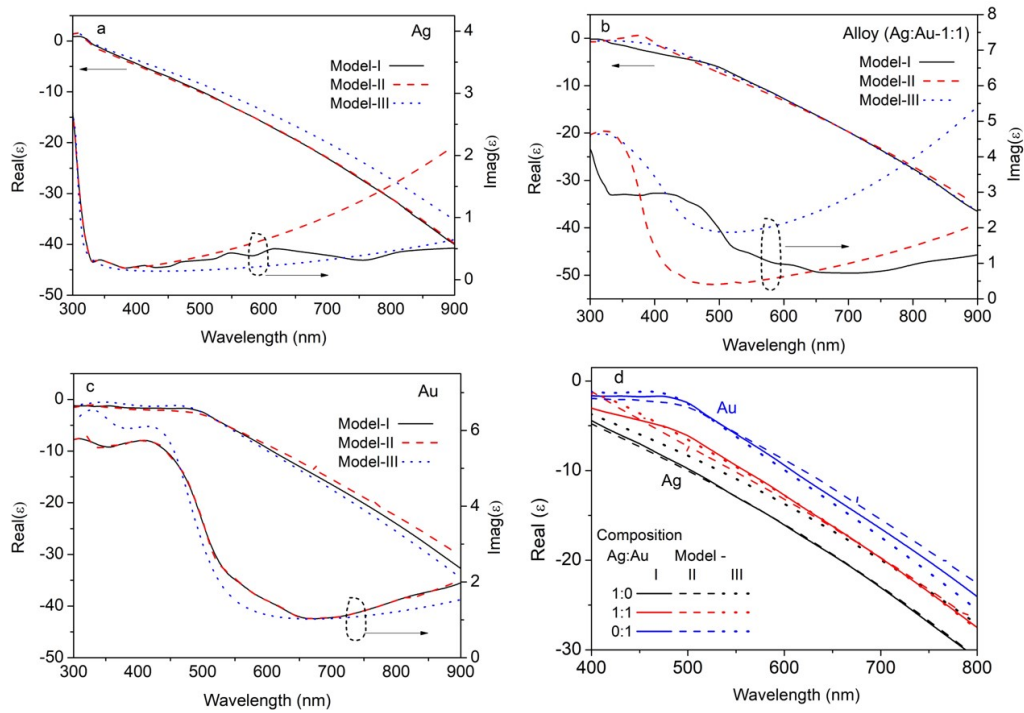


Fig. 3.1 Comparison of model-I, II and III predicted real(ϵ) and imaginary (ϵ) of (a) Ag, (b) 1:1 alloy, (c) Au and combinedly in (d).

For pure metals, all the three models showed similar variation in $Imag(\epsilon)$,

however for 1:1 alloy composition, it varied significantly among the three models. Model-I showed IB edge for both pure Au and Ag, in their alloy, which is not according to the experimental results [138,139], as mentioned above. However, model-II and model-III showed distinct IB edge different from the two metals. Also model-III has shown larger values of $Imag(\varepsilon)$ compared to that of other two models at longer wavelengths which is in line with the experimentally obtained larger absorption in alloys in comparison to pure metals [136].

3.2 Growth of Ag-Au alloy nanoparticle films of varied compositions

For growth of alloy nanoparticles of different compositions, uniform mixing of the two metals at atomic scale is crucial. In this respect, chemical route synthesis is promising to form alloy nanoparticles [133,140]. However, it forms colloidal particles along with different stabilizing agents or species [141]. Using these nanoparticles, it is difficult to produce uniform monolayer of densely packed nanoparticle films as SERS substrates. In PVD methods, deposition of layer by layer mono-metallic films, and subsequent thermal annealing, at very high temperatures is a cumbersome process and is limited in producing uniform alloy nanoparticles of varying compositions [74,75]. As shown in previous chapter, at optimum experimental conditions of PLD, fraction of monolayer film is formed in laser ablation of each pulse. Therefore, sequential laser ablation of two different metal targets alternatively, by adjusting the number of pulses in a sequence can provide a fine control of composition and uniform mixing of both the metals in the deposited nanoparticle films.

Using the sequential PLD, Ag-Au alloy nanoparticle films were deposited on

sapphire and Si substrates. Ag and Au targets were sequentially ablated using KrF excimer laser in a vacuum chamber, at base pressure of $\sim 6 \times 10^{-6}$ mbar. Details of the experimental set-up are same as mentioned in chapter 2. Composition of the films was varied by varying the ratio of ablation pulses of Ag and Au targets as 1:0, 4:1, 1:1, 1:4 and 0:1 within every 100 laser ablation pulses, to ensure mixing of the two metals in the nanoparticles. It may be noted that the ratios 1:0 and 0:1 corresponds to pure Ag and Au films respectively. Thickness of alloy films was controlled by varying the total number of ablation pulses i.e. 2000, 4000 and 6000. The film thickness was obtained from X-ray reflectivity and it was measured to be 1.18 and 1.4 nm for 1000 ablation pulses of Ag and Au respectively. Structural characteristics of these films were obtained from XRD. Fig. 3.2 shows XRD pattern of a thick Ag-Au film deposited with 1:1 ratio of ablation pulse, for total 30000 laser pulses at 300 °C substrate temperature. The figure inset shows GIXRD intensity of Ag-Au films deposited with total 6000 pulses. The peaks at 38.2° , 44.2° , 66.6° , 78.2° and 81.2° of 2θ correspond to (hkl) indices of (111), (200), (220), (311) and (222) planes of face-centred cubic (FCC) phase [142]. This shows Ag-Au alloy are also formed in similar crystalline phase as that of individual metals [142,143]. With increasing Au ablation pulses ratio, the (111) peak shifted systematically from 38.1° to 38.5° , consistent with the lattice constant of pure Ag (4.086 Å) and pure Au (4.078Å) films [142]. This shows that the average lattice constant of Ag-Au alloy films lies in between the two of pure metal films. However, due to same crystalline structure and very close lattice constants of Ag and Au, very small peak shift of 0.4° was observed, and therefore, formation of

alloy from this data alone may not be considered as fully confirmative.

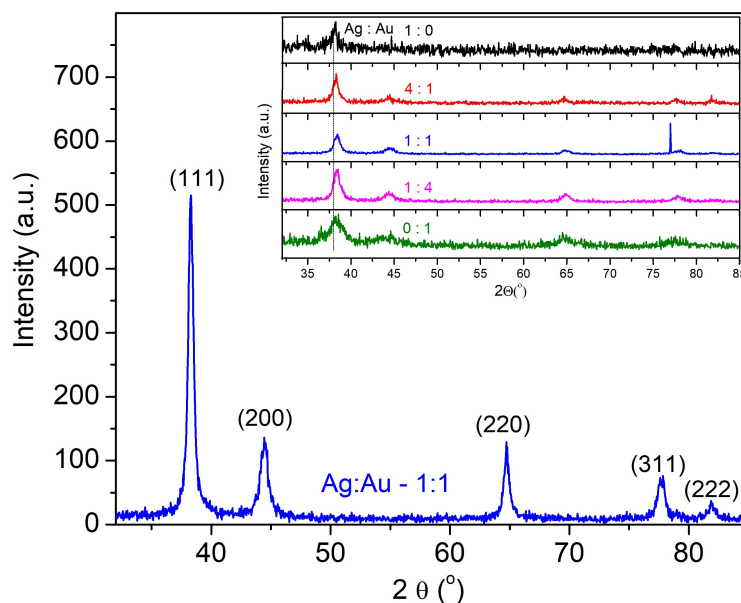


Fig. 3.2 XRD intensity of a thick Ag-Au alloy film grown with 1:1 pulses ratio of Ag and Au with total 30000 pulses; inset: GIXRD intensity pattern of alloy films of different compositions deposited with total 6000 pulses.

Therefore, further investigation using XPS has been carried out on the film grown on Si substrates. The obtained detailed scans were fitted with Gaussian-Lorentzian product functions after background correction using XPS peak-fit software. In order to remove charging effect, static charge correction was done with binding energy (BE) peak value of 284.6 eV of adventitious carbon. Fig. 3.3 (a, b) presents intensity spectra of Au-4f and Ag-3d BE peaks respectively. The figure shows that the BE peak of Ag shifted towards lower energy from 367.97 to 367.7 with increasing Au percentage in alloy films.

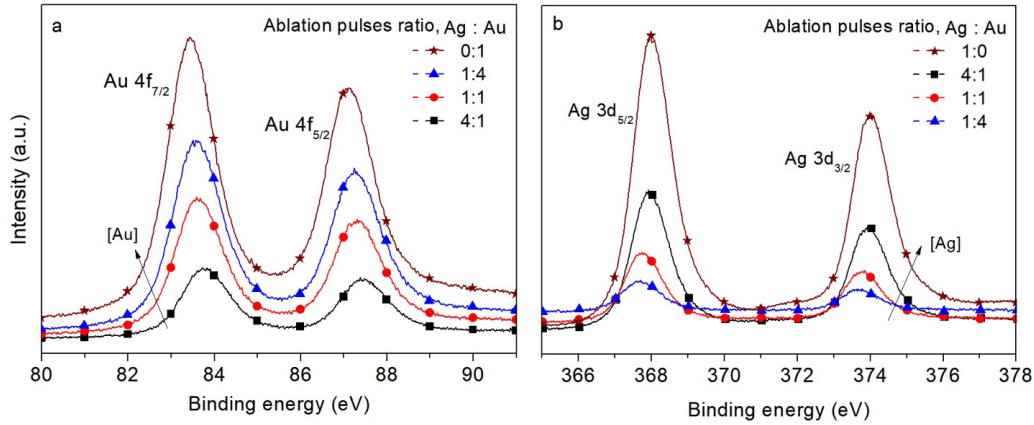


Fig.3.3 Variation of XPS BE spectra (a) Au 4f and (b) Ag 3d core level with alloy composition.

Also, the BE peak of Au shifted from 83.42 eV (Pure Au) to 83.79 eV (Ag rich), i.e. moved towards higher energy with addition of Ag in the films. Tyson et al mentioned that when metals form the alloy, both sp-conduction band and d-band participate in the alloying, involving flow of both conduction and non-conduction charge [144]. In alloying, Au gains non-d conduction charge and loses d-charge, which has been also verified experimentally by X-ray absorption near-edge structure measurements [144,145]. The observed variation in BE of Ag and Au is in consistent with that reported earlier for Ag-Au alloy prepared by other methods [142,144,145]. This confirms alloy formation in the deposited Ag-Au films by sequential laser ablation of Ag and Au separate metal targets. The composition of alloy films was estimated from integrated areas of the BE peaks as per the following relation [146]

$$\frac{Ag[\%]}{Au[\%]} = \frac{I_{Ag} / ASF_{Ag}}{I_{Au} / ASF_{Au}}, \quad \dots (3.4)$$

where, $I_{Ag/Au}$ and $ASF_{Ag/Au}$ are the integrated areas and atomic sensitivity factor respectively of Ag-3d_{5/2} (Au-4f_{7/2}) BE peak [146]. The obtained composition of

Ag-Au films is tabulated in table 3.1. The obtained composition of alloy is found to be slightly lesser than ratio of laser pulses used for deposition.

Table 3.1. Mass thickness and C corrected Binding energy (BE) peak positions of Ag-3d_{5/2} and Au-4f_{7/2} of Ag-Au films.

S No	Ratio of laser pulses (Ag:Au)	Film thickness from XRR	BE peak Ag-3d _{5/2}	BE peak of Au-4f _{7/2}	Film composition from XPS (Ag:Au)	Film composition from EDS (Ag:Au)
i.	1:0	4.8 nm	367.97 eV	-	-	-
ii.	4:1	5 nm	367.96 eV	83.79 eV	73: 27	-
iii.	1:1	5.1 nm	367.8 eV	83.61 eV	43 : 57	43.4 : 56.6
iv.	1:4	5.3 nm	367.7 eV	83.56 eV	17 : 83	-
v.	0:1	5.5 nm	-	83.42 eV	-	-

This is due to difference in ablation yield of Ag and Au metals, which depends on their optical and thermal properties [78]. The Ag:Au composition was also confirmed with EDX measurements for the film grown with 1:1 ratio of laser pulses and Fig. 3.4 shows its EDX spectrum. The obtained composition this film is 43.4:56.6, which is close to that obtained from the XPS measurements, showing relatively higher percentage of Au than Ag. The obtained composition is also in consistent with the observation of film thickness showing higher deposition of Au (1.4 nm) than Ag (1.18 nm) for same number (1000) of ablation pulses.

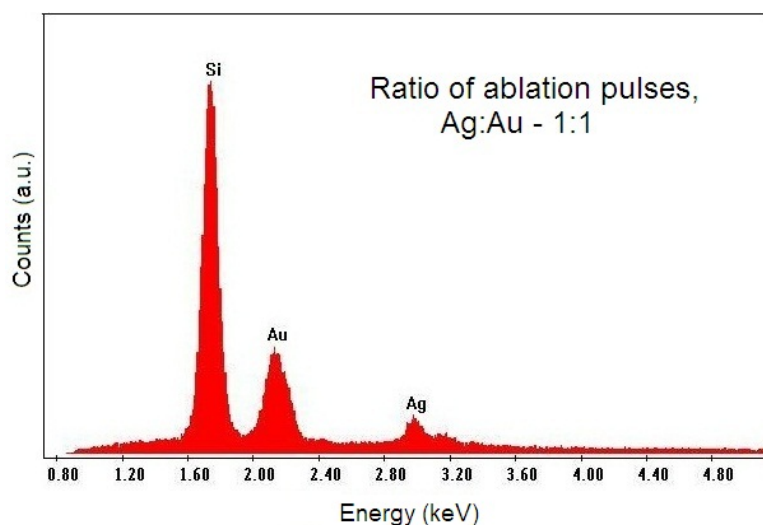


Fig. 3.4 EDS spectrum of Ag-Au alloy film.

In this sequential laser ablation process, thickness of each individual metal deposited before ablation of the other target is $\sim < 0.1$ nm, much lesser than thickness (~ 0.5 nm) of monolayer. Further, at 300°C , the diffusion distances of Ag and Au on oxide substrates for 0.1 s (time between two successive ablation pulses) are about 350 and 190 nm respectively, obtained from Eq. 2.24. This distance is sufficiently longer for capturing of adatoms by the nearest nanoparticles, resulting atomic level mixing of metals, and formation of alloy nanoparticles.

3.3 Optical response and LSPR characteristics of Ag-Au alloy nanoparticle films

The LSPR characteristics of the grown Ag-Au alloy films of varied thicknesses at 300°C substrate temperature was characterized from transmission spectra. Fig. 3.5 (a-c) presents UV-Vis. transmission of films produced with total 2000, 4000 and 6000 ablation pulses respectively. All these spectra show LSPR excitation, that showed consistent red-shift of LSPR wavelength with increasing Au percentage in alloy. For a fixed composition, the LSPR band also showed red-shift with film

thickness (varied from total ablation pulses). With alloy composition, the LSPR tuning was found to be in the range of about 450-640 nm, 470-690 nm and 490-780 nm for the films grown with 2000, 4000 and 6000 pulses respectively. Further, in each spectrum there is only one LSPR band which consistently red-shifted with composition in all the three cases, indicating formation of alloy nanoparticles otherwise two separate bands corresponding to Ag and Au would have been obtained [142,147,148].

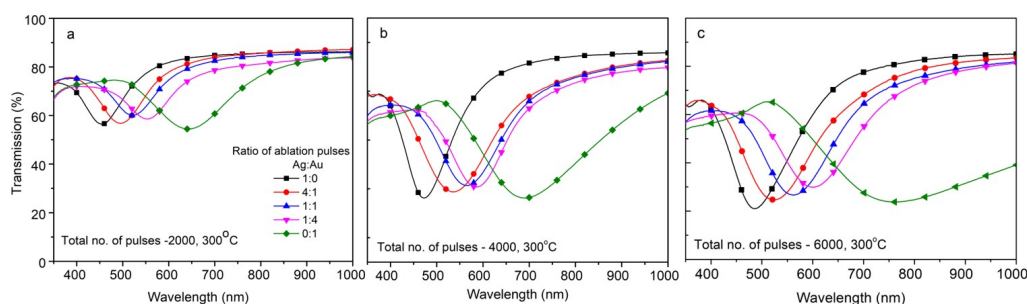


Fig. 3.5 Transmission of Ag-Au alloy films deposited with total (a) 2000 (b) 4000 and (c) 6000 pulses and varied ratio of laser pulses of Ag and Au.

Variation of LSPR wavelength with Au percentage is not exactly linear. Almost linear variation of LSPR wavelength with Au percentage in Ag-Au alloy can be observed for monodisperse spherical nanoparticles, grown by chemical reduction method [133,147]. In present case of Ag-Au alloy nanoparticle films, the LSPR response is determined by not only composition, but also significantly affected by the presence of substrate, aspect ratio and volume filling fraction, as mentioned in chapter 2. For pure Ag and Au films, the IB absorption edge (below which transmission decreases at shorter wavelengths) was observed at ~ 350 and 520 nm respectively. In case of Ag-Au films, consistent red-shift of IB edge was observed with Au percentage.

In these films single IB absorption edge, instead of two corresponding to each metal, confirms the grown nanoparticles are in alloy form. The LSPR excitation (resulting dip in transmission spectra) consists of absorption (proportional to volume, V) and scattering (proportional to V^2) (refer eq. 1.5 and 1.6). For each composition at higher number of pulses, the films have shown decreased transmission, which is due to increased extinction by the formed large size nanoparticles. For alloy films, the LSPR strength (ΔT ; Fig. 2.4) is relatively lesser in comparison to pure metal films. This is due to relatively higher damping of alloys compared to monometallic films [136]. Further the LSPR bandwidth of pure Au films, was found to be higher than that of pure Ag films. The LSPR bandwidth is influenced by both intrinsic and extrinsic factors (size and shape). For 30 nm size of Ag and Au nanoparticle, LSPR bandwidth calculated from Mie theory is about 15 and 55 nm respectively. The observed difference is attributed to the intrinsic variation in dielectric function of Ag and Au. For Au, broader $\text{Re}(\epsilon_{Au})$ and large value of $\text{Imag}(\epsilon_{Au})$ near LSPR wavelength result large LSPR bandwidth [12]. Apart from this, in case of Au films, large distribution in size and shape of nanoparticles, which was confirmed through AFM, also contributed to the observed inhomogeneous broadening.

Fig. 3.6 presents AFM images of Ag-Au alloy nanoparticles deposited with 2000 pulses at 300°C growth temperature for different ratio of ablation pulses of the metals. All the films showed closely spaced nanoparticles of average size of about 26, 19, 17.5, 21 and 25 nm for 1:0, 4:1, 1:1, 1:4 and 0:1 ratio of Ag:Au laser pulses respectively. Fig. 3.7 presents the AFM images along with line profile scan of the

films grown with total 4000 pulses at 300°C with different ratio of Ag:Au laser pulses. Compared to previous case (Fig. 3.6), the average particle size increased for all the compositions and is about 30, 25, 23, 25 and 31 nm for 1:0, 4:1, 1:1, 1:4 and 0:1 ratio of Ag:Au laser pulses respectively. Increase of particle's average size with increasing total number of laser pulses, is attributed to growth and coalescence of early formed nanoparticles. Ag films deposited with 2000 laser pulses showed lesser particle number density compared to that of Au film. However, with increasing number of pulses to 4000, the number density of Au films is found to be lesser than Ag. Lower nucleation density of Ag film grown with lesser number of pulses is due to higher diffusion coefficient of Ag ($1.1 \times 10^{-8} \text{ cm}^2/\text{s}$) compared to Au ($3.6 \times 10^{-9} \text{ cm}^2/\text{s}$) which also resulted in larger nanoparticles [108]. Though, as the films grow, by increasing total ablation pulses, the earlier formed nanoparticles start to coalesce, resulting large size nanoparticles with decreased number density [149], as observed for Au film grown with 4000 ablation pulses, tabulated in table 3.2. In case of Ag films, larger average size and low particle density can be due to its higher diffusion coefficient, whereas in case of Au films this could be because of higher coalescence. Further in both the cases, the average particle size was found to be lesser in alloy films than that compared to monometallic films. Correspondingly the particle number density of alloy films was higher than that of monometallic films.

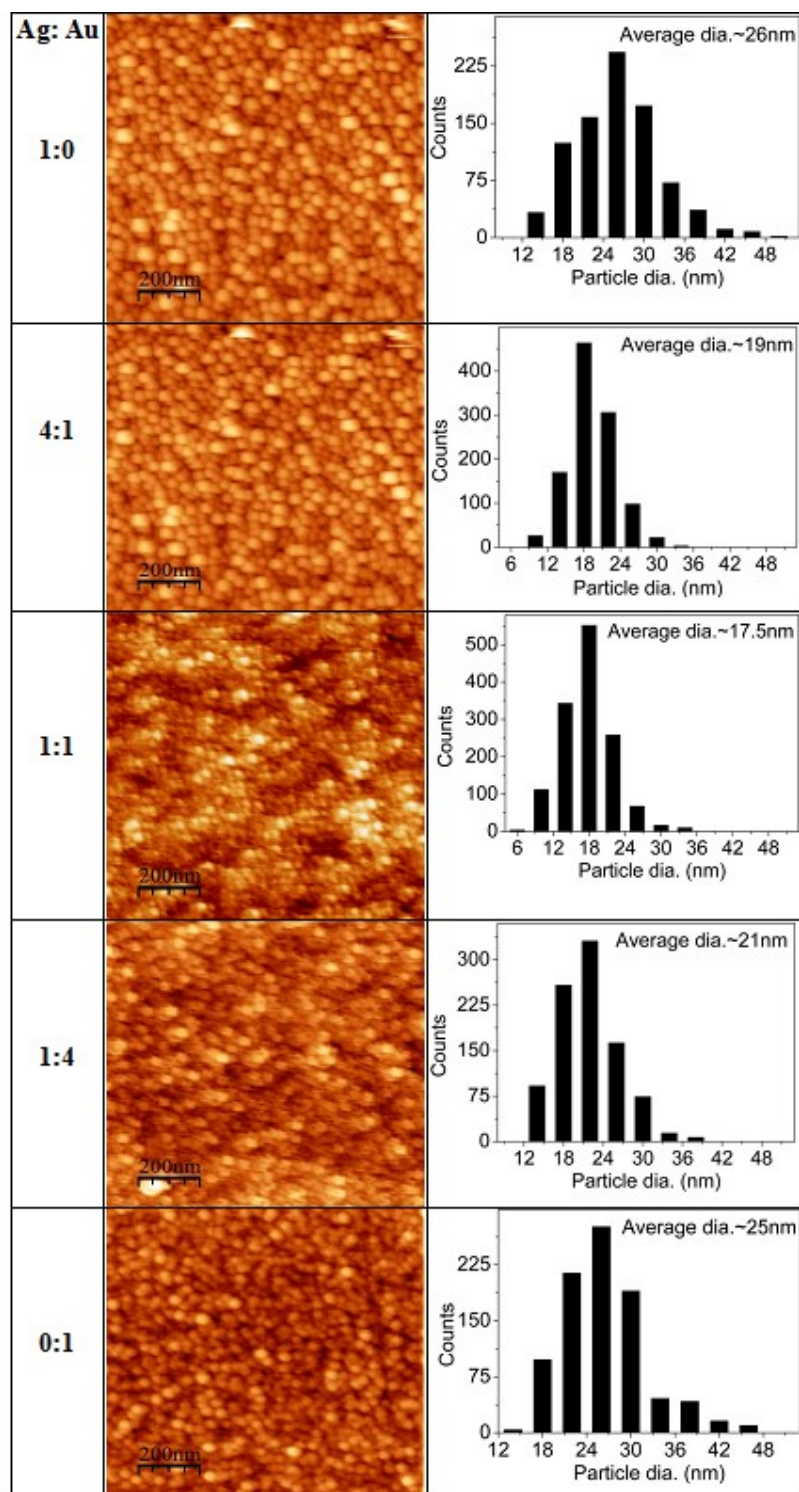


Fig.3.6 AFM images along with distributions of diameter of Ag-Au nanoparticles grown with total 2000 pulses at 300 °C temperature.

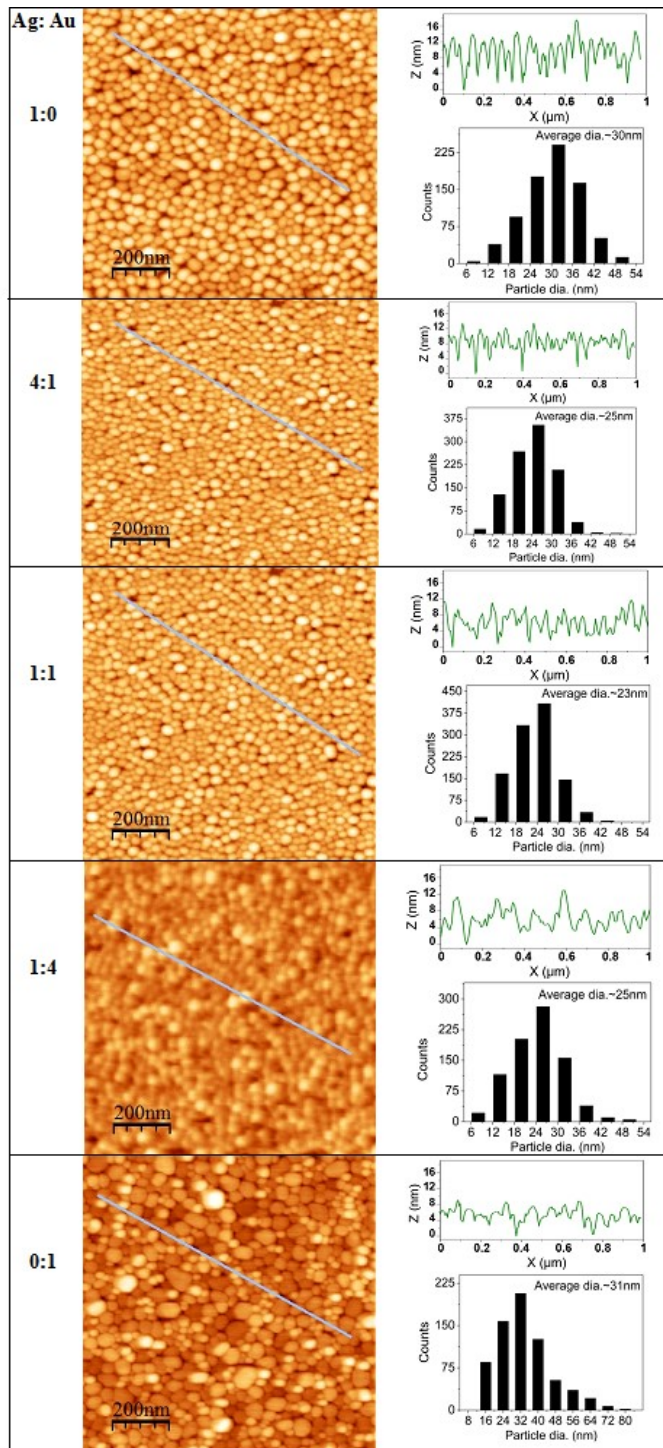


Fig.3.7 AFM images along with line scan and distribution of diameter of Ag-Au nanoparticles grown with total 4000 pulses at 300 °C temperature.

The height profile analysis as presented in Fig. 3.7 showed average particle height of

about 12 nm and 8 nm for Ag and Au films respectively. This shows larger aspect ratio of about 3.8 for the formed Au nanoparticles compared to 2.8 for Ag nanoparticles. Also, Au films showed particle size distribution. Large aspect ratio Au nanoparticles with broad size distribution was also reported for Ag, Au and alloy nanoparticles formed with gas-phase deposition method [150]. This was attributed to larger Au-oxide interaction and lower mobility of Au ad-atoms compared to Ag. These morphological observations reveal that the extrinsic parameter (broad particle size distribution and high aspect ratio) also contributes to the observed large inhomogeneous broadening at longer wavelengths in the transmission spectrum of Au films grown with 4000 pulses.

Table 3.2 Average diameter (nm) and number density (cm⁻²) of nanoparticles in Ag-Au films deposited with different ratio of Ag and Au ablation pulses.

Ratio of laser pulses (Ag:Au)		1:0	4:1	1:1	1:4	0:1
Total pulses: 2000 @ 300°C	Avg. dia. (nm)	26	19	17.5	21	25
	Particle density	8.8x10 ¹⁰	1.1x10 ¹¹	1.4x10 ¹¹	9.7x10 ¹⁰	9.4x10 ¹⁰
Total pulses: 4000 @ 300°C	Avg. dia. (nm)	30	25	23	25	31
	Particle density	8.1x10 ¹⁰	9.6x10 ¹⁰	1x10 ¹¹	8.5x10 ¹⁰	6.9x10 ¹⁰
Total pulses: 4000 @ RT	Avg. dia. (nm)	24	22	23	24	19

In order to observe the effect of substrate temperature on LSPR tunability of Ag-Au films, these films were also deposited at RT. Fig. 3.8 (a,b) show UV-Vis. transmission of Ag-Au films deposited at RT with varied ratio of laser pulses of Ag

and Au for total 2000 and 4000 pulses respectively. LSPR response was observed for Ag and Ag rich films only, whereas Au and Au rich films showed almost constant transmittance at longer wavelength, i.e. characteristic of percolated or continuous films. Further, the LSPR response of Ag and Ag rich films was found to be red-shifted from that of the films grown at 300°C substrate temperature. In order to understand these observations, morphology of these films was characterized using AFM. Fig. 3.9 presents the AFM images of RT films deposited with total 4000 laser pulses along with corresponding line scan and particle size distribution.

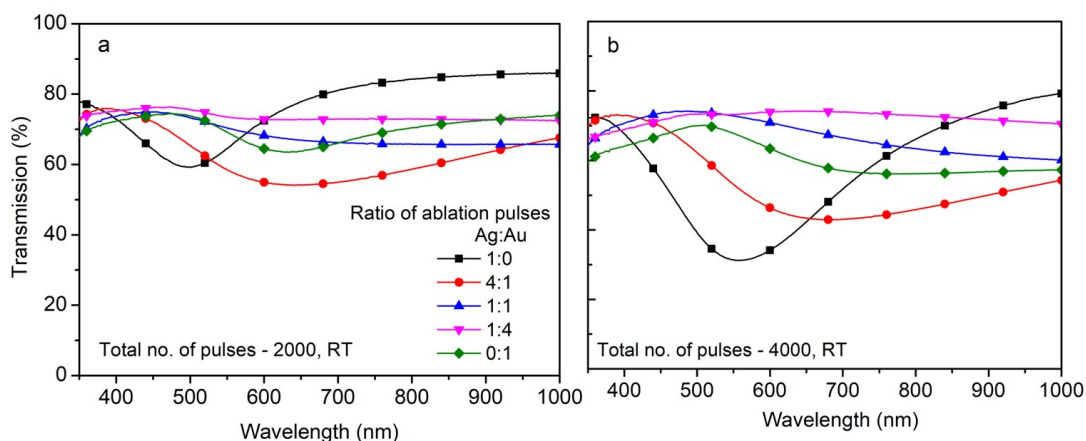


Fig. 3.8 UV-Vis. transmission spectra of Ag-Au alloy films deposited at RT for (a) 2000 and (b) 4000 total pulses.

Ag and Ag-rich films showed formation of nanoparticles of average height of ~6 nm, whereas other films morphology reveals the particles did not exhibit distinct boundary and had lesser height of about 2-3 nm. This is due to almost 10 times lower diffusion coefficient of Au adatoms compared to that of Ag, which led to higher nucleation density, at initial stage, and further deposition turned Au films growth into almost continuous form.

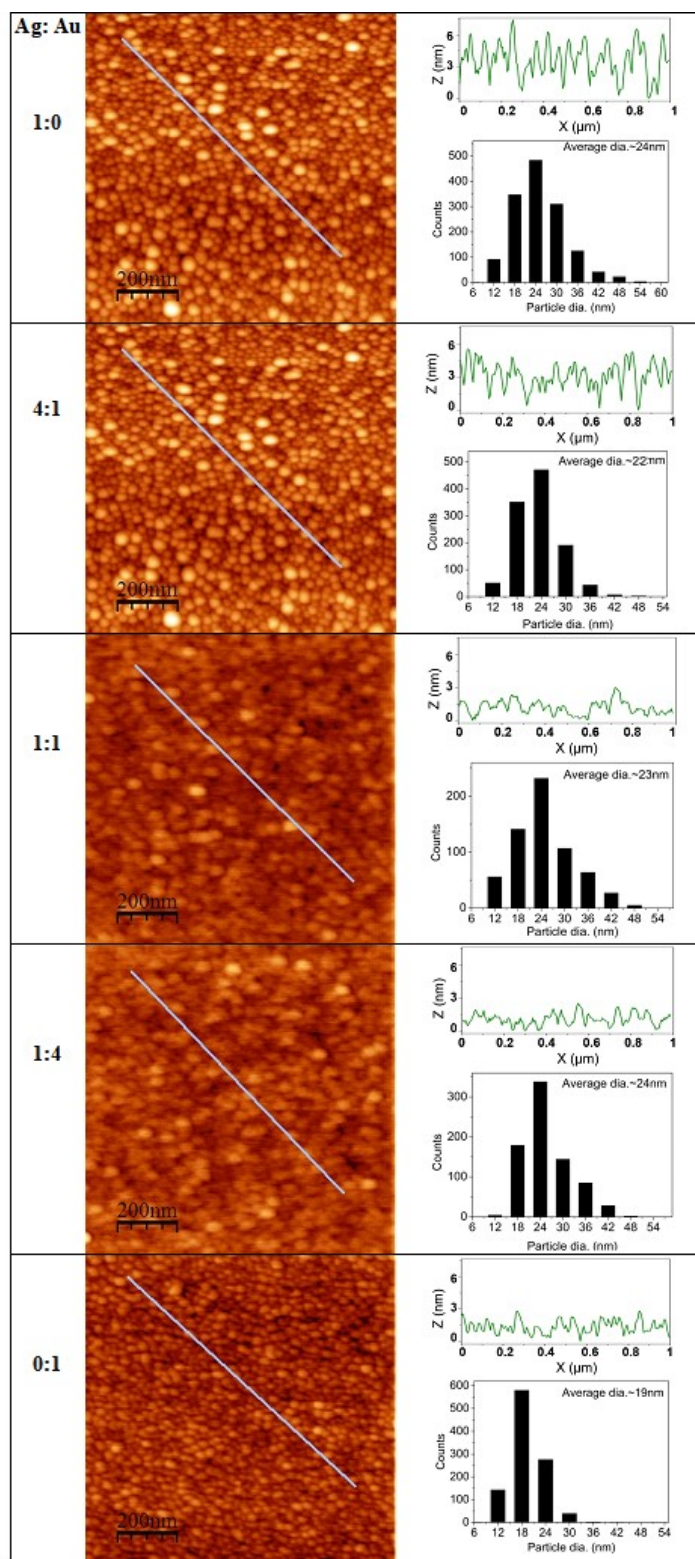


Fig.3.9 AFM images along with line scan and distributions of diameter of Ag-Au nanoparticles grown with total 4000 pulses at RT.

It is also consistent with observation of no LSPR response in Au and Au rich films. Though the average diameter of particles in Ag and Ag rich films deposited at RT is smaller than those grown at 300°C, the red-shift of LSPR band can be due to increased volume filling fraction (revealed from average height).

3.4 Analytical calculation of LSPR response of Ag-Au alloy nanoparticle films

Ag-Au alloy dielectric response predicted by the three models was used for calculating ϵ_{eff} of alloy nanoparticle films (Eq. 2.1) which was further used for calculating the transmission (Eq. 2.6) of these films. In these calculations, the ϵ_{eff} of alloy nanoparticle films which is function of i) metal volume filling fraction (q), and ii) dielectric function of metal. For nanoparticle films, the q value is related to average particle height ' h ' and mass thickness ' t_m ', as $q = t_m \cdot h$. The values of t_m and h were determined from XRR and AFM height profile analysis respectively. Fig. 3.10 presents the calculated UV-Vis. transmission of Ag-Au nanoparticles films deposited at 300°C for total 4000 laser pulses of different compositions shown in table 3.2. The q values are found to be in range of 0.45 – 0.6, which is consistent with that obtained for closely spaced nanoparticle films [111], and also confirmed by AFM analysis. From the figure, it can be observed that all the three dielectric function models have predicted LSPR wavelength tuning with film composition. For alloy films, the observed variation in LSPR wavelength is less than 10 nm as predicted by the three models. The predicted LSPR in range 460-600 is close to that observed experimentally, as shown in Fig. 3.10(d). Though all these models showed similar variation in LSPR response with alloy composition but, transmission spectra below

500 nm i.e. near IB edge, the variation is different. Particularly in model-I, all the alloy films showed IB edge at about 500 nm close to Au films, which do not match with the experimentally observed transition spectra (refer Fig. 3.5(b)). However, the spectra predicted by model-II and model-III, shows continuous red-shift of IB edge from Ag towards Au with increasing Au percentage, as observed experimentally. This occurs to alloy nanoparticles in which the IB edge is in between that of two metals. This further confirms alloy nanoparticles formation in the grown films.

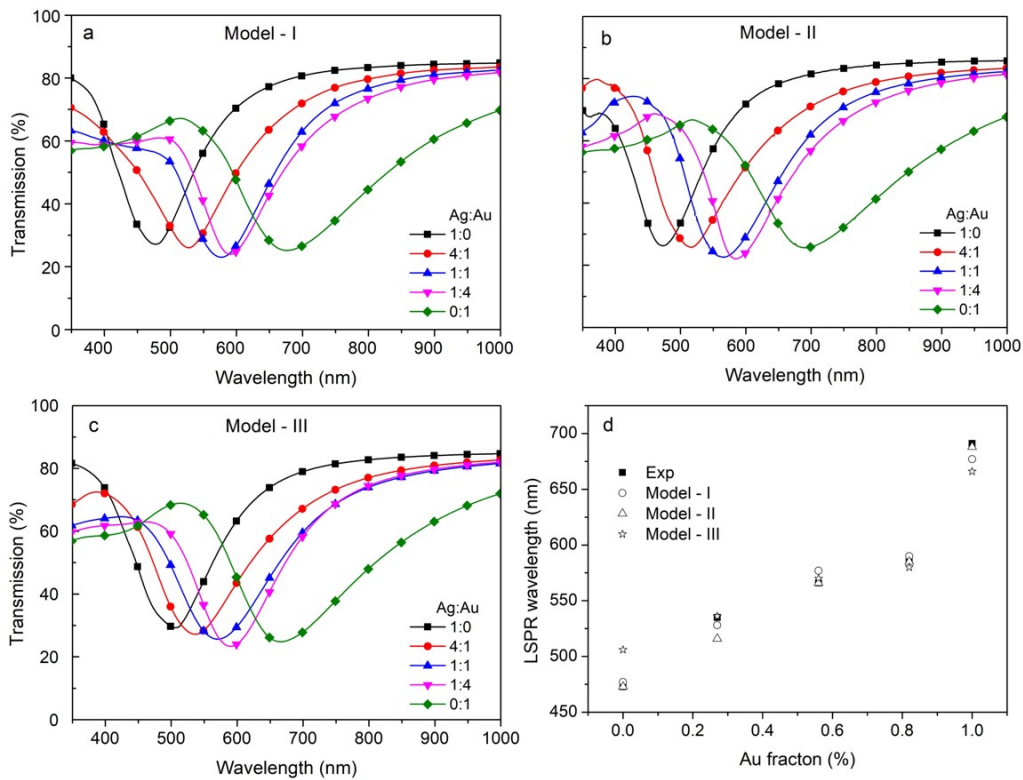


Fig. 3.10 Calculated transmission of Ag-Au alloy films of varied compositions deposited with total 4000 ablation pulses at 300°C, using (a-c) three analytical models and (d) comparison of experimentally observed LSPR wavelength with that obtained from analytical models.

Further, it can be noticed that, for monometallic films, model-III predicted ~30

nm red-shift of LSPR wavelength for Ag and ~15 nm blue-shift in LSPR wavelength of Au films. As mentioned earlier, in model-I and II the dielectric response of Ag and Au have been taken from the experimental data provided by JC and Palik [31,115], whereas in model-III, analytical model predicted data was used. Therefore, the observed LSPR resonance wavelength shift for mono-metallic films for model-III can be attributed to deviation of its dielectric response from experimental JC data at longer wavelengths, as shown in Fig.3.1. However, for alloy nanoparticle films, the transmission spectra predicted by model-III is close to those observed experimentally.

These results reveal that, to predict the LSPR wavelength variation with composition of alloy nanoparticle films, any one of the models can be used. However, model-II and III are accurate in predicting the optical response of alloy nanoparticle films. Further, the range of LSPR wavelength that can be tuned with alloy composition, was calculated, which is shown in Fig. 3.11. For this calculation, aspect ratio of nanoparticles is fixed to be three and model-II has been considered, as it predicts LSPR wavelength for both monometallic and alloy nanoparticle films and is more comprehensible than model-III involving only one parameter i.e. percentage of Au in the films. From the figure, it can be observed that for fixed value of q , as the Au percentage increased from 0 to 100%, the LSPR wavelength red-shifted. Also, for densely packed nanoparticle films, with typical q value of 0.65, the LSPR wavelength varied in the range of 480-650 nm.

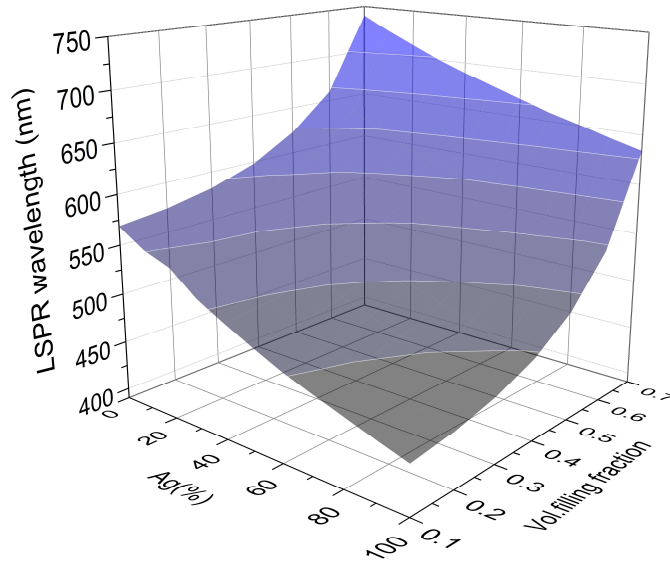


Fig.3.11 LSPR wavelength of Ag-Au films versus volume filling fraction and percentage of Ag in the films.

3.5 Experimental determination of dielectric response of alloy nanoparticle films using spectroscopic ellipsometry

From Fig. 3.2, it can be observed that the dielectric function of bulk Ag-Au alloy predicted by analytical models have certain variations. Further to determine ϵ_{eff} of Ag-Au alloy films with respect to composition and film thickness, Eq. 3.2 requires morphological parameters. For very low mass thickness films, AFM or SEM imaging has limitations in determining the size and shape of nanoparticles. Therefore, in order to experimentally determine the dielectric response, spectroscopic ellipsometry measurements were carried out. For this, two set of Ag-Au nanoparticle films were prepared on glass substrates with varied ratio of laser pulses as 2:1 (50:25) and 1:2 (25:50) within every 75 pulses in sequential PLD process at 400°C substrate temperature. The total number of ablation pulses was 1000, 2000, 4000 to 8000 for deposition of different thickness films. Under these growth conditions, pure Ag and

Au films were also grown for total 20000 laser pulses at RT, and from X-ray reflectivity, the film thickness was found to be ~ 0.75 and 0.8 nm respectively for deposition of 1000 ablation pulses. Fig.3.12 presents the variation of LSPR wavelength and strength (ΔT) of these Ag-Au films grown with different total number of pulses. The obtained results are similar to the previous set of samples (section 3.2), which further confirms the applicability of sequential PLD for deposition of Ag-Au films on different substrates exhibiting tunable LSPR wavelength with ratio of ablation pulses.

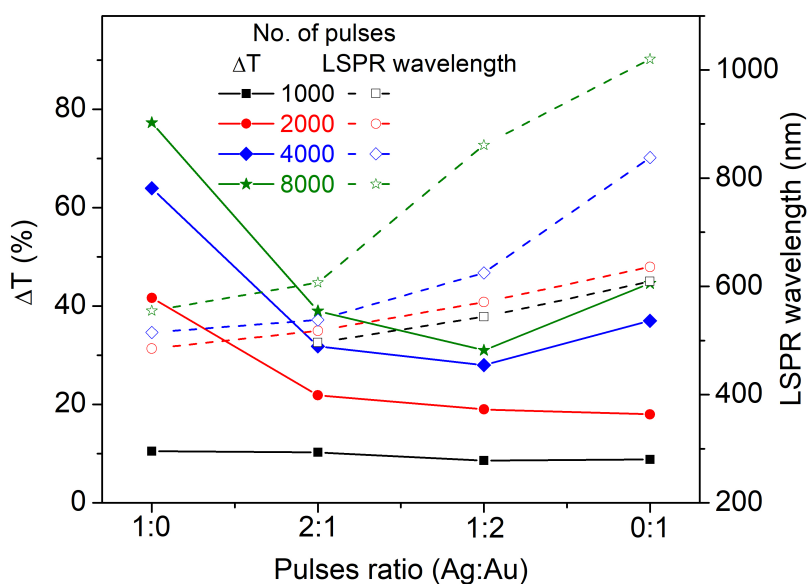


Fig.3.12 Variation of LSPR strength (ΔT) and wavelength with Ag:Au laser pulses ratio.

For ellipsometry measurements, the films were deposited on glass substrates whose back-side is roughened to avoid back-side reflections. Ellipsometry measurements were performed at four different angle of incidence (AOI). Fig. 3.13 presents the both measured (symbols) and model fitted (lines) ellipsometry data with MSE less than 5. For fitting, the procedure based on gaussian oscillators was applied,

as mentioned in section 2.3. Fig. 3.14 (a and b) show $\text{real}(\varepsilon)$ and $\text{imag}(\varepsilon)$, extracted from fitting of ellipsometry data of Ag-Au alloy films deposited with different ratio of laser pulses of Ag and Au respectively. For all the compositions, the Real $\varepsilon(\omega)$ showed positive values unlike the bulk films which show negative values at longer wavelengths, refer Fig. 3.1.

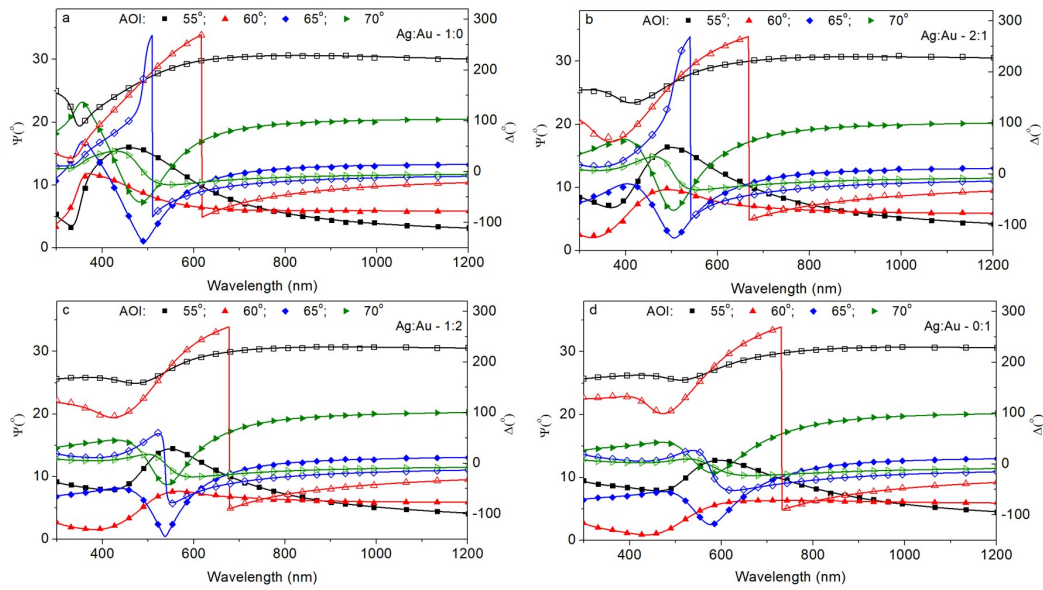


Fig. 3.13 Experimentally observed (symbols) ellipsometry parameters (Ψ : solid, Δ : open) at four AOI along with model fitted data (lines) obtained for Ag-Au alloy nanoparticle films deposited with total 2000 laser pulses.

The variation of *Real* $\varepsilon(\omega)$, and *Imag* $\varepsilon(\omega)$ with wavelength, shows characteristics response of bound electron along with resonant absorption characteristics. This arises from spatial confinement of free electrons resonance oscillations (plasmon resonance excitation) in the films. It can be observed that the peak in *Imag* $\varepsilon(\omega)$ shows red-shift with increasing Au percentage in the films. This is in line with the observed red-shift of LSPR wavelength, as shown in Fig. 3.12. Also, the magnitude of *Imag* $\varepsilon(\omega)$ is

found to increase with Au percentage at shorter wavelengths, which can be attributed to higher absorption losses of Au as compared to Ag.

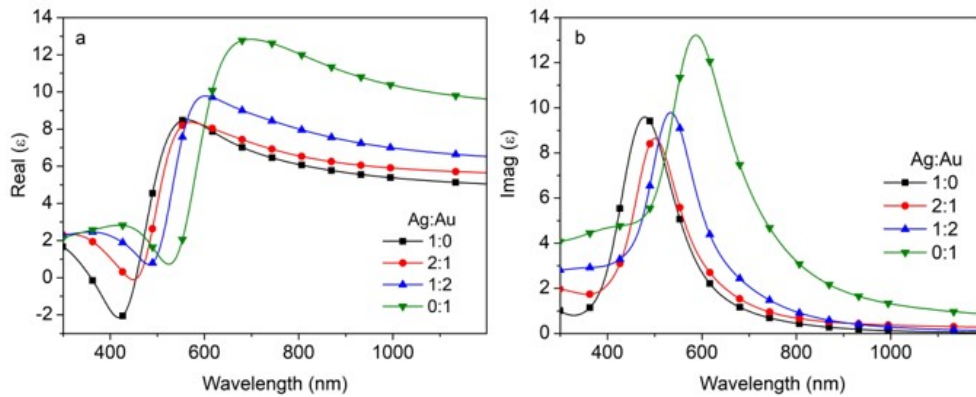


Fig. 3.14 Variation of (a) real ϵ_{eff} and (b) imag ϵ_{eff} of Ag-Au alloy films deposited with total 2000 laser pulses for varied ratio of Ag and Au laser pulses.

Using this experimentally determined ϵ_{eff} , the transmission spectra was calculated for these alloy films. Fig. 3.15 compares the calculated and experimentally observed transmission of Ag-Au films deposited with varied ratio of Ag and Au pulses.

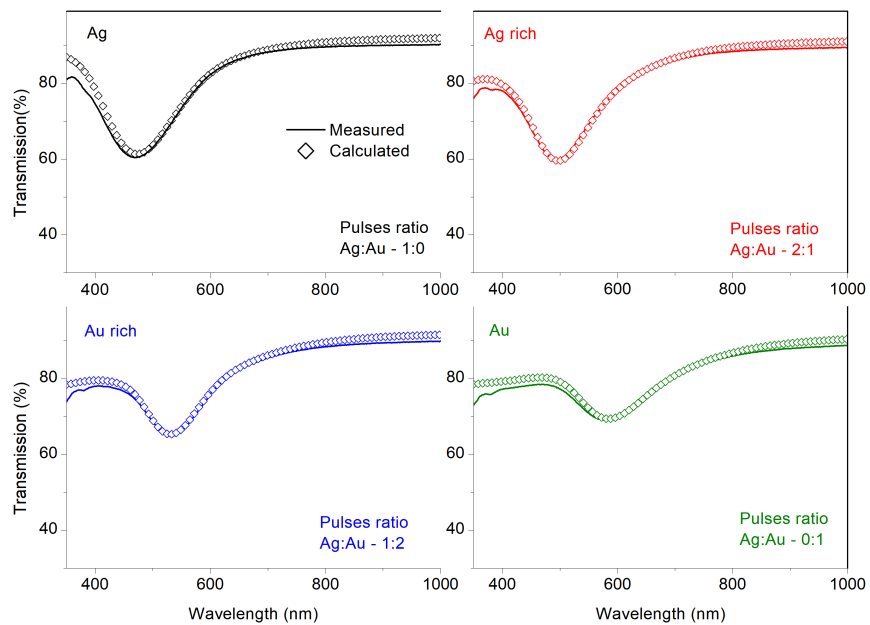


Fig. 3.15 Comparison of calculated (open symbol) and experimental (solid line) transmission of Ag-Au alloy films deposited with total 2000 laser pulses.

For all the compositions, the calculated transmission spectra match well with the experimental data, ensuring the obtained dielectric response of alloy films is accurate. Following the same procedure, the dielectric response of different mass thickness films is calculated from spectroscopy ellipsometry data. Fig. 3.16 shows the variation of $\text{Imag } \epsilon(\omega)$ of Ag and Ag rich alloy films grown with varied total ablation pulses. Peak in $\text{Imag } \epsilon(\omega)$ is increased, broadened and red-shifted with total number of ablation pulses. This is consistent with the earlier observations of red-shift and broadening of LSPR band attributed to larger size of nanoparticles with increasing film thickness. For both the compositions of the films, the peak edge position remained almost same, showing same IB edge for the fixed composition of the films.

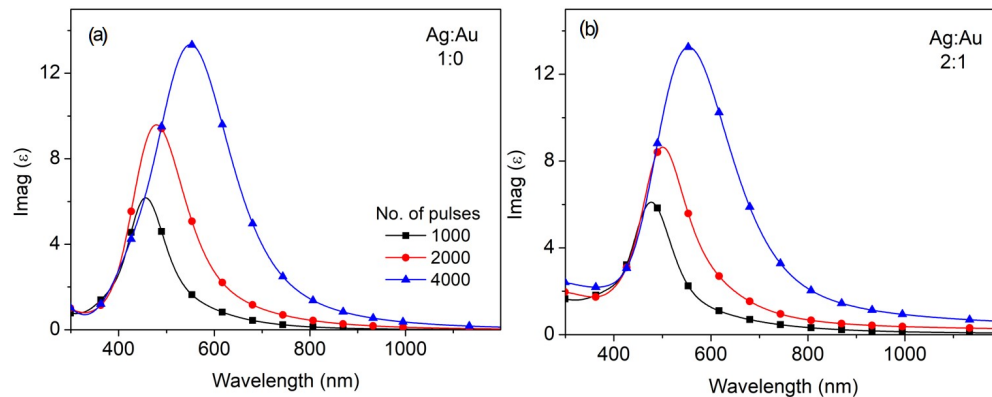


Fig. 3.16 $\text{Imag } (\epsilon_{eff})$ of Ag-Au films deposited with total 2000 pulses and (a) 1:0 and (b) 2:1 ratio of Ag and Au laser pulses.

3.6 SERS response of Ag-Au nanoparticle films

The above results, reveal that LSPR wavelength tunable densely packed nanoparticles films of different Ag-Au alloy compositions can be fabricated using sequential PLD. A typical AFM image is presented in Fig. 3.17, showing formation of closely spaced nanoparticles exhibiting hot spots as required for SERS substrates. In

previous chapter LSPR tuning was shown with film thickness, where nanoparticles size and density varied significantly.

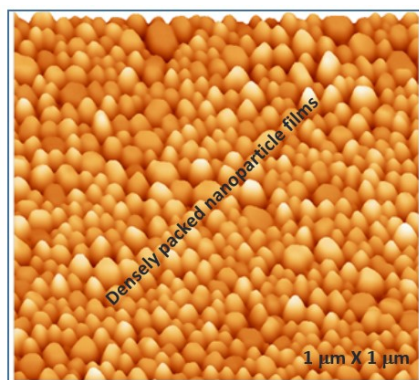


Fig. 3.17 Typical AFM image of closely spaced noble metal nanoparticle film grown by PLD.

In this case, the obtained LSPR tuning is achieved with alloy composition, without much change of the number density and size. The SERS intensity is influenced by morphological parameters i.e. size of nanoparticles, number of hot spots and intrinsic dielectric response of the nanoparticles at Raman excitation wavelength [60,61,130]. The SERS spectra was measured with Horiba Raman spectrometer at two different excitation wavelengths of 488 nm (Ar ion laser) and 633 nm (He-Ne laser) using Rh6G dye as probe, in presence of Ag-Au films of different thicknesses deposited with 1000, 2000, 4000 and 8000 ablation pulses and with different ratio of Ag:Au ablation pulses. The grown nanoparticle films were incubated in 500 nM aqueous solution of Rh6G dye. After 10 min., these films were drawn out of the solution and dried in air. SERS signal was collected from four locations of each sample, for 10 s integration time, and average of these measurements is considered before background correction [128]. Fig. 3.18 presents the SERS intensity of Rh6G dye obtained with

488 nm excitation wavelength, in presence of Ag-Au alloy films deposited with different number of ablation pulses. The films grown with 1000 pulses, forming very small size nanoparticles and weak LSPR response, did not show significant SERS peaks. The film produced with 2000 to 8000 pulses have shown SERS signal with different peaks at about 611, 774, 1187, 1311, 1364, 1506, 1576, and 1651 cm^{-1} , corresponding to different vibrational modes of Rh6G molecule [60,130,130]. For same measurement conditions, intensity of the SERS peaks was found to be higher in case of Ag and Ag rich alloy films as compared to that obtained with Au and Au rich films. For example, for the films deposited with total 2000 pulses the SERS EF (using Eq. 2.25) of the characteristic 1364 cm^{-1} peak, was found to be about 6.2×10^5 , 1.3×10^6 and 2.2×10^5 for Ag, Ag rich alloy and Au rich alloy films respectively. The films deposited with 4000 pulses showed SERS EF of about 1.6×10^6 , 4.9×10^5 and 1.2×10^5 for Ag, Ag rich and Au rich films respectively. The highest EF was obtained for Ag rich film produced with 2000 pulses and pure Ag film deposited with 4000 pulses. Further increasing film thickness, i.e. the film deposited with 8000 pulses, only Ag film showed SERS peaks, with lesser intensity, about 18 times lower than that observed with Ag films grown with 4000 pulses. These results show that both mass thickness and alloy composition strongly influence the SERS response. Local field enhancement at hot spot (region in between nanoparticles) is the highest when the laser wavelength used for Raman measurement is close to LSPR wavelength [12,60].

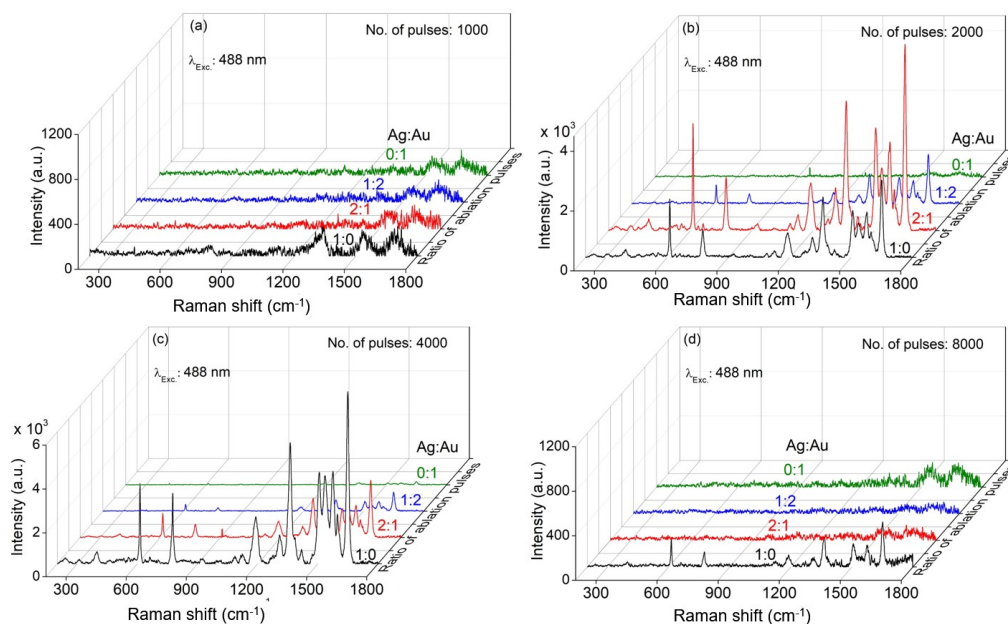


Fig. 3.18 SERS intensity of Rh6G Dye molecules obtained with 488 nm excitation wavelength, in presence of Ag-Au alloy films deposited with varied total number of laser pulses.

In the grown Ag-Au alloy films, the LSPR wavelength is red-shifted by increasing film thickness from total ablation pulses and Au percentage in the films. For lower film thickness (grown with 2000 pulses) Ag rich alloy film and at higher thickness (with 4000 pulses) pure Ag film exhibited LSPR excitation, close to Raman measurement excitation wavelength, resulting the highest SERS EF. When film thickness is increased further, the LSPR wavelength for all the compositions red-shifted considerably compared to the wavelength used for Raman measurement. Therefore, SERS intensity reduced significantly for thick films.

Fig. 3.19 (a-d) presents the SERS intensity of Rh6G dye obtained with 633 nm excitation wavelength, in presence of Ag-Au nanoparticle films. Similar to previous case (Fig. 3.18), the films grown with 1000 pulses showed weak SERS response, in

which pure Au films showed slightly better signal. For the films deposited with 2000 and 4000 pulses, the alloy films showed highest SERS intensity as compared to that shown by monometallic films. SERS enhancement factor for 1364 cm^{-1} peak was found to be about 2.8×10^4 , 5.2×10^4 , 6.1×10^4 and 2.6×10^4 for Ag, Ag rich, Au rich and Au films respectively for the films deposited with total 2000 pulses. For thicker films deposited with 4000 pulses, SERS EF was about 5.6×10^4 , 1.5×10^5 and 1×10^5 for Ag, Ag rich and Au rich films respectively. With increasing film thickness by 8000 pulses, high SERS EF was observed for pure Ag film. Fig. 3.19 (d) also shows Raman spectrum of Rh6G dye of $100\text{ }\mu\text{M}$, obtained without nanoparticle film, which did not show Raman signal even at 200 times higher concentration. For the films deposited with total 1000 laser pulses, SERS signal were also measured with 50 s integration time.

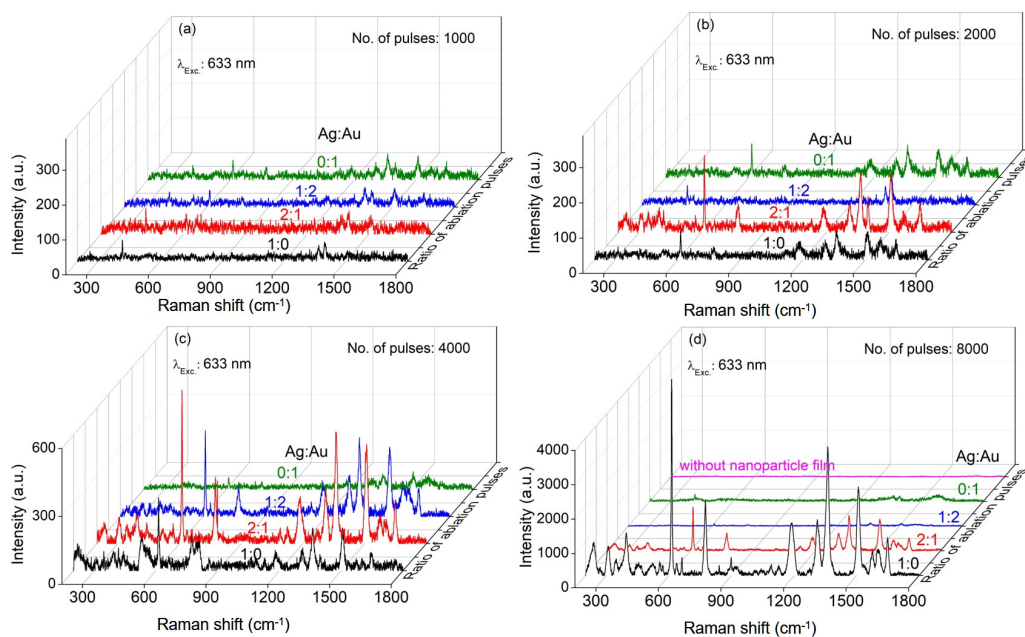


Fig. 3.19 SERS intensity of Rh6G Dye molecules obtained with 633 nm excitation wavelength, in presence of Ag-Au alloy films.

Fig. 3.20 presents the SERS intensity obtained with 633 nm excitation wavelength, in presence of these Ag-Au films. In this case, intensity of the peaks increased by 2 to 2.5 times for all the film compositions, compared to that obtained with 10 sec integration time as presented in Fig. 3.19 (a). This shows that by increasing integration time, limit of detection of SERS can be improved. The above results show that maximum SERS EF for both 488 and 633 nm excitation wavelengths was observed for Ag and Ag rich films. A figure of merit, that accounts near-field enhancement at resonance wavelength, depends on dielectric response of metal [17]. For Ag, the figure of merit is about 20 times more than that of Au [17]. Due to this, Ag nanoparticle films would result higher SERS EF, as compared to Au, when excited at their LSPR wavelengths.

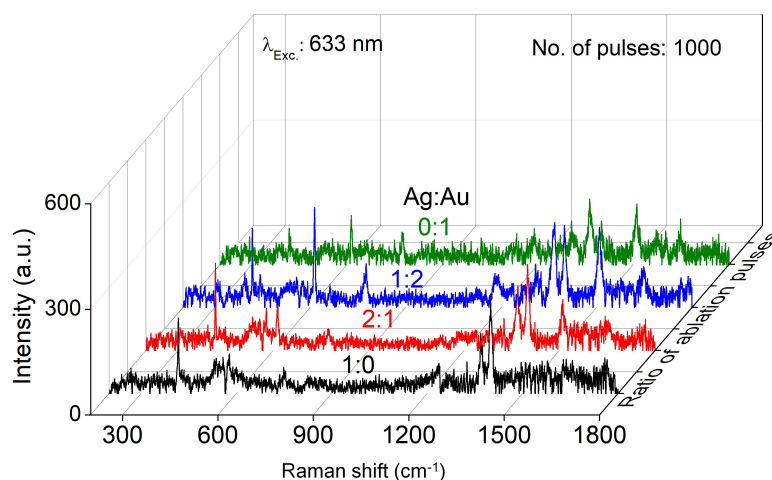


Fig. 3.20 SERS intensity of Rh6G dye molecules in presence of Ag-Au alloy films measured with 50 s (5X) integration time.

In the present case, the LSPR wavelength was varied with varying mass thickness and composition of films. At low films thickness, particle size is small and

their number density is high. For higher thickness films, average size of particles increased and number density decreased. For smaller nanoparticles of size < 10 nm, LSPR is significantly damped by surface scattering, as a result LSPR resonance and near-field enhancement are weak [151]. Therefore, for the films grown with 1000 pulses, SERS signal is significantly low. For nanoparticles of average size 25-40 nm, LSPR excitation occurs mainly in dipolar mode (without higher order modes) that results strong near-fields [151,152]. In present case, for films grown with 4000 and 8000 pulses, average size of the nanoparticles was about 20-35 nm. These films resulted into highest SERS signal, when the excitation wavelength of Raman measurement is close to the LSPR wavelength. These results show that using PLD, closely spaced pure and alloy nanoparticle films of tunable LSPR wavelength can be obtained by varying composition or film thickness, as shown in Fig. 3.21.

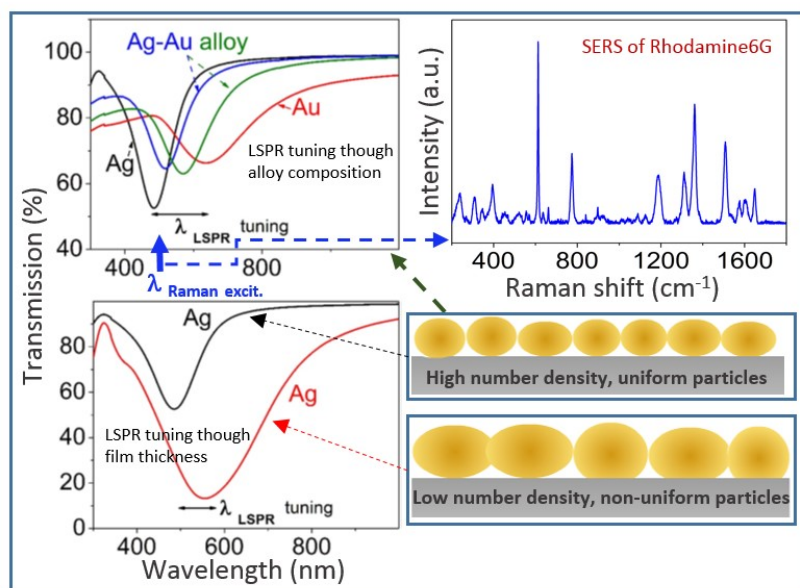


Fig. 3.21 Comparison of LSPR tuning by varying alloy composition and film thickness for application of efficient SESRS substrate.

These Ag-Au films with optimum particle size and tunable LSPR, can act as efficient SERS substrates at multiple wavelength for trace molecule detection.

3.7. Summary

Sequential ablation of two individual metal targets Ag and Au, by a nanosecond pulsed laser was shown to be promising for deposition of Ag-Au alloy films of desired composition. The alloy composition of film was varied by changing the ratio of laser pulses of Ag and Au, and film thickness was controlled from total ablation pulses. The alloy composition was determined using XPS, which is in close agreement with that obtained from EDS. High substrate temperature during the film growth played a key role in producing nanoparticles, and consequently LSPR response, which varied with Ag-Au alloy composition. The LSPR wavelength was found to be red-shifted with Au percentage and thickness of the films. Tuning of LSPR wavelength was obtained in the entire visible-near IR range. Closely spaced nanoparticle films were produced at 300°C substrate temperature growth, with average size of particles in the range 18-30 nm and number density in the range of $7 \times 10^{10} - 1.4 \times 10^{11} \text{ cm}^{-2}$. As compared to Ag and Ag rich films, Au and Au rich films were formed with larger particle size distribution. Dielectric response of alloy was determined from three analytical models and using these, optical transmission of alloy nanoparticle films was calculated. These models well predicted the variation of LSPR wavelength with films' composition. The model based on composition weighted linear sum of individual metals could not reproduce experimental transmission spectra, particularly $\leq 500 \text{ nm}$ wavelength i.e. in the IB transition region. The other two

models, one based on composition weight IB absorption and other based on joint density of states, showed better prediction of transmission. The dielectric response of alloy films of different composition and thicknesses was also determined experimentally using spectroscopic ellipsometry without using the morphological parameters. In this case, multi Gaussian oscillator model was used to fit the ellipsometry data to extract the real and imaginary dielectric response. The effective dielectric response (ϵ_{eff}) of Ag-Au nanoparticle films showed systematic variation of IB edge with Au percentage of films and reproduced the experimental transmission spectra. The $\text{Imag}(\epsilon_{eff})$ showed red-shift and increased amplitude peak with Au percentage and film thickness (for fixed composition). At two different excitation wavelengths, the SERS response of these LSPR wavelength tunable films was determined with Rh6G dye (500 nm) as probe. Films of low thickness (< 5 nm) did not produce significant Raman signal. Higher thickness Ag and Ag rich alloy films possessing LSPR band, close to excitation wavelength used for Raman measurement, resulted high SERS EF in the range of 10^5 - 10^6 . Variation of alloy composition helped in tuning of LSPR wavelength near to excitation wavelength of Raman measurement, without significant change of average size of nanoparticles. These results infer that the Ag-Au alloy nanoparticle films exhibiting tunable LSPR wavelength in entire wavelength region are useful for efficient SERS measurement at different excitation wavelengths.

Chapter 4

Laser ablation and light irradiation based synthesis of spherical and triangular Ag nanoparticles for SERS application

In the previous chapter 3, we observed that PLD grown Ag-Au alloy nanoparticles in the form of densely packed films have shown to be very good for SERS based molecular detection at very low concentration of analyte at different wavelengths of Raman measurement. Among these, Ag and Ag rich nanoparticle films have produced the highest SERS signal. However, these Ag and Ag rich nanoparticle films are not stable in atmosphere for longer time period of about few months. They react with sulphur and oxygen, present in atmosphere, as a result their plasmonic as well as SERS response decreases considerably with time, which is termed as atmospheric tarnishing [91,92]. These nanoparticle films should be used within few weeks of their preparation, else need to be protected with help of special packing for longer period of use, to preserve the plasmon response. On the other hand, laser ablation of Ag target in a liquid medium can also produce nanoparticles, this process is also known as liquid phase pulsed laser ablation (LPPLA). However, in pure solvents, the produced nanoparticles get aggregated in a short time interval. Introducing a specific surface capping agent, the obtained nanoparticles are stable for longer duration, typically few years. Ag nanoparticles in presence of specific reagents when subjected to light irradiation, transform into triangular shaped nanoplates. These triangular nanoplates possessing sharp edges are also better for SERS applications [15,23,32]. There is no detailed study on LPPLA based growth of spherical Ag

nanoparticles and subsequent photo-mediated shape transformation for producing triangular nanoplates, in aqueous solution containing single reagent.

To utilize the strong enhancement of SERS signal offered by Ag nanoparticles of different morphologies in colloidal form (with longer shelf life), a detailed study on LPPLA followed by light irradiation-based synthesis of spherical and triangular Ag nanoparticles is presented in this chapter. Transformation of spherical to triangular shape nanoparticles is accompanied with significantly red-shifted LSPR, which is also useful for wavelength tuning and SERS measurements at different excitation wavelengths. Producing non-spherical nanoparticles requires specific capping agent, which preferentially attach to certain facets of the seed nanoparticles during their growth. This approach relies on face blocking theory, widely applied for formation of different shapes of Ag or Au plasmonic nanoparticles of tunable optical responses [22,97,98,153]. Attachment or blocking of certain specific crystal facets by the capping agent, directs anisotropic growth on other facets and dictate the final shape of the nanoparticles. Growth of non-spherical nanoparticles requires different chemical reagents for kinetic control to facilitate both capping action and reduction of metal salts (source of metal atoms for the growth) that occur simultaneously at relatively slow rate. Chemical route synthesis of Ag triangular nanoplates are widely prepared using polyol process [97,154,155]. In chemical reduction-based methods, various chemical reagents are used at a specific concentration and their mixing order [153-56]. A marginal variation in this recipe significantly affects the size and shape distribution of the formed nanoparticles. On the other hand, photo-responsive nature of Ag and

also strong plasma excitation in Ag nanoparticle was found to be helpful in transformation of spherical seed nanoparticle into triangular nanoplates in presence of a light source [157,158]. In general, the required seed nanoparticles are grown in presence of strong reducing agents e.g. sodium borohydride, whereas high yield photo-mediated shape transformation occurs in presence of a mild reducing agent like tri-sodium citrate (TSC) [97,98,159,160]. The wavelength of light used for irradiation decides the size of nano-plates and also associated plasmonic response [158].

In LPPLA process, the nanoparticles are formed by ablation of metal target where the used chemical species mainly function as capping agent rather than reducing agent [162-164]. TSC being a good capping agent, also helps in efficient shape transformation of Ag nanoparticles. Therefore, synthesis of Ag nanoparticles in TSC solution using LPPLA can result in both spherical and triangular nanoparticles in single reagent. A detailed study on synthesis of Ag nanoparticles in TSC by LPPLA and subsequent shape transformation via light irradiation is not reported in the literature. This chapter presents this novel method of synthesis of spherical and triangular shape Ag nanoparticles in a single reagent TSC and determine the optimum process parameter for their use in SERS application.

4.1 Growth of colloidal Ag nanoparticles by laser ablation

For LPPLA experiments, a 2nd harmonic nanosecond pulsed Nd: YAG laser (wavelength: 532 nm, pulse duration: 9 ns, pulse repetition rate: 10 Hz and pulse energy: 100 mJ) with fluence of $\sim 5 \text{ J/cm}^2$ was used for ablation of Ag target. The spot size was about 2 mm^2 ($2 \times 10^{-2} \text{ cm}^2$). Ag metal target (99.9% pure) was ablated in a

beaker with 10 mL de-ionized (DI) water or TSC solution of different concentrations. The beaker was continuously rotated during laser ablation of 30 min. duration. The solution pH was varied with HCl or NaOH. Variation of optical absorbance with laser ablation time during growth of Ag nanoparticle in DI water is shown in Fig. 4.1(a). The absorbance peak at about 400 nm wavelength is characteristic LSPR response of Ag nanoparticles. In this case, the absorbance peak is asymmetric and extended up to 1000 nm which can be attributed to presence of non-spherical and irregular shaped nanoparticles. With ablation time, increase in absorbance is marginal and is observed in entire wavelength range. Fig.1(b) shows TEM image of grown nanoparticles in DI water. It shows formation of aggregated and interconnected irregular shape nanoparticles. This is because in pure water, the nanoparticles are formed without surface capping, as a result they get attracted by weak van der Waals force, leading to aggregation.

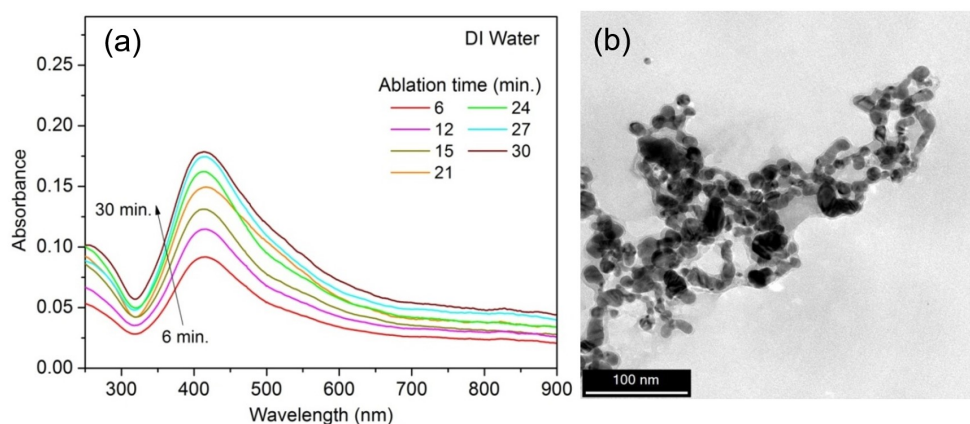


Fig. 4.1 Variation of (a) absorbance of Ag nanoparticles with ablation time during growth and (b) its TEM image after 30 min. ablation.

4.2 Effect of citrate concentration on laser ablation-based growth of colloidal Ag nanoparticles

Fig. 4.2(a-c) shows variation of absorption spectra of Ag nanoparticles grown in 0.5, 10 and 100 mM citrate solution respectively. The absorbance was found to be increased in citrate solution as compared to pure water. Further, growth in 10 mM citrate solution resulted the highest peak absorbance. The absorbance peak around 400 nm increased with ablation time without change in absorbance at longer wavelengths (> 600 nm). The TEM image of nanoparticles produced in 10 mM citrate is shown in Fig. 4.2(d), showing formation of well dispersed and almost spherical nanoparticles. Size distribution of the nanoparticles is presented in inset of Fig. 4.2 (b) showing average diameter of ~ 13 nm. This reveals that in presence of TSC, LPLPA method produced nanoparticles are isolated from each other. This is because citrate being a good surface capping agent possessing negative charge, provides stability to the nanoparticles and inhibits their aggregation.

Fig. 4.3(a) presents variation of peak absorbance (at ~ 400 nm) versus ablation time for varied citrate concentrations in range of 0.05 to 100 mM. For all citrate concentrations, peak absorbance value enhanced with laser ablation period. In order to see clearly the effect of TSC concentration, Fig. 4.3(b) presents variation of maximum peak absorbance versus concentration of citrate, obtained for laser ablation of 30 min. duration. This graph shows that for a given ablation period, the LSPR peak absorbance of Ag nanoparticles first increased up to 10 mM TSC concentration, and afterwards it decreased. For citrate concentration less than 10 mM, increase in absorbance is attributed to formation of isolated nanoparticles with citrate capping. It may be noted that isolated Ag nanoparticles would exhibit LSPR at about 400 nm

wavelength however, if some of the nanoparticles get aggregated, it results in high absorbance at longer wavelength region also.

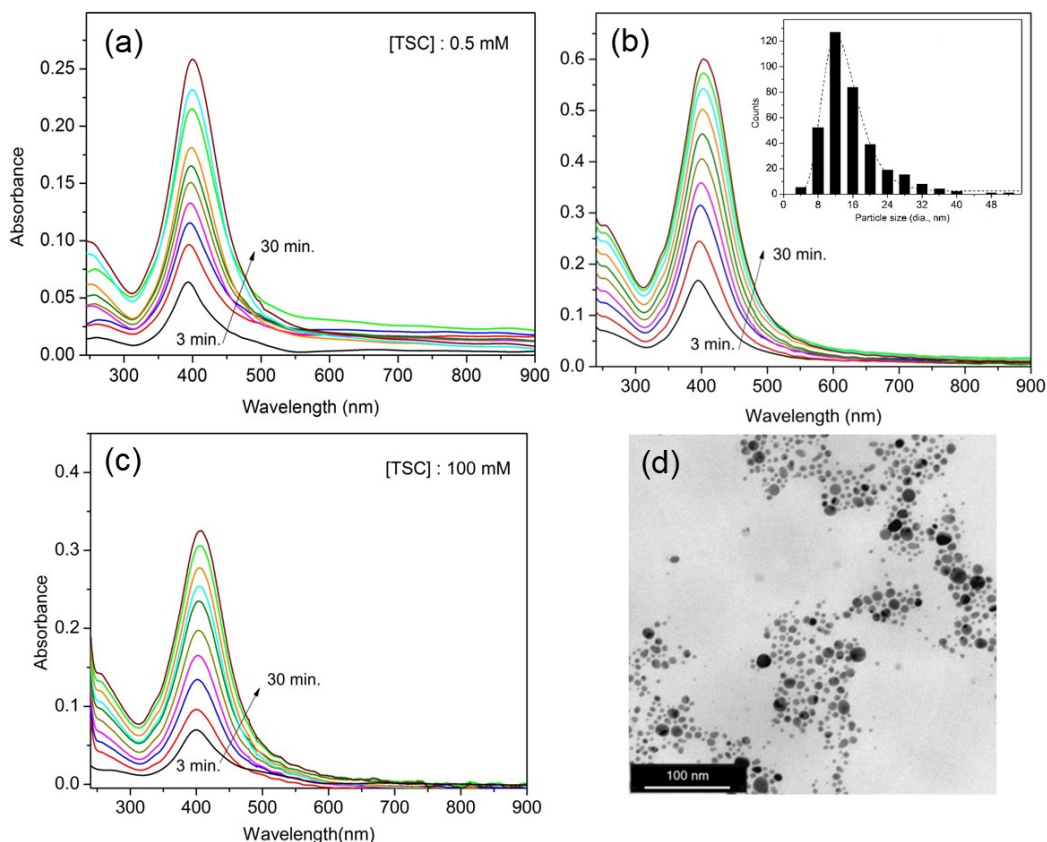


Fig. 4.2 Variation of absorbance of Ag nanoparticles with ablation time during growth in citrate solution of (a) 0.5 mM, (b) 10 mM; inset: particle size distribution (c) 100 mM and (d) TEM image of Ag nanoparticles obtained in 10 mM citrate solution.

Presence of longer wavelength absorbance at lower citrate concentration and absence of the same, at higher citrate concentrations (refer Fig. 4.1 & 4.2) reveals that 10 mM is the optimum concentration for formation of isolated and high concentration Ag nanoparticles. Further decrease in LSPR absorbance for higher citrate concentrations could be due to suppression of nanoparticles concentration due to

formation of citrate complexes with Ag clusters [160]. Decreased stability of nanoparticles could be because of increased ionic strength in the solution [165].

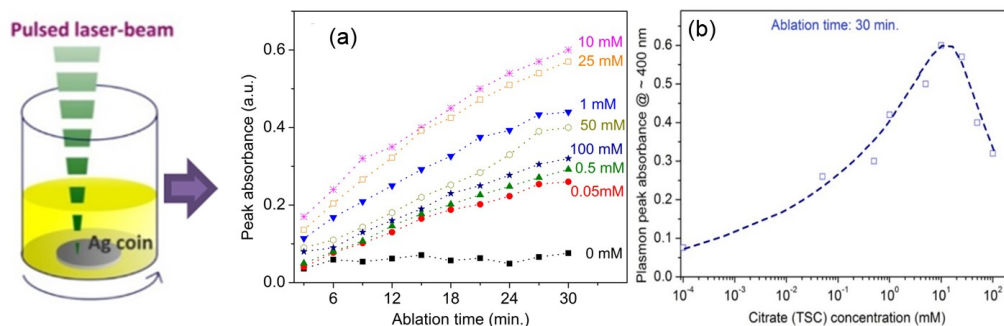


Fig. 4.3 Schematic of laser ablation of Ag coin producing Ag nanoparticle solutions, and the obtained variation of peak absorbance versus (a) laser ablation time and (b) citrate concentration.

In literature, it is mentioned that at high citrate concentration, various Ag-citrate complexes are formed which hinder growth of Ag nanoparticles in the chemical reduction method [160]. In the present experiments, at very high citrate concentration (≥ 50 mM), formation of a white color precipitate on the Ag coin, at the laser ablation region was noticed. In addition to this, to understand the stability of Ag nanoparticles grown at different TSC concentrations, zeta potential measurement was carried out. At citrate concentrations of 1, 10 and 75 mM, the observed zeta potential is about -37, -33 and -18 mV respectively. It reveals smaller zeta potential values i.e. less than -20 mV, at high citrate concentration, which is because of reduced ionic double layer at this high ionic strength. As a result of this, stability of Ag nanoparticles was decreased.

4.3 Calculation of number concentration of Ag nanoparticles

Since laser ablation was carried out with 532 nm wavelength at which Ag

nanoparticles have significantly low absorbance, as a result of this self-absorption of the laser beam by the nanoparticle is significantly low. It helped in producing higher concentration of nanoparticle with increasing the ablation time. Number concentration (N) of nanoparticles in the grown solutions has been calculated using Mie theory and experimentally observed absorbance (A). The relation between the two is given as [166]:

$$A(\lambda) = \frac{\sigma_{ext}(\lambda)d_0N}{2.303} \quad \dots (4.1)$$

where d_o is cuvette path length and σ_{ext} is the extinction cross section of Ag nanoparticle, which is obtained using Mie theory [20]. This theory provides exact electrodynamic solution of Maxwell equations in spherical coordinate system and has been widely used for explaining optical response of metal nanoparticles of varied sizes [12,14,15,23,93,166]. The solution of Maxwell equations are obtained by determining the scalar electromagnetic potential from multipole expansion of incoming electric and magnetic fields for a sphere of radius R [20]. Optical response of this spherical particle of complex refractive index $n(R)$, can be presented in terms of scattering and absorption cross section. For the given plane wave electromagnetic field (E_{inc}, H_{inc} where $E_{inc} = E_0 \exp\{i(\sqrt{\epsilon_d})kr\}$), the energy conservation, in terms of time averaged Poynting vectors, follows $S_{tot} = S_{inc} + S_{sc} + S_{ext}$, where S_{tot} is the total power per unit area flowing through the medium, S_{inc} is power per unit area corresponding to the incoming wave i.e. $= \frac{1}{2} \text{Re}\{E_{inc} \times H_{inc}^*\}$ and the same for scattered fields (E_{sc}, H_{sc}) is $S_{sc} = \frac{1}{2} \text{Re}\{E_{sc} \times H_{sc}^*\}$. The last term $S_{ext} = \frac{1}{2} \text{Re}\{E_{inc} \times H_{sc}^* + E_{sc} \times H_{inc}^*\}$ is the power flow per unit area arising from the interference of the

incident and scattered fields. These powers when integrated across any arbitrary closed surface containing the particle, gives the energy absorbed and scattered by the particle, given as $W_{abs} = - \int S_{tot} ds$ (the negative sign shows the inward energy flow toward the particle) and $W_{sc} = \int S_{sc} ds$ respectively. The corresponding particle absorption and scattering cross sections are $\sigma_{abs} = W_{abs} / |S_{inc}|$ and $\sigma_{sc} = W_{sc} / |S_{inc}|$ respectively. Thus, the total Mie extinction consists of absorption and scattering modes, whose contribution depends on size and complex refractive index of the particle and is expressed as [20]:

$$\sigma_{ext} = \frac{2\pi}{k^2} \sum_{L=1}^{\infty} (2L+1) \text{Re}[a_L + b_L] , \quad \dots (4.2)$$

$$a_L = \frac{m \psi_L(mx) \psi_L'(mx) - \psi_L'(mx) \psi_L(x)}{m \psi_L(mx) \eta_L'(x) - \psi_L'(mx) \eta_L(x)} , \quad b_L = \frac{\psi_L(mx) \psi_L'(x) - m \psi_L'(mx) \psi_L(x)}{\psi_L(mx) \eta_L'(x) - m \psi_L'(mx) \eta_L(x)} , \dots (4.3)$$

where, k is the wave vector of incident light, a_L and b_L represent coefficients of Mie scattering in terms of spherical Riccati-Bessel functions (ψ_L and η_L), which depend on (i) particle dielectric response i.e. relative refractive index $m = n(R)/n_s$ (n_s is refractive index of the surrounding medium with zero absorption), and (ii) size parameter $x = kR$. L is order of spherical multipole excitations, 1 for dipole fields, 2 for quadrupole, 3 for octupole etc. In calculation of extinction spectra of nanoparticles, wavelength dependent dielectric function of nanoparticles should be used in the calculation. For Ag nanoparticles, extinction spectra predicted by Palik data [31] is more accurate than that obtained from Jhonson and Christy data [166]. For smaller size nanoparticles, the electron damping increases and modifies the bulk dielectric electron damping frequency from Γ_0 with $\Gamma_0 + A v_f / R$, in which A is fitting parameter (between 1-3) and v_f is Fermi velocity of electrons [166,167].

Fig. 4.4 shows the absorbance spectra of Ag nanoparticle produced in 10 mM citrate solution for laser ablation of 30 minutes along with calculated absorption spectra. A good fitting of the experimental spectra was observed for number concentration of about 1.1×10^{12} nanoparticles per mL with the size range shown in fig. 4.2 (b). The obtained concentration range is similar to that reported for chemical route synthesis for the observed size of Ag nanoparticles [166]. In the present case of laser ablation method, the nanoparticle concentration can be easily controlled by changing the ablation time. In order to show the same, Fig. 4.4 also presents the absorption spectra of Ag nanoparticle for 50 minutes of laser ablation. Significant increase in absorption with ablation time shows that the concentration of nanoparticles increased to about 1.6×10^{12} nanoparticles per mL. This shows that in this LPPLA method, the concentration of nanoparticles can be increased higher than that usually obtained by chemical-based synthesis.

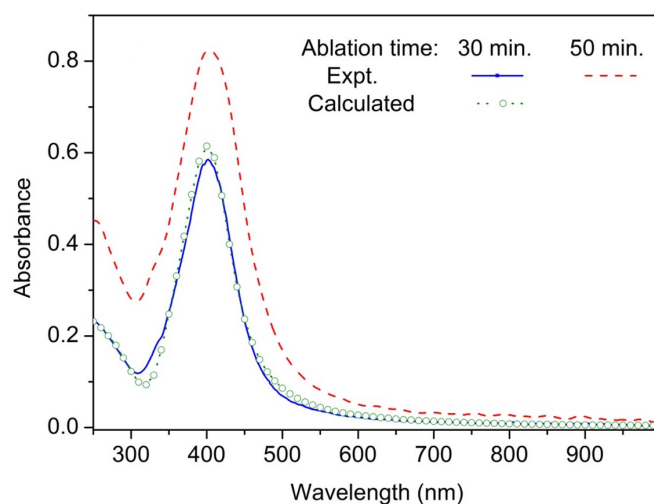


Fig. 4.4 Experimental and calculated absorbance of Ag nanoparticles.

Such high concentration nanoparticles are useful for colorimetric sensors for detection of various species. In developing these sensors, knowledge of nanoparticles formation

and their stability at different pH condition is important.

4.4 Effect of pH on growth of Ag nanoparticles by laser ablation

The produced nanoparticles in TSC solution are stable because of citrate ions capping on the surface of nanoparticles. The characteristics of capping layer can be modified from pH of the solution. In addition to this, solution pH plays an important role in formation of Ag nanoparticles during their growth from the laser ablated plume. Therefore, formation of Ag nanoparticle in 10 mM citrate solution at different pH condition in range of 3 to 11 has been studied. pH of the solution was varied with HCl for low pH and NaOH for high pH. Fig. 4.5(a) presents UV-Vis. absorption of these nanoparticles grown at various pH conditions. It can be observed that at low pH (less than 7) of solution, the absorbance is significantly low, even in presence of citrate. In this case, the obtained light yellowish colour Ag nanoparticle solution faded out within few hrs. of synthesis. At high pH conditions, absorbance of the grown Ag nanoparticle was found to be significantly high. For more detailed understanding, variation of LSPR absorbance with pH of the solution at different citrate concentrations is shown in Fig. 4.5(b). The figure shows that at low pH (< 6) the absorbance is lesser and becomes higher at larger pH and the role of pH is almost same for all the concentration of citrate. At low pH, lower LSPR absorbance corresponds to lesser concentrations of nanoparticles, which could be because of dissolution of nanoparticles in presence of HCl which is added for adjusting the pH value. The reactivity of Ag enhances in nanoparticle form, as a result AgCl is formed in presence of chloride ions [160,168]. At low pH and higher citrate concentration, the

LSPR absorbance decreased considerably. This could be due to addition of relatively higher amount of HCl to obtain the particular pH of the solution at high citrate concentrations. Further citrate has three pKa values of 3.1, 4.7 and 6.4, so in acidic conditions protonation of citrate molecules could also decrease the charge stability the nanoparticles [169].

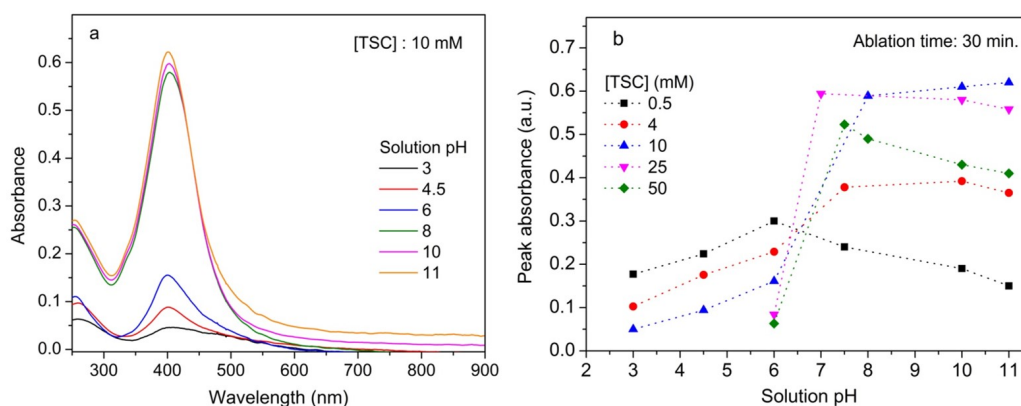


Fig. 4.5 (a) Absorption spectra of Ag nanoparticles produced in varied pH conditions and (b) variation of LSPR absorbance with pH value of the solution.

Fig. 4.6 presents the XRD spectra of the Ag nanoparticle produced in 10 mM citrate at three pH values of 3, 7.5 and 10. At the low pH, the grown Ag nanoparticle have shown diffraction peaks at 32.2° and 46.2° corresponding to (200) and (220) indices of AgCl (JCPDS file no. 31-1238) [168,170]. In addition to this, smaller diffraction peak at about at 38° of (111) plane of metallic Ag, is also obtained. It confirms formation of AgCl compound at low pH condition, as a result nanoparticle are not stable in metallic form, and consequently the LSPR response faded with time. However, Ag nanoparticles produced at high pH have shown multiple diffraction peaks which corresponds to FCC phase of metallic Ag, showing that these nanoparticles are stable.

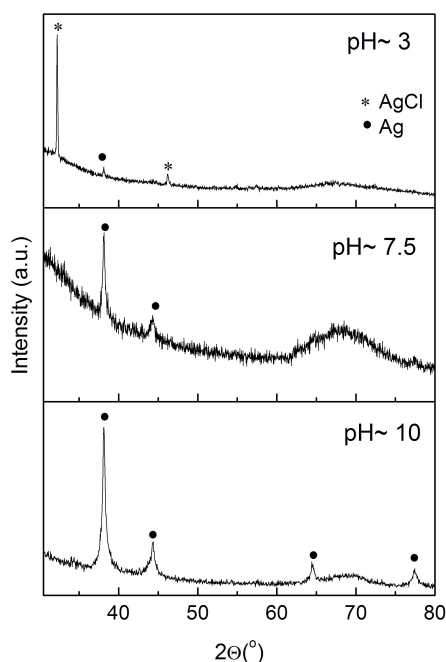


Fig. 4.6 XRD spectra of Ag nanoparticles produced at different pH conditions.

4.5 Light irradiation of LPPLA grown Ag nanoparticles

For photo-mediated shape transformation, the Ag nanoparticles grown via LPPLA method has been irradiated with conventional sodium lamp of 150 W power, whose spectra is shown in Fig. 4.7(a). For the irradiation period of about 6-12 hrs., the initial yellow colour Ag nanoparticles solution is turned into green colour and for about 24 hrs. of irradiation, it further changed into blue colour. Fig. 4.7(b) presents the photographs of Ag nanoparticles of as grown and after different period of light irradiation. The variation in UV-Vis. absorption of these nanoparticles at fixed intervals of irradiation has been measured. Fig. 4.7(c) presents UV-Vis. absorption of Ag nanoparticle formed in 10 mM citrate and its variations up to 24 hrs. of light irradiation. This figure shows significant change in absorption band in the whole visible wavelength region, which could be due to change in morphology of nanoparticles from light irradiation. Since the change in absorption band mainly

occurred in visible range, as a result it has shown change in colour of nanoparticle solution as shown in Fig. 4.7(b).

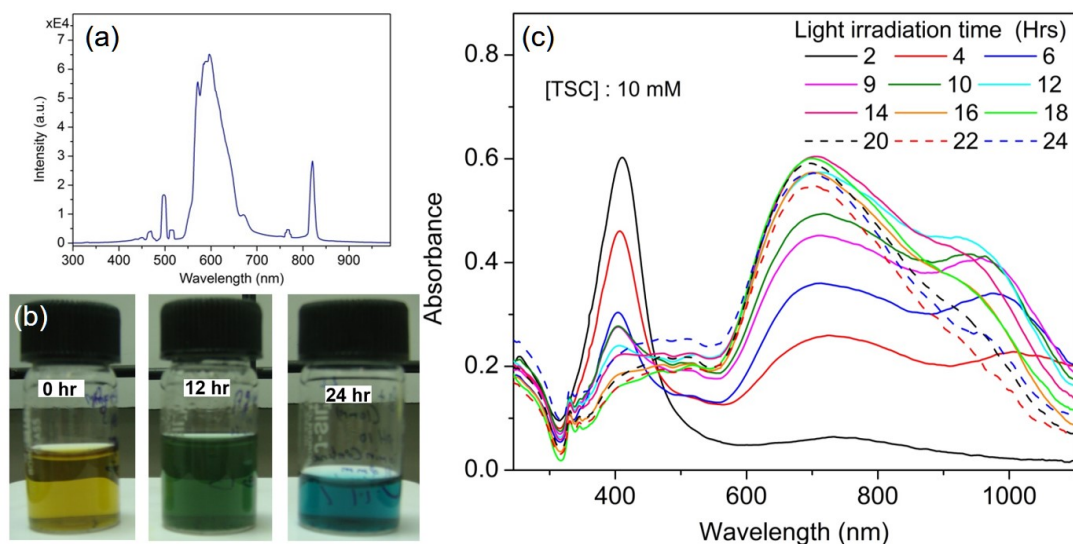


Fig. 4.7 (a) Intensity spectrum of the irradiation lamp, (b) photographic image of Ag nanoparticles and (c) absorption spectra after different irradiation time.

The LPPLA grown spherical Ag nanoparticle have exhibited characteristics narrow band LSPR absorption peak near about 400 nm, however with light irradiation this peak decreased consistently along with evolution of broad absorbance at about 600-1100 nm wavelength. Considerable decrease in 400 nm LSPR band indicates decrease of spherical nanoparticle concentration with light irradiation. Fig. 4.8(a) and (b) present TEM images showing the morphology of Ag nanoparticles after 6 and 24 hrs. of light irradiation respectively. After 6 hrs. of irradiation, the image shows smaller size spherical and also triangular shape nanoparticles. However, after 24 hrs. of irradiation, the nanoparticles mostly transformed into triangular shape nanoplates. From these TEM images, it can be observed that nanoparticle shape transformation occurs at initial stage of irradiation but the yield of triangular nanoparticle increased

with irradiation time.

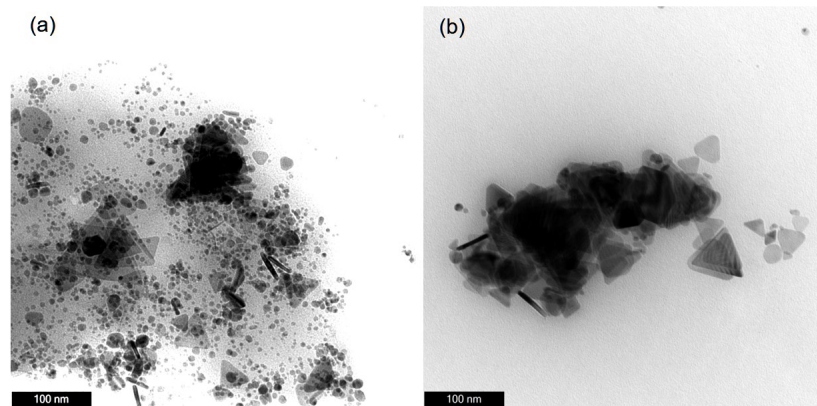


Fig. 4.8 TEM images of Ag nanoparticles obtained after (a) 6 hrs. and (b) 24 hrs. of light irradiation.

From TEM images, it can be observed that triangular shape nanoplates are produced after light irradiation. From the detailed characteristics of the absorption spectra presented in Fig. 4.7(c), small and sharper peaks, near about 340 and 470 nm wavelengths can be observed, which is attributed to out of plane and in-plane quadrupole resonances of triangular nanoplates respectively [171-173]. The single narrow LSPR band of Ag nanoparticles transformed into a broad hump around 450 nm, attributed to out of plane dipole resonance of Ag triangular nanoplates [171-173]. The significant absorbance in long wavelength region ≥ 600 nm, corresponds to in-plane dipole resonance absorption of Ag triangular nanoplates. The variation of peak absorbance with irradiation time is shown in Fig. 4.9, which shows that characteristics of this band varied with irradiation time. At initial stage of light irradiation, the in-plane dipole resonance increased significantly and after 12 hrs. of irradiation, it changed marginally. Also, this plasmon band consisted of two peaks initially, which gradually appeared as single strong absorption band at 700 nm after 12

hrs. of irradiation time.

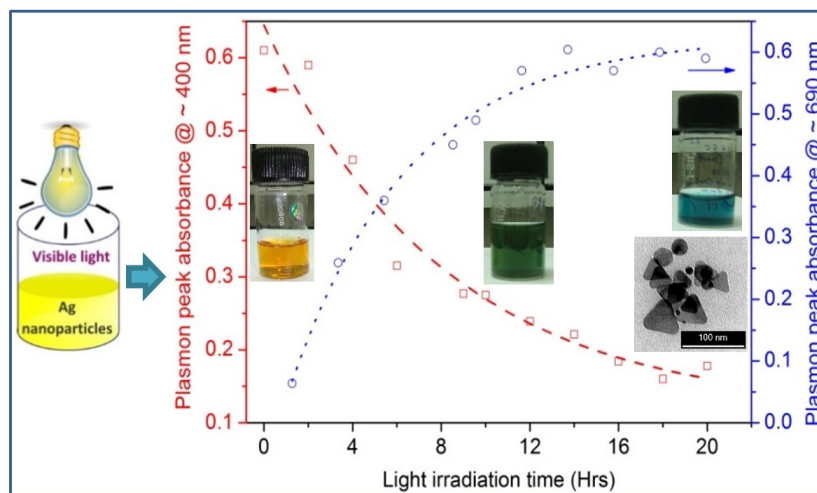
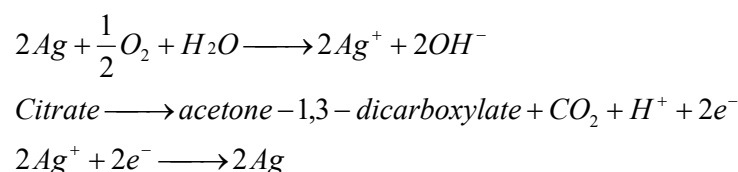


Fig. 4.9 Variation in peak absorbance of Ag nanoparticles at ~400 and ~690 nm with irradiation time.

The double peak structure can be attributed to presence of Ag nanoplates of varied sizes as observed in Fig. 4.8 (a). In photo-induced synthesis of Ag nanoplates, it has been shown that the LSPR excitation driven near-field produces Ag nanoplates, exhibiting in-plane dipole resonance, slightly red-shifted from the wavelength of light irradiation [174]. Therefore, in the present case, narrowing of this LSPR band around 700 nm at longer time of irradiation could be attributed to high intensity of lamp irradiation around 600-650 nm, which eventually narrow down the size distribution of Ag nanoplates. This is also in consistent with the TEM image shown in Fig. 4.8 (b).

Growth of anisotropic nanoparticles is mostly governed by the kinetics and further involvement of photo-mediated processes add additional parameters to control the shape transformation [97,98,174,175]. In photo-assisted growth of anisotropic Ag nanoparticles, dissolved oxygen causes etching of smaller spherical seed Ag nanoparticles and produces Ag^+ ions. The citrate molecules present in the solution

provide preferential capping of (111) facets and also undergo oxidation near nanoparticles which absorb or scatter the incident light, reducing Ag^+ ions in the solution and induces the shape transformation. The overall reaction of the process can be written as [98]:



In the above process, wavelength of the incident light governs the final size of the nanoplates [97,98]. During initial stage of the irradiation, preferential capping of citrate molecules leads to splitting of plasmon resonance into longitudinal and transverse modes [97]. The larger near-field of longitudinal mode further directs the anisotropic growth of Ag, and increases anisotropy in the shape of nanoparticles [97,174]. The shape transformation ceases once the nanoparticles shape is elongated enough, that could not further excite plasmon resonance at the wavelength of incident light, used for irradiation. The triangular shape of the nanoplates has been shown to be result of hexagonal symmetry of FCC lattice of Ag nanoparticles [97]. The spherical Ag seed nanoparticles, grown by either chemical reduction method using strong reducing agent or LPPLA method, generally consists of stacking faults in the hexagonal lattice arrangement, which after irradiation, is left with triangular shape of nanoplates [97]. The triangular nanoplates has been identified to be covered with (111) facets, which because of low surface energy did not grow. In order to conform this, XRD measurements of the Ag nanoparticles before and after light irradiation was also carried out. Fig. 4.10 compares the XRD intensity spectra of Ag nanoparticles in DI

water and optimum citrate concentration of 10 mM at different irradiation times. Ag nanoparticles before irradiation, showed intensity peak at 38.12°, along with a minor peak at 44.3°, corresponding to (hkl) indices of (111) and (200) of FCC crystalline phase of metallic Ag. The (111) peak in case of citrate grown Ag nanoparticles is relatively more broadened compared to that observed with nanoparticles grown with DI water. This can be attributed to growth of smaller size nanoparticles in presence of citrate, as observed from TEM images of Fig. 4.1 (b) and 4.2 (d). After light irradiation, other peaks at 64.5°, 77.4° and 81.4° of (hkl) indices of (220), (311) and (222) respectively were also observed in the XRD spectra, confirming FCC crystalline phase of Ag nanoplates. Without irradiation, the ratio of intensity peaks of (111) and (200) was found to be ~ 1.6, which significantly increased to 3 and 6.1 after light irradiation of 6 and 24 hrs. respectively. This confirms that nanoplates formed after light irradiation has crystalline asymmetric growth of preferred orientation.

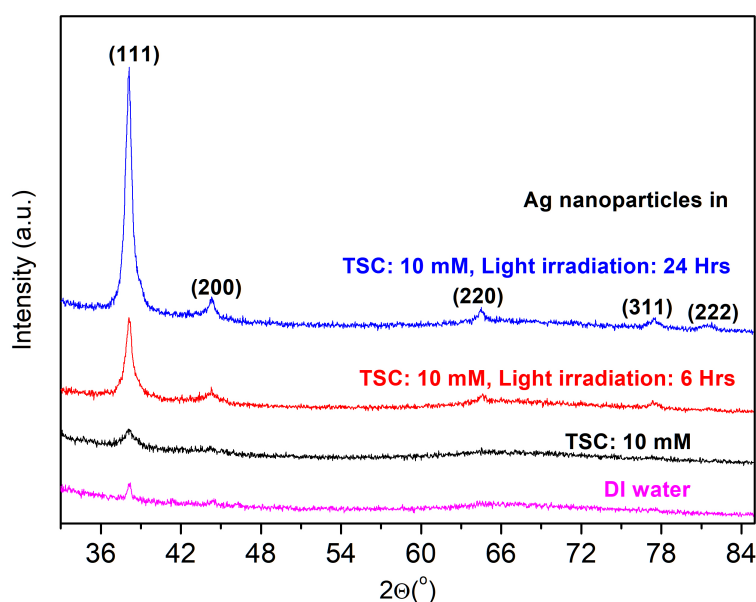


Fig. 4.10 XRD spectra of Ag nanoparticles before and after light irradiation.

4.6 Effect of citrate concentration on photo-mediated shape transformation

Absorption spectra of light irradiated Ag nanoparticles grown with varied citrate concentrations is presented in Fig. 4.11 (a,b). After 6 hrs. of irradiation, Ag nanoparticles, grown in citrate solution of concentration 1-10 mM, resulted in increased longer wavelength absorption i.e. in-plane dipolar LSPR band of nanoplates. Increasing the citrate concentration to 25 mM, the longer wavelength absorption band decreased and was not obtained above 25 mM. After 24 hrs. of irradiation, this in-plane dipole LSPR peak further enhanced along with decrease in peak absorbance of spherical Ag nanoparticles at ~ 400 nm. Also, at very high citrate concentrations > 25 mM, light irradiation of 24 hrs. resulted de-colorization and formation of black precipitate, indicating aggregation of Ag nanoparticles. It may be noted that during chemical synthesis of Ag nanoparticles, presence of large amount of citrate compared to Ag^+ ions, reduced growth of nanoparticles, which was attributed to formation of different Ag-citrate complexes [160]. In present experimental conditions of photo-induced transformation of shapes, Ag^+ ions are reduced by citrate molecules, which would be slowed down by i) formation of Ag-citrate complex at larger citrate concentrations and ii) un-stability of Ag nanoparticles due to high ionic strength of the medium [165]. From above findings, it can be inferred that 10 mM concentration of citrate is the optimum concentration for both formation of spherical Ag nanoparticles by LPPLA and triangular nanoplates by photo-mediated shape transformation.

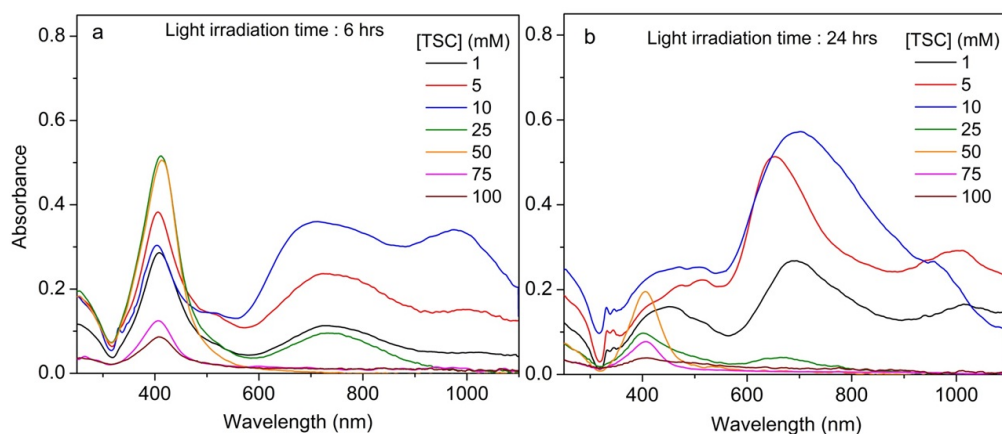


Fig. 4.11 Absorption spectra of Ag nanoparticles formed in varying concentrations of citrate after (a) 6 hrs. and (b) 24 hrs. of irradiation.

4.7 Effect of Ag ions on photo-mediated shape transformation

As mentioned above, the photo-mediated transformation of nanoparticle shapes proceeds by reduction of Ag^+ ions through citrate molecules. Hence, effect of Ag^+ ions during light irradiation of Ag nanoparticle solution was studied by adding AgNO_3 of final concentration of about 0.1 or 0.2 mM. Fig. 4.12 (a,b) presents UV-Vis. absorption of Ag nanoparticles formed in 10 mM citrate at varied irradiation time, in presence of 0.1 and 0.2 mM of AgNO_3 respectively. In contrast to the previous case, the LSPR peak ~ 400 nm was found to increase after 2 hrs. of irradiation time with slight red-shift of ~ 4 nm, which could be due to growth of initial Ag nanoparticles by presence of citrate and Ag^+ ions. The absorbance value at about 1000 nm also increased, when compared to Fig. 4.11. This shows that formation of both smaller and larger size nanoplates occurs in presence of added Ag^+ ion. Fig. 4.12 (c, d) shows TEM images of the Ag nanoparticles after 6 and 24 hrs. of irradiation in presence of 0.2 mM AgNO_3 respectively. Formation of smaller as well as large triangular nanoplates can be observed along with hexagonal and other intermediate shape

nanoparticles after 6 hrs. of irradiation. As observed in Fig.4.12 (d), most of these nanoparticles turned into triangular shape with broad size distribution after 24 hrs. of irradiation, resulting broad absorption band. It may be noted that light irradiation of TSC and AgNO₃ solution without spherical seed Ag nanoparticles, did not produce any formation of nanoparticles and the solution remained colorless. This shows that presence of Ag seed nanoparticle exhibiting LSPR response is important for photo-mediated shape transformation process.

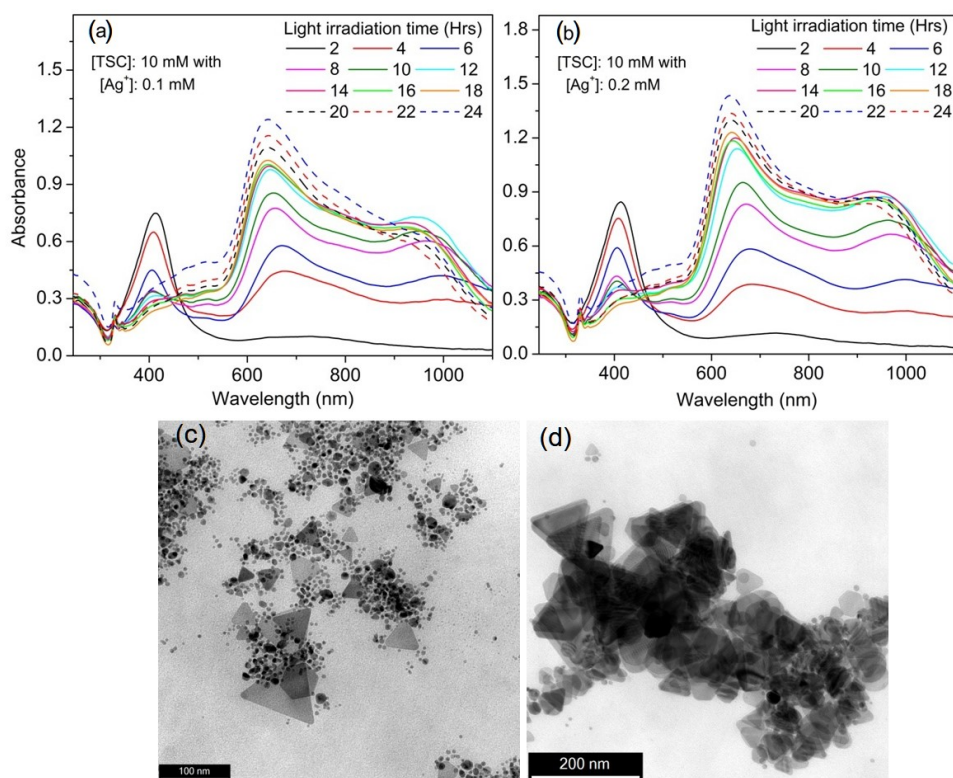


Fig. 4.12 UV-Vis. absorption of Ag nanoparticles formed in 10 mM citrate solution and irradiated in presence of silver salt of (a) 0.1 mM and (b) 0.2 mM and TEM images obtained after (c) 06 hrs. and (d) 24 hrs. of irradiation.

Effect of citrate concentration in presence of Ag⁺ ions was also studied and Fig. 4.13 (a,b) presents UV-Vis. absorption spectra of Ag nanoparticles formed in varied

concentrations of citrate after 6 and 24 hrs. of irradiation respectively. Similar to previous case of without additional Ag^+ ions, increase of citrate concentration from 1 to 10 mM, enhanced the in-plane dipole LSPR peak at ~ 600 nm, and above 10 mM, it decreased. In contrast to the earlier case (refer Fig. 4.7c), the absorbance above ≥ 600 nm increased significantly, which shows improved formation of nanoplates. At citrate concentration of 25 mM, after 6 hrs. of irradiation, the obtained in-plane LSPR peak above 600 nm was found to be enhanced compared to the previous case of without Ag^+ ions (Fig. 4.11). This shows that after addition of Ag^+ , the effective ratio of citrate to Ag^+ ion is decreased, and the nanoplates could also be formed at relatively higher citrate concentration. However, after 24 hrs. of irradiation, the in-plane dipole LSPR peak decreased, indicating that the formed nanoparticles are not stable, due to high ionic strength. Fig. 4.13 (c, d) show TEM images of Ag nanoparticles formed in 25 mM citrate concentration after irradiation of 6 and 24 hrs. respectively, in presence of added AgNO_3 solution. It shows formation of smaller size nanoplates compared to those obtained at 10 mM citrate concentration, (Fig. 4.12 (c)). This is also in line with the observed absorption spectra showing smaller and single absorption band in > 600 nm region for the case of 25 mM citrate concentration. Further irradiation of these nanoparticles up to 24 hrs. produced irregular shape nanoparticles as shown in Fig. 4.13(d), which could be due to limited growth of nanoparticles at high citrate concentration [160].

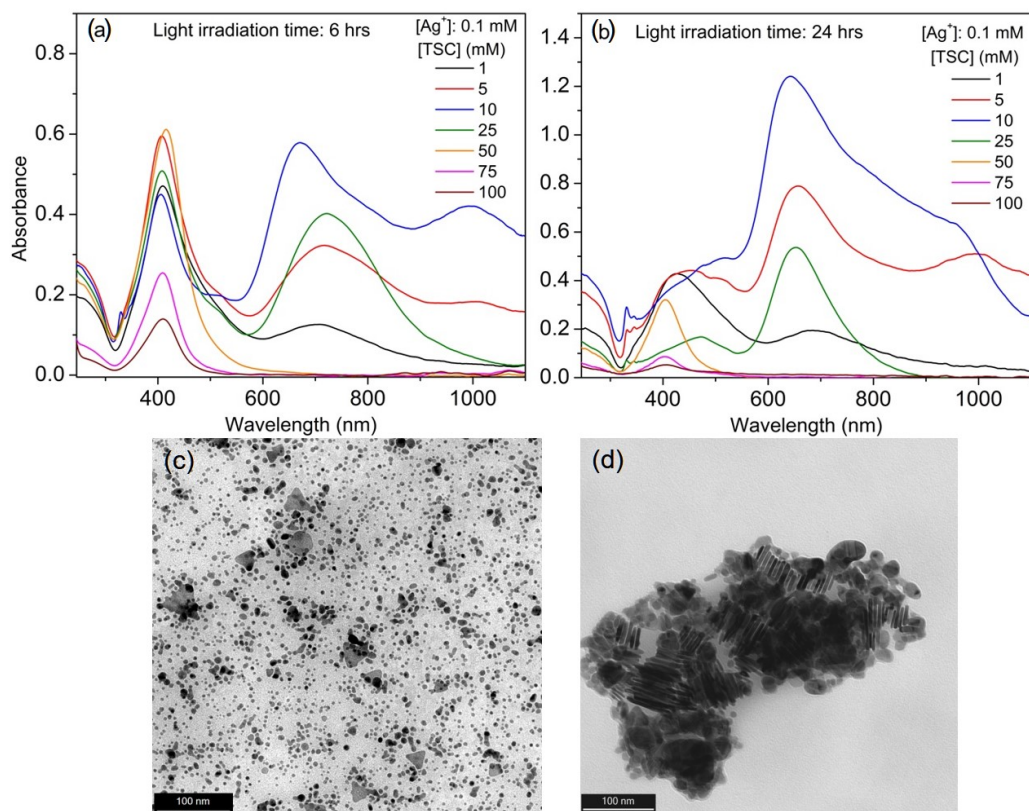


Fig. 4.13 UV-Vis. absorption of Ag nanoparticles formed in varied concentrations of citrate and irradiated in presence of 0.1 mM silver salt for (a) 6 hrs (b) 24 hrs, and TEM images of Ag nanoparticles formed in 25 mM citrate after irradiation of (c) 06 hrs. and (d) 24 hrs.

4.8 Effect of solution pH on shape transformation of Ag nanoparticles

As observed in section 4.4, stable and high concentration spherical Ag nanoparticles were obtained in pH range of 7.5-10. Effect of pH on photo-mediated shape transformation was also observed. Fig. 4.14 (a) presents UV-Vis. absorption of Ag nanoparticles formed in 10 mM citrate concentration with pH 10 after different irradiation time. The variation in absorbance with irradiation time is found to be similar to that observed without pH modification. Comparing it with Fig. 4.7(c) shows that the in-plane dipole LSPR absorption peak of Ag nanoplates has lesser absorbance

with narrow shoulder at ~ 1000 nm wavelength. In literature, it has been shown that pH condition modifies the size and shape distribution of nanoparticles in photo-induced shape transformation, and high pH condition of ~ 12 almost stopped the transformation process by limiting the source of Ag ions due to formation of AgOH compound [165,170]. Therefore, in present case also, relatively smaller and narrow absorption peak at longer wavelength suggest limited formation of smaller Ag nanoplates. The UV-Vis. absorption of Ag nanoparticles at pH 10 condition after addition of Ag^+ ions of 0.1 and 0.2 mM, was also monitored and shown in Fig. 4.14 (b) and (c) respectively.

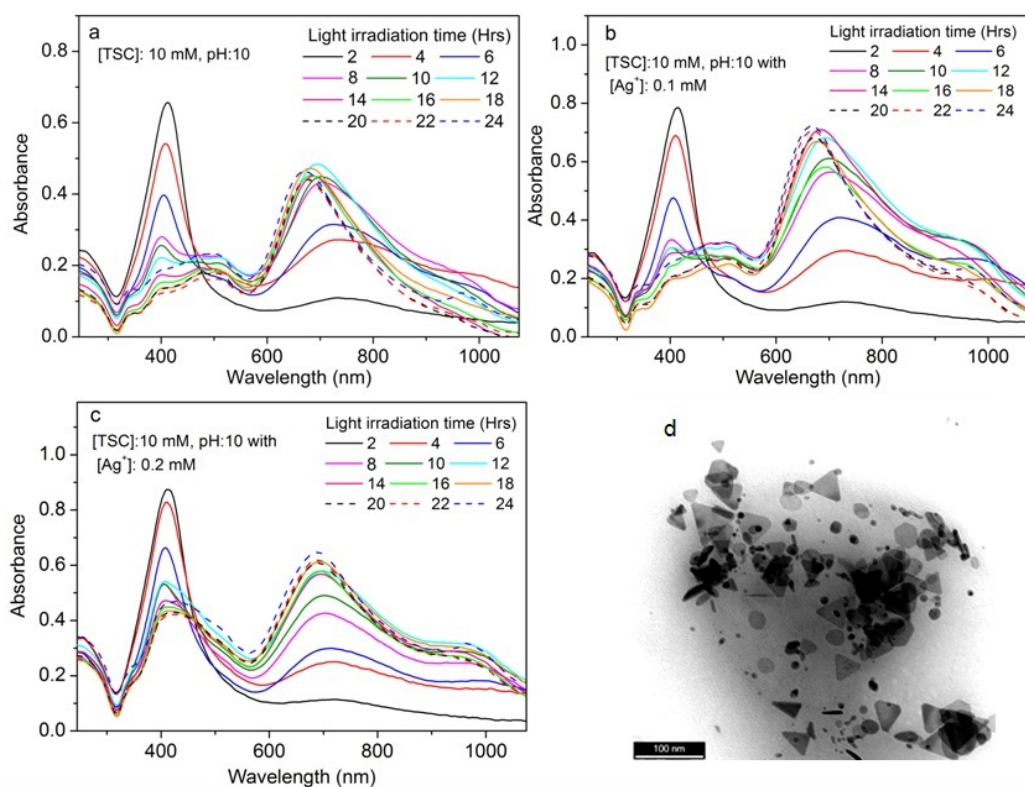


Fig. 4.14 UV-Vis. absorption of Ag nanoparticles formed in 10 mM citrate of pH 10 (a) before and after addition of AgNO_3 solution of (b) 0.1 mM and (c) 0.2 mM, at different irradiation time and its (d) TEM image after 24 hrs. of light irradiation time.

It can be observed that after addition of Ag^+ ions, the peak at longer wavelength increased, similar to the previous case of neutral solution, due to additional supply of Ag^+ ions for growth of nanoplates. Fig. 4.14(d) show TEM image of Ag nanoparticles after 24 hrs. of irradiation in pH 10 condition in presence of added Ag^+ ion. Formation of different asymmetric shape nanoparticles other than triangular nanoplates can be observed in the figure. This shows that high pH condition of 10 could not produce high yield of Ag nanoplates.

4.9 SERS response of spherical and triangular shape Ag nanoparticles

For Raman measurements, spherical Ag nanoparticles, obtained in 10 mM citrate solution by 30 min. of ablation period, were used. Triangular shape Ag nanoparticles were obtained after 24 hrs. of irradiation of these spherical nanoparticles in presence of AgNO_3 of 0.2 mM concentration. Spherical Ag nanoparticles and triangular Ag nanoplates were centrifuged to one tenth of its original volume and mixed with dye solution of desired concentration. The obtained mixture was dispersed through sonication and then drop coated on thoroughly cleaned glass slides. Raman spectra were obtained using micro-Raman set-up (Horiba 800) in back scattering geometry 632.8 nm He-Ne Laser as excitation source, with overall spectral resolution of $\sim 1 \text{ cm}^{-1}$. Fig.4.15 presents the SERS spectra of Rh6G dye of 1 μM and 500 nM concentration in presence of different shapes of Ag nanoparticles. In case of spherical Ag nanoparticles, the Raman intensity of the dye is significantly low. Presence of triangular shape Ag nanoparticles resulted ~ 14 times higher intensity ($\sim 1364 \text{ cm}^{-1}$)

compared to that from spherical Ag nanoparticles. This is attributed to intense near-field around the triangular nanoplates having sharp edges or corners [22,23]. Also, for spherical nanoparticles, the LSPR wavelength is ~ 400 nm, which is quite far from the excitation wavelength of laser used for Raman measurements. For Ag triangular nanoplates, the LSPR is very strong around this excitation wavelength, which could be the reason for the observed strong Raman signal. Fig. 4.15(b) shows SERS spectra of the dye of 500 nM concentration. This indicates that presence of nanoparticles and also their LSPR excitation play an important role in obtaining strong SERS signal from the analyte molecule, which has to be detected.

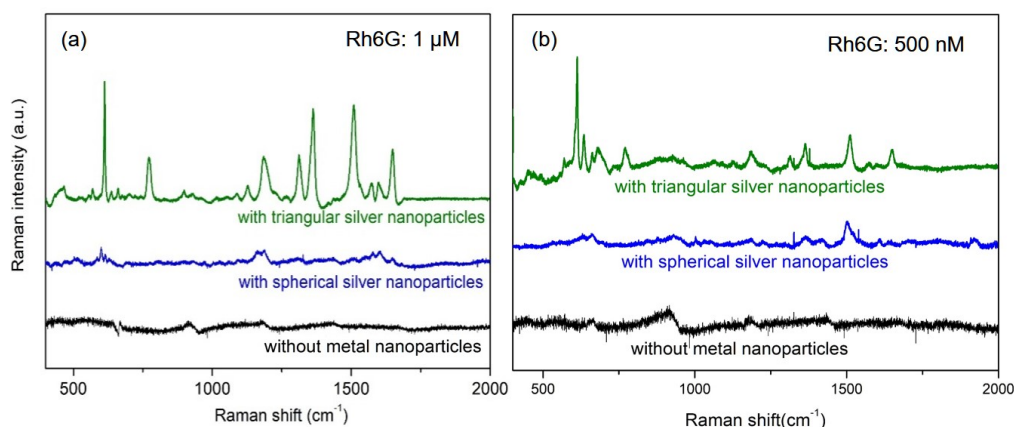


Fig. 4.15 SERS spectra of Rh6G molecules of (a) 1 μ M and (b) 500 nM concentration in presence of spherical and triangular Ag nanoparticles.

Fig. 4.16 shows SERS intensity of 1 μ M MB dye in presence of spherical and triangular shape Ag nanoparticles. Intense Raman peaks at $\sim 446, 479, 598, 680, 777, 809, 900, 1035, 1223, 1326, 1392, 1427$ and 1626 cm^{-1} were observed corresponding to different vibrational modes of MB dye, as reported in literature [176].

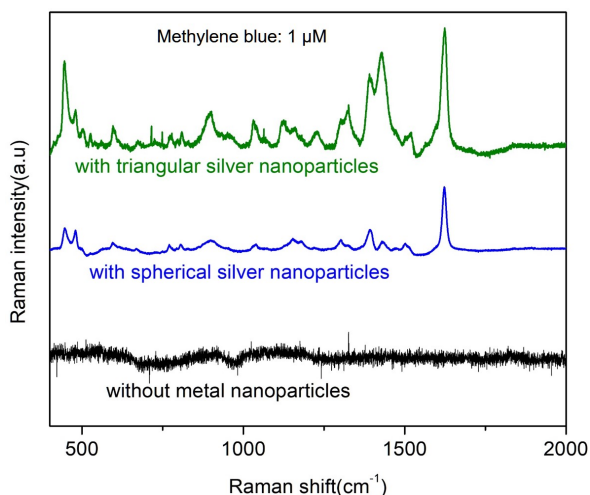


Fig. 4.16 SERS spectra of MB molecules of 1 μ M concentration in presence of spherical and triangular Ag nanoparticles.

Similar to the previous case, the peak intensity is higher in case of triangular shape Ag nanoparticles. than those obtained with spherical shape Ag nanoparticles. This confirms that the obtained SERS enhancement is due to local field enhancement, rather than chemical enhancement, and is irrespective of the type of dye molecules.

4.10 Summary

Growth of high concentration of Ag nanoparticles in aqueous citrate solution has been demonstrated using laser ablation of Ag target in liquid media. This method is versatile in producing nanoparticles in wide concentration range of citrate and also in pure DI water. The nanoparticle produced in either DI water or low concentration of citrate (< 0.05 mM), were found to aggregate to form interconnected nanostructure. At optimum concentration of about 10 mM, this method has resulted almost spherical and isolated spherical nanoparticles of desired concentration, proportional to laser ablation time, which is difficult to achieve through citrate reduction based chemical

synthesis. For 30 min. ablation at 100 mJ pulse energy, the experimentally measured absorption spectrum and that calculated with Mie theory revealed about 1.1×10^{12} nanoparticle/mL. At optimum citrate concentration, this method resulted nanoparticles of relatively smaller average size of about 13 nm in TSC alone, without aid of strong reducing agent like sodium borohydride. Irradiation of these spherical nanoparticles under conventional sodium lamp efficiently transformed into triangular nanoplates having strong LSPR over a wide wavelength range above 600 nm. During this light irradiation, external addition of Ag^+ ions, initially increased the LSPR absorbance of at about 400 nm and later it considerably increased absorbance of Ag nanoplates. LPPLA grown nanoparticles grown at TSC concentration >25 mM and pH ~ 10 resulted formation of smaller size triangular nanoplates after light irradiation. These results reveal 532 nm laser wavelength used in these experiments, does not interfere with the absorption of spherical Ag nanoparticles produced by LPPLA is promising for producing desired concentration of smaller size nanoparticles in wide range 5-25 mM of citrate concentrations. The produced spherical and triangular Ag nanoparticles are stable with shelf life more than one year and LSPR response spanning in the entire visible and near IR region are promising for various applications. The grown triangular Ag nanoplates are also shown to be useful for detection of different dyes at low concentration of about 1 μM through SERS technique.

Chapter 5

Studies on optical and photo-catalytic dye degradation response of Au cube-ZnO core-shell nanoparticles

Plasmonic noble metal-semiconductor composite nanostructures are important for various applications like photo-catalysis, water splitting, decomposition of organics and gas sensing [7,65,177]. In photo-catalysis, light energy absorbed by photocatalyst nanomaterial is utilized for chemical transformation. This requires suitable photo-catalyst with sufficient band gap having conduction band and valence band energy levels such that they fulfill the requisite redox potential for the required chemical reactions. Zinc oxide (ZnO) is well known n-type, wide band gap, non-toxic semiconductor with potential for photocatalytic processes [67,68]. Presence of noble metal nanoparticles in the form of composite material has been shown to enhance the overall photo-catalysis by affecting the processes involved in photocatalysis [177].

Among different metal-semiconductor composite nanostructures, core-shell nanoparticles have generated research interest due to distinct features, which are not possible with other configurations [100,178]. In presence of ZnO shell layer, aggregation of Au nanoparticles can be circumvented, and it also prevents corrosion of metal nanoparticles in strong chemical environmental conditions. Moreover, core-shell geometry also provides the maximum interface between metal nanoparticle and semiconductor surface, helpful for better charge transfer. Metal nanoparticles coated with CTAC/CTAB can be directly used for synthesis of core-shell nanoparticles in the ascorbic acid assisted growth method. In this regard, Au

nanocubes which are formed in CTAC solution becomes promising, because their optical response can be tuned over wide wavelength range and possess sharp corners and edges attractive for SERS application also. Variation in optical response of Au nanocube during growth of ZnO shell layer has not been studied yet in literature. This chapter addresses the optical response of Au-ZnO core-shell nanoparticles, effect of annealing on their crystalline quality, photo-catalytic activity of these nanoparticles towards degradation of cationic methylene blue (MB) and anionic (MO) dye of varied concentrations under different pH conditions.

5.1 Discrete dipole approximation for arbitrary shape nanoparticles

Discrete dipole scattering method is an open source numerical method for calculating the scattering and absorption of an arbitrary shape material of known dielectric response, based on the following framework [179,180]. It is well established that dielectric response of a material is related to polarizability of its constituent atoms, which is given by Clausius-Mossotti relation. Similarly, an object or target can be approximated as an array of N polarizable points i.e. point dipoles with inter-dipole spacing ' d '. Thus, cubic sub-volume of the target is d^3 and for N number of such dipoles, the total volume of the target is $V = Nd^3$, which gives d as $(V/N)^{1/3}$. In this way, the optical response of the target can be numerically obtained from self-consistent solutions for the oscillating dipole moments P_s , where s is the position of the occupied site, varying from 1 to N . For each dipole, the polarization $P_s = \alpha_s E_s$, where E_s is the electric field at point r_s , which is sum of the incident electric field $E_{inc,s} = E_o \exp^{i(k \cdot r - \omega t)}$ and combination from rest of the $N-1$ dipoles [180]. Therefore,

$$E_s = E_{inc,s} - \sum_{s \neq j} A_{s,j} P_j, \quad \dots (5.1)$$

where, the second term is the field at r_s due to dipole P_j at position r_j . $A_{s,j}$ is a matrix with diagonal element as $A_{ss} = (\alpha_s)^{-1}$. The scattering problem gets reduced to get P_s by solving 3N complex linear equations [180],

$$\sum_{j=1}^N A_{s,j} P_j = E_{inc,s}. \quad \dots (5.2)$$

After obtaining P_s , the extinction (C_{Ext}) and absorption (C_{Abs}) cross-sections are calculated from the following equations.

$$C_{Ext} = \frac{4\pi k}{|E_o|^2} \sum_{s=1}^N \text{Im}(E_{inc,s}^* \cdot P_s), \quad \dots (5.3)$$

$$C_{Abs} = \frac{4\pi k}{|E_o|^2} \sum_{s=1}^N \left[\text{Im}\{P_s \cdot (\alpha_s^{-1})^* P_s^*\} - \frac{2}{3} k^3 |P_j|^2 \right]. \quad \dots (5.4)$$

For infinite cubic lattice of dipoles, the polarizability α_s can be taken from the Clausius Mossotti relation, first used by Purcell and Pennypacker for DDA [181],

$$\alpha_s = \frac{3d^3}{4\pi} \frac{\epsilon_s - 1}{\epsilon_s + 2}, \quad \dots (5.5)$$

where, ϵ_s is the complex dielectric response of the target material at location r_s . However, for finite size targets, radiative reaction correction terms of the order of $(kd)^2$ and $(kd)^3$ have been proposed based on lattice dispersion relation analytical model [180], in the wavelength limit $kd \ll 1$,

$$\alpha_{LDR} = \frac{\alpha_s}{1 + (\alpha_s / d^3) \left[\left(c_1 + c_2 m^2 + c_3 m^2 \sum_{s=1}^3 (\hat{a}_s \hat{e}_s)^2 \right) (kd)^2 - (2/3)(kd)^3 \right]}, \dots (5.6)$$

where c_1 (-1.891531), c_2 (0.1648469) and c_3 (-1.7700004) are constants, \hat{a} and \hat{e} are unit vectors which define the direction and polarization state of the incident light and $m^2 = \epsilon$

of the target material. This modification in the polarizability holds good for the condition $|m|kd < 1$, i.e. inter-dipole spacing is much smaller than the wavelength of the interacting electromagnetic field in the target material. Therefore, DDA provides the best results for targets with not too large dielectric constant ($|m| \leq 2$). Another condition for validity of this method, is that N should be large (or d should be small) enough to describe the target shape satisfactorily. For target volume V , if a_{eff} is the effective radius $[=(3V/4\pi)^{1/3}]$ then,

$$N > \frac{4\pi}{3} |m|^3 (ka_{eff})^3. \quad \dots (5.7)$$

The extinction spectra of Au nanocubes was calculated with water as surrounding medium. Fig. 5.1(a) presents the extinction efficiency of Au nanocubes of different edge lengths. The extinction peak increased and red-shifted with the edge length of cubes. This is because the light scattering of nanoparticles scales with square of the volume, resulting large extinction. Peak red-shift can be attributed to retardation effect in large size nanoparticles [3,12]. When the nanoparticles with corners are formed, the particle edges are not sharp. Therefore, the calculation was also performed for Au nanocubes with smoothed edges, as shown in Fig. 5.1 (b). Edge smoothing in calculations was performed following the procedure mentioned by Jayabalan *et al* [182], which involves removing the nearest neighbor point dipoles having the least co-ordination number. With increasing percentage of edge smoothing of the cube, such that cube volume is reduced by 3, 5 and 8%, the extinction peak showed blue-shift of about 30, 34 and 42 nm in the LSPR peak respectively.

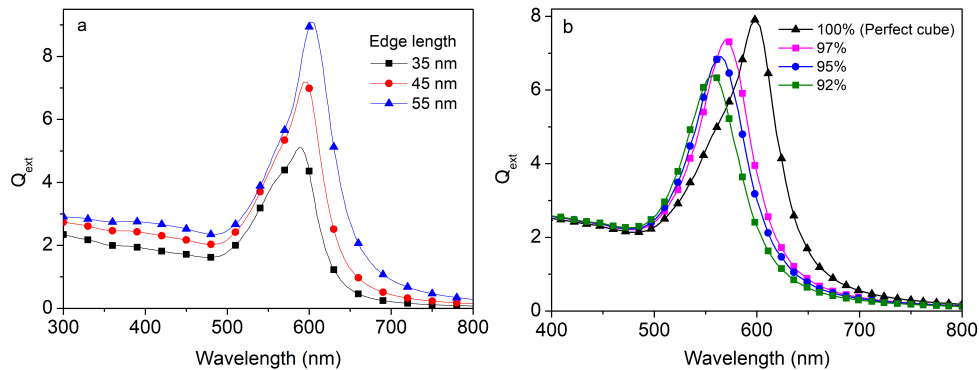


Fig. 5.1 Extinction efficiency of Au nanocubes of (a) varied edges lengths, and (b) with smoothed edges.

5.2 Growth of Au-ZnO core-shell nanoparticle

In synthesis of core-shell nanoparticles, the shell layer can be grown via different methods like precipitation, hydrothermal, multi-step cation exchange etc [100-102]. Cetyl-trimethyl ammonium bromide / chloride (CTAB/CTAC) surfactant assisted growth method is suitable to form core-shell nanoparticles with arbitrary shape metal nanoparticles [106]. It is a two-step process, which involves growth of CTAC coated metal nanoparticles followed by growth of ZnO shell layer.

Au nanocubes were grown by seed-mediated growth process. For this, Au seed particles were prepared by chemical reduction of HAuCl_4 (10mM, 24 μL) in CTAC (100mM, 1mL) solution with sodium borohydride (10mM, 0.06 mL). The seed nanoparticles were diluted 100 times and used for growth of Au nanocubes in growth solution consisting of HAuCl_4 (2.1mL, 10mM), AgNO_3 (0.45mL, 10mM), HCl (0.9mL, 1M) and CTAC (45 mL, 100mM) along with ascorbic acid (AA) (0.45 mL, 0.1 M). After the addition of seed nanoparticles, within half an hour, the transparent growth solution is converted to deep blue color in transmitted light.

For synthesis of Au-ZnO core-shell nanoparticles, AA assisted method of Yang *et al* was applied [106]. The grown Au nano-cubes were re-dispersed in CTAB (720 mL, 3 mM) after centrifugation. This solution was mixed with AA (40 mL, 100mM), zinc nitrate (40 mL, 150 mM) and HMT (40 mL, 150 mM) and stirred, before putting in water bath at $\sim 90^{\circ}\text{C}$ for four hrs. The solution color changed gradually from blue to magenta, which could be due to change in dielectric constant around the Au nanocubes or de-aggregation of Au nanocubes or spheroidization of cubes. TEM imaging was performed which showed shell layer formation around the Au nanocubes, confirming that the change in color is due to growth of shell layer. The concentration of CTAB was very crucial in obtaining core-shell nanoparticles as well as their stability in the solution. At high CTAB concentration of about 10 mM or more, the obtained nanoparticles were found to be highly dispersed and took more than 20 days to settle down in the solution. On the other hand, optimum CTAB concentration of about 2-5 mM allowed formation of uniform shell layer and nanoparticles settled down in about 3-4 hrs., helpful for their easy collection and washing. The formed core-shell nanoparticles were washed with DI water two times and then dried in form of powder. These nanoparticles were subsequently annealed at various temperatures in range 100-600 $^{\circ}\text{C}$ in muffle furnace for four hrs.

Fig. 5.2(a) presents morphology of Au nanocubes obtained from SEM, showing that the formed nanoparticles have sharp edges with average edge length of about 48 nm. Fig. 5.2 (b,c) and 5.2(d) shows TEM images of as grown and annealed Au-ZnO core-shell nanoparticles respectively. TEM image of as-grown nanoparticles shows

formation of uniform spherical shell layer on Au nanocubes, with average diameter of ~ 160 nm for core-shell nanoparticles.

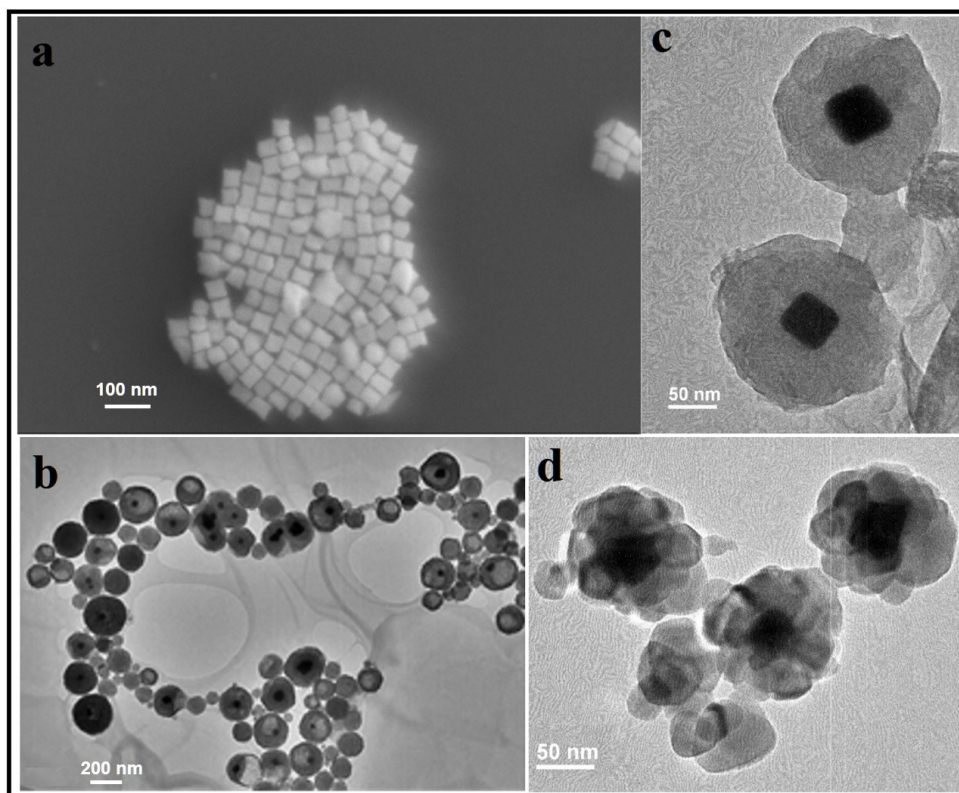


Fig. 5.2 (a) SEM image of Au nanocubes, and TEM images of Au-ZnO core shell nanoparticles (b, c) before and (d) after annealing.

At optimum CTAB concentration, edges of the Au cubes in the as-grown core-shell nanoparticles, get smoothed with growth of shell layer. Fig. 5.2(d) present the TEM image of these nanoparticles after annealing at 600 °C. It can be observed that after annealing the nanoparticles remained as core-shell and isolated particles without mixing.

The shape of Au nanocubes was transformed after annealing. Further, it can be noticed that the ZnO shell was transformed into small size nano-crystallites in the range of 11-15 nm, around the core. The TEM images also reveal that with annealing,

the initial uniform ZnO shell layer transformed into mesoporous structure. The formed porous ZnO shell structure can be advantageous for improved adsorption / diffusion of dye molecules / reactant species for photocatalysis.

5.3 Optical absorption of Au-ZnO nanoparticles during growth of shell layer

Fig. 5.3 shows variation of absorption spectra at different growth time intervals during shell layer growth. At the initiation stage, the spectra consist of absorbance peak at about 595 nm only corresponding to LSPR excitation in Au nanocubes. After 30 min. of growth, the spectra consist of another absorption edge ~ 350 nm, revealing formation of ZnO layer. In addition, LSPR wavelength of Au nanoparticles showed marginal blue-shift up to ~ 560 nm. After further growth, ZnO absorption edge remained the same, however the Au LSPR excitation peak slightly red-shifted to 566 nm.

During growth of ZnO shell layer on Au nanocubes, AA and CTAB presence is essential [106]. The mechanism of shell formation is shown to be two-step process, which involves selective deposition of $[\text{Zn}(\text{OH})_4]^{2-}$ around Au nanoparticles and subsequent dehydration to form dense ZnO shell layer. In the first step, AA forms complex $[\text{AA}-\text{Zn}(\text{OH})_4]^{2-}$ which interact with CTAB molecules around Au nanoparticles forming $\text{CTAB}-[\text{AA}-\text{Zn}(\text{OH})_4]^{2-}$. The repeated units of this form net-like structure around the nanoparticles. In the second step, hydroxyl condensation at high temperature results into formation of ZnO shell layer. In core-shell nanoparticles, red-shift of plasmon excitation peak with respect to pure Au nanocubes is due to increase in refractive index with formation of ZnO layer. However, at initial

stage of ZnO growth, the observed blue-shift of LSPR peak could be due to change in morphology of the Au nanoparticles. Nanoparticles with sharp edges like cubes and triangular prisms, heating can induce smoothening of their corners or edges [182-184].

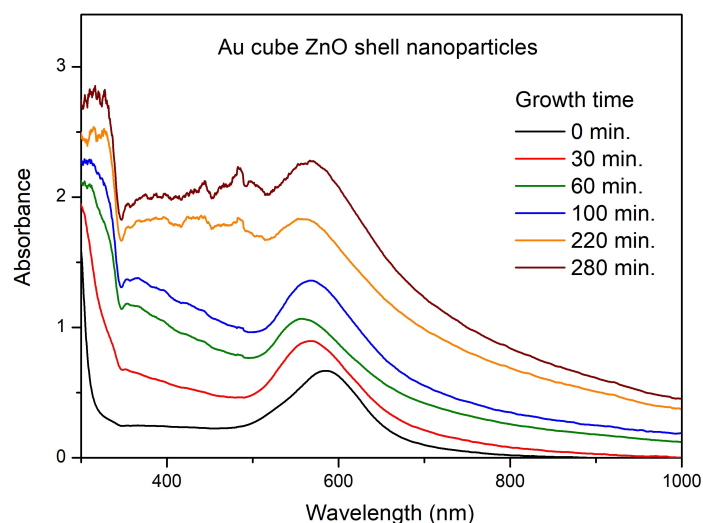


Fig. 5.3 Optical absorption spectra of core-shell nanoparticles during growth.

The atoms on surface of nanoparticles, particularly at edges require less thermal energy to rearrange, because of their low co-ordination number. Fig. 5.1 (b) shows that about 3% edge smoothening resulted 15 nm blue-shift in LSPR. Therefore, at the initial stage, the observed blue-shift in the LSPR peak is due to edge smoothening of Au nanocubes because of high temperature growth of ZnO shell layer. With the ZnO layer growth, nanoparticle shape deformation is restricted and it exhibited red-shifted LSPR because of increased refractive index of the surrounding [99].

5.4 Effect of annealing on optical response and structural characteristics of core-shell nanoparticles

During synthesis of core-shell nanoparticles, surfactants were used. Therefore, annealing was carried out for the grown nanoparticles. Fig.5.4(a) shows UV-Vis. absorption spectra of core-shell nanoparticles after annealing at 100 °C, 300 °C and 600 °C. With annealing, the absorbance varied about ZnO band edge. Distinct exciton peak around 360-375 nm was noticed after annealing of the nanoparticles. Observation of exciton peak \sim 370 nm indicates improved crystallinity of ZnO [99,185]. Without Au nanocubes, pure ZnO was also synthesized under the same experimental conditions and the obtained powder is annealed. Inset of the figure shows variation of UV-Vis. absorption of pure ZnO nanoparticle annealed at 100, 300 and 600°C. These spectra show presence of excitonic absorption after annealing, similar to the core-shell nanoparticles. This assures that crystallinity of ZnO nanoparticle is improved after annealing process. Fig. 5.4(b) shows FTIR spectra of the as-grown and 600 °C annealed Au-ZnO core-shell and pure ZnO nanoparticles. In all the spectra, significant absorption band at about 510 cm^{-1} is observed, attributed to Zn-O vibration of ZnO [102,106].

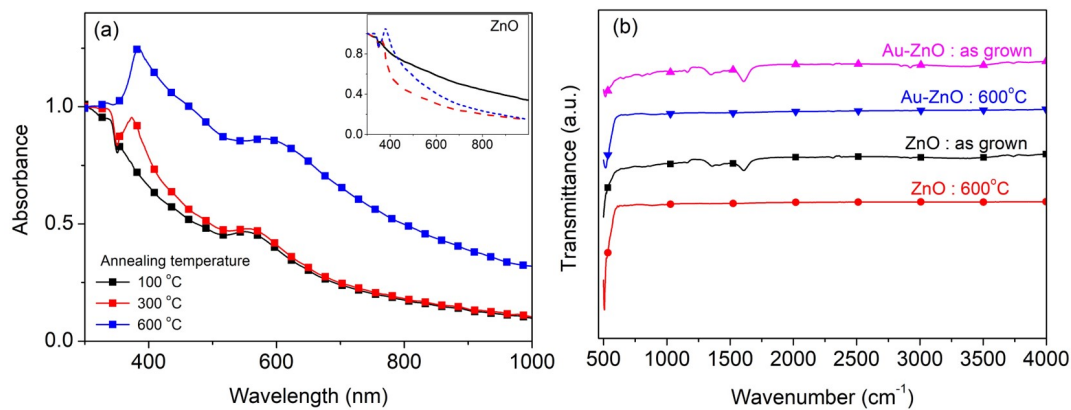


Fig. 5.4 (a) Optical absorption spectra and (b) FTIR spectra of annealed Au-ZnO

core-shell nanoparticles.

As-grown ZnO and Au-ZnO nanoparticles showed different absorption bands in 1010-2010 cm^{-1} range, corresponding to CTAB molecules [106,187]. The observed bands in 1305-1610 cm^{-1} is attributed to bending vibration of C-H. Bands at ~ 2861 and 2921 cm^{-1} are shown to arise from stretching vibration of C-H of methylene and methyl groups of CTAB [106,187]. The wide band at $\sim 3445 \text{ cm}^{-1}$ has been attributed to stretching vibration of hydroxyl groups [187]. These bands were not observed in case of annealed ZnO and A-ZnO nanoparticles. It further confirms that annealing has led to removal of different molecular species used in the growth process.

Effect of annealing at different temperatures on crystallinity of Au-ZnO core-shell nanoparticles was analyzed using XRD. Fig.5.5 shows XRD spectra of as-grown and annealed core-shell nanoparticles. In all the core-shell nanoparticles, XRD peaks of both Au and ZnO were observed. The peaks at 38.22° , 44.36° , 64.57° and 77.5° corresponding to FCC phase of Au metal were observed. The peaks at 31.67° , 34.44° , 36.24° , 47.55° , 56.47° , 62.98° and 68.07° correspond to Wurtzite hexagonal structure of ZnO [188,189]. The figure shows that intensity of XRD peaks of Au nanoparticles remained almost same for all the annealed samples. However, the peak intensity of ZnO significantly increased with annealing temperature. This confirms improved crystallinity of the ZnO shell layer after annealing and is in agreement with observations made from absorption spectra (Fig. 5.3).

The compositional characteristic of Au-ZnO core-shell nanoparticles was analyzed using XPS. Fig. 5.6 (a-c) compares BE spectrum of Zn-2p, O-1s and Au-4f

core levels respectively of Au-ZnO core-shell and pure ZnO nanoparticles, annealed at 600°C. The splitting between core levels of Zn 2p, in Fig. 5.6 (a), is found to be about 23.2 eV.

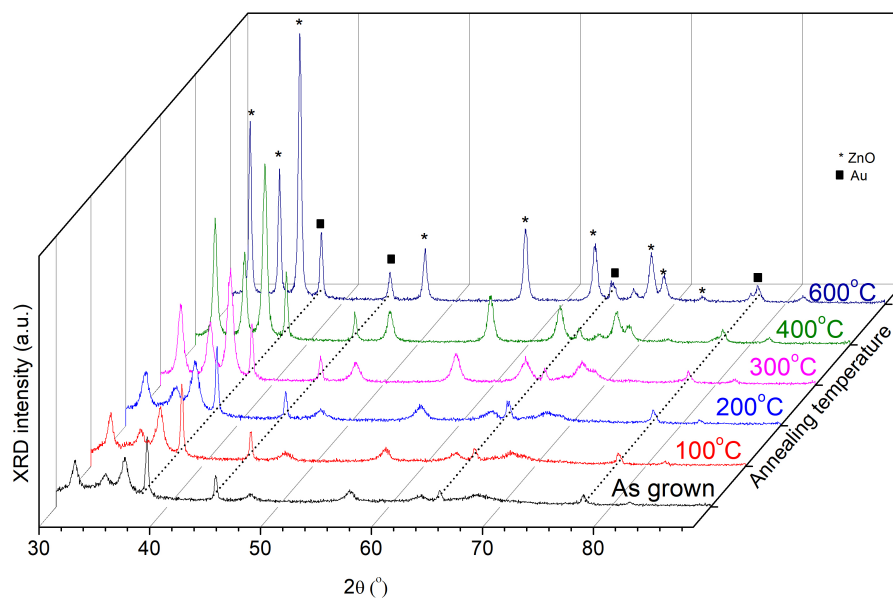


Fig. 5.5 XRD intensity of as-grown and annealed Au-ZnO core-shell nanoparticles.

This is found to be similar for both ZnO and Au-ZnO nanoparticles showing that Zn exist in Zn^{2+} state [188,190]. The BE peak of O is de-convoluted in two peaks; at about 530.3 and 532 eV for pure ZnO and, 530.4 and 532.3 eV for Au-ZnO core-shell nanoparticles. BE peak at ~ 530 eV is attributed to oxygen of ZnO lattice with complete coordination number [188,190,191]. The BE peak at higher energy has been attributed to oxygen of surface adsorbed OH group. These observations are in line with other reported results related to Au-ZnO nano-composites [190,191]. The binding energy spectra of Au-4f peaks at 83.05 and 86.85 eV, are overlapped with that of Zn-3p in Au-ZnO core-shell nanoparticles. Au peak positions are found to be shifted towards lower BE from that of the metallic Au at 84.0 and 87.67 eV [188,191],

which can be due to charge transfer from ZnO to Au in Au-ZnO core-shell nanoparticles. This is because donor level of ZnO lies close to the fermi level (5.4 eV) of Au [188,191]. The above results show that Au exist in metallic state in the grown Au-ZnO nanocomposite and charge transfer took place at the interface.

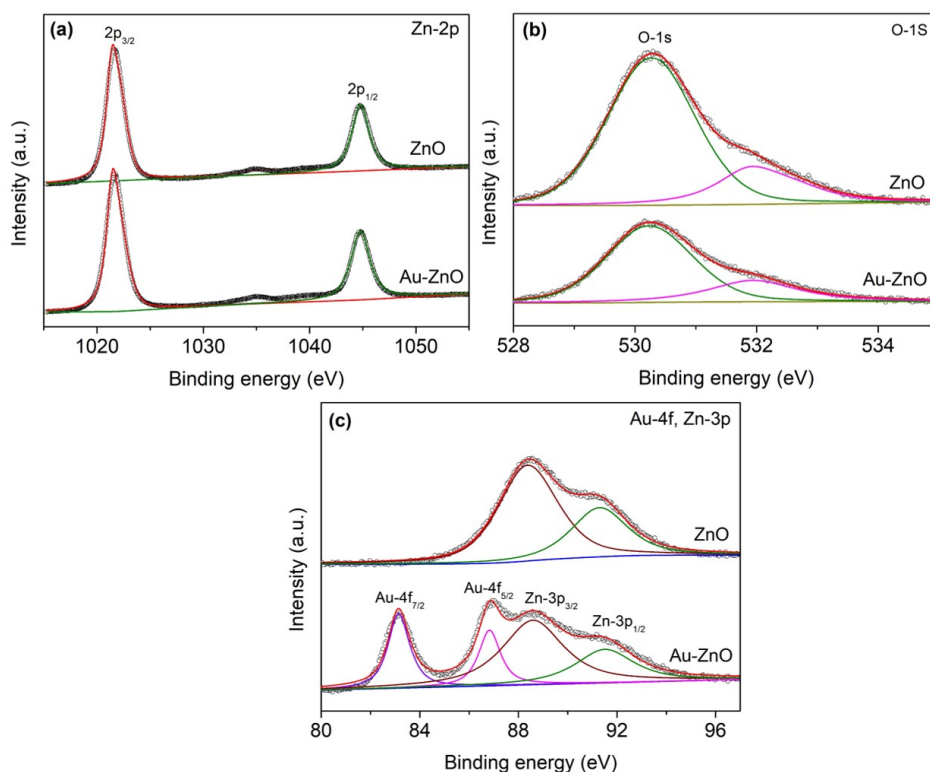


Fig.5.6 XPS BE spectrum of (a) Zn-2p, (b) O-1s and (c) Au-4f, Zn-3p of Au-ZnO core-shell and ZnO nanoparticle.

5.5 Photocatalytic dye degradation kinetics

Dye degradation is heterogeneous photocatalytic process which is driven by photo-generated charge carriers in nanoparticles and subsequently produced ROS. In this process, dye molecules adsorbed on surface of photocatalyst i.e. nanoparticles react with photo-generated ROS. If C is the concentration of dye and θ is fractional surface coverage, then under equilibrium condition, rate of adsorption becomes equal

to rate of desorption, which can be written as,

$$k_1 C (1 - \theta) = k_{-1} \theta, \quad \dots (5.8)$$

where k_1 (L/mole) and k_{-1} (dimensionless) are the equilibrium constants for adsorption and desorption processes respectively [190]. From the above equation, fractional coverage of the nanoparticles, is given as,

$$\theta = \frac{KC}{1 + KC} \quad \dots (5.9)$$

where, K (k_1/k_{-1}) is the Langmuir adsorption equilibrium coefficient [190,193]. The above expression is also known as Langmuir adsorption equation which is valid for monolayer coverage of dye molecules on photocatalyst [191]. Since, the dye degradation rate is proportional to the number of adsorbed dye molecules, therefore,

$$-\frac{dC}{dt} \propto \theta; \quad -\frac{dC}{dt} = k \frac{KC}{1 + KC}, \quad \dots (5.10)$$

where k is proportionality constant. It depends on other experimental conditions like type of incident radiation, dissolved oxygen, temperature etc [192,194]. This model is known as Langmuir Hinshelwood (LH) model. At very low dye concentration, $KC \ll 1$, the degradation rate becomes linear function of the dye concentration C , with degradation rate constant as kK :

$$-\frac{dC}{dt} = kKC \quad \dots (5.11)$$

This shows exponential variation of dye concentration in the photocatalysis process. Most of the experimental results have been fitted with exponential function, and the rate constant of the process has been reported [192-194]. However, applicability of this limiting case and deviation from this model has been addressed based on the results of the dye degradation at varied concentrations of the dye [194].

5.6 Photo-degradation of MB dye

Au-ZnO core-shell nanoparticle was used as photo-catalyst for photocatalytic degradation of MB dye. Photo-degradation process was carried out under UV light irradiation (02 Nos. 8W each, Phillips) in presence of varied amounts of photocatalyst in the range of (0.2-3 g/L). Before light irradiation, photocatalyst mixed dye solution was stirred for one hour in dark condition to ensure dye adsorption on the photocatalyst. Fig. 5.7 (a-c) shows absorption spectra of dye at different irradiation time intervals in presence of as-grown, 600°C annealed Au-ZnO core-shell and pure ZnO nanoparticles respectively. In presence of as-grown nanoparticles, absorbance of dye did not vary much over 200 min. of light irradiation.

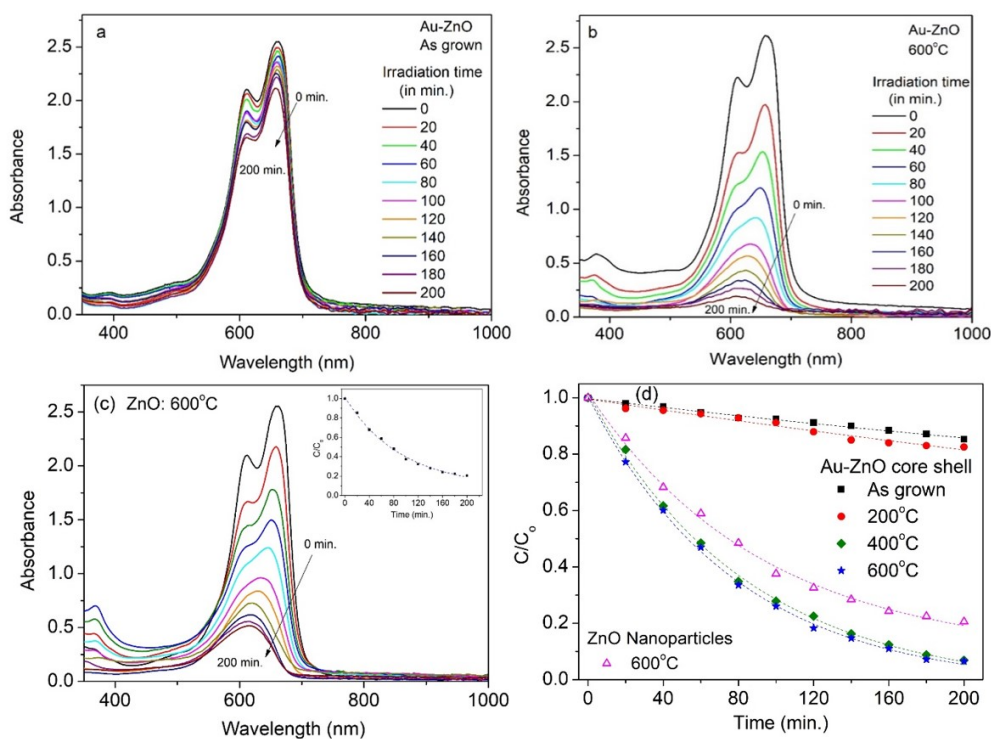


Fig.5.7 Absorbance spectra of MB dye versus irradiation time in presence of (a) as-grown, 600°C annealed (b) Au-ZnO and (c) ZnO nanoparticles, (d) corresponding

normalized dye concentration.

However, in presence of 600 °C annealed either Au-ZnO core-shell or pure ZnO nanoparticles, absorbance peak of MB dye significantly reduced for light irradiation of about 200 min. Fig. 5.7 (d) presents the normalized dye concentration versus irradiation time. It can be observed that in presence of as-grown and 200 °C annealed core-shell nanoparticles, the change in peak absorbance is considerably small as compared to that observed for nanoparticles annealed ≥ 400 °C. Peak absorbance (A) of the dye is related to its concentration (C) as: $A = \xi C d_o$, where ξ is molar extinction coefficient, and d_o is cuvette path length. Degradation efficiency, at a given irradiation time, is

$$\eta(\%) = \left(1 - \frac{C}{C_o}\right) 100 = \left(1 - \frac{A}{A_o}\right) 100, \quad \dots (5.12)$$

where, C (A) and C_o (A_o) are concentration (absorbance) of the dye after and before light irradiation respectively. For 3 hrs. of light irradiation, the degradation efficiency of 600 °C annealed Au-ZnO core-shell nanoparticles was observed to be about 95%, and for ZnO nanoparticles, it is about 80%. Larger efficiency of dye degradation in case of Au-ZnO core-shell nanoparticle, compared to pure ZnO nanoparticle can be attributed to improvement in separation of photo-generated charges and increased ROS generation in Au-ZnO composite [65,188,190,191]. Under light irradiation, photo-generated electrons can transfer from ZnO to Au, and decreases electron-hole recombination, thus enhancing the probability of ROS generation. The mesoporous ZnO shell formed after annealing can facilitate easy charge transfer to dissolved oxygen or direct reduction of dye molecules [195]. High

degradation efficiency in presence of Au nanoparticles, compared to pure ZnO is similar to other results reported in literature [195].

In all the above cases, the variation of peak absorbance (or concentration) can be fitted with exponential form that shows linear rate kinetics of the process.

$$-\frac{dC}{dt} \propto [C] \quad ; \quad -\frac{dC}{dt} = k_{app}[C] \quad \dots (5.13)$$

where, k_{app} represents apparent first order rate constant. From exponential fitting, k_{app} is found to be about 1.1×10^{-3} , 1.19×10^{-2} and $1.26 \times 10^{-2} \text{ min}^{-1}$, for core-shell nanoparticles annealed at 200 °C, 400 °C and 600 °C respectively. Annealing of core-shell nanoparticles above ≥ 400 °C, has resulted almost one order higher magnitude of rate constant.

For all the photocatalytic experiments shown now onwards, 600°C annealed Au-ZnO core-shell nanoparticles (CS600) has been used. Effect of type of UV irradiation on photo-degradation of dye was analyzed Fig. 5.8(a) presents the normalized dye concentration versus irradiation time for 50 μM MB dye, mixed with 1g/L of CS600, under UV-A and UV-C lamp irradiation and their combination. Dye photo-degradation efficiency was found to be higher under UV-C irradiation compared to UV-A light. Fig. 5.8 (b) shows that maximum emission of UV-A light occurs at 365 nm, which is close to ZnO absorption edge. This will result better light absorption and charge carrier generation, therefore resulting faster degradation process. Combination of the two lamps (UV-A and UV-C) irradiation resulted degradation efficiency in between that obtained with individual lamps. Combination of these lamps has been used for all the measurements.

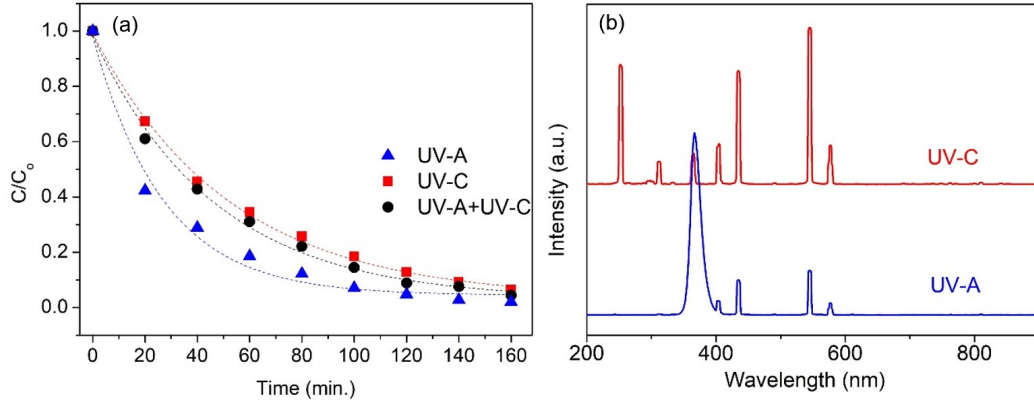


Fig.5.8 Comparison of (a) dye degradation process under irradiation of UV-A and UV-C light and (b) their intensity pattern.

In order to know that the observed exponential decay of dye degradation is limiting case of LH kinetics (Eq. 5.10), the degradation process was studied for varied initial concentrations (5-75 μM) of the dye. Fig. 5.9 (a) presents the normalized dye concentration versus irradiation time for varied initial concentrations of dye mixed with 1g/L of CS600. It may be noted that in all the cases, the absorbance decreased exponentially. At low dye concentration it is exponential, however, it tends toward linear at higher initial concentration $\geq 50 \mu\text{M}$. The concentration of dye at which $KC \ll 1$ was determined by obtaining K value from the relation of k_{app} with dye concentration [196,197]. At initial stage, before light irradiation, $[C] = [C_0]$,

$$k_{app}C_0 = \frac{kKC_0}{1 + KC_0}, \quad \dots (5.14)$$

which after rearrangement, becomes,

$$\frac{1}{k_{app}} = \frac{1}{kK} + \frac{C_0}{k}. \quad \dots (5.15)$$

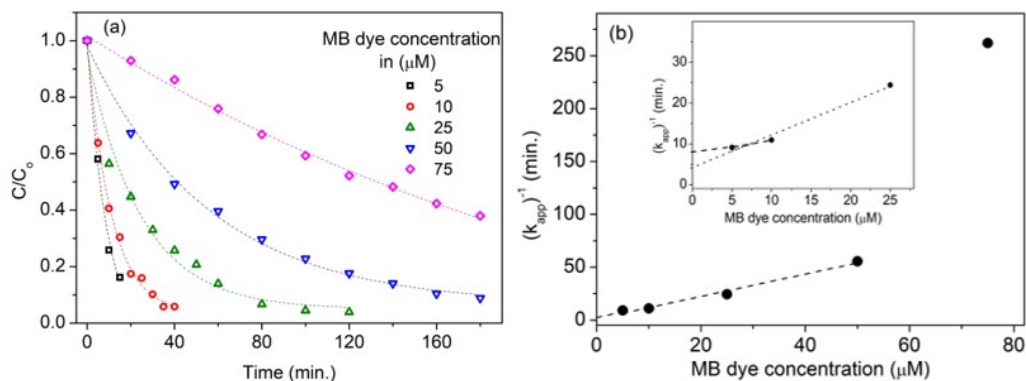


Fig. 5.9 (a) Normalized dye concentration versus irradiation time (b) inverse of apparent rate constant for different initial dye concentrations.

Fig. 5.9(b) shows variation of $(k_{app})^{-1}$ with initial dye concentration. The figure shows that up to 50 μM dye concentration, inverse of the apparent rate constant follows a linear relationship. From the straight-line fitting ($\chi^2 = 0.977$), the K value comes out to be $0.86 \text{ L}\mu\text{M}^{-1}$. This value was found to depend on the range of dye concentration. By fitting the straight line up to 10 μM , the K value was $0.049 \text{ L}\mu\text{M}^{-1}$. This shows that at lower dye concentration, K value is small enough to consider the degradation process as a limiting case of LH model. However, for higher dye concentrations $> 50 \mu\text{M}$, the degradation process deviates from it. Such deviations have been reported to be arising from change in adsorption rate constant with and without irradiation, number of reactive sites after irradiation and variation in reaction order under irradiation [194-197]. This shows that though the variation in dye concentration can be fitted with exponential function, the degradation process follows first order kinetics, only at very low initial concentrations of $< 10 \mu\text{M}$.

In order to find the optimum loading of photocatalyst (CS600) for dye degradation, the photo-catalytic process was analyzed at different amounts of

nanoparticles in the range of 0.2 to 3 g/L. Fig. 5.10 (a) and (b) show the normalized dye concentration versus duration of UV irradiation for 25 and 50 μM initial dye concentrations respectively in presence of different amount of photo-catalyst (CS600). For both the cases, increasing the amount of photocatalyst enhanced the degradation process. This is due to availability of more photocatalyst surface for adsorption of dye as well as light absorption.

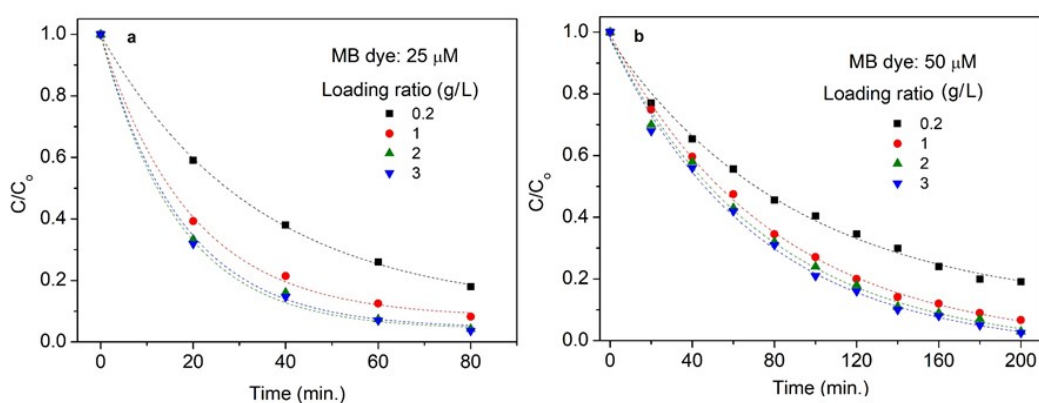


Fig. 5.10 Normalized dye concentration versus irradiation time for MB dye of initial concentration (a) 25 and (b) 50 μM , in presence of different loading of photocatalyst.

For low dye concentration (25 μM), increasing the photocatalyst amount 0.2 - 3 g/L, efficiency of photo-degradation increased from 82% to 96%, in about 80 min. of irradiation. However, for 50 μM concentration of dye, the same degradation occurred over 200 min. of light irradiation time. For the same amount of photocatalyst, more surface area will be available for case of low concentration (25 μM) of dye, resulting faster degradation process. It can be noted that, at higher loading of photocatalyst from 2 to 3 g/L, increase in photo-degradation rate constant is relatively small. For high loading of the photocatalyst, the light absorbed by the entire photocatalyst becomes low, since maximum incident light is absorbed in upper layer of solution.

Consequently, after optimum loading (depends on the geometry of the reaction setup) increasing photo-catalyst amount did not increase the photoabsorption. Further in case of high amount of photocatalyst, aggregation of nanoparticles resulting reduced surface area, has also been reported to show saturation effect on efficiency of dye degradation with photocatalyst loading [192,193].

5.6.1 Effect of presence of various scavengers

Photo-degradation of dyes involves different chemical reactions, driven by various ROS generated by photocatalyst. To understand role of different ROS, degradation experiments were performed in presence of various scavengers (chemical species), which selectively consume particular ROS, generated during photocatalysis. The major ROS involved in dye degradation process, as mentioned in literature, are hydroxyl radical ($\cdot\text{OH}$), superoxide ($\cdot\text{O}_2^-$) and singlet oxygen ($^1\text{O}_2$), apart from electrons and holes [195,198-202]. In this study, effect of three different scavengers, namely sodium salt of ethylenediaminetetraacetic acid (EDTA- Na_2) as hole scavenger [195,198,199], sodium azide (NaN_3) as $^1\text{O}_2$ and $\cdot\text{OH}$ scavenger [200-202] and iso-propyl alcohol (IPA) as a $\cdot\text{OH}$ scavenger [195,198-200], is addressed on photo-degradation of dyes. Fig. 5.11 (a-c) shows the normalized dye concentration versus light irradiation for 50 μM MB dye mixed with 1g/L of CS600 and EDTA- Na_2 , NaN_3 , and IPA scavengers respectively. In all the cases, presence of scavenger decreased the dye degradation efficiency. Increasing the concentration of EDTA- Na_2 from 0.01 mM to 2.5 mM, photo-degradation efficiency reduced from 80% to 16%, refer Fig. 5.11 (a). Since EDTA- Na_2 acts as hole scavenger, suppression in

photo-degradation process in its presence shows that holes play important role in dye degradation. Photo-generated holes can influence photo-degradation process in following ways: i) it can cause direct oxidation of dye molecules and degrade them, ii) it produces highly reactive $\cdot\text{OH}$ radicals when react with water molecules or OH^- ions in the solution [195,199]. Thus EDTA-Na_2 can cause suppression in direct oxidative degradation of dye molecules or decrease in generation of $\cdot\text{OH}$ radicals, both decreases the dye degradation efficiency. Fig. 5.11(b) shows that presence of NaN_3 also significantly reduced the degradation efficiency with increase of its concentration.

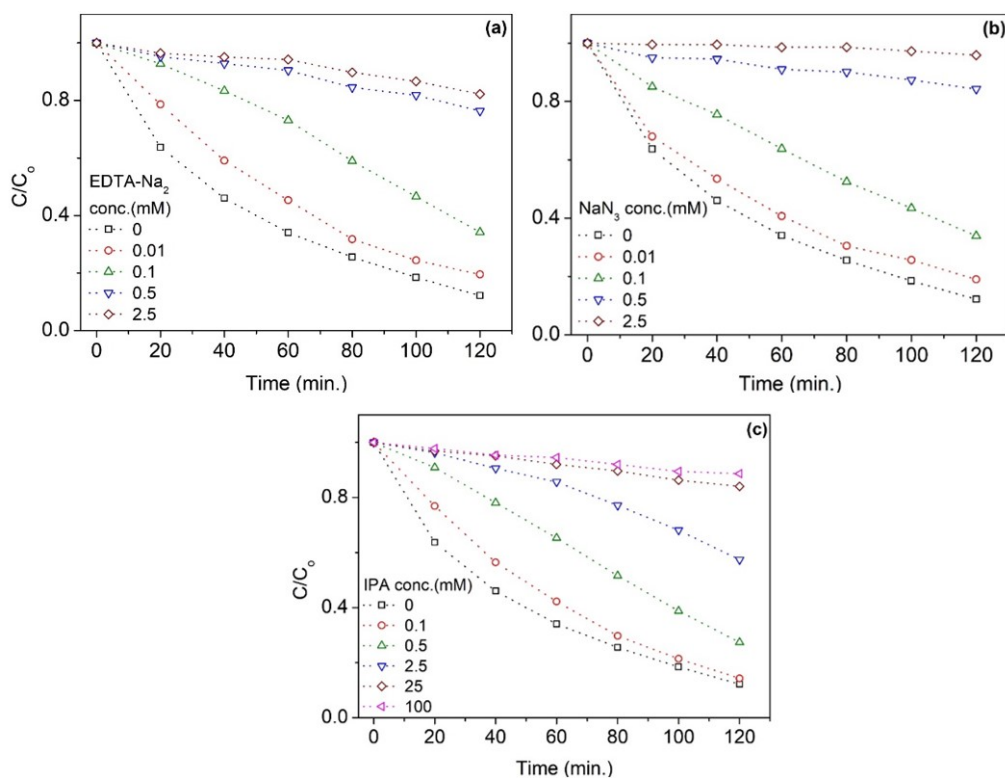


Fig. 5.11 Normalized dye concentration versus irradiation time for MB dye [50 μM] mixed with 1g/L of CS600 and scavengers (a) EDTA- Na_2 , (b) NaN_3 and (c) IPA of varied concentrations.

It has been reported that NaN_3 can scavenge effectively both $^1\text{O}_2$ and $\cdot\text{OH}$ radicals with scavenging rate of $\sim 7.7 \times 10^8$ and $1.4 \times 10^{10} \text{ M}^{-1}\text{s}^{-1}$ respectively [201]. Due to scavenging of multiple species, it has shown highest inhibition of degradation process. Fig. 5.11(c) presents effect of IPA of varied concentrations on photo-degradation efficiency. For the same scavenger concentration, IPA showed mild effect on inhibition of degradation process as compared to EDTA-Na_2 and NaN_3 . IPA scavenges $\cdot\text{OH}$ radical with scavenging rate of about $1.1 \times 10^9 \text{ M}^{-1}\text{s}^{-1}$, which is almost one order of magnitude lesser than that of NaN_3 [201]. In order to further verify the role of $\cdot\text{OH}$ radicals, IPA concentration was increased from 2.5 mM to 25 mM and 100 mM. High concentration of IPA, resulted complete inhibition of photo-degradation of the dye. These results show that $\cdot\text{OH}$ radicals play an important role in dye degradation process. In presence of EDTA-Na_2 , $\cdot\text{OH}$ radical formation is suppressed due to scavenging of holes, and other two scavengers directly suppress the $\cdot\text{OH}$ radicals. As a result, in presence of these scavengers, the photo-degradation was significantly decreased.

To compare photo-degradation of dye by low power UV lamp irradiation with 300W Xenon lamp, the degradation process was also carried out with Xenon lamp irradiation. Fig. 5.12 shows normalized dye concentration versus xenon lamp irradiation time for 50 μM MB dye mixed with CS600 photocatalyst, without and with scavengers. Without scavenger, the degradation rate constant increased by about 1.5 times compared to that observed with irradiation under UV lamp. With IPA, EDTA-NA_2 and NaN_3 scavengers of 2.5 mM concentration, photo-degradation dye

efficiency was found to be ~ 80%, 42% and 12% respectively, compared to 95%, which is observed without scavenger. At a given concentration of scavenger, inhibition of dye degradation for different scavengers was found to be in order $\text{NaN}_3 > \text{EDTA-Na}_2 > \text{IPA}$, i.e. same as observed with UV irradiation.

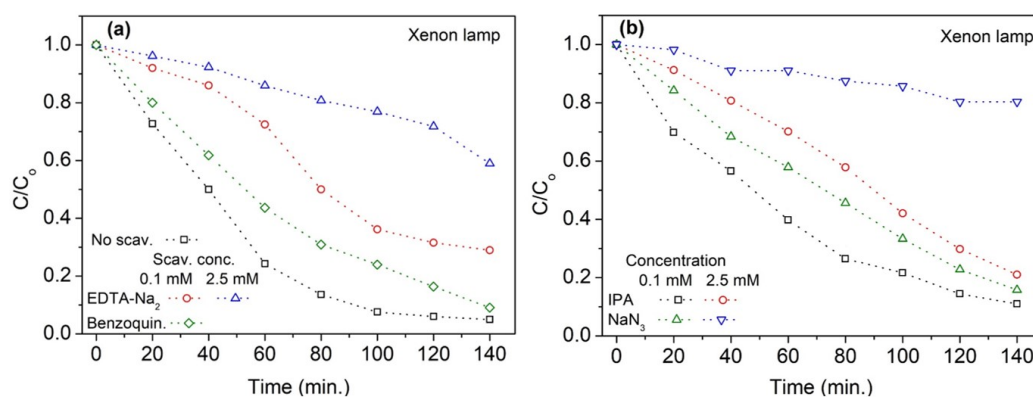


Fig. 5.12 Normalized dye concentration versus xenon lamp irradiation for MB dye ($50 \mu\text{M}$) mixed with 1g/L of CS600 without and with scavengers.

The inhibition of photo-degradation of dye by these scavengers is observed to be relatively low under xenon lamp irradiation. This can be attributed to faster degradation of dye under xenon lamp irradiation, due to relatively high intensity as compared to UV lamps.

5.6.2 Effect of pH

As mentioned above, dye degradation process involves adsorption of dye molecule on photocatalyst surface and subsequent reactions with various ROS. The adsorption characteristics of photocatalyst varies with its surface charge characteristics. To determine surface charge at different pH values, of Au-ZnO core-shell nanoparticles, measurement of zeta potential was performed with the help of zeta analyzer (Malvern Instruments). Table 5.1 presents the observed zeta potential

values of 600 °C annealed core shell nanoparticles in different pH conditions. In general, when oxide nanoparticles (e.g. ZnO, TiO₂) are dispersed in water, the water molecules get adsorbed on surface of nanoparticles, causing their surface to be hydroxylated [192,198]. Under low pH conditions, protonation of hydroxylated surface results positive surface charge on the nanoparticles. Under high pH condition, de-protonation of hydroxylated surface produces negative surface charge of the nanoparticles [198]. The table shows that with increasing pH i.e. OH⁻ ion concentration, the surface charge of core-shell nanoparticles consistently became negative.

Table 5.1 Zeta potential (ζ) of 600°C annealed Au-ZnO core-shell nanoparticles (CS600)

pH value	3	Neutral	8	10	12
ζ (mV)	32.4	22	- 4.04	- 13.3	- 56.8

Fig. 5.13 (a, b) shows the normalized dye concentration versus UV irradiation time for 50 μ M MB mixed with 1g/L of CS600 at different pH, along with neutral solution. For low pH of about 3, the dye degradation rate was found to be about $1.4 \times 10^{-2} \text{ min}^{-1}$, lesser than that observed with neutral solution ($1.5 \times 10^{-2} \text{ min}^{-1}$). With increase of solution pH, the degradation rate also increased, and at pH \sim 12, complete photo-degradation occurred within UV lamp irradiation of 40 min. For this case, degradation rate constant was found to be about $2.2 \times 10^{-1} \text{ min}^{-1}$ which is almost 15 times of that observed for neutral solution at pH 12 condition. From this, it can be

inferred that high pH condition favors photo-degradation process of dye. It can be attributed to increased negative charge on the nanoparticles at higher pH conditions, leading to better dye adsorption on surface of nanoparticles. Further, increasing OH⁻ ion concentration also favors generation of more ·OH radicals. At pH ~12, photo-degradation of dye was also analyzed in presence of scavengers. Fig. 5.14 (b) shows the normalized dye concentration versus UV irradiation time for 50 μM MB dye mixed with 1g/L of CS600 along with scavengers of high concentration. The figure depicts that under high pH condition, dye degradation occurred even in presence of scavengers. Thus, effect of scavengers was found to be limited for degradation of cationic MB dye, under high pH condition. Therefore, by varying pH conditions, effect of different scavenging species can be circumvented in treatment of cationic dye based waste water.

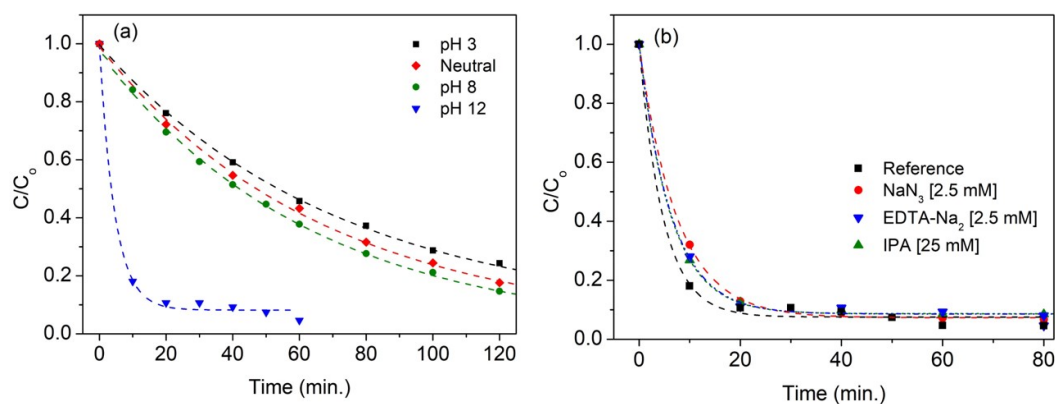


Fig. 5.13 Normalized dye concentration versus irradiation time for MB dye [50 μM] mixed with 1 g/L of CS600 (a) under varied pH condition (b) and different scavengers.

Fig. 5.14 presets the photographic image of core-shell nanoparticles and UV lamp irradiated MB solution when mixed with these nanoparticles. It shows that

annealed nanoparticles result complete degradation of MB dye in 2-3 hrs. in neutral condition and within 30 min. (0.5 hrs.) at high pH conditions; whereas in presence of as-grown core-shell nanoparticles or annealed nanoparticles with different scavengers, dye degradation does not occur. In this case, with increase of pH of the solution, the dye degradation efficiency improved significantly.

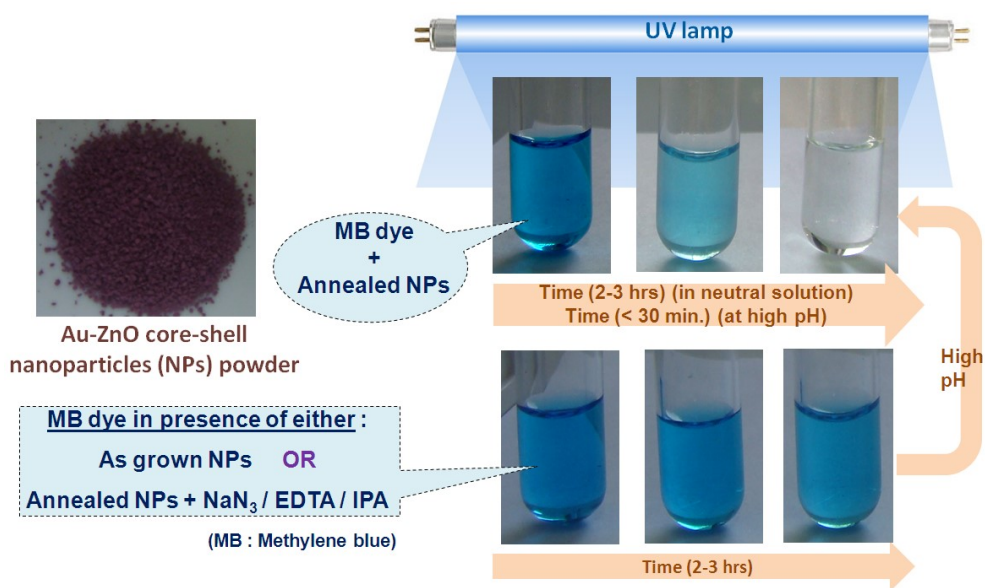


Fig. 5.14 Photographic image of core-shell nanoparticles and effect of UV irradiation time, pH and scavenger on degradation of MB solution when mixed with these nanoparticles.

5.7 Photo-degradation of MO dye

The waste water effluent contains different types of dyes which can be cationic or anionic in nature. To identify, utility of the core-shell nanoparticle for photo-degradation of anionic dyes, photocatalytic measurements were also carried out with anionic methyl orange (MO) dye. It is an azo dye, widely used in textile, food, printing and pharmaceutical industries [199]. Fig. 5.15(a) presents absorption spectra

of MO dye mixed with 1g/L of CS600 after different irradiation time interval. Peak absorbance at about 470 nm, arising from π to π^* transition of di-methylamino electron donors in MO [193], decreased with irradiation time and almost suppressed in about 140 min. of irradiation. Fig. 5.15(b) presents the normalized concentration versus irradiation time for varied initial concentrations of MO dye, mixed with 1g/L of CS600. The value of k_{app} decreased with increasing initial MO concentration, which are 1.8×10^{-2} , 1.3×10^{-2} , 4.6×10^{-3} , and $2.1 \times 10^{-3} \text{ min}^{-1}$, for 10, 25, 50 and 100 μM dye concentrations respectively.

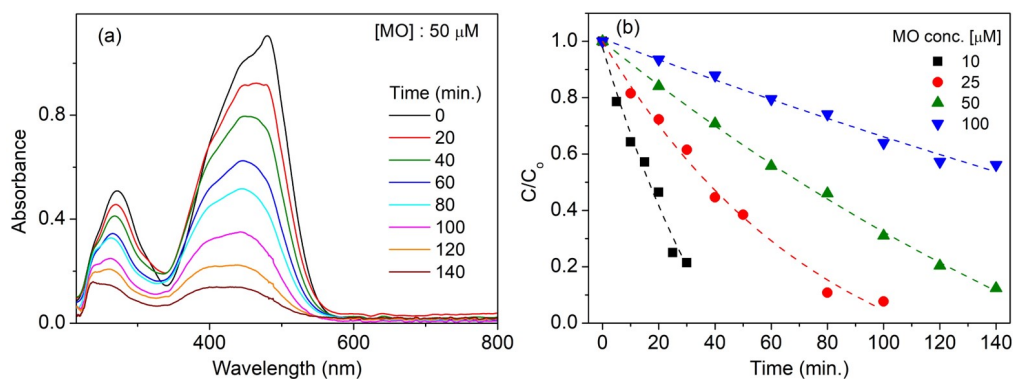


Fig. 5.15 Variation of (a) absorbance of MO dye and (b) normalized dye concentration versus irradiation time for varied concentrations of MO dye mixed with 1g/L of CS600.

For same experimental conditions and dye concentration, degradation of MO was found to be slower as compared to that of MB dye. The apparent degradation rate constant of MO dye is ~ 2.86 times smaller than that of MB dye, for 50 μM initial concentration. MO consists of azo bond $-\text{N}=\text{N}-$, whose bond energy is higher compared to other chromophore bond $\text{C}=\text{N}$, present in MB dye (thiazine dyes) [198]. This variation could be due to associated higher bond energy and variation of

adsorption characteristics of dye molecules on surface of photocatalyst. Larger time for photocatalytic degradation of azo dyes compared to thiazine and rhodamine dyes is also reported in literature [198]. Fig. 5.16 present the normalized dye concentration versus irradiation time for 50 μM MO dye mixed with 1g/L of CS600 and NaN_3 , EDTA- Na_2 and IPA scavengers. Similar to case of MB dye, 2.5 mM concentration of NaN_3 and EDTA- Na_2 significantly reduced the degradation efficiency from 80% (without scavenger) to about 10% and 12% respectively. IPA of higher concentrations ≥ 25 mM inhibited the dye degradation to about 14%. Variation in degradation efficiency with scavenger concentration follows the same trend as obtained in case of MB dye, shown in the previous section. This shows that ROS involved in photo-degradation of both cationic and anionic dyes remained same.

Effect of pH during photo-degradation of anionic MO dye was also analyzed. Fig. 5.16(d) presents the normalized concentration versus UV irradiation time, for 50 μM MO dye mixed with 1g/L of CS600 at different pH conditions. It shows that both low pH ~ 3 and high pH ~ 12 resulted relatively faster degradation as compared to neutral condition. At pH 10 and 12, the degradation rate constants were found to be about 1.3×10^{-2} and $4 \times 10^{-2} \text{ min}^{-1}$ respectively, which are 2.7 and 8.3 times higher than that obtained in neutral solution i.e. $4.8 \times 10^{-3} \text{ min}^{-1}$. Though, at high pH, adsorption of MO dye on negative charge core-shell nanoparticles is suppressed, but significant increase of $\cdot\text{OH}$ radical could be responsible for the observed higher degradation rate constant.

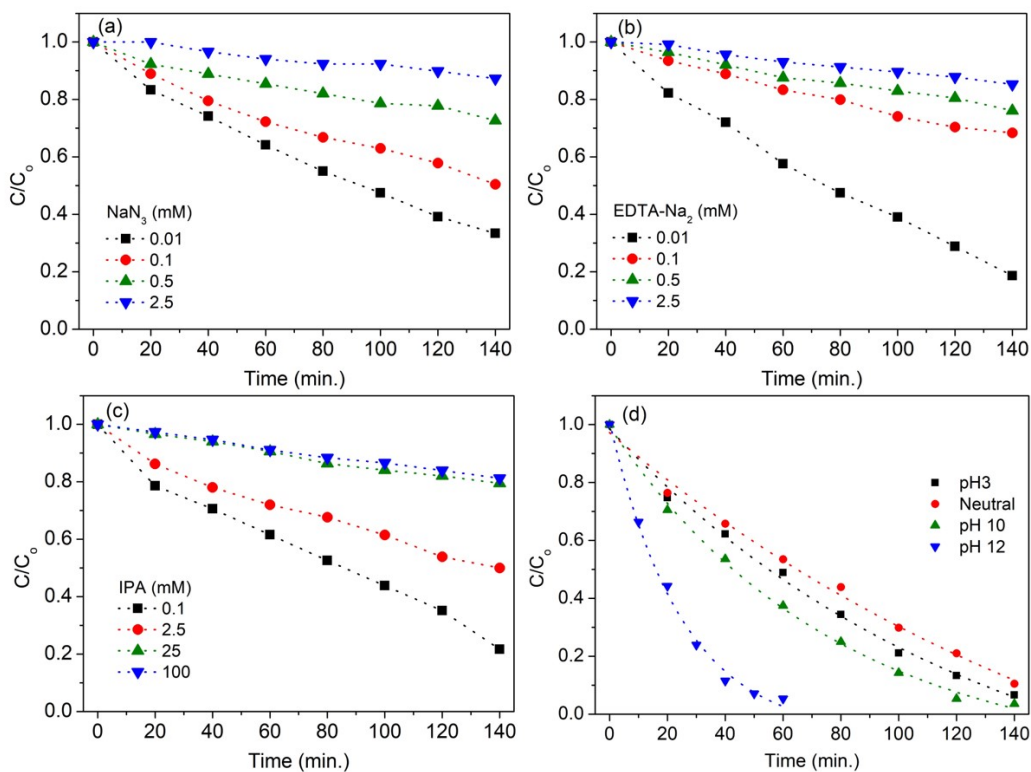


Fig. 5.16 Normalized dye concentration versus irradiation time for MO dye [50 μM] mixed with 1g/L of CS600 and (a) NaN_3 , (b) EDTA-Na_2 , (c) IPA scavengers and (d) at different pH conditions.

5.8 Summary

Synthesis of Au cube-ZnO core-shell nanoparticle was carried out using CTAB-AA assisted hydrothermal method. For this, first Au nanocubes of about 45 nm edge length, were prepared and used for subsequent formation of ZnO shell layer of ~ 55 nm thickness. During initial stage of ZnO shell layer growth, LSPR peak of Au nanocubes in the optical absorption spectra showed blue-shift of about 35 nm, due to heating induced smoothening of sharp edges of Au nanoparticles. Growth of ZnO layer further resulted red-shift in LSPR peak wavelength. DDSCAT calculations revealed that 5% edge smoothening produces 32 nm blue-shift of the LSPR

wavelength. The produced core-shell nanoparticle powder was annealed at different temperatures up to 600°C. Annealing was found to be important for removal of chemical species and improving the crystalline quality of the nanoparticles. Photocatalytic response of core-shell nanoparticles was studied by degradation of cationic MB and anionic MO dyes with UV light irradiation. For MB dye, degradation efficiency of > 95 % was achieved for nanoparticles annealed at ≥ 400 °C, with 1g/L loading. Increasing the photocatalyst loading from 0.2-3 g/L, did not continuously increase the degradation efficiency and showed saturation at higher loading, for both 25 and 50 μM initial dye concentration. For optimum loading of 1g/L of photocatalyst, the dye absorbance varied exponentially with irradiation time at low initial dye concentrations < 30 μM , which turned towards linear at higher (> 50 μM) dye concentration. Though irradiation with high intensity xenon lamp resulted 1.5 times increase in degradation rate constant compared to low power UV lamps, which are more economic for industrial application. Role of different ROS was determined using three scavengers and the degradation process was found to be inhibited with increasing concentration of scavengers. Degradation measurements of cationic MB and anionic MO dyes in presence of scavengers showed that $\cdot\text{OH}$ radical play important role in degradation process of both the dyes, which was further substantiated with measurements at high pH conditions. Degradation of MB and MO dyes under high pH condition (pH 12) resulted 15 and 8.3 times higher degradation rate constant respectively compared to neutral solution. Also, the effect of scavengers is found to be lesser at high pH conditions. These results show that the grown Au-ZnO

core-shell nanoparticles are efficient photocatalyst for degradation of both cationic MB and anionic MO dyes under low power UV lamp irradiation, which can find application in waste water treatment.

Chapter 6

Photo-catalytic degradation of different dyes and their mixtures using Au decorated ZnO nanorods

The photocatalytic process involves adsorption of dye molecules on the surface of photocatalyst and subsequent reactions driven by ROS, produced by the photocatalyst. As a result, size and morphology of photocatalyst nanoparticles play an important role on dye degradation process. ZnO nanoparticles of varied morphologies has been shown to exhibit photocatalytic response in which nanorods are one of the widely studied nanostructures. This is because, ZnO nanorods can be produced either in dispersed form in aqueous solution or can be grown on different substrates like glass, Si, ITO etc [200,201]. This has enabled study of photocatalysis in liquid media, as well as on immobile substrates which has been used as photo-electrodes and for other photocatalysis processes like water splitting, fuel generation etc [7]. Further one dimensional nanorods provide longer conduction path to charge carriers, helpful for charge separation and ROS generation [16,65,104]. This is because, ZnO nanorods has polar faces at the ends i.e. Zn-terminated $\{0001\}$ and O-terminated $\{000\bar{1}\}$ exhibiting high surface energy [65]. Exposure to polar surfaces result formation of more hydroxyl radicals available for redox reactions [65,104]. In the previous chapter, photocatalytic response of Au-ZnO core-shell nanoparticles has been addressed. Hydrothermal growth method has been used for synthesis of both core-shell Au-ZnO and ZnO nanorods structures in the present study. However, presence of AA and CTAB surfactant in core-shell nanoparticles allows selective deposition of ZnO in

form of shell layer. Due to presence of surfactants during synthesis of core-shell nanoparticles, relatively smaller particles with higher degree of dispersability, is achieved which limits easy settling of the nanoparticles. However, in this case, annealing was found to be crucial to enhance the photocatalytic response of these core-shell nanoparticles. In contrast to this, hydrothermal synthesis of ZnO nanorods involves only Zn salt precursor and hexamethylenetetramine (HMT) without other surfactants. Here, HMT allows to grow nanorods by preferentially adsorbing to non-polar faces inhibiting growth at that surface and allows directional growth in the form of rods [65]. For these reasons, and to compare the photocatalytic response with core-shell geometry, ZnO nanorods has been chosen in this study. Further, effect of presence of metal nanoparticles on these nanorods for photocatalysis process has been addressed. Comparison of these core-shell and decorated nanoparticles towards photocatalysis of different dyes and at various pH conditions will provide useful information in designing efficient photocatalytic reactor for degradation of dyes. This chapter addresses synthesis of ZnO nanorods and subsequent deposition of Au nanoparticle using photo-reduction process, comparison of their photocatalytic response for different cationic and anionic dyes and their mixture under varied pH conditions.

6.1 Synthesis of Au nanoparticle decorated ZnO nanorods

For synthesis of Au decorated ZnO nanocomposites, first ZnO nanorods were grown using hydrothermal method. In this process, equi-molar solution of zinc nitrate hexahydrate and HMT was stirred and then placed in water bath at about 90 °C for

4-5 hrs. The settled white precipitate was washed two times with DI water and annealed at different temperatures for 4 hours in air ambiance. Au nanoparticles were deposited on these ZnO nanorods by photo-reduction of Au salt in presence of UV light or nanosecond second harmonic Nd:YAG laser. Loading of Au nanoparticles was controlled by varying Au salt concentration and UV or laser light irradiation time. For photo-reduction growth of Au nanoparticles on ZnO nanorods, 50 mg ZnO nanorod powder was dispersed in 5 mL methanol, and Au salt (HAuCl_4) solution of varied quantity (0.4-5 mL) was added and stirred in dark. The solution was irradiated under UV lamp for 2 hrs. with continuous stirring. The color of the solution changed from white to pink or violet, indicating formation of Au nanoparticles. Fig 6.1 presents the photographic images of the prepared ZnO nanopowder and after irradiation in presence of 2 and 5 mL of 25 mM HAuCl_4 solution. The figure shows a distinct change in color of the nanopowders from pink to brown, with increasing concentration Au salt. Morphology of the grown ZnO nanopowder were characterized using scanning electron microscope (Sigma, Zeiss).



Fig. 6.1 Photographic images of the ZnO nanopowder (a) before and after UV irradiation in presence of (b) 2 and (c) 5 mL of 25 mM HAuCl_4 solution.

Fig. 6.2 presents SEM images of ZnO nanopowder before and after loading of Au nanoparticles. The figure shows formation of well-defined ZnO nanorods of about

62 nm diameter and few micron length. Presence of HAuCl_4 and UV irradiation resulted formation of almost spherical Au nanoparticles on the surface of nanorods. Au nanoparticle density increased with increasing the quantity of Au salt during irradiation. In presence of large amount of HAuCl_4 , formation of large aggregates of Au nanoparticles on the surface of ZnO nanorods has been noted, refer Fig. 6.2 (c). This shows that photoreduction process can deposit Au nanoparticles without other chemical reagent and nanoparticle density can be controlled by varying concentration of Au salt.

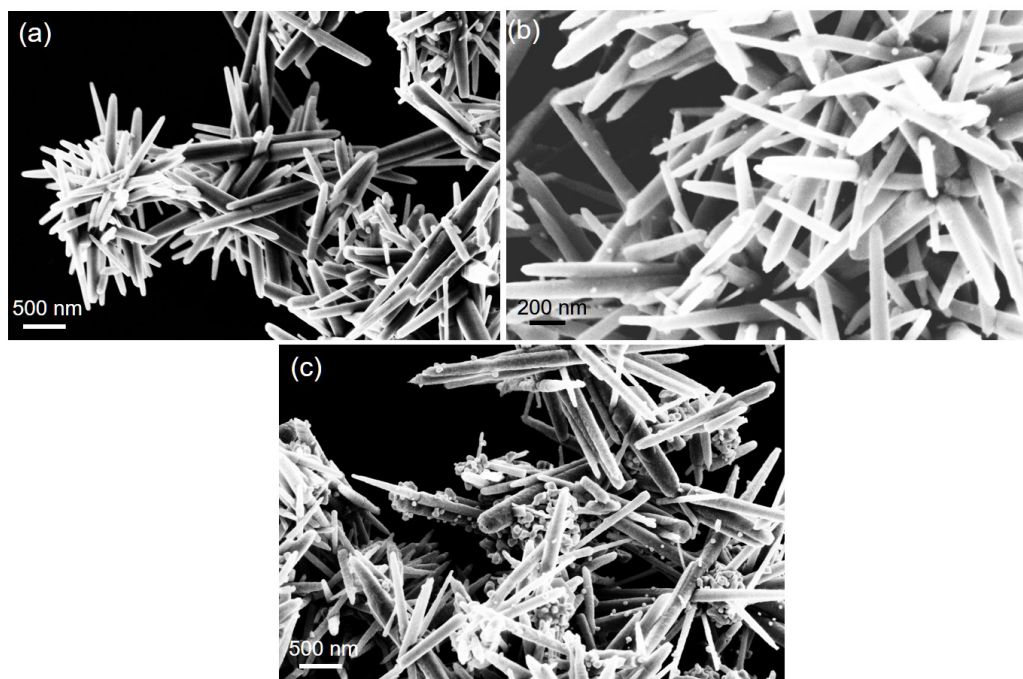


Fig. 6.2 SEM images of the ZnO nanopowder (a) before and after UV irradiation in presence of (b) 2 and (c) 5 mL of 25 mM HAuCl_4 solution.

6.2 Structural and compositional properties

Crystalline quality of grown ZnO nanorods, before and after Au nanoparticle deposition was analyzed using X-ray diffraction (XRD). The XRD pattern of samples

was collected using X-ray diffractometer (Bruker) with Cu K α (wavelength 1.54 Å) X-ray source. As discussed in chapter (5), it was found that annealing of core-shell nanoparticles is important for improving crystalline quality as well as their photocatalytic response. Therefore, effect of annealing on the grown ZnO nanorods by hydrothermal method, was also studied. Fig. 6.3(a) shows XRD pattern of as grown nanorods and that annealed at 200 °C, 400 °C and 600 °C for 04 hrs. In all the cases, diffraction peaks at about 31.7°, 34.4°, 36.2°, 47.5°, 56.5°, 62.9°, 67.8° and 77.5° were observed corresponding to hexagonal Wurtzite crystal structure of ZnO [188,189].

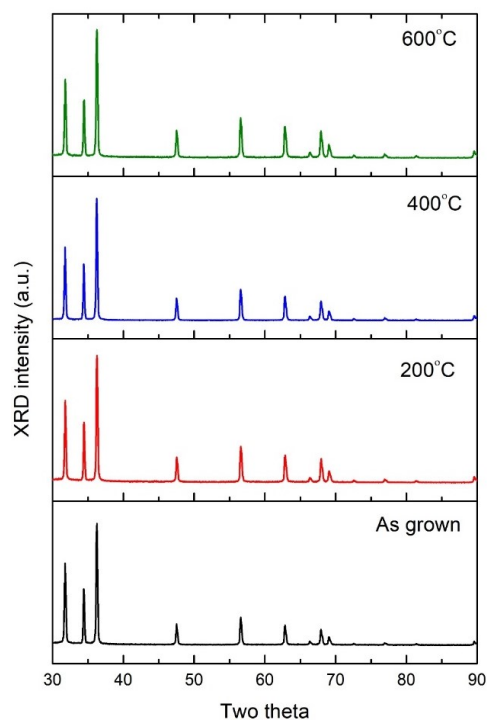


Fig. 6.3 XRD spectra of the ZnO nanorods annealed at different temperatures.

This shows that in the present case (without CTAB and AA, which are used for core-shell nanoparticles) the as-grown nanorods are crystalline and annealing did not affect much on their crystalline quality. In order to be ensured of removal of chemical

species used during ZnO synthesis, nanorods annealed at 600° C was used, for all the experiments. Fig. 6.4 compares XRD spectra of ZnO nanorods before and after deposition of Au nanoparticles. In Au-ZnO nanorods, additional peaks at 38.2°, 44.3°, 64.5° and 77.5° were noticed, which correspond to FCC crystal phase of metallic Au [188]. This confirms that Au nanoparticles formed by photoreduction process are metallic in nature. It can be observed that ZnO intensity and the 2θ peak positions remained unchanged with respect to pure ZnO. This confirms that crystalline quality of ZnO is unaffected by photo-deposition of Au nanoparticles.

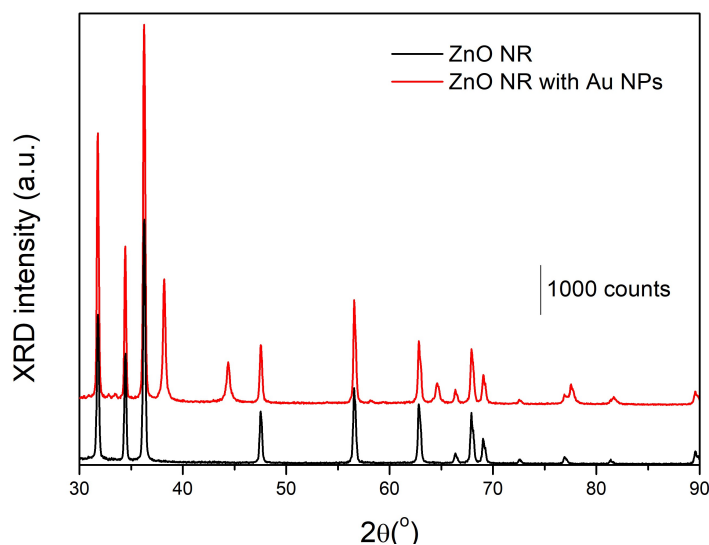


Fig. 6.4 XRD spectrum of ZnO nanorods before and after deposition of Au nanoparticles.

The elemental composition analysis of Au-ZnO nanorods were carried out using X-ray photoelectron spectroscopy. These measurements were performed with Al K α (1486.6 eV) radiation source (DAR-400, Omicron Nanotechnology). The binding energy (BE) shift of the adventitious carbon peak from its standard value of 284.6 eV was taken as a measure of static charge correction. Fig. 6.5 shows the binding energy

(BE) spectra of O-1s, Zn-2p and Au-4f peaks of Au-ZnO nanorods. The O-1s peak could be de-convoluted into two peaks. The BE peak at 530.28 eV is attributed to oxygen in ZnO crystal lattice and higher BE peak at 532.06 is related to C=O bond of molecular species involved in the synthesis [188,190,191]. Fig. 6.5(b) presents the BE spectrum of Zn-2p level. The BE peaks were obtained at 1021.72 and 1044.71 eV, which are very close to that observed for Zn in ZnO nanoparticles as reported in literature [188,191].

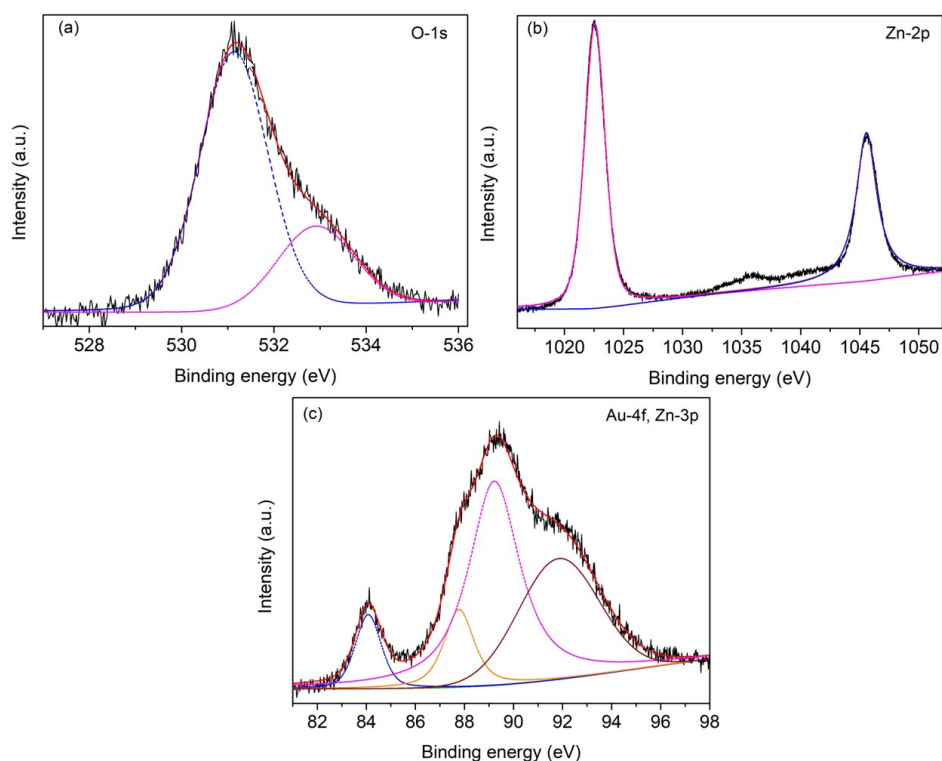


Fig. 6.5 XPS intensity spectra of (a) O 1s, (b) Zn-2p and (c) Au-4f binding energy peaks of Au nanoparticle decorated ZnO nanorods.

The Au BE spectrum is shown in Fig. 6.5 (c), which is overlapped with Zn 3p BE peak. After deconvolution, the Au 4f_{7/2} and 4f_{5/2} were found to be 83.23 and 86.93 eV respectively. It may be noted that these values are at lower binding energy side from

that of the bulk metal observed at 84.0 and 87.6 eV. This shift can be attributed to charge transfer between ZnO and Au nanoparticles. Similar lower BE shift has been observed for Ag and Au decorated ZnO nanostructures [188,191].

Zeta potential measurements of these nanoparticles were also carried out. The surface charge of ZnO nanorods was found to be about 25.7 mV for neutral (water) solution which decreased towards negative value i.e. 5.5 mV and - 44.6 mV at pH ~ 10 and 12 respectively. For acidic conditions, the zeta potential increased towards more positive value i.e. 30.2 mV and 33.1 mV for pH ~ 4.5 and 3 respectively. Variation in surface charge of ZnO is attributed to change in surface hydroxylation characteristics of ZnO nanoparticles, as mentioned in section 5.7.2. The negative surface charge at high pH value resulted from de-protonation of hydroxylated surface of ZnO [192,198]. As the pH value decreased towards acidic conditions, protonation of hydroxylated surface resulted increasing positive surface charge of the nanorods, which is similar to that observed for Au-ZnO core-shell nanoparticles.

6.3 Photocatalytic response of Au decorated ZnO nanorods

The photocatalytic response of ZnO nanorods was studied by degradation of four different dyes namely MB, MO, Rh6G and RhB, having characteristic absorption peaks at 650, 450, 560 and 540 nm respectively. These studies were carried out under UV lamps (Phillips, ~ 8 W, 02 Nos.) irradiation. The chemical structure of these dyes are shown in Fig. 6.6.

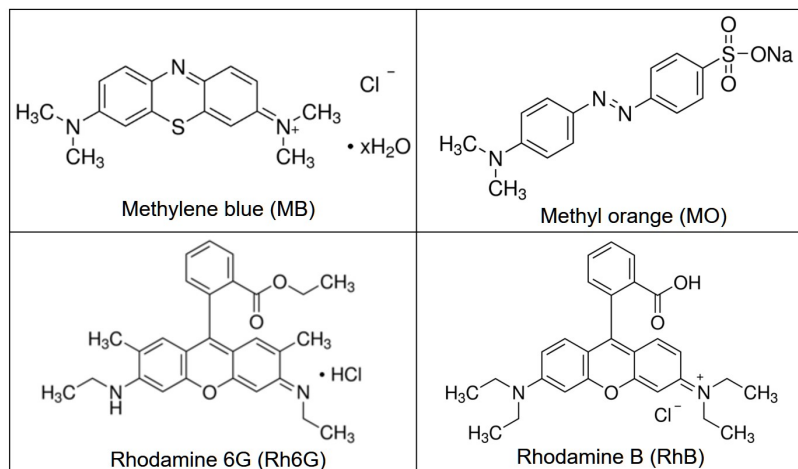


Fig. 6.6 Chemical structure of the dyes used for photocatalytic degradation.

Varied amounts (1-5 mg/mL) of ZnO nanorod powder were mixed with aqueous solution of dyes of concentration in the range of 1-50 μM . Before light irradiation, these solutions were stirred for about 1 hr in dark. During light irradiation, 1 mL of solution was extracted and centrifuged at fixed time intervals, and optical absorbance of dye was measured. Optical absorption measurements were performed using a fiber optic CCD spectrograph (AvaSpec3068) with broad band balanced deuterium-halogen lamp. The dye degradation experiments were repeated at least two times and variation was found to be within 10%. At first, photocatalytic response of ZnO nanorods without and with Au nanoparticles of different densities were compared, by degradation of MB dye of 50 μM initial concentration under UV light irradiation. Fig. 6.7 presents variation of normalized concentration of MB dye with irradiation time.

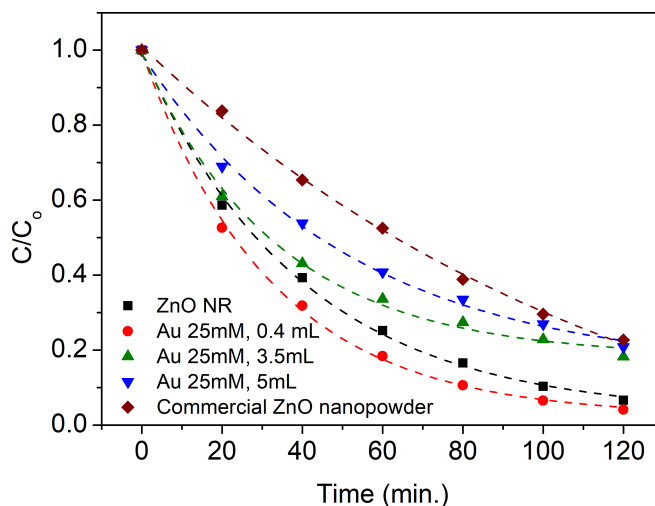


Fig. 6.7 Variation of normalized concentration of MB dye with irradiation time in presence of ZnO nanorods without and with Au nanoparticles.

For comparison, dye degradation in presence of commercial ZnO nanopowder (Sigma Aldrich, Product ID: 677450, average particle dia. < 50 nm) is also presented. The peak absorbance decreased exponentially in all the cases. The degradation rate constant was found to be 2.5×10^{-2} , 3.09×10^{-2} , 2.95×10^{-2} and $1.96 \times 10^{-2} \text{ min}^{-1}$ in case of pure ZnO nanorods and that obtained after irradiation with 0.4, 3.5 and 5 mL of HAuCl₄. This shows that loading of Au nanoparticles on ZnO, when UV irradiated with 0.4 mL of 25 mM HAuCl₄, resulted the fastest degradation process, with the highest degradation rate constant. Presence of Au nanoparticles have shown to increase the degradation rate constant which has been attributed to efficient charge separation process and more generation of ROS species compared to pure ZnO nanoparticles [65]. However, when Au quantity increases, they start acting as carrier recombination centers [65], thus decreasing the photocatalytic activity. Decorated ZnO nanorods with optimum Au nanoparticles, i.e. irradiated with 0.4 mL of 25 mM HAuCl₄, has been taken for all the measurements, shown onwards. In presence of

commercial ZnO nanopowder, the dye degradation rate constant was found to be $0.8 \times 10^{-2} \text{ min}^{-1}$, which is about 3 and 3.8 times lesser than that observed for pure ZnO and optimum Au decorated ZnO nanorods. Relatively better photocatalytic response can be attributed to purity and crystalline quality of the grown ZnO nanoparticles. In order to observe the versatility of the grown Au-ZnO nanorods, photocatalytic degradation measurements were performed with different dyes. Fig. 6.8 (a-d) presents the variation in normalized concentration of four dyes of varied concentration with irradiation time, in presence of Au decorated ZnO nanorods. For all the cases, the dye concentration varied exponentially for low initial dye concentration, and tended towards linear at larger initial concentrations. The apparent rate constants (k_{app}) were obtained from exponential fitting, and variation of (k_{app})⁻¹ (which represent characteristic decay time) with concentration of dye is also shown in the figure. It can be observed that for all the dyes, variation of (k_{app})⁻¹ is linear at low dye concentrations and deviated towards higher value at higher (>30 μM) dye concentrations. This is similar to that observed with core-shell nanoparticles as shown in previous chapter. At a given dye concentration, photocatalytic degradation rate of different dyes was found to be in the order as: MB > MO > RhB > Rh6G. For example, at 30 μM concentration dye degradation rate constant was observed as 6.4×10^{-2} (MB), 1.8×10^{-2} (MO), 1.6×10^{-2} (RhB) and 1.5×10^{-2} (Rh6G). This shows that for the same amount of photocatalyst degradation rate is considerably varying for different dyes. This could be due to variation in adsorption characteristics (depend on dye molecular size, charge of photocatalyst and dye molecule, pH condition),

chemical bond enthalpy of the dyes [202]. The reason for slow degradation of MO with respect to MB dye has been mentioned in section 5.8. The slowest degradation rate of rhodamine dyes could be due to their large molecular size (refer figure 6.1) which limits the amount of dye adsorbed on the photocatalyst [168]. From Fig. 6.8, it can be observed that in case of rhodamine dyes at 30 μM concentration, the variation of normalized concentration approaching towards linear as compared to exponential form at lower concentrations. However, for MB and MO dyes, this behavior (changing from exponential to linear) was observed at higher initial dye concentration ($> 50 \mu\text{M}$). From these observations along with dye degradation kinetics discussed in previous chapter, it can be concluded that in case of rhodamine dyes at very low concentration of ($<1 \mu\text{M}$) the process approaches to first order as per LH model. Further, the observed dye degradation rate of MB and MO dyes is larger than that observed with Au-ZnO core-shell nanoparticles as presented in previous chapter. This could be due to presence of relatively high amount of ZnO in the present case i.e. in Au-ZnO nanorods, amount of Au is about 3.8 wt%, whereas in core-shell nanoparticles, it is about 30%. Thus, for same amount of photocatalyst, weight of ZnO, which primarily absorbs the incident UV light, is larger in case of nanorods. Also, nanorods possess polar facets, which have been shown to produce more $\cdot\text{OH}$ radicals [65,105].

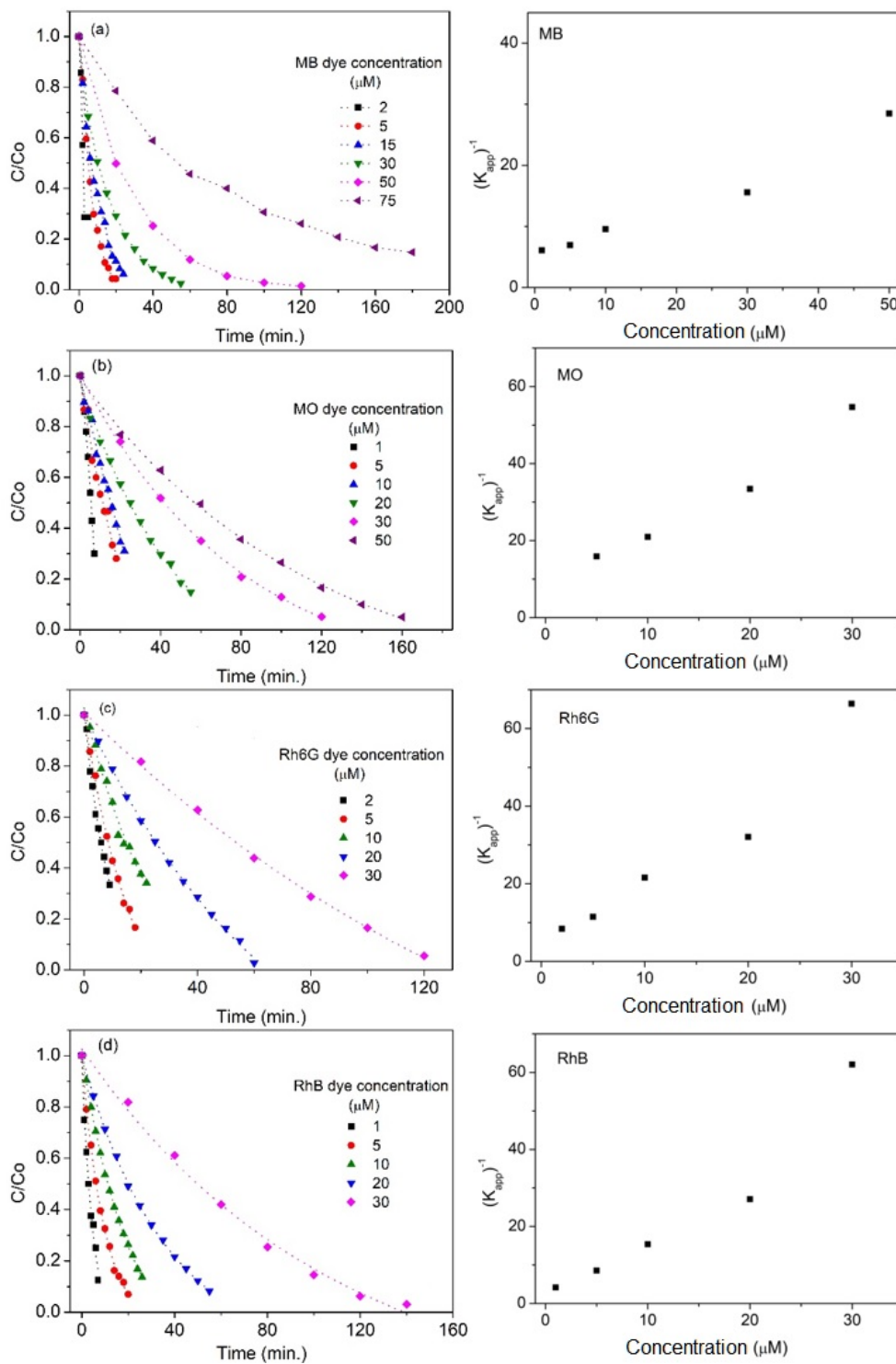


Fig. 6.8 Variation of normalized concentration of (a) MB, (b) MO, (c) Rh6G, and (d) RhB dyes and corresponding $(k_{app})^{-1}$ with irradiation time in presence of Au-ZnO nanorods.

6.3.1 Effect of scavengers

Fig. 6.9 (a-c) presents the variation of normalized concentration with light irradiation time of initial 50 μM MB dye in presence of Au-ZnO nanorods in presence of EDTA- Na_2 , NaN_3 and IPA scavengers of different concentrations respectively. The figure shows in all cases, dye degradation efficiency decreased with increasing scavenger concentration. Fig. 6.9 (a) shows at 2.5 mM of EDTA- Na_2 , the degradation efficiency decreased to about 26% from 98% (without scavengers). Fig. 6.9 (b) shows that presence of NaN_3 of 0.1, 0.5 and 2.5 mM, the degradation efficiency was limited to about 60 %, 30% and 5% respectively. Fig. 6.9 (c) shows that IPA of relatively higher concentration about 2.5 mM only resulted considerable effect of inhibition of dye degradation efficiency.

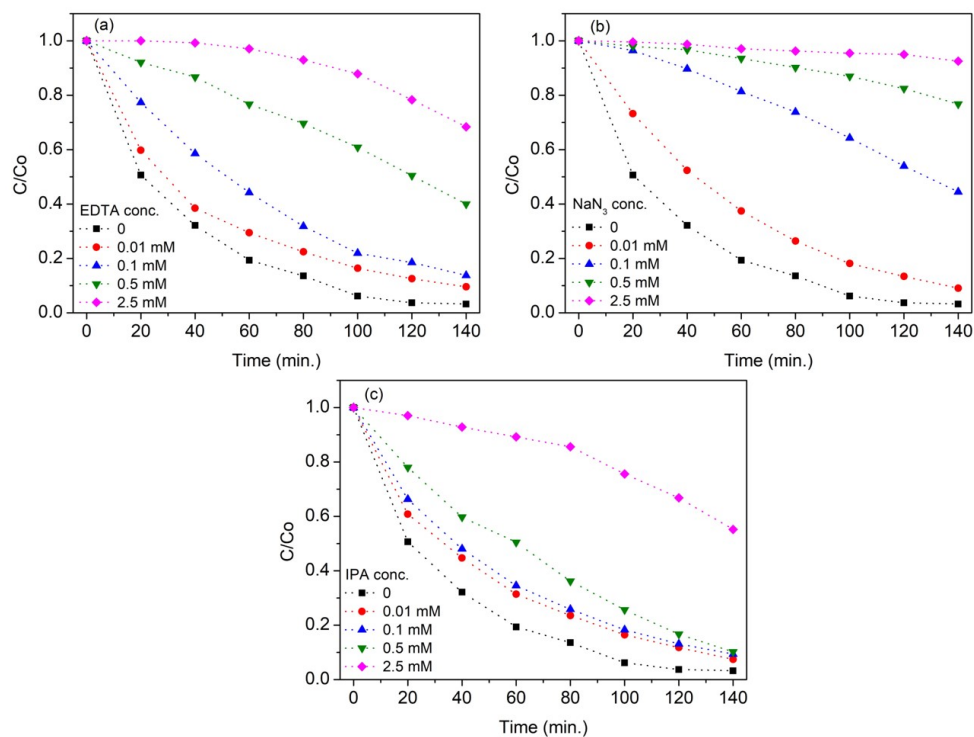


Fig. 6.9 Variation of normalized concentration of 50 μM MB dye with irradiation time, in presence of (a) EDTA- Na_2 , (b) NaN_3 and (c) IPA of varied concentrations.

The effect of different scavengers is similar to that observed in previous chapter with core-shell nanoparticles. Significant effect of NaN_3 is due to its scavenging effect for both $\cdot\text{OH}$ radical and $^1\text{O}_2$. EDTA-Na_2 scavenge photogenerated holes, as a result, it suppresses formation of $\cdot\text{OH}$ radical. IPA acts as $\cdot\text{OH}$ scavenger with almost 10 times lesser reaction rate constant compared to that of NaN_3 . Due to this reason, high concentration of IPA only resulted into inhibition of dye degradation process. Fig. 6.10 (a-c) presents the effect of these scavengers on MO dye degradation at $50\ \mu\text{M}$ initial concentration. Presence of EDTA-Na_2 of 0.1, 0.5 and 2.5 mM concentration decreased the degradation efficiency from 92% to about 60%, 18% and 7% respectively. Similarly, addition of NaN_3 of 0.1, 0.5 and 2.5 mM concentration resulted decrease in degradation efficiency to 68%, 30% and 11% respectively. At 25 mM concentration of IPA resulted $\sim 26\%$ degradation efficiency. This shows that ROS involved in the degradation process of these dyes are similar, when photocatalysis is carried out either in presence of Au decorated ZnO nanorods or Au-ZnO core-shell nanoparticles.

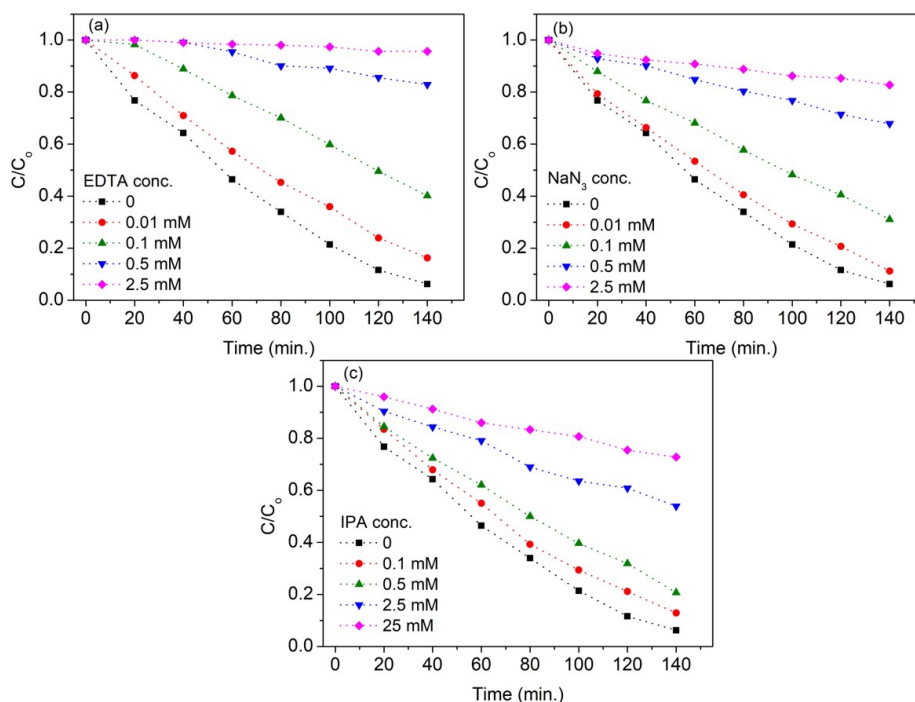


Fig. 6.10 Variation of normalized concentration of 50 μM MO dye with irradiation time, in presence of (a) EDTA- Na_2 , (b) NaN_3 and (c) IPA of varied concentrations.

Further effect of the three scavengers on degradation of Rh6G and RhB dyes at 30 μM initial concentration is presented in Fig. 6.11 and 6.12 respectively. These figures show that in case of rhodamine dyes, degradation is almost inhibited in presence of 2.5 mM of EDTA- Na_2 and 25 mM IPA and at 2.5 mM NaN_3 the inhibition was found to be relatively less. The main source of hydroxyl radical is from either capture of holes by hydroxide ions or reactions of superoxide with water molecules. Relatively higher inhibition of dye degradation in presence of EDTA- Na_2 (hole scavenger) of these dyes shows that photogenerated holes can also cause oxidative reactions with the dye molecules. To know the effect of hydroxyl ion concentration on the photocatalysis, the degradation of all the dyes was also carried out at different pH conditions

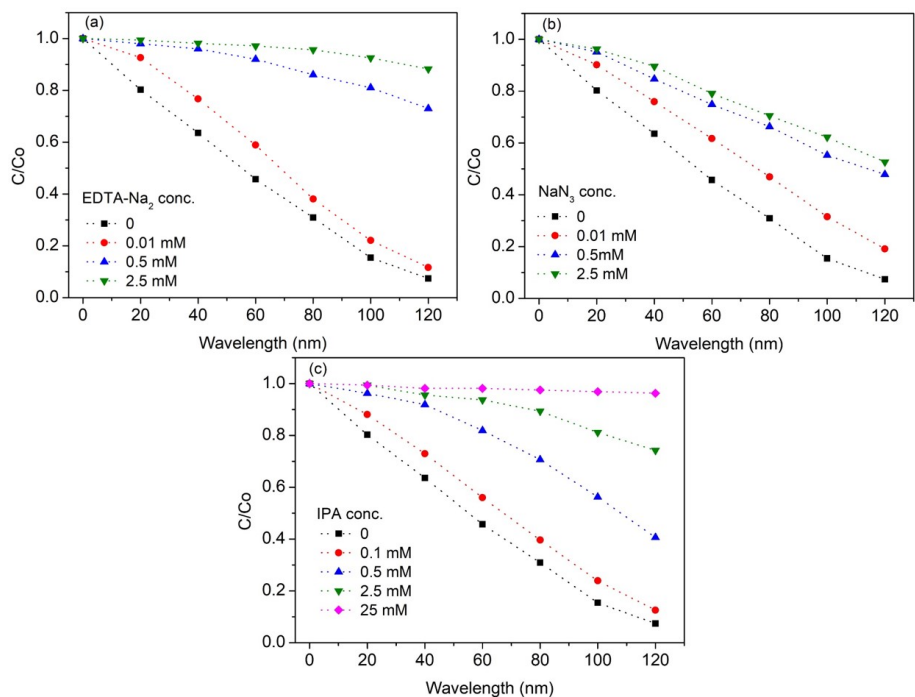
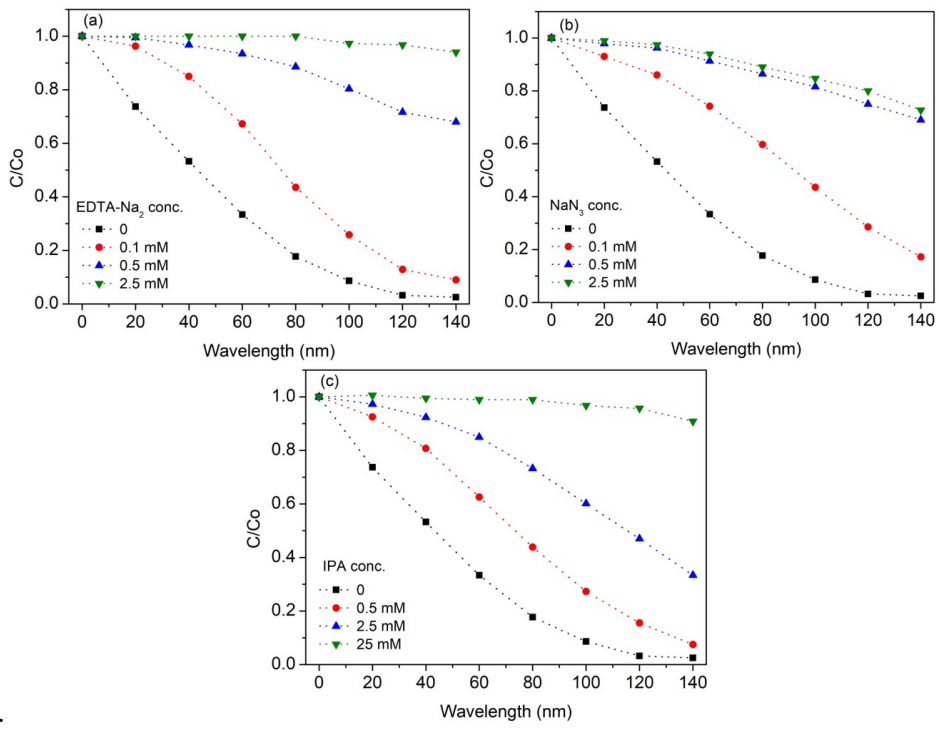


Fig. 6.11 Variation of normalized concentration of 30 μM Rh6G dye with irradiation time, in presence of (a) EDTA- Na_2 , (b) NaN_3 and (c) IPA of varied concentrations.



6.12 Variation of normalized concentration of 30 μM RhB dye with irradiation time, in presence of (a) EDTA- Na_2 , (b) NaN_3 and (c) IPA of varied concentrations.

6.3.2 Effect of pH

Fig. 6.13 presents variation of normalized concentration of the four dyes in presence of Au-ZnO nanorods at different pH conditions. As mentioned above the nanoparticles possess negative surface charge at high pH condition and positive charge at low pH. MB is a cationic dye, whose adsorption on the photocatalyst is expected to be more at high pH condition. The figure shows that with increasing pH, MB dye degradation became faster. At high pH, higher concentration of $\cdot\text{OH}$ radicals is expected, which could promote MB dye degradation. Fig. 6.13 (b) shows variation MO dye degradation at different pH conditions. It shows that at lower pH 3-4.5, the dye degradation is marginally better than that in neutral solution this could be due to enhanced adsorption of this anionic dye adsorption on positive charge photocatalyst at this pH range. This is unlike to the case of Au-ZnO core-shell nanoparticles for which pH 12 condition resulted larger degradation rate constant. The observed difference may be due to Au-ZnO nanorods have shown positive zeta potential up to pH 10, favoring adsorption of MO dye. However, at pH 12, sudden change of zeta potential to negative (- 44.6 mV) could suppress the dye adsorption which result in lower dye degradation. In case of Rh6G and RhB dyes, variation of pH over wide range between 3-10 did not show significant change in dye degradation. Rh6G is cationic dye which has positive n-ethyl group. At high pH conditions, electrostatic interaction between n-ethyl group of Rh6G with negatively charged photocatalyst can be expected. However, low dye degradation rate both rhodamine dyes at very high pH \sim 12 condition suggests that simple electrostatic interaction alone is insufficient to explain

the observed results. These results show that for different dyes, the reaction conditions need to be optimized accordingly depending on the chemical structure of dye to obtain maximum degradation rate constant.

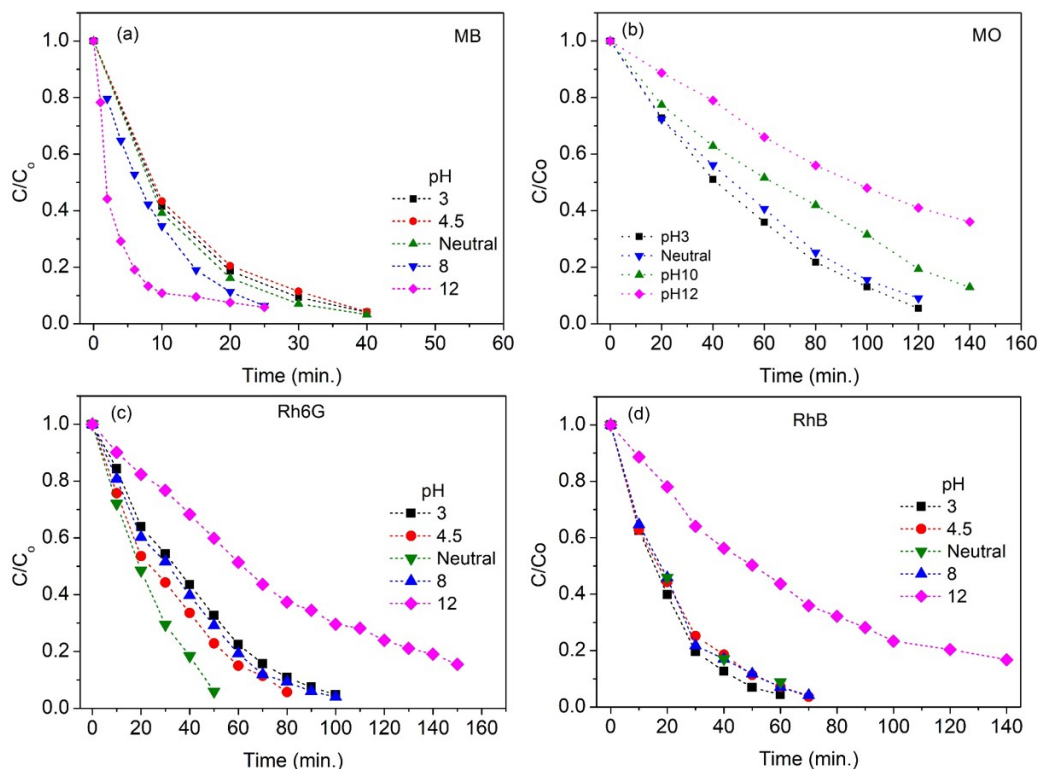


Fig. 6.13 Variation of normalized concentration of (a) MB, (b) MO, (c) Rh6G, and (d) RhB dyes with irradiation time at different pH conditions of the solution, in presence of Au-ZnO nanorods.

6.5 Degradation of mixed dyes at different pH conditions

Four combinations of mixed dye solutions: (i) MB and Rh6G, (ii) MB and RhB, (iii) MB and MO and (iv) Rh6G and RhB were irradiated in presence of 1g/L Au-ZnO nanorods. Fig. 6.14 (a-d) presents the absorption spectra of these mixed dyes with 30 μ M concentration of each dye in neutral condition. The figure shows that absorption of both dyes decreased with irradiation time. From the peak absorbance variation of

individual dyes, for MB dye, which shows absorbance at about 650 nm, the degradation is faster with respect to the other dyes. This shows that in either individual dye or in mixture of dyes irradiation, MB dye degradation is relatively faster in comparison to that of other dyes. Fig. 6.14 (d) shows low absorbance after 120 min. of irradiation, in the combination of RhB and Rh6G (both show absorbance at about 520 nm). However, for the combination of these dyes with MB, almost complete degradation of the dyes was observed within 100 min. of irradiation. It shows that the dyes which show slower degradation, (in individual irradiation, refer Fig. 6. 7), also takes relatively more time of degradation in their mixture.

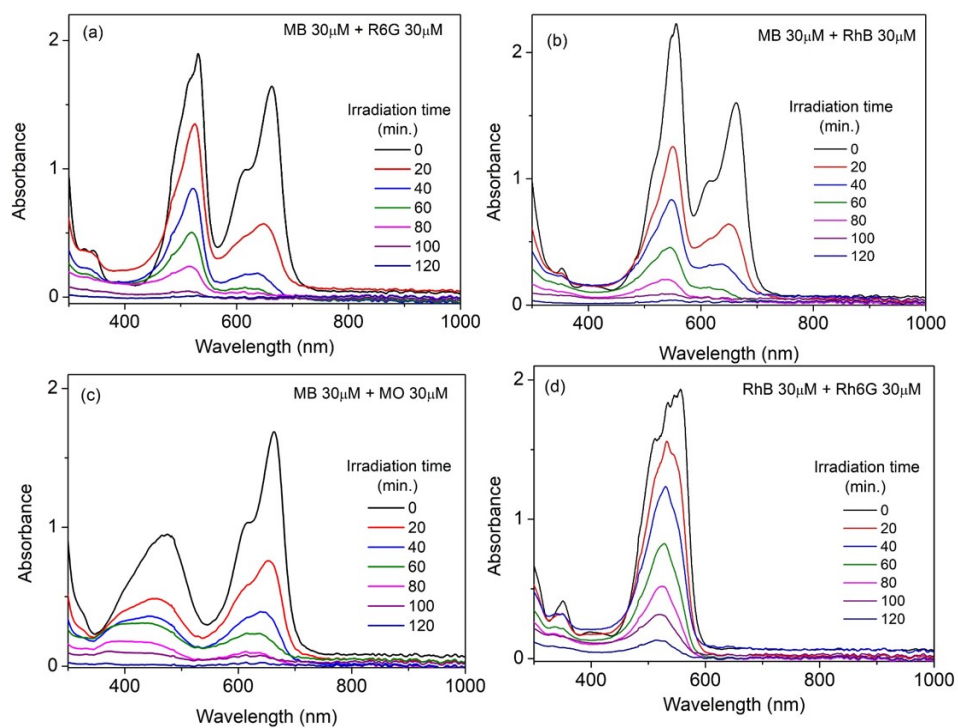


Fig. 6.14 Variation of absorbance of mixed dyes of 30 mM concentration each, (a) MB+Rh6G, (b) MB+RhB, (c) MB+MO and (d) RhB+Rh6G, with irradiation time in presence of Au-ZnO nanorods.

Photocatalytic degradation of these mixed dyes was also studied at pH~12

condition. Fig. 6.15 presents the absorption spectra of mixed dyes, in presence of 1g/L photo-catalyst loading, at pH ~12 condition. In case of the mixtures containing MB dye, its peak absorbance also suppressed within 10-20 min. of irradiation, which is similar to that observed in individual MB dye irradiation at this pH condition. It also shows at this high pH, the other dyes degradation became slow. Therefore, it can be concluded that at pH 12 condition, in MB dye mixtures, fast degradation of MB in about 10 min. of irradiation favors selective degradation of one dye. However, at this pH, mixture of rhodamine dyes i.e. Rh6G and RhB did not result complete dye degradation, even for longer period of 120 min. of irradiation.

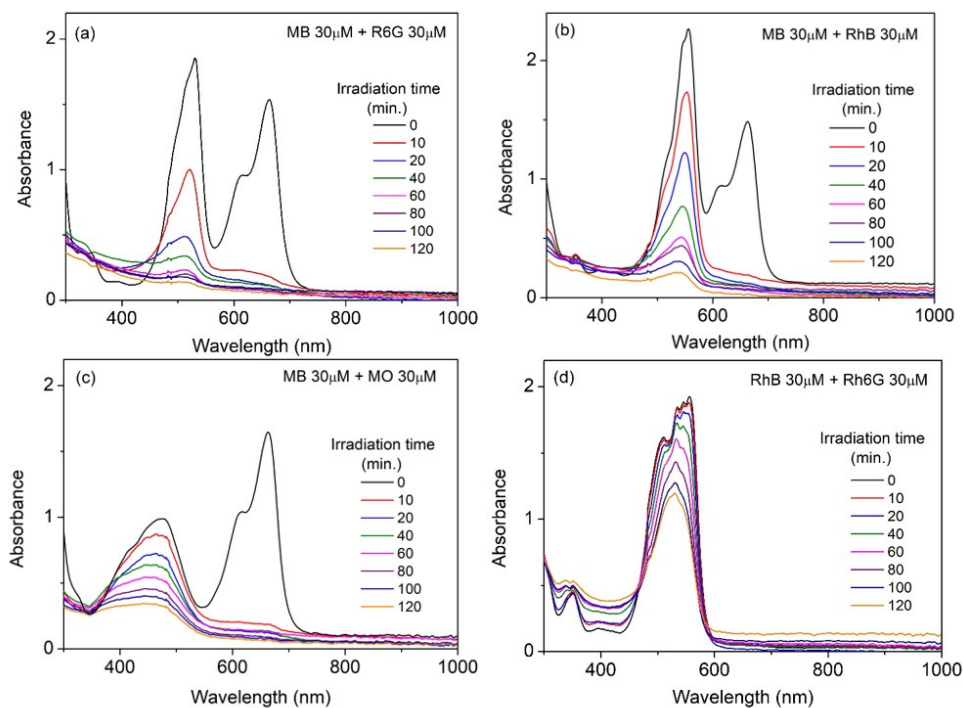


Fig. 6.15 Variation of absorbance of mixed dyes of 30 mM concentration each, (a) MB+Rh6G, (b) MB+RhB, (c) MB+MO and (d) RhB+Rh6G, with irradiation time at pH 12, in presence of Au-ZnO nanorods.

Fig. 6.16 presents variation of absorption spectra of mixed dyes with irradiation

time in presence 1g/L photo-catalyst at pH~3 condition. All the mixed dye combinations resulted decrease in peak absorbance of both the dyes. For this case, the degradation of MB dye was found to degrade slowly as compared to the previous case of high pH condition. The overall degradation in this condition is similar to that observed for the neutral condition as shown in Fig. 6.13. This shows that degradation of dyes has shown marginal variation in pH range of 3-10. However, at pH~12, MB dye has shown significantly high degradation but the other dyes degradation became slow, i.e. at this condition, MB dye has shown selective degradation.

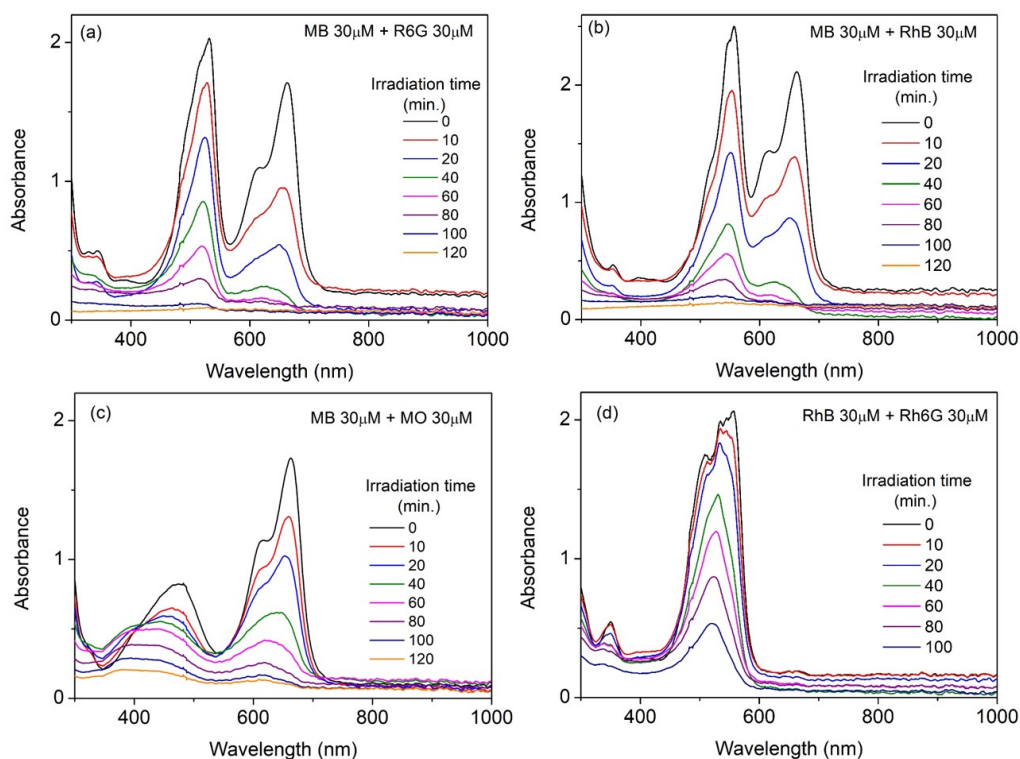


Fig. 6.16 Variation of absorbance of mixed dyes of 30 mM concentration each, (a) MB+Rh6G, (b) MB+RhB, (c) MB+MO and (d) RhB+Rh6G, with irradiation time at pH 3, in presence of Au decorated ZnO nanorods.

6.6 Transient Response of Ag-ZnO nanoparticle films

To study the effect of ZnO coating on the transient response of free-electrons in metal nanoparticles we have grown Ag nanoparticle films without and with ZnO using PLD. Three films were grown for performing the transient measurements: i) as-grown Ag nanoparticle film, ii) Ag nanoparticle film coated with ZnO grown by 3000 laser pulses and iii) Ag nanoparticle film coated with ZnO grown by 6000 laser pulses. Compared to earlier studies which were mainly on Au, Ag was specifically chosen in the present case to avoid inter-band contributions in the transient response measurements. Fig. 6.17 shows the absorption spectra of these three films. The as-grown Ag nanoparticle film shows a LSPR peak at about 500 nm. With increasing ZnO coating, the LSPR peak was found to red-shift. Further the LSPR peak strength also increases with the thickness of the coating. Such red-shift and increase in strength of LSPR of Ag nanoparticle is expected when coated with a material of higher refractive index [12].

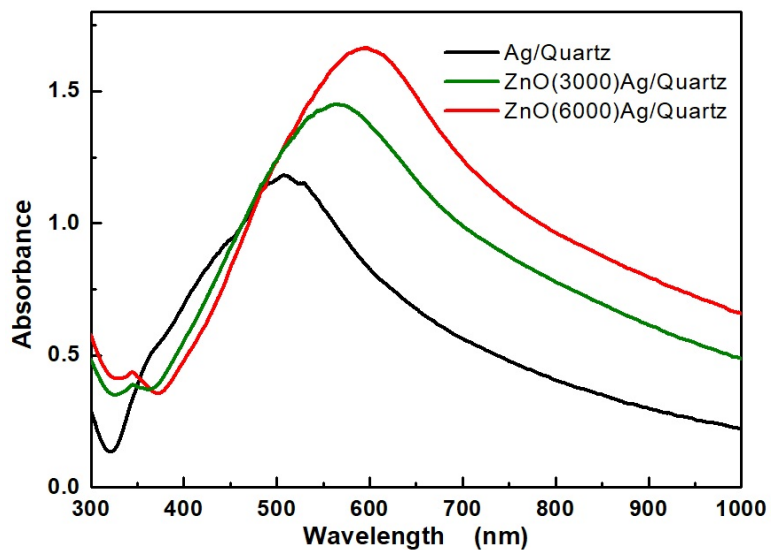


Fig 6.17 The absorbance spectra of Ag nanoparticle and Ag-ZnO nanoparticle films.

Fig. 6.18 presents the structural characterization of the Ag and Ag-ZnO films using AFM (Multimode-8, Bruker). The as-grown Ag nanoparticle film showed formation of nanoparticles with an average peak-to-peak height variation of about 35 nm. After coating with ZnO layer grown 3000 pulses, the image shows a granular structure on top of the nanoparticles.

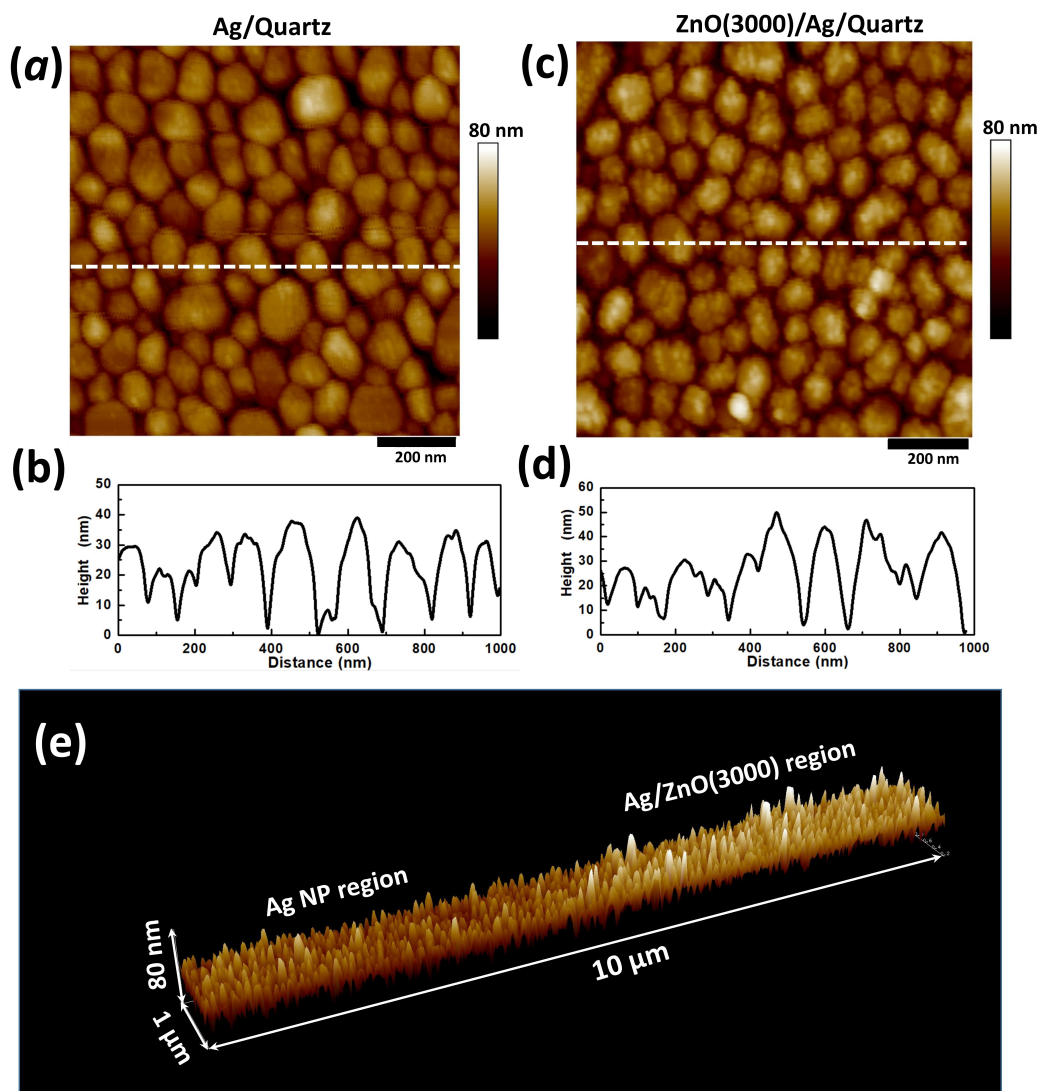


Fig 6.18 Representative AFM images and corresponding height profiles of (a) and (b) Ag nanoparticle film and (c) and (d) Ag nanoparticle film coated with 3000 pulses of

ZnO. (e) shows the AFM scan on a region of pure Ag to Ag coated with ZnO in 3D.

In the present case, the peak-to-peak height was found to be increased compared to that of the pure Ag film. In-order to correctly estimate the average thickness of ZnO coating, AFM measurement was performed on a regime of pure Ag to Ag coated with ZnO. Fig.6.18 (e) shows the 3D image of the AFM scan. From this image, the average thickness of ZnO was estimated to be ~15 nm.

Transient absorption measurements were performed on these samples using a standard pump-probe configuration (Fig 6.19). For this measurement, a 35 femtosecond oscillator-amplifier-optical parametric amplifier (OPA) laser system was used. The repetition rate of the laser was 1 KHz. The second harmonic of the 800 nm fundamental beam was used as the pump beam (400 nm). While the probing was done at 500 nm using the output from the OPA. The pulse width of the laser at the sample location was measured to be nearly 120 fs. The peak intensity of pump beam at the sample location was $\sim 42 \text{ GW/cm}^2$. The intensity of the probe beam was nearly $1/20^{\text{th}}$ of the pump intensity.

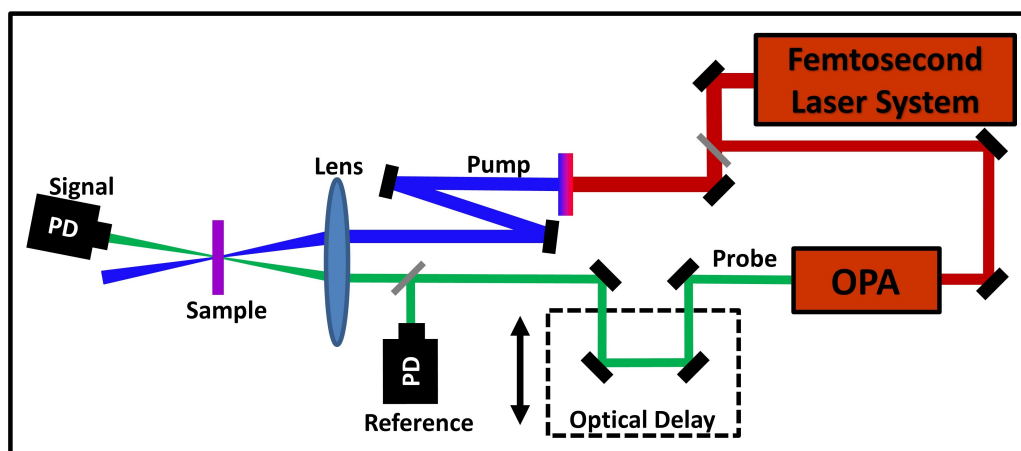


Fig 6.19 The schematic of the transient absorption measurement setup.

Fig. 6.20 shows the measured transient transmission signal normalized to the peak. With the arrival of the pump pulse, the $\Delta T/T$ quickly increases and reaches a maximum by about 350 fs. At later times the $\Delta T/T$ decays with in next few picoseconds. A single exponential decay function was fit to the recovery part of the signal. The estimated best fit for the decay times were 2.4 ps, 1.7 ps and 1.9 ps for the as grown Ag nanoparticle film, Ag-ZnO film with 3000 and 6000 pulses of ZnO respectively. When excited at plasmon resonance by an ultrafast optical pulse, plasmon oscillations are induced. The coherence is lost, plasmons decay to single particle states. Within next few hundreds of femtoseconds the free-electrons thermalize mainly through electron-electron scattering [203,204]. At the end of this thermalization process, the temperature of free electrons reaches a maximum. In case of noble metals, this thermalization takes about 300 to 500 fs depending on the excitation intensity.

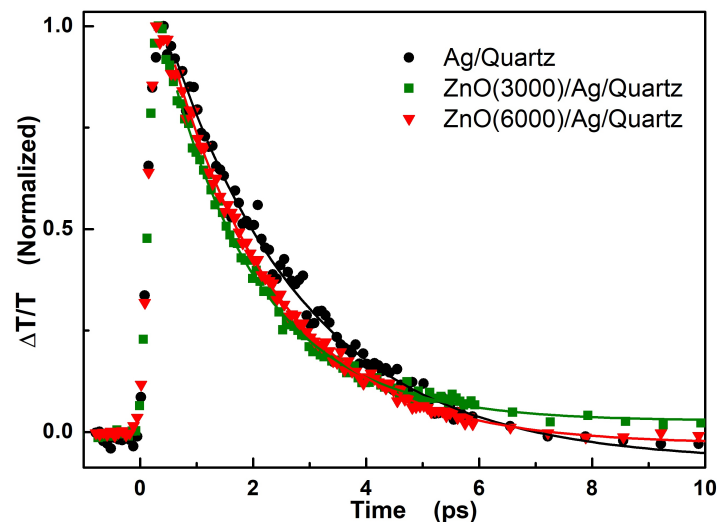


Fig 6.20 The transient transmittance of the Ag and Ag-ZnO nanoparticle films. The solid line shows the best fit to the decay part with single exponential function.

The maximum change in transmission ($\Delta T/T$) occur when the electrons reaches maximum change in temperature [205,206]. In the preset case all the samples reach its maximum by about 350 fs showing that the electron-electron thermalization process does not get modified by the additional coating of ZnO. If the coating of ZnO did form any compound with Ag or partial alloying, it would have resulted in modifying the electron-electron thermalization process. Since the coating is only on the top surface the electron-electron thermalization process which happens inside Ag is not expected to be changed.

At the end of thermalization, the electrons will be at a much higher temperature compared to that of the lattice. At later times the electrons will deliver the heat to the lattice through electron-phonon interaction. At the end of this electron-lattice thermalization, the overall temperature of electrons reduces since the specific heat capacity of the lattice is much higher than the electrons. This shows up as the decay of $\Delta T/T$ in the transient measurement [204-206]. The as grown Ag nanoparticle showed an electron-lattice thermalization time of the order of 2.4 ps. While after coating with ZnO the electron-lattice thermalization time was found to decrease slightly. This could be due to scattering of electrons at the Ag-ZnO interface [205,207]. Such scattering at interfaces and lattice defects are expected to increase the electron-lattice coupling [208]. Further studies on charge transfer characteristics in these composites is useful in realizing their other applications like photovoltaics, water splitting etc.

6.7 Summary

Large scale synthesis of ZnO nanorods was realized by low cost hydrothermal method. These nanorods were decorated with Au nanoparticles of different concentrations by photo-reduction of Au salt of varied concentrations. Au nanoparticles in pure metallic form were formed on the ZnO nanorods. Crystalline quality of ZnO nanorods was found to not much affected by annealing at high temperatures (up to 600°C) unlike core-shell nanoparticles. Photocatalytic response of Au decorated ZnO nanorods (with optimum loading of Au nanoparticles) produced larger degradation rate constant compared to pure ZnO nanorods. These Au decorated ZnO nanorods were further used for degradation of different dyes and their mixtures. Degradation of rhodamine dyes (Rh6G, RhB) was found to be slower compared to MB and MO dyes. For rhodamine dyes, the peak absorbance decay varied from exponential to linear at low dye concentration of 30 μM , which occurred $\geq 50 \mu\text{M}$ for MB and MO dyes. In the mixed solution, the degradation rate was found to decrease, when MB was mixed other dyes. At high pH condition ($\sim\text{pH}12$), faster degradation of MB within 10-20 min. lead to selective degradation of MB dye. Transient studies on Ag and Ag-ZnO nanoparticle films shows a slight reduction in electron-lattice thermalization time. This is attributed to the increased electron-lattice coupling at the interface between Ag and ZnO.

References

1. “Surface-Enhanced Raman Spectroscopy: Concepts and Chemical Applications”, S. Schlücker, *Angewandte Chemie*, **2014**, 53(19), 4756-4795.
2. “Detection of explosives by surface enhanced Raman scattering using substrate with a monolayer of ordered Au nanoparticles”, T. F. Chen, S. H. Lu, A. J. Wang, D. Zheng, Z. L. Wu, Y. S. Wang, *Appl. Surf. Sci.*, **2014**, 317, 940-945.
3. “Exploitation of localized surface plasmon resonance”, E. Hutter, J.H. Fendler, *Adv. Mater.*, **2004**, 16, 1685-1706.
4. “Localized Surface Plasmon Resonance Sensors”, K. M. Mayer, J. H. Hafner, *Chem. Rev.*, **2011**, 111, 3828-3857.
5. “Plasmon-Based Colorimetric Nanosensors for Ultrasensitive Molecular Diagnostics”, L. Tang, J. Li, *ACS Sens.* **2017**, 2(7), 857-875.
6. “Plasmonic nanoantennas”, V. Giannini, A.I. Fernández-Domínguez, S.C. Heck, S.A. Maier, *Chem. Rev.*, **2011**, 111, 3888-3912.
7. “State-of-the-art progress in diverse heterostructured photocatalyst towards promoting photocatalytic performance”, H. Li, Y. Zhong, W. Tu, J. Ye, Z. Zou, *Adv. Funct. Mat.*, **2015**, 25, 998-1013.
8. “Plasmon-induced hot-electron generation at nanoparticle/metal-oxide interfaces for photovoltaic and photocatalytic devices”, C. Clavero, *Nature Photonics*, **2014**, 8, 95-103.
9. “Plasmonics for improved photovoltaic devices”, H.A. Atwater, A. Polman, *Nature Materials*, **2010**, 9, 205-213.
10. “Plasmonics: merging photonics and electronics at nanoscale dimensions”, Ozbay E, *Science*, **2006**, 311,189-193.
11. “Plasmonics-Fundamentals and Applications”, S. A. Maier, *Springer*, **2007**.
12. “Optical Properties of Metal Clusters”, U. Kreibig, M. Vollmer, *Springer-Verlag*, Berlin, **1995**.
13. “Searching for better plasmonic materials”, West, P. R. et al., *Laser Photon. Rev.* **2010**, 4, 795–808
14. “I. H. Noble metals on the nanoscale: optical and photothermal properties and some applications in imaging, sensing, biology, and medicine”, Jain, P. K., Huang, X. & El-sayed, *Acc. Chem. Res.* **2008**, 41,1578-1586.
15. “K. S. Gold and silver nanoparticles in sensing and imaging sensitivity of plasmon response to size, shape, and metal composition”, El-Sayed, M. A. & Lee, *J. Phys. Chem. B*, **2006**, 110,19220-19225.

16. “Applications of gold nanoparticles in cancer nanotechnology”, W. Cai, T. Gao, H. Hong, J. Sun, *Nanotechnol Sci Appl.* **2008**, 1, 17-32.
17. “Quantifying the Efficiency of Plasmonic Materials for Near-Field Enhancement and Photothermal Conversion”, A. Lalis, G. Tessier, J. Plain, G. Baffou, *J. Phys. Chem. C*, **2015**, 119, 25518-25528.
18. “A review of the optical properties of alloys and intermetallics for plasmonics”, M. G. Blaber, M. D. Arnold, M. J. Ford, *J. Phys.: Condens. Matter*, **2010**, 22, 143201.
19. “Introduction to Solid State Physics, 6th edition, John Wiley & Sons”, C. Kittel, Inc., New York, **1986**.
20. “Absorption and scattering of light by small particles”, C. F. Bohren and D. R. Huffman, *Wiley-Interscience*, New York, **1983**.
21. “Surface Plasmons on Metal Nanoparticles: The Influence of Shape and Physical Environment”, C. Noguez, *J. Phys. Chem. C*, **2007**, 111, 10, 3806-3819.
22. “Maneuvering the surface plasmon resonance of silver nanostructures through shape-controlled synthesis”, Wiley, B. J. et al., *J. Phys. Chem. B*, **2006**, 110, 15666-15675.
23. “The Optical Properties of Metal Nanoparticles: The Influence of Size, Shape, and Dielectric Environment”, K. L. Kelly, E. Coronado, L. L. Zhao and G. C. Schatz, *J. Phys. Chem. B*, **2003**, 107, 668.
24. “Modelling the optical response of gold nanoparticles”, V. Myroshnychenko et al, *Chem. Soc. Rev.*, **2008**, 37, 1792-1805.
25. “Light trapping in mesoporous solar cells with plasmonic nanostructures”, W. R. Erwin, H. F. Zarick, E. M. Talbert, R. Bardhan, *Energy Environ. Sci.*, **2016**, 9, 1577-1601.
26. <https://www.sigmaaldrich.com/technical-documents/articles/materials-science/nanomaterials/gold-nanoparticles.html>.
27. https://www.aatbio.com/resources/extinction-coefficient/Rhodamine_6G.
28. “Design principles for particle plasmon enhanced solar cells”, K. R. Catchpole and A. Polman, *Appl. Phys. Lett.*, **2008**, 93, 191-113.
29. “H. A. Plasmonic Nanostructure Design for Efficient Light Coupling into Solar Cells”, Ferry, V. E., Sweatlock, L. A., Pacifici, D., Atwater, *Nano Lett.*, **2008**, 8, 4391-4397.
30. “Principles of nano-optics”, L. Novotny, B. Hecht, *Cambridge University Press*, New York, **2006**.
31. “Handbook of Optical Constants of Solids”, E. D. Palik (editor), *Academic Press*, San Diego, **1985**.
32. “Chemically Isolating Hot Spots on Concave Nanocubes”, M. Rycenga, M.R. Langille, Michelle L. Personick, T. Ozel, C.A. Mirkin, *Nano Lett.*, **2012**, 12, 6218-6222.

33. "Synthesis and optical properties of silver nanobars and nanorice", Wiley, B. J. et al., *Nano Lett.* **2007**, 7, 1032-1036.
34. "Z. Y. Mesoscopic and microscopic strategies for engineering plasmon-enhanced Raman scattering", Li, *Adv. Opt. Mater.*, **2018**, 6, 170-1097.
35. "Observation of near-field coupling in metal nanoparticle chains using far-field polarization spectroscopy", S.A. Maier, M.L. Brongersma, P.G. Kik, H.A. Atwater, *Phys. Rev. B*, **2002**, 65, 193-408.
36. "Surface enhanced fluorescence and Raman scattering by gold nanoparticle dimers and trimers", Z. Zhang, P. Yang, H. Xu, H. Zheng, *J Appl. Phys.*, **2013**, 113, 033-102.
37. "Active control of plasmonic colors: emerging display technologies", K. Xiong, Daniel Tordera, Magnus P Jonsson and Andreas B Dahlin", *Rep. Prog. Phys.*, **2019**, 82, 024501, 1-18.
38. "Plasmonic color generation", A. Kristensen et al, *Nature Rev. Materials*, **2016**, 2, 16088, 1-14.
39. "Nanoplasmonic sensing of metal-halide complex formation and the electric double layer capacitor", Dahlin A B, Zahn R, Voros J, *Nanoscale* **4**, **2012**, 2339-51.
40. "Conducting polymer electrochemical switching as an easy means for designing active plasmonic devices", Leroux Y R, Lacroix J C, Chane-Ching K I, Fave C, Felidj N, Levi G, Aubard J, Krenn J R, Hohenau A, *J. Am. Chem. Soc.*, **2005**, 127, 16022.
41. "Electromechanically tunable plasmonic nanowires operating in visible wavelengths", M. Miyata, A. Kaijima, Y. Nagasaki, J. Takahara, *JACS Photonics* **2016**, 3, 2268-74.
42. "A mechanically tunable plasmonic structure composed of a monolayer array of metal-capped colloidal spheres on an elastomeric substrate", X.L. Zhu, L. Shi L, X.H. Liu, J. Zi, Z.L.Wang, *Nano. Res.*, **2010** 3 807-812.
43. "Plasmonic Hot Electron Solar Cells: The Effect of Nanoparticle Size on Quantum Efficiency", P. Reineck, D. Brick, P. Mulvaney, U. Bach, *J. Phys. Chem. Lett.* **2016**, 7, 20, 4137-4141.
44. "Detection of chemical pollutants in water using gold nanoparticles as sensors: a review", C. Wang, Chenxu Yu, *Rev Anal Chem.*, **2013**, 32(1): 1-14.
45. "One-step, room temperature, colorimetric detection of mercury (Hg²⁺) using DNA/nanoparticle conjugates", Xue, X. Wang, F. Liu, X., *J. Am. Chem. Soc.* **2008**, 130, 3244-3245.
46. "A colorimetric lead biosensor using DNAzyme-directed assembly of gold nanoparticles" J. Liu, Y. Lu, *J. Am. Chem. Soc.*, **2003**, 125, 6642 - 6643.
47. "A. Colorimetric nitrite and nitrate detection with gold nanoparticle probes and kinetic end points", W. L. Daniel, M.S. Han, J.S. Lee, C. Mirkin, *J. Am. Chem. Soc.*, **2009**, 131, 6362 - 6363.
48. "Silver nanoparticles as a cyanide colorimetric sensor in aqueous media" S. Hajizadeh, K. Farhadi, M. Forougha, R. Sabzia, *Anal. Methods*, **2011**, 3, 2599-2603.

49. “Highly precise plasmonic and colorimetric sensor based on enzymatic etching of nanospheres for the detection of blood and urinary glucose”, H.Jang, D.Min, *RSC Adv.*, **2015**,5, 14330-14332.
50. “Optical organophosphate sensor based upon gold nanoparticle functionalized fumed silica gel”, J.D. Newman, J.M. Roberts, G.J. Blanchard, *Anal. Chem.*, **2007**, 7, 3448 - 3454.
51. “Enzyme-linked immunosorbent assay and colloidal gold immunoassay for ochratoxin A: investigation of analytical conditions and sample matrix on assay performance.” X.H. Wang, T. Liu, N. Xu, Y. Zhang, S. Wang, *Anal. Bioanal. Chem.* **2007**, 289, 903- 911.
52. “Selective detection of mercury (II) ion using nonlinear optical properties of gold nanoparticles”, G. K Darbha, A.K. Singh, U.S. Rai, E. Yu, P.C. Ray, *J. Am. Chem. Soc.*, 2008, 130, 8038-8043.
53. “Thermo-plasmonics: using metallic nanostructures as nano-sources of heat”, G. Baffou, R. Quidant, *Laser & Photonics reviews*, **2013**, 7, 171-187.
54. “3D self-assembly of aluminium nanoparticles for plasmon-enhanced solar desalination”, Lin Zhou, Yingling Tan, Jingyang Wang, Weichao Xu, Ye Yuan, Wenshan Cai, Shining Zhu & Jia Zhu, *Nature Photonics*, **2016**, 10, 393-398.
55. “The importance of plasmonic heating for the plasmon-driven photodimerization of 4-nitrothiophenol”, R.M. Sarhan, W. Koopman, R. Schuetz, T. Schmid, F. Liebig, J.Koetz, M. Bargheer, *Scientific Reports*, **2019**, 9, 3060.
56. “Preparation of Large-Area Uniform Silicon Nanowires Arrays through Metal-Assisted Chemical Etching,” M. Zhang, K. Peng, X. Fan, J.Jie, Rui-Qin Zhang, Shuit-Tong Lee, Ning-Bew Wong, *J. Phys. Chem. C*, **2008**, 112, 12, 4444-4450.
57. “Principles of Surface-Enhanced Raman Spectroscopy: And Related Plasmonic Effects”, Eric Le Ru and Pablo Gabriel Etchegoin, *Elsevier Science*, **2008**.
58. “Surface-enhanced Raman scattering: from noble to transition metals and from rough surfaces to ordered nanostructures”, Z.Q. Tian, B. Ren, D.Y. Wu, *J. Phys. Chem. B* **2002**, 106, 37.
59. “Highly sensitive, uniform, and reproducible surface-enhanced Raman spectroscopy from hollow Au-Ag alloy nanourchins”, Z. Liu, *et al. Adv. Mater.* **26**, 2431-2439 (2014).
60. “Nanosphere arrays with controlled sub-10-nm gaps as surface-enhanced Raman spectroscopy substrates”, H. Wang, C. S. Levin, N. J. Halas, *J. Am. Chem. Soc.*, **2005**, 12, 14992-14993.
61. “Thickness-gradient dependent Raman enhancement in silver island films”, T. W. H. Oates, S. Noda, *Appl. Phys. Lett.*, **2009**, 94, 053106.
62. “Mesoscopic and microscopic strategies for engineering plasmon-enhanced Raman scattering”, Z.Y. Li, *Adv. Opt. Mater.*, **2018**, 6,1701097.

63. "Controlled fabrication of silver nanoneedles array for SERS and their application in rapid detection of narcotics", Yang, Y. et al., *Nanoscale*, **2012**, 4, 2663-2669.
64. "Rigorous justification of the $|E|^4$ enhancement factor in Surface Enhanced Raman Spectroscopy" E.C. Le Ru, P.G. Etchegoin, *Chem. Phys. Lett.*, **2006**, 423, 63-66.
65. "Steering charge kinetics in photocatalysis: intersection of materials syntheses, characterization techniques and theoretical simulations", S. Bai, J. Jiang, Q. Zhang, Y. Xiong, *Chem. Soc. Rev.*, **2015**, 44, 2893.
66. "Review on the criteria anticipated for the fabrication of highly efficient ZnO-based visible-light-driven photocatalysts", M. Pirhashemi, A. Habibi-Yangjeh, S.R. Pouran, *J. Ind. Eng. Chem.* **2018**, 62, 1-25.
67. "Review on the improvement of the photocatalytic and antibacterial activities of ZnO", K. Qi, Bei Cheng, Jiaguo Yu, Wingkei Ho, *J. Alloys and Compounds*, **2017**, 727, 792-820.
68. "Au-ZnO bullet-like heterodimer nanoparticles: synthesis and use for enhanced nonenzymatic electrochemical determination of glucose", D.R. Kumar, D. Manoj, J. Santhanalakshmi, *RSC Adv.* **2014**, 4, 8943-8952.
69. "ZnO nanodisks decorated with Au nanorods for enhanced photocurrent generation and photocatalytic activity", P. She et al, *New J. Chem.*, **2018**, 42, 3315-3321.
70. "Fabrication of Au/GO/ZnO composite nanostructures with excellent photocatalytic performance", Ji-Eun Lee, N.T. Khoa, S.W. Kim, E.J. Kim, S.H. Hahn, *Materials Chemistry and Physics*, **2015**, 164, 29-35.
71. "Influence of temperature dependent morphology nonlocalized surface plasmon resonance in ultra-thin silver island films", N. Venugopal, A. Mitra, *Appl. Surf.Sci.*, **2013**, 285, 357-372.
72. "Formation of gold nanoparticles in heat-treated reactive co-sputtered Au-SiO₂ thin films", P. Sangpour, O. Akhavan, A.Z. Moshfegh, M. Roozbehi, *Appl. Surf. Sci.* **2007**, 254, 286-290.
73. "Characterization of TiO₂/Au/TiO₂ films deposited by magnetron sputtering on polycarbonate substrates", D. Kim, *Appl. Surf.Sci.*, **2010**, 257, 704-707.
74. "Preparation and characterization of surface plasmon resonance tunable gold and silver films", R Gupta, M.J.Dyer and W.A.Weimer, *J. of Appl. Phys*, **2002**, 92, 5264-5271.
75. "Ultrathin, ultrasmooth, and low-loss films via wetting and annealing", W. Chen, K.P. Chen, M.D. Thoreson, A.V. Kildishev, V.M. Shalaev, *Appl. Phys. Lett.*, **2010**, 97, 211-107.
76. "A study of growth and thermal de-wetting behaviour of ultra-thin gold films using transmission electron microscopy", Sudheer, P. Mondal, V. N. Rai, A. K. Srivastava, *AIP Advances*, **2017**, 7:7, 075303, 1-13.
77. "Influence of process parameters on surface plasmon resonance characteristics of

- densely packed gold nanoparticle films grown by pulsed laser deposition”, S. Verma, B. T. Rao, S. Rai, V. Ganesan, L. M. Kukreja, *Appl. Surf. Sci.*, **2012**, 258, 4898-4905.
78. “Pulsed Laser Deposition of Thin Films: Applications-Led Growth of Functional Materials”, R. Eason, *John Wiley & Sons, Inc.*, Hoboken, New Jersey, **2006**.
 79. “Dynamics of the plume produced by nanosecond ultraviolet laser ablation of metals”, B. Toftmann, J. Schou, J.G. Lunney, *Phys. Rev. B*, **2003**, 67, 104-101.
 80. “Pulsed laser deposition of nanoparticle films of Au”, T. Donnelly, S. Krishnamurthy, K. Carney, N. McEvoy, J.G. Lunney, *Appl. Surf. Sci.*, **2007**, 254, 1303-1306.
 81. “Silver-gold compound metal island films prepared by using a two-step evaporation method”, K. Baba, T. Okuno, M. Miyagi, *Appl. Phys. Lett.*, **1993**, 62, 437.
 82. “Electronic Structure of Noble-Metal-Noble-Metal Alloys”, D. Beaglehole, *Phys. Rev. B*, **1972**, 6, 4883.
 83. “Wavelength Tuning of Surface Plasmon Resonance by Annealing Silver-Copper Nanoparticles”, M. Hirai and A. Kumar, *J. Appl. Phys.*, **2006**, 100, 014-309.
 84. “Dielectric functions of growing silver films determined using dynamic in-situ spectroscopic ellipsometry”, T. W. H. Oates, L. Ryves, M. M. M. Bilek, *Optics Express*, **2008**, 16, 2302-2314.
 85. “Spectroscopic Ellipsometry: Principles and Applications”, H. Fujiwara, *John Wiley & Sons Ltd*, England, **2007**.
 86. “Optical effect of the substrate on anomalous absorption of aggregated silver films”, T Yamaguchi, S. Yoshida and A. Kinbara, *Thin Solid Films*, **1974**, 21, 173-187.
 87. “Substrate Effect on the Plasmon Resonance of Supported Flat Silver Nanoparticles”, M. Valamanesh, Y. Borensztein, C. Langlois, E. Lacaze, *J. Phy. Chem. C*, **2011**, 115, 2914-2922.
 88. “Optical properties of closely packed nanoparticle films: spheroids and nanoshells”, V.A. Fedotov, V. I. Emel’yanov, K. F. Macdonald, N. I. Zheludev, *J. Opt. A: Pure Appl. Opt*, **2004**, 6, 155-160.
 89. “Introduction to the Maxwell Garnett approximation: tutorial”, V. Markel. *Journal of the Optical Society of America, A. Optics, Image Science, and Vision, Optical Society of America*, **2016**, 33(7).
 90. “Gold nanoparticle thin films”, T. Ung, L.M. Liz-Marzán, P. Mulvaney, *Colloids Surf. A*, **2002**, 202, 19-126.

91. "The effect of atmospheric tarnishing on the optical and structural properties of silver nanoparticles", T.W.H. Oates, M. Losurdo, S. Noda, K. Hinrichs, *J. Phy.D: Appl. Phys.* **2013**, 46, 145-308.
92. "Rapid tarnishing of silver nanoparticles in ambient laboratory air", McMahon, M. & Lopez, R. & Meyer III, Harry & Feldman, Leonard & Haglund, Richard. *Applied Physics B.*, **2005**, 80, 915-921.
93. "Modelling of Formation of Gold Nanoparticles by Citrate Method", S. Kumar, K. S. Gandhi, R. Kumar, *Ind. Eng. Chem. Res.*, **2007**, 46, 10, 3128-3136.
94. "Studies on interdependent optical properties of Rhodamine 6G dye and gold nanoparticles at different dilutions of aqueous solutions", S. Verma, B.T. Rao, A.K. Srivastava, H.S. Patel, S. Satapathy, M.P. Joshi, V.K. Sahu, L.M. Kukreja, J. Lumin, **2014**, 155, 153-164.
95. "Effect of citrate ratio and temperature on gold nanoparticle size and morphology", M. Tran, R. DePenning, M. Turner, S. Padalkar, *Materials Research Express*, **2016**, 3(10).
96. "What factors control the size and shape of silver nanoparticles in the citrate ion reduction method", Z.S. Pillai, P.V. Kamat, *J. Phys. Chem. B*, **2004**, 108, 945-951.
97. "Formation kinetics of silver triangular nanoplates", T.C.R. Rocha, H. Winnischofer, E. Westphal, D. Zanchet, *J. Phys. Chem. C*, **2007**, 111, 2885-2891.
98. "Photovoltage mechanism for room light conversion of citrate stabilized silver nanocrystal seeds to large nanoprisms", X. Wu, P.L. Redmond, H. Liu, Y. Chen, M. Steigerwald, L. Brus, *J. Am. Chem. Soc.*, **2008**, 130 (29), 9500-9506.
99. "Facile approach to synthesize Au@ZnO core-shell nanoparticles and their application for highly sensitive and selective gas sensors", S.M. Majhi, P. Rai, Y. Yu, *ACS Appl. Mat. Interfaces*, **2015**, 7 (18), 9462-9968.
100. "Core-shell Au@ZnO nanoparticles derived from Au@MOF and their sub-ppm level acetone gas-sensing performance", W. Li, X. Wu, N. Han, J. Chen, W. Tang, Y. Chen, *Powder Technol.* **2016**, 304, 241-247,

101. "Nano-epitaxial growth of uniform and precisely size-tunable core/shell nanoparticles and their enhanced plasmon driven photocatalysis", M. Wang, X. Pang, D. Zheng, Y. He, L. Sun, C. Lin, Z. Lin, *J. Mater. Chem. A*, **2016**, 4, 7190-7199.
102. "Investigating the multiple roles of polyvinylpyrrolidone for a general methodology of oxide encapsulation", H. Sun, et al., *J. Am. Chem. Soc.*, **2013**, 135, 9099-9110.
103. "Unravelling surface plasmon decay in coreshell nanostructures toward broadband light-driven catalytic organic synthesis". H. Huang, L. Zhang, Z. Le, R. Long, C. Zhang, Y. Lin, K. Wei, C. Wang, L. Chen, Zhi-Yuan Li, Q. Zhang, Y. Luo, Y. Xiong, *J. Am. Chem. Soc.*, **2016**, 138, 6822-6828,
104. "Shape and Size Effects of ZnO Nanocrystals on Photocatalytic Activity", A. McLaren, T. Valdes-Solis, G. Li, S. Chi Tsang, *J. Am. Chem. Soc.*, **2009**, 131, 12540-12541.
105. "Ultra-selective acetone-gas sensor based ZnO flowers functionalized by Au nanoparticle loading on certain facet", P. Wang, T. Dong, C. Jia, P. Yang, *Sens. Actuators B Chem.*, **2019**, 288, 1-11.
106. "Ascorbic acid assisted growth of high-quality M@ZnO: a growth mechanism and kinetics study", Y. Yang, S. Han, G. Zhou, L. Zhang, X. Li, C. Zou, S. Huang, *Nanoscale*, **2013**, 5, 11808-118819.
107. "Gas dynamics and film profiles in pulsed-laser deposition of materials", S. I. Anisimov, D. Bauerle, B. S. Lukyanchuk, *Phys. Rev. B*, **1993**, 48, 12076 -12081.
108. "Crystal orientation and surface morphology of face-centered-cubic metal thin films deposited upon single-crystal ceramic substrates using pulsed laser deposition", A. J. Francis, P. A. Salvador, *J. Mat. Res*, **2007**, 22, 89-102.
109. "Influence of the deposition parameters on the synthesis of nanocomposite materials produced by pulsed laser deposition", J. Gonzalo, R. Serna, J.M. Requejo, J. Sol'is, C.N. Afonso, A. Naudon, *App. Surface Science*, **2002**, 154-155, 449-453.
110. "Optical properties of discontinuous gold film: finite size effects", D. Dalacu, L. Martinu, *J. Opt. Soc. Am. B*, **2001**, 18, 85-92.

111. “Effective dielectric response of nanostructured layers”, H. Wormester, E. S. Kooij, B. Poelsema, *Phys. Stat. Sol. (a)*, **2008**, 205, 756-763.
112. “Effects of particle size and spacing on the optical properties of gold nanocrystals in alumina”, J. Wang, W. M. Lau, Q. Li, *J. Appl. Phys.*, **2005**, 97, 114303.
113. “The Physics of Thin Film Optical Spectra”, O Stenzel, Springer, **2005**.
114. “An analytical model for the optical properties of gold”, P.G.Etchegoin, E.C.Le Ru, M.Meyer, *J. Chem. Phy.*, **2006**, 125, 164705.
115. “Optical constants of the noble metals”, P. B. Johnson, R. W. Christy, *Phys. Rev. B*, **1972**, 6, 4370.
116. “Guide to using WVASE^R Spectroscopy ellipsometry data acquisition and analysis software J.A.Woollam”, Co. Inc., **2012**.
117. “Dielectric properties of ultrathin metal films around the percolation threshold”, M. Hövel, B. Gompf, and M. Dressel, *Phys. Rev. B*, **2010**, 81, 035-402.
118. “Thin Solid Films”, H. Martin, G. Bruno, M. Dressel, **2011**, 519, 2955-2958.
119. “Optical properties of Au-TiO₂ and Au-SiO₂ granular metal thin films studied by spectroscopic ellipsometry”, H. Bakkali, E. Blanco, M. Dominguez, M.B. de la Mora, C. Sanchez-Ake, *Appl. Surf. Sci.*, **2017**, 405, 240-246.
120. “Optical properties of gold island films-a spectroscopic ellipsometry study”, *Thin Solid Films*, M. Loncaric, J. Sancho-Parramon, H. Zorc, **2011**, 519, 2946-2950.
121. “Optical Properties of Solids”, F. Wooten, *Academic Press*, New York **1972**.
122. “Optical properties of metallic films for vertical-cavity optoelectronic devices”, A. D. Rakić, A. B. Djurišić, J. M. Elazar, and M. L. Majewski, *Appl. Opt.*, **1998**, 37, 5271-5283.
123. “Spectrophotometric Characterization of Thin Copper and Gold Films Prepared by Electron Beam Evaporation: Thickness Dependence of the Drude Damping

- Parameter”, O. Stenzel, S. Wilbrandt, S. Stempfhuber, D. Gäbler, S.J. Wolleb, *Coatings*, **2019**, 9, 181, 1-13.
124. “Tuning gold nanorod-nanoparticle hybrids into plasmonic fano resonance for dramatically enhanced light emission and transmission”, Z.-K. Zhou, et al., *Nano Lett.* **2011**, 11 (1), 49-55.
125. “Temperature-dependent morphology evolution and surface plasmon absorption of ultrathin gold island films”, H. Sun, M. Yu, G. Wang, X. Sun, J. Lian, *J. Phys. Chem. C*, **2012**, 116, 9000-9008.
126. “Evidence for capping-layer effects on the morphology and plasmon excitation of Ag nanoparticles”, D. Lantiat, D. Babonneau, S. Camelio, F. Pailloux, M.F. Denanot, *J. Appl. Phys.*, **2007**, 102, 113518.
127. “Coverage induced regulation of Au nanoparticles during pulsed laser deposition”, V. Resta, J. Gonzalo, C. N. Afonso, E. Piscopiello, J. G. Lopez, *J. Appl. Phys.* **2011**, 109, 094302.
128. “A general background subtraction algorithm for biomedical Raman spectroscopy”, M.K. Swami, H.S. Patel, S.K. Majumder, P.K Gupta, Proceedings 5th International Symposium on Modern Problems in Laser Physics, Novosibirsk, Russia, **2008**.
129. “Combinatorial surface-enhanced Raman spectroscopy ellipsometry of silver island films”, T. W. H. Oates, H. Sugime, S. Noda, *J. Phys. Chem. C*, **2009**, 113, 4820-4828.
130. “Plasmon coupling of R6G-linked gold nanoparticle assemblies for surface-enhanced Raman spectroscopy”, M. V. Rigo, J. Seoa, Wan-Joong Kim, S. Soo Jung, *Vibrational Spectroscopy*, **2011**, 57, 315-318.
131. “Plasmonic biocompatible silver-gold alloyed nanoparticles”, G.A. Sotiriou, G.D. Etterlin, A. Spyrogianni, F. Krumeich, J. Leroux, S.E. Pratsinis, *Chem. Commun.*, **2014**, 50, 13559-13562.
132. “Efficient dielectric function for FDTD simulation of the optical properties of silver and gold nanoparticles”, F.Hao P.Nordlander, *Chem. Phys. Lett.*, **2007**, 446, 115-118.

133. "Alloy formation of gold-silver nanoparticles and the dependence of the plasmon absorption on their composition", S. Link, Z.L. Wang, M.A. El-Sayad, *J. Phys. Chem. B*, **1999**, 103, 35-29.
134. "Online monitoring of alloyed bimetallic nanoparticle formation by optical spectroscopy" V. I. Belotelov, G. Carotenuto, L. Nicolais, A. Longo, G. P. Pepe, P. Perlo, A. K. Zvezdin, *J. Appl. Phys.* **2006**, 99, 044-304.
135. "Optical properties of $(\text{Au}_x\text{Ag}_{1-x})_n$ clusters embedded in alumina: Evolution with size and stoichiometry", M. Gaudry, J. Lerme, E. Cottancin, M. Pellarin, J. L. Vialle, M. Broyer, B. Prevel, M. Treilleux, and P. Melinon, *Phys. Rev. B*, **2001**, 64, 085407.
136. "An Analytic Model for the Dielectric Function of Au, Ag, and their Alloys", D. Rioux, S. Vallie`res, S. Besner, P. Mu~noz, E. Mazur, and M. Meunier, *Adv. Opt. Mater.* **2014**, 2, 176.
137. "Bimetallic Ag-Au nanoparticles: Extracting meaningful optical constants from the surface-plasmon extinction spectrum", Moskovits, I. Srnova-Sloufova, and B. Vlc`kova, *J. Chem. Phys.* **2002**, 116, 10435.
138. "The optical constants of Au, Ag and their alloys in the energy region from 2.4 to 4.4 eV", K. Ripken, *Z. Phys.*, **1972**, 228, 250.
139. "Comparative study of the electronic structure of noble-metal-noble-metal alloys by optical spectroscopy", J. Rivory, *Phys. Rev. B*, **1997**, 15, 3119.
140. "Surface enrichment of Ag atoms in Au/Ag alloy nanoparticles revealed by surface enhanced Raman scattering spectroscopy", K. Kim, K.L. Kim, S.J. Lee, *Chem. Phys. Lett.*, **2005**, 405, 77.
141. "Nanoparticles and intracellular applications of surface-enhanced Raman spectroscopy", J. Taylor, A. Huefner, L. Li, J. Wingfield, S. Mahajan, *Analyst*, **2016**, 141(17), 5037-5055.

142. "Dodecanethiol-Derivatized Au/Ag Bimetallic Nanoparticles: TEM, UV/VIS, XPS, and FTIR Analysis", S.W. Han, Y. Kim, K. Kim, *J. Coll. Inter. Sci.*, **1998**, 208, 272-278.
143. "Interaction of oxygen with supported Ag–Au alloy catalysts", D. I. Kondarides, X. E. Verykios, *J. Catal.*, **1996**, 158, 363.
144. "Charge redistribution in Au-Ag alloys from a local perspective" C. C. Tyson, A. Bzowski, P. Kristof, M. Kuhn, R. Sammynaiken, and T. K. Sham, *Phys. Rev. B*, **1992**, 45, 8924.
145. "Charge Flow and Compensation in Gold Alloys", R. E. Watson, J. Hudis, and M. L. Perlman, *Phys. Rev. B*, **1971**, 4, 4139.
146. "Handbook of X-Ray Photoelectron Spectroscopy", C. D. Wagner, W. M. Riggs, L. E. Davis, J. F. Moulder, Perkin-Elmer Corp., Minnesota, USA, **1979**.
147. "Synergistic Effect in an Au-Ag Alloy Nanocatalyst: CO Oxidation" J. Liu, A. Q. Wang, Y. Chi, H. P. Lin, and C. Mou, *J. Phys. Chem. B*, **2005**, 109(1), 40.
148. "Au, Ag and Au:Ag colloidal nanoparticles synthesized by pulsed laser ablation as SERS substrates" M. Vinod, K.G. Gopchandran, *Progress in Natural Science: Materials International*, **2014**, 24, 569-578.
149. "On the growth mechanism of pulsed-laser deposited vanadium oxide thin films", C.V. Ramana, R.J. Smith, O.M. Hussain, C.M. Julien, *Mater. Sci. Eng. B*, **2004**, 111, 218-225.
150. "Photon emission spectroscopy of single oxide-supported Ag-Au alloy clusters" W. Benten, N. Nilius, N. Ernst, H.J. Freund, *Phys. Rev. B*, **2005**, 72, 045403.
151. "Size dependence of the plasmonic near field measured via single nanoparticle photo-imaging", C. Deeb, X. Zhou, J. Plain, G.P. Wiederrecht, R. Bachelot, *J. Phys. Chem. C* 117 (20) (**2013**) 10669-10676.
152. "Optimal size of silver nanoparticles for surface enhanced Raman spectroscopy", K.G. Stamplecoskie, J.C. Scaiano, *J. Phys. Chem. C*, **2011**, 115, 1403-1409.

153. "Controlling the synthesis and assembly of silver nanostructures for plasmonic Applications", M. Rycenga, C.M. Cobley, J. Zeng, W. Li, C.H. Moran, Q. Zhang, D. Qin, Y. Xia, *Chem. Rev.*, **2011**, 111, 3669-3712.
154. "Rapid transformation from spherical nanoparticles, nanorods cubes, or bipyramids to triangular prisms of silver with PVP, citrate and H₂O₂", M. Tsuji, S. Gomi, Y. Maeda, M. Matsunaga, S. Hikino, K. Uto, T. Tsuji, H. Kawazumi, *Langmuir* **2012**, 28, 8845-8861.
155. "Shape transformation of silver nanospheres to silver nanoplates induced by redox reaction of hydrogen peroxide" T. Parnklang, B. Lamlua, H. Gatemala, C. Thammacharoen, S. Kuimalee, B. Lohwongwatana, S. Ekgasit, *Mater. Chem. Phys.*, **2015**, 153, 127-134.
156. "Growth pathways of silver nanoplates in kinetically controlled synthesis: bimodal versus unimodal growth", M.H. Kim, D.K. Yoon, S.H. Im, *RSC Adv.*, **2015**, 5, 14266-14272.
157. "The relevance of light in the formation of colloidal metal nanoparticles", M. Grzelczak, L.M. Liz-Marzan, *Chem. Soc. Rev.*, **2014**, 43, 2089-2097.
158. "Controlling anisotropic nanoparticle growth through plasmon excitation", R. Jin, Y.C. Cao, E. Hao, G.S. Métraux, G.C. Schatz, C.A. Mirkin, *Nature*, **2003**, 425, 487-490.
159. "A systematic study of the synthesis of silver nanoplates: is citrate a magic reagent?", Q. Zhang, N. Li, J. Goebel, Z. Lu, Y. Yin, *J. Am. Chem. Soc.* **2011**, 133 (46), 18931-18939.
160. "Role of citric acid in the formation of silver nanoplates through a synergistic reduction approach", X.C. Jiang, C.Y. Chen, W.M. Chen, A.B. Yu, *Langmuir*, **2010**, 26, 64400-4408.
161. "Plasmon induced photochemical synthesis of silver triangular prisms and pentagonal bipyramids by illumination with light emitting diodes", M.D. Bordenave, A.F.

- Scarpettini, M.V. Roldán, N. Pellegrini, A.V. Bragas, *Mater. Chem. Phys.*, **2013**, 139, 100-106.
162. “Laser ablation synthesis in solution and size manipulation of noble metal nanoparticles”, V. Amendola, M. Meneghetti, *Phys. Chem. Chem. Phys.*, **2009**, 11, 3805-3821.
163. “What controls the composition and the structure of nanomaterials generated by laser ablation in liquid solution?”, V. Amendola, M. Meneghetti, *Phys. Chem. Chem. Phys.*, **2013**, 15, 3027-3046.
164. “Dynamics of silver nanoparticle formation and agglomeration inside the cavitation bubble after pulsed laser ablation in liquid”, P. Wagener, S. Ibrahimkuty, A. Menzel, A. Plech, S. Barcikowski, *Phys. Chem. Chem. Phys.*, **2013**, 15, 3068-3074.
165. “Interaction of colloidal nanoparticles with their local environment: the (ionic) nano environment around nanoparticles is different from bulk and determines the physic-chemical properties of the nanoparticles”, C. Pfeiffer, et al., *J. R. Soc. Interface*, **2014**, 11, 20130931.
166. “Rapid method to estimate the concentration of citrate capped silver nanoparticles from UV-visible light spectra”, D. Paramelle, A. Sadovoy, S. Gorelik, P. Free, J. Hopley, D.G. Fernig, *Analyst*, **2014**, 139, 4855-4861.
167. “Optical absorption spectra of nanocrystal gold molecules”, M.M. Alvarez, J.T. Khoury, T.G. Schaaff, M.N. Shafiqullin, I. Vezmar, R.L. Whetten, *J. Phys. Chem.*, **1997**, 101, 3706-3712.
168. “High chemical reactivity of silver nanoparticles toward hydrochloric acid”, L. Li, Y. Zhu, *J. Colloid Interface Sci.*, **2006**, 303, 415-418.
169. “Water-soluble gold nanoclusters with pH-dependent fluorescence and high colloidal stability over a wide pH range via co-reduction of glutathione and citrate”, W. Ding, Y. Liu, Y. Li, Q. Shi, H. Li, H. Xia, D. Wang, X. Tao, *RSC Adv.* **4**, **2014**, 22651-22659

170. "Photo-mediated synthesis of silver triangular bipyramids and prisms: the effect of pH and BSPP" J. Zhang, M.R. Langille, C.A. Mirkin, *J. Am. Chem. Soc.*, **2010**, 132 (35), 12502-12510.
171. "Colloidal gold and silver triangular nanoprisms", J.E. Millstone, S.J. Hurst, G.S. Metraux, J.I. Cutler, C.A. Mirkin, **2009**, *Small* 5 (6), 646-664.
172. "Photoinduced conversion of silver nanospheres to nanoprisms", R. Jin, Y.W. Cao, C.A. Mirkin, K.L. Kelly, G.C. Schatz, J.G. Zheng, *Science*, **2001**, 294, 1901-1903.
173. "Tuning the localized surface plasmon resonance of silver nanoplatelet colloids" A. Singh, J. Jayabalan, R. Chari, H. Srivastava, S. Oak, *Journal of Physics D: Applied Physics*, **2010**, 43, 335401.
174. "Silver nanodisk growth by surface plasmon enhanced photoreduction of adsorbed [Ag⁺]", M. Maillard, P. Huang, L. Brus, *Nano Lett.* 3, **2003**, (11), 1611-1615.
175. "Photovoltage and photocatalyzed growth in citrate-Stabilized colloidal silver nanocrystals", P.L. Redmond, X. Wu, L. Brus, *J. Phys. Chem. C*, **2007**, 111, 8942-8947.
176. "Surface-enhanced Raman scattering of methylene blue adsorbed on cap-shaped Silver nanoparticles". G. Xiao, S. Man, *Chem. Phys. Lett.*, **2007** 447, 305-309.
177. "Plasmonic photocatalysis", R.X. Zhang, Y. L. Chen, Ru-Shi Liu, D. P. Tsai, **2013**, 76(4), 046401.
178. "Noble metal-metal oxide nanohybrids with tailored nanostructures for efficient solar energy conversion, photocatalysis and environmental remediation", X. Liu, J. Iocozzia, Y. Wang, X. Cui, Y. Chen, S. Zhao, Z. Li, Z. Liu, *Energy Environ. Sci.*, **2017**, 10, 402-434.
179. "Application of fast-Fourier transform techniques to the discrete dipole approximation", J.J. Goodman, B.T. Draine, P.J. Flatau, *Opt. Lett.*, **1990**, 16 1198-1200.

180. "Discrete dipole approximation for scattering calculations", J. B.T Draine, P.J. Flatau, *Opt. Soc. Am. A*, **1994**, 11, 1491-1499.
181. "Scattering and absorption of light by nonspherical dielectric grains," E. M. Purcell and C. R. Pennypacker, *Astro-phys. J.*, **1973**, 186, 705-714.
182. "Effect of edge smoothening on the extinction spectra of metal nanoparticles", J. Jayabalan, A. Singh, R. Chari, *Appl. Phys. Lett.*, **2010**, 97, 041904.
183. "Aggregated nanoplatelets: optical properties and optically induced de-aggregation" ,J. Jayabalan, A. Singh, Ramachari, H. Srivastava, P.K. Mukhopadhyay, A.K. Srivastava, S.M. Oak, *J. Phy.: Cond. Mater.*, **2008**, 20, 445222.
184. "Correlating the structure, optical spectra, and electrodynamics of single silver nanocubes", J.M. McMahon, Y. Wang, L.J. Sherry, R.P. Van Duyne, L.D. Marks, S.K. Gray, G.C. Schatz, *J. Phys. Chem. C*, **2009**, 113(7), 2731-2735.
185. "Au@ZnO core-shell nanostructures with plasmon induced visible-light photocatalytic and photoelectrochemical properties", X. Shao, B. Li, B. Zhang, L. Shao, Y. Wu, *Inorg. Chem. Front.*, **2016**, 3, 934-943.
186. "Complete Au@ZnO core-shell nanoparticles with enhanced plasmonic absorption enabling significantly improved photocatalysis", Y. Sun, Y. Sun, T. Zhang, G. Chen, F. Zhang, D. Liu, W. Cai, Y. Li, X. Yang, C. Li, *Nanoscale*, **2016**, 8(20) 10774-10782.
187. "Shape effects in plasmon resonance of individual colloidal silver nanoparticles", J.J. Mock, M. Barbic, D.R. Smith, D.A. Schultz, S. Schultz, *J. Chem. Phy.*, **2002**, 116, 6755.
188. "Multifunctional Au-ZnO plasmonic nanostructures for enhanced UV photodetector and room temperature NO sensing devices", N. Gogurla, A.K. Sinha, S. Santra, S. Manna, S. Kumar, *Sci. Rep.*, **2014**, 4, 6483.
189. "Synthesis of structural and optical characterization of surfactant capped ZnO nanocrystalline", K. Raja, P.S. Ramesh, D. Geetha, T. Kokila, R. Sathiyapriya, *Spectrochim. Acta A. Mol. Biomol. Spectrosc.*, **2015**, 136 B, 155-161.

190. "Au-ZnO bullet-like heterodimer nanoparticles: synthesis and use for enhanced nonenzymatic electrochemical determination of glucose", D.R. Kumar, D. Manoj, J. Santhanalakshmi, *RSC Adv.*, **2014**, 4 8943-8952.
191. "Fabrication of Au/GO/ZnO composite nanostructures with excellent photocatalytic performance", Ji-Eun Lee, N.T. Khoa, S.W. Kim, E.J. Kim, S.H. Hahn, *Mater. Chem. Phys.*, **2015**, 164, 29-35.
192. "Photocatalytic degradation pathway of methylene blue in water, A. Houas, H. Lachheb, M. Ksibi, E. Elaloui, C. Guillard, J. Herrmann", *Appl. Catal. B: Environ.* **2001**, 31, 145-157.
193. "Photocatalytic degradation of azo dyes. Pilot plant investigation", A. Petrella, G. Boghetich, M. Petrella, P. Mastrorilli, V. Petruzzelli, D. Petruzzelli, *Ind. Eng. Chem. Res.*, **2014**, 53(7), 2566-2571.
194. "Correct use of the Langmuir–Hinshelwood equation for proving the absence of a synergy effect in the photocatalytic degradation of phenol on a suspended mixture of titania and activated carbon", N.G. Asenjo, R. Santamaría, C. Blanco, M. Granda, P. Álvarez, R. Menéndez, *Carbon*, **2013**, 55, 62-69.
195. "Synergistically enhanced photocatalysis from plasmonic and Co-catalyst in Au @ ZnO-Pd ternary core-shell nanostructures", B. Li, R. Wang, X. Shao, L. Shao, B. Zhang, *Inorg. Chem. Front.*, **2017**, 4, 2088-2096.
196. "Photocatalytic degradation of the herbicide imazapyr: do the initial degradation rates correlate with the adsorption kinetics and isotherms?", M.F. Atitar, A. Bouziani, R. Dillert, M. El Azzouzi, D.W. Bahnemann, *Catal. Sci. Technol.*, **2018**, 8, 985-995.
197. "Kinetic modeling of liquid phase photocatalysis on supported TiO₂ nanoparticles in a rectangular flat-plate photoreactor", A.R. Khataee, M. Fathinia, S. Aber, *Ind. Eng. Chem. Res.*, **2010**, 49, 12358-12364.

198. "Comparative study of the photocatalytic performance for the degradation of different dyes by ZnIn₂S₄: adsorption, active species, and pathways", T. Liu, L. Wang, X. Lu, J. Fan, X. Cai, B. Gao, R. Miao, J. Wang, Y. Lv, *RSC Adv.*, **2017**, 7, 12292-12300.
199. "Synthesis a novel multilamellar mesoporousTiO₂/ZSM-5 for photo-catalytic degradation of methyl orange dye in aqueous media", H. Znad, K. Abbas, S. Hena, Md.R. Awual, *J. Environ. Chem. Eng.*, **2018**, 6 (1), 218-227.
200. "Enhanced UV activation of electrochemically doped Ni in ZnO nanorods for room temperature acetone sensing, H. Ahn, Y. Wang, S. H. Jee, M. Park, Y. S. Yoon, and D. J. Kim," *Chem. Phys. Lett.*, **2011**, 511, 331-335.
201. "Fabrication of flexible dye-sensitised solar cells with photoanodes composed of periodically aligned single crystalline vertical ZnO NRs by utilising a direct metal transfer method," J. J. Kim, K. S. Kim, and G. Y. Jung, *J. Mater. Chem.*, **2011**, 21, 7730-7735.
202. "Mechanistic Insights into Photodegradation of Organic Dyes Using Heterostructure Photocatalysts" Y. Chiu *et al*, *Catalysts*, **2019**, 9, 430.
203. "Ultrafast Surface Plasmon Resonance Landau Damping and Electron Kinetics in Metal Nanoparticles" C. Guillon, P. Langot, N. Del Fatti, F. Vallee, *Ultrafast Phenomena in Semiconductors and Nanostructure Materials VIII*. **2004**, 65-77.
204. "Ultrafast Electron Dynamics and Optical Nonlinearities in Metal Nanoparticles", C. Voisin, C. Dimitris Christofilos, N. Del Fatti, F. Vallee, *J. Phys. Chem. B* 2001, 105, 2264-2280.
205. "Origin and Time Dependence of Higher-order Nonlinearities in Metal Nanocomposites" J. Jayabalan, *J. Opt. Soc. Am B*, **2011**, 28, 2448-2455.
206. "In Non-Equilibrium Dynamics of Semiconductors and Nanostructures", F. Vallee, *CRC Press: New York*, **2005**, 101-142.

207. "Counting the Electrons Hopping in Ultrafast Time Scales in an Ag-CdTe Hybrid Nanostructure", A. Singh, S. Gurung, R. Chari, J. Jayabalan, *J. Phys. Chem. C*, DOI: 10.1021/acs.jpcc.9b07426.
208. "Plasmonic coupling at a metal/semiconductor interface" T. Shijing *et al*, *Nature Photonics*, **2017**, 11, 806-812.

Thesis Highlight

Name of the Student: Shweta Verma

Name of the CI/OCC: RRCAT

Enrolment No.: PHYS03201504012

Thesis Title: Studies on plasmonic responses of metal nanoparticles of varied morphologies and their interaction with semiconductor nanostructures

Discipline: Physical Sciences **Sub-Area of Discipline:** Nanoparticles and applications

Date of viva voce: 04-07-2020

Noble metal nanoparticles (NPs) show strong optical response and enhanced electric near field due to localized surface plasmon resonance (LSPR) excitation. This thesis addresses simplified growth methods based on pulsed laser ablation for Au and Ag-Au alloy NP films and colloidal Ag NPs with tunable optical response suitable for SERS at multiple excitation wavelengths. Effect of different morphological parameters, particle-particle and particle-substrate interactions on variation of LSPR response of NP films has been determined using effective medium theory and verified with experimental results. By varying film thickness or altering alloy composition, LSPR tuning can be controlled close to SERS excitation wavelength to obtain maximum SERS signal for trace detection of 500 nanomolar Rhodamine 6G dye. The produced SERS substrates has potential for trace molecular detection for food safety, narcotics, explosives etc.

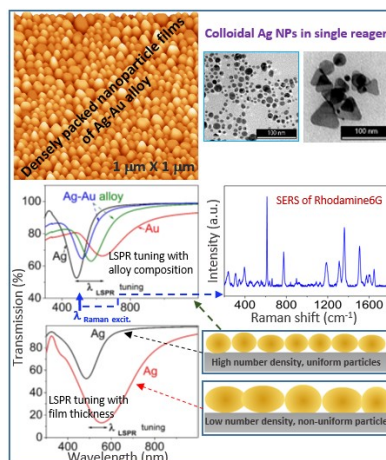


Fig. Densely packed Ag-Au NP films and Ag NP for SERS based detection of Rh6G dye [500 nm].

Au-ZnO nanocomposites have been shown to be promising for various light harvesting applications. In this work, optimum conditions for photocatalytic degradation of different dyes

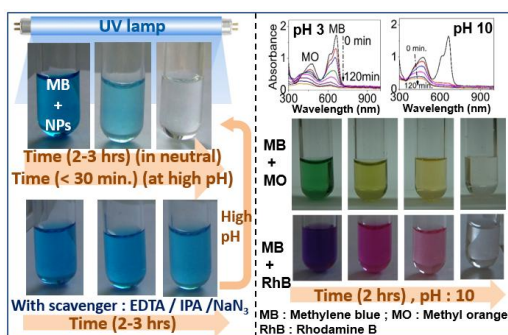


Fig. Au-ZnO NPs for photocatalytic degradation of MB dye and binary mixtures. Degradation is selective at high pH and simultaneous at low pH.

and their mixtures with Au-ZnO core-shell and Au NP decorated ZnO nanorods has been determined. Study with different scavengers revealed hydroxyl radical playing prominent role in dye degradation. pH strongly influenced surface charge characteristics of photocatalyst, as a result cationic dye has shown faster degradation at high pH, even in case of binary mixture with anionic or zwitterionic dyes leading to selective degradation. Using Langmuir Hinshelwood model, concentration range of different dyes for the limiting cases for first and zeroth order degradation kinetics has been determined. These environmental friendly Au-ZnO NPs with the adopted scalable synthesis and dye degradation in low power UV light shows this method can be cost effective for treatment of dye effluents.

and their mixtures with Au-ZnO core-shell and Au NP decorated ZnO nanorods has been determined. Study with different scavengers revealed hydroxyl radical playing prominent role in dye degradation. pH strongly influenced surface charge characteristics of photocatalyst, as a result cationic dye has shown faster degradation at high pH, even in case of binary mixture with anionic or zwitterionic dyes leading to selective degradation. Using Langmuir Hinshelwood model, concentration